The Effects of Single- and Dual-Energy Quantitative Computed Tomography on Volumetric Bone Mineral Density Assessment and Strain Analysis in the Proximal Humerus

by

Daniel Beshay

A thesis

presented to the University of Waterloo

in fulfillment of the

thesis requirement for the degree of

Master of Science

in

Kinesiology

Waterloo, Ontario, Canada, 2024

© Daniel Beshay 2024

Author's Declaration

I hereby declare that I am the sole author of this thesis. This is a true copy of the thesis, including any required final revisions, as accepted by my examiners.

I understand that my thesis may be made electronically available to the public.

Abstract

A common and difficult orthopedic injury, proximal humerus fractures frequently require surgery to restore functional shoulder motion. For optimal patient outcomes and to inform treatment choices, accurate evaluation of fracture stability and healing progress is essential. A thorough combination of the use of computational loads through finite element modeling (FEM) with innovative imaging methods to evaluate proximal humerus fractures was used to predict their fracture locations based on volumetric bone mineral density (vBMD).

To quantify fracture characteristics, vBMD, and morphological changes related to proximal humerus fractures, 2 different imaging modalities were used. The effectiveness of single energy quantitative (SEQCT) and dual-energy quantitative computed tomography (DEQCT) was compared. BONE and STD reconstruction kernels, an algorithmic procedure, were parameters that were changed post-processing to alter the frequency content of images obtained from the SEQCT and DEQCT scanners. These imaging techniques enable a multidimensional study, giving rise to a deeper comprehension of fracture locations, bone quality, and provide preliminary steps to inform risk factors.

To achieve this objective, fourteen cadaveric shoulders (n = 7 left, n = 7 right) were scanned under each scanning modality and post-processed into both BONE and STD reconstruction kernel, respectively. Four different images were created per shoulder scan: SEQCT BONE/STD and DEQCT BONE/STD, creating a total of 56 different possible images. Density in volumetric bone mineral density (vBMD) was calculated in the humeral head, metaphysis, and diaphysis regions, for each imaging modality. Image processing software was utilized to create 3D models of the humerus and highlighting the selected regions. Specimen-specific slope/intercept was used to convert from native Hounsfield Units (HU) to equivalent vBMD [mg_{K2HPO4}/cm^3]. Strain measurements were calculated using FEMs derived from each proximal humerus model and are reported as maximum and minimum principal strain through visual representations and histograms according to each region, showcasing differences in them between BONE and STD reconstruction kernel.

BONE reconstruction kernel showcased higher values in both HU and vBMD measures than STD reconstruction kernel in SEQCT with significant differences seen respectively between reconstruction kernels in HU and vBMD ($p < 0.05$) in all three regions. Strong correlations ($R^2 = 0.99$) between BONE and STD image-based density (HU and vBMD) by bone region (Humeral Head, Metaphysis, and Diaphysis) was observed in SEQCT. On the other hand, BONE reconstruction kernel

vBMD was not higher than STD reconstruction kernel in all regions when looking at individual cadavers in DEQCT. Only the metaphysis showcased this whereas the diaphysis had four models that didn't follow this trend and one model in the humeral head. vBMD differences arise from anatomical differences while scanning such either as a full torso or an isolated shoulder. Strong correlations (R^2 = 0.99 & 0.98) between BONE and STD image-based density (vBMD) in the humeral head and metaphysis, respectively. The r-squared was lower in the diaphysis region (0.86).

Fracture location predictions are possible from the FEM visual representation in both maximum/minimum principal strain with the aid of the figure showcasing strain levels in the three regions. These qualitative and respective quantitative data are cadaver dependent as each cadaver was influenced according to anatomical differences such as bone quality, comorbidities, age, patient activity levels and more. The FE models generated showcased that 7 out of the 7 models generated from SEQCT predict fracture location in the metaphysis region and 7 out of the 7 models generated from DEQCT also predict fracture location in the metaphysis region.

As they clarify the significance of fracture morphology, bone quality, and loading circumstances on fracture location, the study's findings shed light on the relationship between imaging parameters and biomechanics of proximal humerus fractures. This research also seeks to assist physicians in choosing the best imaging approach for precise fracture characterization and treatment planning by comparing the performance of several imaging modalities.

Ultimately, the combination of innovative imaging methods with finite element modeling can increase our ability to understand proximal humerus fractures by providing us knowledge on the optimal imaging modality, with the long-term objective of enabling better clinical outcomes for patients with these injuries through improved diagnostic and treatment options.

Acknowledgments

I would like to take this opportunity to extend my most profound appreciation to individuals who have helped support and guide me throughout my master's degree journey and along my research process. This process has been both challenging and immensely rewarding, and I am deeply appreciative of the guidance and encouragement I have received along the way. Importantly, there are a few individuals that I want to extend my deepest acknowledgement and give a special thanks to.

At the top of that list, I would like to start off by giving a special thanks to my Advisor Dr. Nikolas Knowles, for providing me with this incredible opportunity to pursue my master's degree in Kinesiology. Dr. Knowles has pushed me to think critically and offered invaluable insights, opening my eyes to scientific imaging and how it can be so powerfully applied within the field of kinesiology. I am truly grateful for Dr. Knowles' guidance, expertise, and unwavering support throughout this journey. So once again, thank you Dr. Knowles. Additionally, I wish to thank the University of Waterloo for giving me the privilege to undertake this master's program and for providing an environment that encourages interdisciplinary exploration and academic excellence. The resources and opportunities provided by the university have been instrumental in shaping my growth as a researcher.

I would also like to extend my thanks to colleagues Sarah Quayyum, Neeraj Ratnani and thank the assistance of Tamara Maciel from the School of Anatomy, Tony Wales, and Dr. Ting-Yim Lee, PhD, FCCPM, FCOMP for their continuous help and support along the course of this research.

Lastly, I would love to extend my warmest thanks to my parents and sister for their constant push and moral support throughout this whole process. It was by your undivining belief and love that allowed me to always push through it. Having the three of you throughout every step of this process, believing in my capabilities has been the greatest driving force in achieving what I have wanted. Thank you all for the constant support and belief in me.

Table of Contents

Author's Declaration ii

Abstract iii

Acknowledgments v

List of Figures ix

List of Tables xiii

List of Equations xiv

1. Introduction 1

1.1 Objectives 4

1.2 Knowledge Gaps 4

2. Literature Review 5

2.1 Anatomy of the glenohumeral joint and proximal humerus 5

2.2 Injury mechanisms and classification associated with proximal humerus fractures 10

2.3 Medical imaging related to PHFs (DEXA, SEQCT, and DEQCT) 15

2.4 Proximal humerus bone mineral density measures 19

2.5 Finite Element Modeling 22

3. Methodology 24

3.1 Cadaver Demographics, Preparation, and Dissection 26

3.2 Medical Imaging Analysis 28

3.2.1 SEQCT and DEQCT Imaging: 29

3.2.2 Humerus Mask Creation in MIMICS and 3-MATIC: 31

3.3 Finite-Element Generation 33

3.3.1 Finite Element Mesh Generation 33

3.3.2 FEM Material Property Assignment 35

3.3.3 Local coordinate system of the humerus....35
3.3.4 Finite-Element Analysis....37
3.4 Data Collection Errors....38
3.5 Statistical Analysis....38
3.5.1 Specimens....38
3.5.2 Density and morphology....39
3.5.3 FEM Strain Correlations....39
4. Results....40
4.1 Bone Mineral Density....40
4.2 Strain....46
5. Discussion....59
5.1 vBMD in SEQCT....59
5.2 vBMD in DEQCT....60
5.3 Strain in SEQCT....61
5.4 Strain in DEQCT....62
5.5 Limitations....63
5.6 Relevance and clinical implications....64
5.7 Future directions....65
6. Conclusion....67
References....69
Appendix A....76
Appendix B....100
Appendix C....124
Appendix D....125

Appendix E.....131
Appendix F.....137
Appendix G.....154
Appendix H.....160
Glossary.....164

List of Figures

Figure 1.1: Linear and Quadratic tetrahedral element types. 3
Figure 2.1.1: The glenohumeral joint (GHJ), comprised of the humerus and scapula (Knowles, et al., 2016). 6
Figure 2.1.2: Bony landmark and attachment sites of a left proximal humerus. The colours represent the following: red is the Humeral Head, blue is the Greater Tuberosity, yellow is the Anatomical neck and green is the Lesser Tuberosity (Jones, 2021). 7
Figure 2.1.3: Ligaments associated in the proximal humerus for shoulder mobility and stability (Wilson, 2024). 9
Figure 2.2.1: Neer Classification for proximal humerus fractures (Kancherla et al. 2017) 11
Figure 2.2.2: AO/OTA Classification for proximal humerus fractures (Perry, 2020) 12
Figure 2.2.3: HGLS system classification comprised by Hertel (Sukthankar et al. 2013). 13
Figure 3.1: Generation of FEM from DICOM images to 3D models to obtain maximum (tensile) principal strain results. (A – MIMICS project; B – Filled humerus; C -Filled humerus with 2 mm mesh length; D – Surface of the humerus; E – Sliced humerus) 24
Figure 3.2: FE model of humerus showcasing minimum (compressive) principal strain results. (A – Surface of the humerus; B – Sliced humerus) 24
Figure 3.3: Thesis workflow. Cadaver preparation (blue), medical imaging (orange), and finite element modeling (green). 25
Figure 3.1.1: Frontal plane view of incision to segment the arm and torso. 27
Figure 3.2.1: Density Analysis workflow. 28
Figure 3.2.2: Axial representation of an isolated cadaveric shoulder from SEQCT and DEQCT images using BONE and STD reconstruction kernels. Note the variation in contrast across images due to range of intensity values. 30
Figure 3.2.3: Phantom rod calibration used during scanning to compute a linear conversion between Hounsfield Units (HU) and an equivalent density (mgK2HPO4/cc) (left). A clinical QCT scan of a cadaveric shoulder and calibration phantom with sampling of rods of known density (QCT Pro. Bone Mineral Density Software CT Calibration Phantom. Version 5.0 - Revision 20110801. Mindways Software. User Guide) 30
Figure 3.2.4: 3D model (left) of proximal humerus obtained from SEQCT and DEQCT images translated into 3-MATIC, showing the different regions for calculated vBMD in HU units (blue –

humeral head; green – metaphysis; red – diaphysis). HU are obtained choosing highlighted region by reading the average value and converted to vBMD using a specimen-specific calibration slope and intercept. 32

Figure 3.2.6: Placement of custom-made cubes to form the 3 regions of interest..... 33

Figure 3.3.1: A finite element model of a humerus, separated into a 10-node quadratic tetrahedral mesh, consisting of nodes and elements 34

Figure 3.3.2: Coordinate system (SC - Sphere Centre; CF - Circle Fit) 36

Figure 3.3.3: 3D model of proximal humerus showing humerus at 90 degrees abduction with the scapula. Red area marked indicates the glenoid contact area between the humerus and scapula. 37

Figure 4.2.1: 23156R SEQCT maximum (tensile) principal strain with a microstrain set at 4100 for BONE reconstruction kernel (A - Surface of the humerus; B - Sliced humerus) 47

Figure 4.2.2: 23156R SEQCT maximum (tensile) principal strain with a microstrain set at 4100 for STD reconstruction kernel (A - Surface of the humerus; B - Sliced humerus) 47

Figure 4.2.3: 23156R Humeral Head maximum principal differences between BONE and STD reconstruction kernel in SEQCT. The highest reported strain in each reconstruction kernel: BONE = 0.0148; STD = 0.0162. Number of elements exceeding 0.01 strain: BONE = 24; STD = 33. Red line indicates elemental strains of 4100 (tensile) microstrain for trabecular bone. 48

Figure 4.2.4: 23156R Metaphysis maximum principal differences between BONE and STD reconstruction kernel in SEQCT. The highest reported strain in each reconstruction kernel: BONE = 0.0784; STD = 0.0457. Number of elements exceeding 0.022 strain: BONE = 145; STD = 17. Red line indicates elemental strains of 4100 (tensile) microstrain for trabecular bone. 48

Figure 4.2.5: 23156R Diaphysis maximum principal differences between BONE and STD reconstruction kernel in SEQCT. The highest reported strain in each reconstruction kernel: BONE = 0.0186; STD = 0.0181. Number of elements exceeding 0.016 strain: BONE = 3 STD = 2. Red line indicates elemental strains of 6700 (tensile) microstrain for cortical bone. 49

Figure 4.2.6: 23156R SEQCT minimum (compressive) principal strain with a microstrain set at 8300 for BONE reconstruction kernel (A - Surface of the humerus; B - Sliced humerus) 50

Figure 4.2.7: 23156R SEQCT minimum (compressive) principal strain with a microstrain set at 8300 for STD reconstruction kernel (A - Surface of the humerus; B - Sliced humerus) 50

Figure 4.2.8: 23156R Humeral Head minimum principal differences between BONE and STD reconstruction kernel in SEQCT. The lowest reported strain in each reconstruction kernel: BONE = -

0.0182; STD = -0.0213. Number of elements less than -0.014 strain: BONE = 20; STD = 33. Red line indicates elemental strains of 8300 (compressive) microstrain for trabecular bone. 51
Figure 4.2.9: 23156R Metaphysis minimum principal differences between BONE and STD reconstruction kernel in SEQCT. The lowest reported strain in each reconstruction kernel: BONE = -0.0674; STD = -0.0556. Number of elements exceeding -0.03 strain: BONE = 275; STD = 3. Red line indicates elemental strains of 8300 (compressive) microstrain for trabecular bone. 51
Figure 4.2.10: 23156R Diaphysis minimum principal differences between BONE and STD reconstruction kernel in SEQCT. The lowest reported strain in each reconstruction kernel: BONE = -0.0420; STD = -0.0421. Number of elements less than -0.027 strain: BONE = 36; STD = 29. Red line indicates elemental strains of 9800 (compressive) microstrain for cortical bone. 52
Figure 4.2.11: 23156R DEQCT maximum (tensile) principal strain with a microstrain set at 4100 for BONE reconstruction kernel (A - Surface of the humerus; B - Sliced humerus) 53
Figure 4.2.12: 23156R DEQCT maximum (tensile) principal strain with a microstrain set at 4100 for STD reconstruction kernel (A - Surface of the humerus; B - Sliced humerus) 53
Figure 4.2.13: 23156R Humeral Head maximum principal differences between BONE and STD reconstruction kernel in DEQCT. The highest reported strain in each reconstruction kernel: BONE = 0.0145; STD = 0.0168. Number of elements exceeding 0.01 strain: BONE = 15; STD = 120. Red line indicates elemental strains of 4100 (tensile) microstrain for trabecular bone. 54
Figure 4.2.14: 23156R Metaphysis maximum principal differences between BONE and STD reconstruction kernel in DEQCT. The highest reported strain in each reconstruction kernel: BONE = 0.0267; STD = 0.0396. Number of elements exceeding 0.022 strain: BONE = 2; STD = 140. Red line indicates elemental strains of 4100 (tensile) microstrain for trabecular bone. 54
Figure 4.2.15: 23156R Diaphysis maximum principal differences between BONE and STD reconstruction kernel in DEQCT. The highest reported strain in each reconstruction kernel: BONE = 0.0268; STD = 0.0192. Number of elements exceeding 0.016 strain: BONE = 5; STD = 10. Red line indicates elemental strains of 6700 (tensile) microstrain for cortical bone. 55
Figure 4.2.16: 23156R DEQCT minimum (compressive) principal strain with a microstrain set at 8300 for BONE reconstruction kernel (A - Surface of the humerus; B - Sliced humerus) 56
Figure 4.2.17: 23156R DEQCT minimum (compressive) principal strain with a microstrain set at 8300 for STD reconstruction kernel (A - Surface of the humerus; B - Sliced humerus).....56

Figure 4.2.18: 23156R Humeral Head minimum principal differences between BONE and STD reconstruction kernel in DEQCT. The lowest reported strain in each reconstruction kernel: BONE = -0.0240; STD = -0.0249. Number of elements less than -0.014 strain: BONE = 30; STD = 50. Red line indicates elemental strains of 8300 (compressive) microstrain for trabecular bone. 57
Figure 4.2.19: 23156R Metaphysis minimum principal differences between BONE and STD reconstruction kernel in DEQCT. The lowest reported strain in each reconstruction kernel: BONE = -0.0443; STD = -0.0535. Number of elements less than -0.03 strain: BONE = 46; STD = 24. Red line indicates elemental strains of 8300 (compressive) microstrain for trabecular bone. 57
Figure 4.2.20: 23156R Diaphysis minimum principal differences between BONE and STD reconstruction kernel in DEQCT. The lowest reported strain in each reconstruction kernel: BONE = -0.0213; STD = -0.0278. Number of elements less than -0.027 strain: BONE = 0; STD = 1. Red line indicates elemental strains of 9800 (compressive) microstrain for cortical bone. 58

List of Tables

Table 2.1: Comparison between DEXA, SEQCT and DEQCT scanning techniques. 19
Table 3.1: Age and sex of cadaver specimens for imaging with the various techniques.....27
Table 4.1: Density measures in HU and vBMD in humeral head region (n = 11) derived from SEQCT scans of both BONE and STD reconstruction kernels. 40
Table 4.2: Density measures in HU and vBMD in Metaphysis region (n = 12) derived from SEQCT scans of both BONE and STD reconstruction kernels. 41
Table 4.3: Density measures in HU and vBMD in Diaphysis region (n = 12) derived from SEQCT scans of both BONE and STD reconstruction kernels. 42
Table 4.4: Regression parameters (BONE vs STD) obtained from 3D humeral models using HU and vBMD [mg_{K2HPO4}/cc] in SEQCT. 43
Table 4.5: Density measures in vBMD in Humeral head region (n = 10) derived from DEQCT scans of both BONE and STD reconstruction kernels.....44
Table 4.6: Density measures in vBMD in Metaphysis region (n = 10) derived from DEQCT scans of both BONE and STD reconstruction kernels. 44
Table 4.7: Density measures in vBMD in Diaphysis region (n = 10) derived from DEQCT scans of both BONE and STD reconstruction kernels. 45
Table 4.8: Regression parameters (BONE vs STD) obtained from 3D humeral models using vBMD [mg_{K2HPO4}/cc] in DEQCT. 45

List of Equations

*RhoQCT = a + b * HU* 35
*RhoAsh = 0+1*RhoQCT* 35
$E = 0+12486*RhoQCT^{1.16}$ 35

1. Introduction

Proximal humerus fractures (PHFs) are identified as the second most common upper extremity fracture.[4] Both health care costs being notably high and patient outcomes not being maximized arise from the repercussions of challenges and controversies in PHF management.[12] It remains burdensome to manage PHFs surgically due to the variety of factors that influence surgical decision making when coping with PHFs.[10] Such factors include comorbidities, bone quality, age, and activity levels of patients.[10] A complex fracture may be treated by various surgical options such as open reduction and internal fixation (ORIF), closed reduction and percutaneous pinning (CRPP), hemi arthroplasty (HA), reverse shoulder arthroplasty (RSA), or fracture plating. Despite their commonality, these treatments have inconsistent clinical outcomes and high rates of reoperation.[10,17] In complex fracture cases, the ability to visualize fracture morphology is responsible for part of the success and choice of interventions.[5] It is difficult to quantify and understand the parameters associated with common fracture patterns, which contributes to the wide range of surgical outcomes in complex cases.[5]

To overcome these constraints, developed and enhanced imaging techniques were used to optimize fracture evaluation in a cadaveric PHF model. The classification of PHFs using clinical CT is superior to that of X-rays.[5] Effective use of standard single-energy CT (SEQCT) is not limited to quantifying bone and fracture morphology but, limitations such as density measures not being reliable are prevalent. Quantitative CT (QCT) allows repeatable measurements of volumetric bone mineral density (vBMD) using clinical SEQCT images calibrated with known density. Bone mechanical properties are related to quantitative imaging parameters by vBMD, which allows the quantification of temporal bone changes across populations.[9] Clinical scanner resolution limitations result in voxels that include bone, marrow, or other tissues. By using SEQCT alone, it is impossible to differentiate interstitial marrow changes caused by aging, disease, or injury (marrow adiposity, fluid infiltration, or bone healing),[2,3,11,18,] or metal artifacts,[7,14] from bone changes. To obtain more precise quantification of bone changes in injury, disease, aging, and post-surgery, microCT and dual-energy QCT (DEQCT) advanced imaging is recommended compared to SEQCT,[1] allowing for the establishment of common characteristics in complex cases.

Clinical CT technology has advanced to allow dual-energy scanning on clinical scanners with scan times and radiation doses similar to SEQCT.[11] DEQCT enhances the possibility of assessing bone materials and composition in PHFs from marrow changes in injury, disease, or aging.[2,3,11,18] Besides the precision of measurement in bone strength by DEQCT to improve vBMD,[6] metal artifact reduction

image is an asset of DEQCT, [7,14] enhancing visualization and quantitative evaluation at the bone-implant interface. DEQCT has been evaluated for its efficacy in evaluating PHF in clinical populations using image-based characteristics.

The effectiveness of establishing ideal DEQCT parameters for the evaluation and surgical management of PHFs was defined for the first time in this study. Clinical single- and dual-energy QCT enables a thorough assessment of the imaging properties of pre- and post-fracture scenarios through the combination of 3D model load simulations in finite element models (FEMs). In light of recent developments in dual-energy QCT technology and its accessibility in clinical care settings, this imaging modality may offer an efficient and inexpensive means to assess PHFs. This might result in a more effective fracture diagnosis, assessment, and decision-making process regarding surgical versus non-surgical treatment.

Considering the prevalence of these fractures, difficulties in surgical administration, and potential for reproducing fracture patterns in cadaveric models, imaging characteristics to assess PHF surgically provides this capability to ensure better diagnosis. This research serves as a preliminary step in the SEQCT and DEQCT evaluation of non-surgical PHF treatment and fracture healing in patient populations. This research also helps with surgical PHF treatment, informing surgeons with qualitative and the associated quantitative differences between different imaging modalities, influencing surgical decisions. Future studies will include individuals who have experienced a PHF to assess fracture healing in both non-surgical and surgical situations given the expected success. Beyond the confines of acute clinical care settings, DEQCT may offer a quick, affordable imaging method that may be incorporated into randomized control trials comparing and evaluating the effectiveness of PHF therapy.

Both the qualitative and quantitative data obtained from SEQCT and DQECT imaging modalities can be significantly influenced by the choice of image reconstruction kernel employed. Algorithmic procedures called reconstruction kernels are developed to enhance image post-processing and improve image quality. Depending on the objectives of the study, these kernels can either help with image softness or sharpening by altering the frequency content of the image data.[45] The bone edge sharpening (BONE) reconstruction kernel offers better contrast and spatial resolution for bone tissues, making it more appropriate for precise detection of subtle bone abnormalities, fractures, or changes in bone structure. The standard (STD) reconstruction kernel is typically optimized to improve the visualization of soft tissues.[46] It is important to note that reconstruction kernels inherently alter both the

qualitative and associated quantitative data, and these effects cannot be fully accounted for using standardized calibration phantoms alone.[47] Several studies have investigated the effects of reconstruction kernels on volumetric bone mineral density (vBMD) and stiffness estimates derived from SEQCT images of the spine, hip, and animal models.[48,49,50] **However, to date, no studies have compared the effects of reconstruction kernels on SEQCT and DEQCT data or the subsequent use of these images as input for finite element modeling (FEM) analyses.**

Finite element analysis (FEA) is a computational modeling technique that numerically solves complex structural mechanics problems. FEA divides a structure into a mesh of small, interconnected elements, with material behaviors and governing physics equations applied to each element. This allows detailed stress, strain, and deformation analyses to be performed digitally. Tetrahedral elements, utilizing either linear or quadratic integration formulations, are frequently used in continuum-level FEMs and can also be applied to micro-level FEMs, as illustrated in Figure 1.1. These elements are advantageous due to their capability to accurately represent intricate curved geometries with smoother surfaces and their broad use in automatic mesh generation tools.[43] Despite their previous prevalence, linear tetrahedral elements are now less favored in modern finite element modeling because of their high stiffness.[43,63] On the other hand, quadratic tetrahedral elements offer high accuracy and excellent convergence properties. For biomechanics, specimen-specific FEA builds 3D bone models from medical images and replicates loading scenarios for insight into tissue stresses/strains and fracture risk. For the proximal humerus, FEA has become an important tool for evaluating fracture mechanics as it allows assessment of the complex 3D bone stresses noninvasively.[1,10,11] Cadaveric humeri are difficult to obtain and instrument, while FEA modeling provides unlimited simulation capacity once validated. FEA can determine the strain distribution in the proximal humerus under various loading modes and identify high-risk fracture regions.[11,12] Patient-specific FEA based on clinical CT data has potential for individualized fracture risk assessment and to guide treatment.[13]

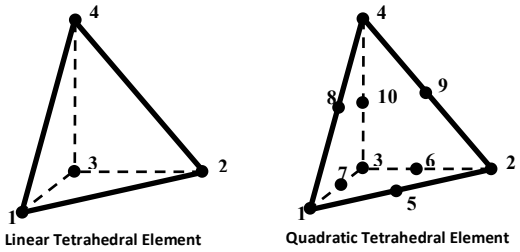


Figure 1.1: Linear and Quadratic tetrahedral element types.

1.1 Objectives

This study aims to develop enhanced imaging techniques to optimize fracture evaluation in a cadaveric PHF model. The purpose of this research includes the following:

i. *Determine differences between BONE and STD reconstruction kernels in both SEQCT and DEQCT by vBMD.*
ii. *Determine regional FEM strains in both SEQCT- and DEQCT-based FEMs and the predicted proximal humerus fracture location based on regional FEM strain thresholds.*

1.2 Knowledge Gaps

This research addresses two knowledge gaps:

i. *Comprehensive comparison of imaging modalities and specific imaging parameters related to PHFs.*

This knowledge gap is looked at by using the two different imaging techniques and identifying differences in vBMD obtained.[21,22,23,24,25] Studies have looked at DEXA and other imaging modalities, but none have directly compared the clinically relevant CT-based imaging parameters in a systematic manner, limiting the ability to determine the best imaging method.[6,7,8] No studies have addressed parameters between SEQCT and DEQCT.

ii. *Comparison of FEM strains based on image parameters and predicted fracture location.*

This knowledge gap compares how high strain locations are altered by two different imaging techniques, to inform biomechanical loading approaches to predict fracture location. Although DEQCT has been shown to improve vBMD estimates and is more strongly correlated to fracture strength than SEQCT,[2,4,5,6] no studies have compared QCT-based FEMs derived from SEQCT and DEQCT models or compared multi-modality density and morphology to FEM strains.

2. Literature Review

2.1 Anatomy of the glenohumeral joint and proximal humerus

The proximal humerus, an essential component of the upper extremity, plays a vital role in facilitating a wide range of arm movements and providing stability to the glenohumeral joint. Understanding the biomechanics and functionality of the shoulder complex requires an understanding of the anatomy of the glenohumeral joint and the proximal humerus. The anatomy of the proximal humerus, with its various bony prominences, articular surfaces, and soft tissue attachments, necessitates a comprehensive understanding of its structure and function to accurately diagnose and manage fractures in this region. Figure 2.1.1 displays the anatomical placing of the glenohumeral joint of the humerus and scapula.

When looking at anatomical descriptions of the shoulder, Halder et al (2000) begins by outlining the glenohumeral joint's articular surfaces, highlighting the significance of the glenoid labrum and its function in enlarging the glenoid cavity.[12] The superior, middle, and inferior glenohumeral ligaments, which offer stability to the joint in various situations, are discussed in further detail in the paper.[12] The proximal humerus consists of distinct anatomical structures, including the humeral head, greater tuberosity, lesser tuberosity, and humeral shaft. The humeral head articulates with the glenoid fossa of the scapula, forming the glenohumeral joint, which allows for shoulder mobility and abduction-adduction movements. Halder et al (2000) describes the shoulder complex as having the greatest mobility of all joints. The greater tuberosity, located laterally and superiorly, serves as the attachment site for the rotator cuff tendons, specifically the supraspinatus, infraspinatus, and teres major,[62] and plays a crucial role in shoulder stability and abduction as seen in Figure 2.1.2. In Figure 2.1.2, the colours represent the following: red is the Humeral Head, blue is the Greater Tuberosity, yellow is the Anatomical neck and green is the Lesser Tuberosity. The Intertubercular groove sits between the Greater and Lesser Tuberosity. The lesser tuberosity, situated medially and anteriorly, also serves as an attachment point for the subscapularis tendon, contributing to the stability of the shoulder joint and facilitating internal rotation. The humeral shaft connects the proximal and distal parts of the humerus, providing structural support and allowing for the transmission of forces during upper limb movements.

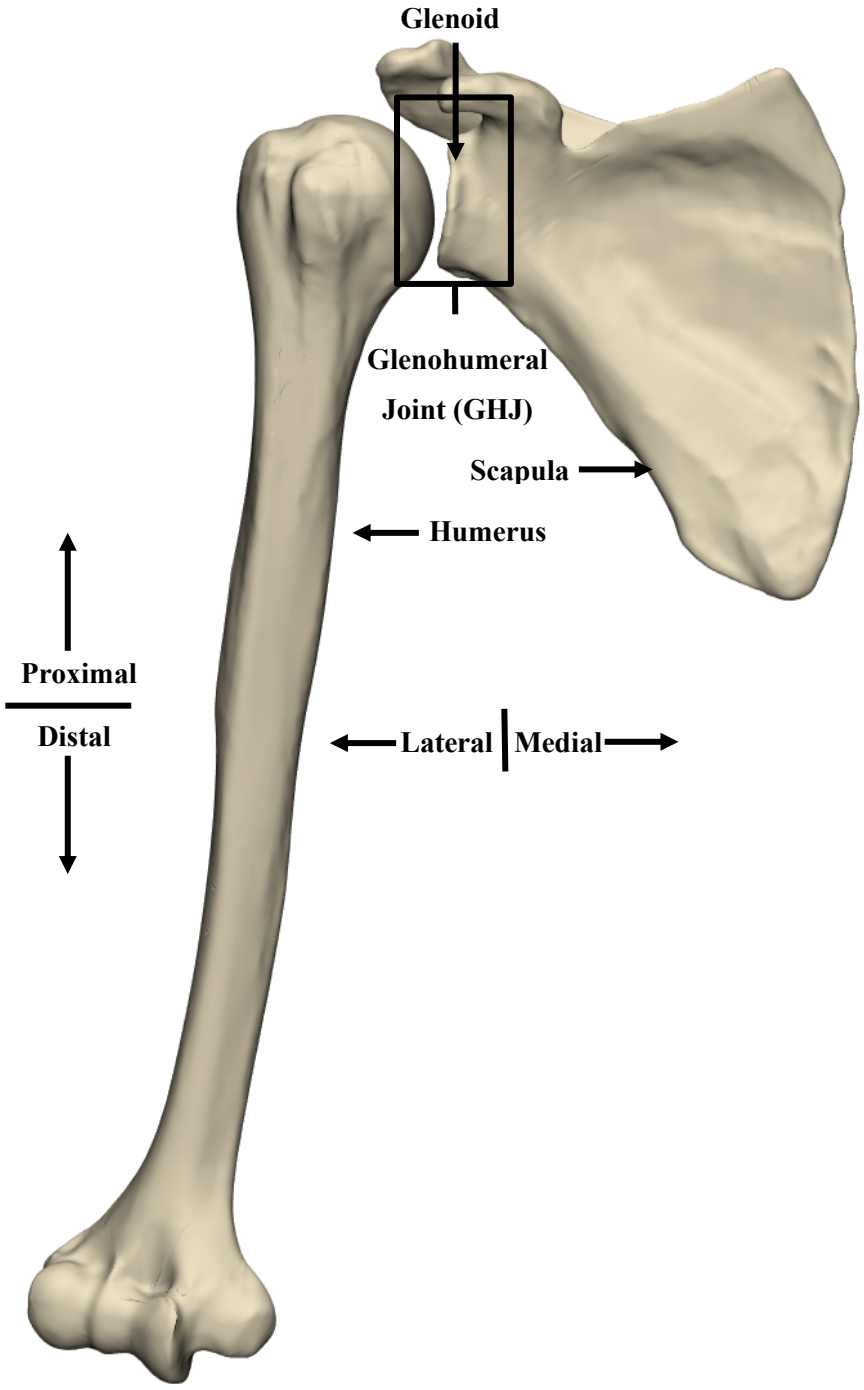


Figure 2.1.1: The glenohumeral joint (GHJ), comprised of the humerus and scapula (Knowles, et al., 2016).

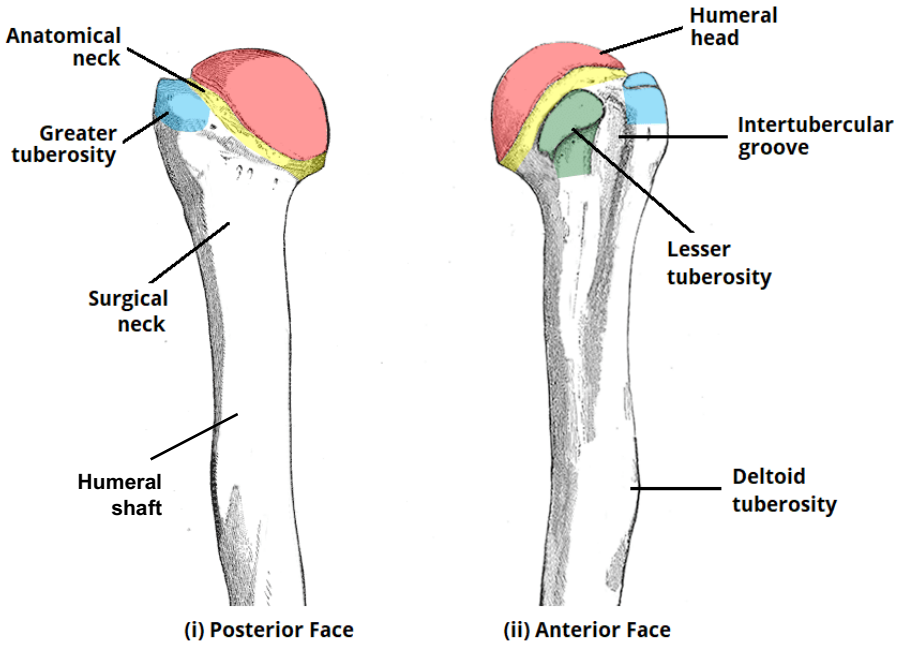


Figure 2.1.2: Bony landmark and attachment sites of a left proximal humerus. The colours represent the following: red is the Humeral Head, blue is the Greater Tuberosity, yellow is the Anatomical neck and green is the Lesser Tuberosity (Jones, 2021).

The humeral head is the spherical part of the proximal humerus that articulates with the glenoid fossa of the scapula to form the glenohumeral joint. It provides support and allows the shoulder to move freely to perform a range of different motions, including flexion, extension, abduction, adduction, and rotation. The humeral head also serves as an attachment point for several muscles and tendons involved in shoulder movement, such as the rotator cuff muscles.

An emphasizes on the function of the rotator cuff muscles in maintaining joint stability and coordinating complicated movements, which include the supraspinatus, infraspinatus, teres minor, and subscapularis is also relevant. Halder et al (2000) goes on to talk about the subacromial region and its connection to impingement syndromes, emphasizing the need of good biomechanics for optimal shoulder function. The lesser tuberosity is a tiny bony protrusion on the proximal humerus that is positioned medially. It serves as an attachment point for the subscapularis muscle. The lesser tuberosity contributes to internal rotation and shoulder joint stabilisation.[12]

The long cylindrical section of the proximal humerus that joins the proximal and distal ends is known as the humeral shaft. It acts as an attachment place for many muscles, including the deltoid and

pectoralis major, and gives structural support and stability to the bone. The nutritional artery, which provides blood to the bone, is similarly housed in the humeral shaft.[13]

The glenohumeral joint, a synovial joint between the humeral head and the glenoid fossa of the scapula, is inherently unstable due to the shallowness of the glenoid fossa and the disproportion in size and congruency of the articular surfaces. Recurrent trauma can lead to erosion of the anterior glenoid margin and labrum, contributing to shoulder instability. Alice et al (2021) concluded that the range of glenohumeral abduction in the coronal plane is limited to 60-90° with the humerus in internal rotation, but allowing external rotation increases the abduction range to 90-120°. Three ligaments, the Superior Glenohumeral Ligament (SGHL), Middle Glenohumeral Ligament (MGHL), and Inferior Glenohumeral Ligament (IGHL) play a critical role in shoulder stability and function. The SGHL forms a U-shaped anterior suspension around the long head of biceps brachii tendon, while the MGHL originates just inferior to the SGHL and inserts into the humerus near the lesser tuberosity (Figure 2.1.3). The IGHL, the thickest of the three, attaches to the anterior, inferior, and posterior margins of the glenoid labrum. These ligaments collectively provide stability in various directions. Innervation of the shoulder region primarily arises from C5, C6, and C7, with contributions from C4. Neural input to the shoulder joint capsule involves the suprascapular, auxiliary, and lateral pectoral nerves. Understanding the anatomy and innervation of the glenohumeral joint is crucial for comprehending shoulder stability, injury mechanisms, and potential interventions to address musculoskeletal morbidity.[14]

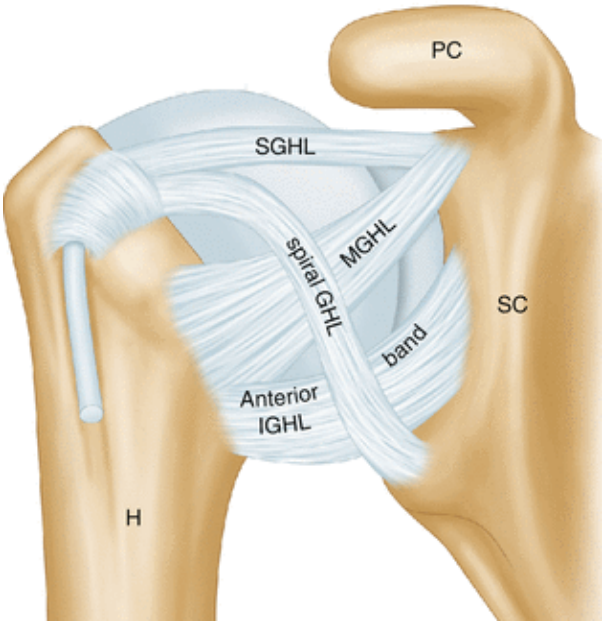


Figure 2.1.3: Ligaments associated in the proximal humerus for shoulder mobility and stability (Wilson, 2024).

Each component of the proximal humerus serves a distinct anatomical function and contributes to the overall function of the shoulder joint. Understanding these components' precise functions and interactions is critical for detecting and treating fractures, as well as planning surgical procedures and rehabilitation protocols for regaining optimal shoulder function. Understanding the anatomical differences and biomechanics of the proximal humerus allows researchers to investigate innovative fracture fixing procedures, rehabilitation regimes, and advances in implant design. We can improve patient outcomes, optimize surgical methods, and improve the overall management of fractures in this key location by constantly expanding our knowledge of the anatomy of the proximal humerus. The proximal humerus is comprised of several distinct bony subsections that are important when considering fractures in this region.[34] The head of the humerus is mostly articular cartilage covering the bony epiphysis, with the anatomical neck separating it from the surgical neck and tubercles. The surgical neck is the most common fracture site as it is the narrowest part of the proximal humerus shaft (Figure 2.1.2).[33]

Fractures often occur through the surgical neck due to its thin cortical bone and poor muscular attachments.[32] The metaphysis flares distally from the surgical neck as it connects to the wider

diaphyseal shaft. The greater and lesser tubercles project from this metaphyseal region and are also potential sites of proximal humerus fractures.[31]The tubercles are more resistant to fracture due to the thick cortical bone and robust rotator cuff muscle attachments. However, when fractured they become important fragments that require surgical fixation to restore function.[30] Understanding the bony subsections of the proximal humerus is clinically important when evaluating and treating common fractures in this region.

2.2 Injury mechanisms and classification associated with proximal humerus fractures

Proximal humerus fractures are a common injury caused by a variety of trauma injuries. Understanding the damage mechanisms that cause these fractures is critical for establishing effective prevention strategies and enhancing treatment methods. Because of its complicated anatomy and biomechanical properties, the proximal humerus is prone to fractures. While the exact mechanisms of injury can vary, certain factors contribute to the occurrence of proximal humerus fractures.

An aging population, increased incidence of falls, and higher rates of osteoporosis are significant contributors to the growing rates of these fractures.[15] Falls, especially among older adults, are a leading cause of proximal humerus fractures. However, high-energy trauma, such as motor vehicle accidents and sports-related injuries, can also result in these fractures.[15,18,19] Proximal humerus fractures account for a large fraction of upper extremity injuries, showing a varied range of fracture forms with distinct anatomical characteristics and clinical implications. The classification systems commonly used to categorize proximal humerus fractures include the Neer classification (Figure 2.2.1) defining fracture fragments based on displacement and angulation, the AO/OTA classification (Figure 2.2.2), and the Hertel classification (Figure 2.2.3). Hertel's classification divides the proximal humerus head into 4 distinct parts: head (H), greater tuberosity (G), lesser tuberosity (L) and shaft (S), giving the HGLS classification system as seen in Figure 2.2.3.[35] This classification allows all fracture planes between any of the 4 major distinct parts to be classified, giving 14 possible combinations to distinguish a humerus fracture. These systems consider characteristics such as fracture site, displacement, amount of fracture fragments, and humeral head or tuberosity involvement. Fracture types observed in the proximal humerus include anatomical neck fractures, surgical neck fractures, greater and lesser tuberosity fractures, and articular surface fractures.[17] The complicated nature of proximal humerus fractures provides difficulties with management, which requires comprehensive treatments that take into account the fracture pattern, patient characteristics, and treatment goals.[15,16] Therefore, developing

fracture prevention methods, enhancing treatment options, and enhancing patient outcomes all depend on a detailed understanding of the damage mechanisms resulting in proximal humerus fractures.[16]

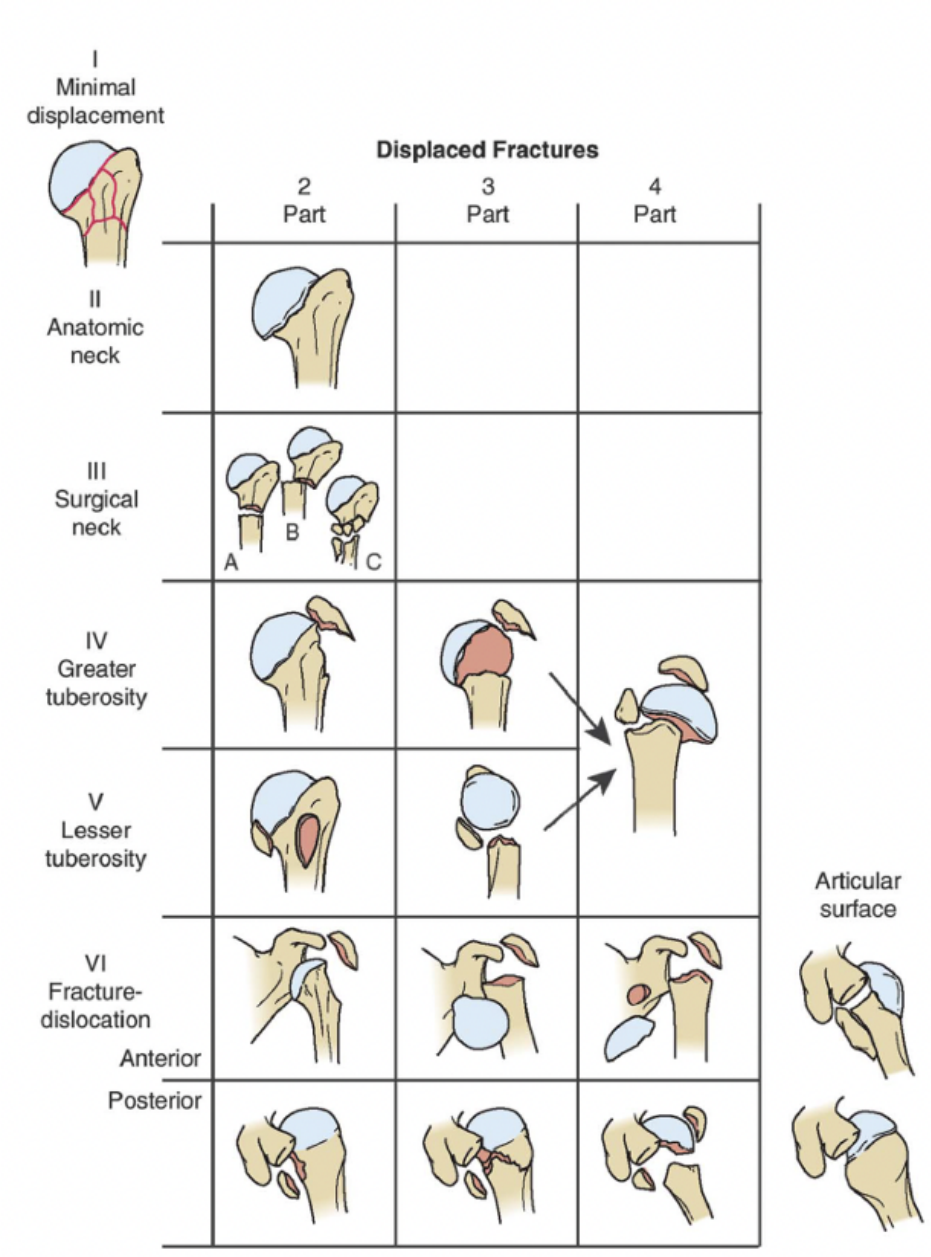


Figure 2.2.1: Neer Classification for proximal humerus fractures (Kancherla et al. 2017)

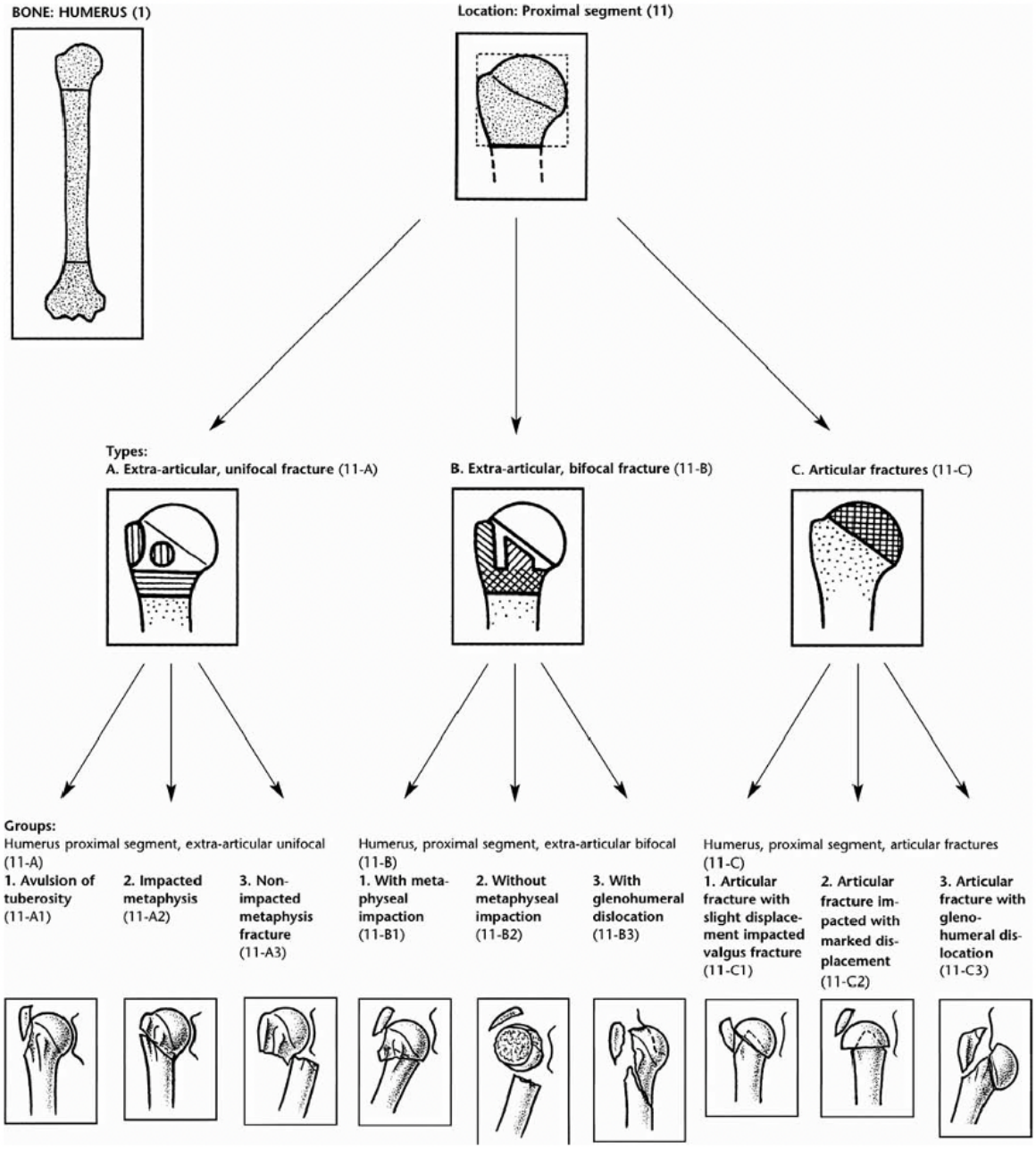


Figure 2.2.2: AO/OTA Classification for proximal humerus fractures (Perry, 2020)

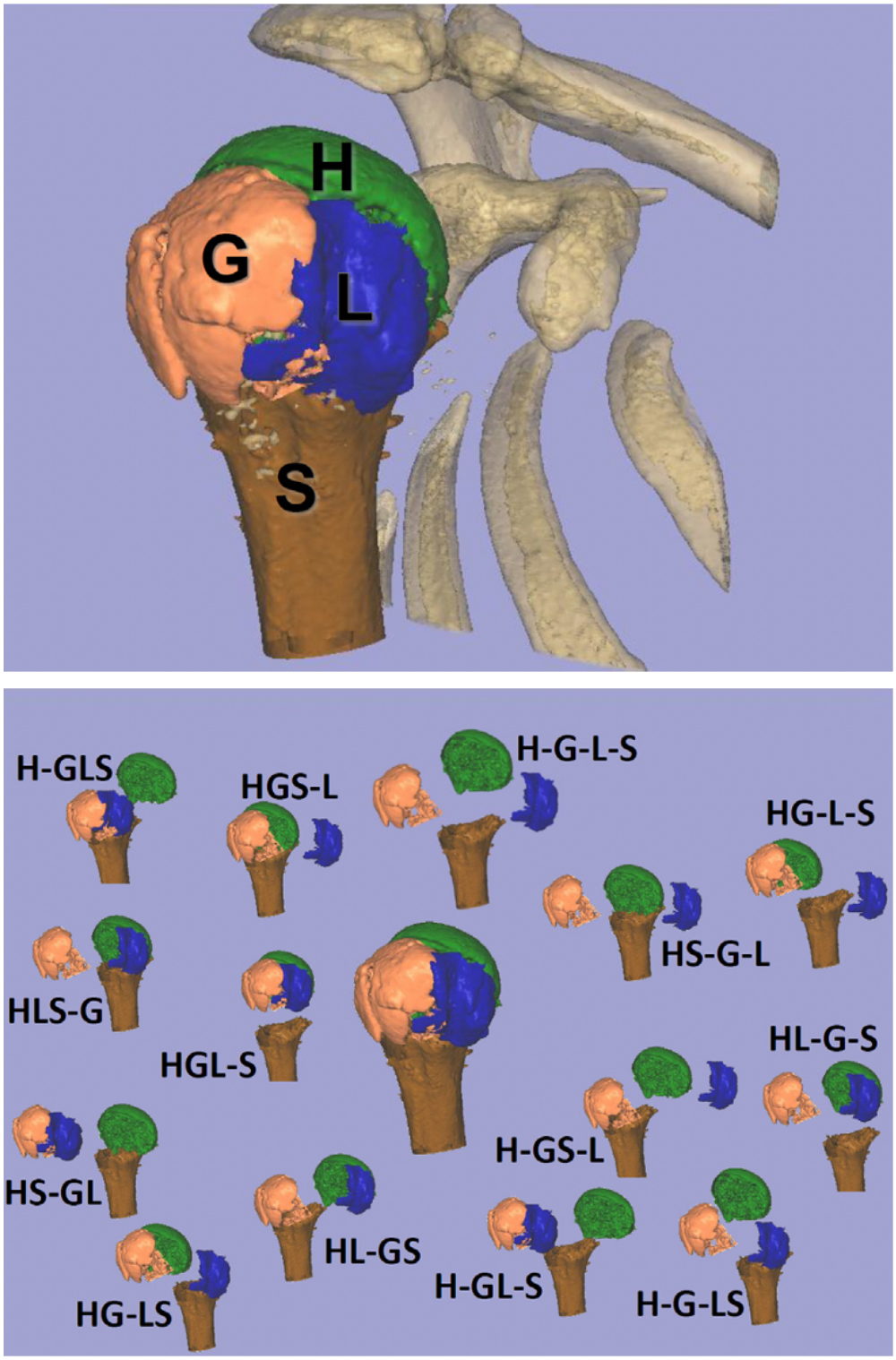


Figure 2.2.3: HGLS system classification comprised by Hertel (Sukthankar et al. 2013).

Sheehan et al (2013) concluded that there is no gender-based variation in the incidence of proximal humerus fractures, which make up about 5% of all fractures and can be divided into direct and indirect processes. Direct fractures occur when the humerus experiences a high-energy nonaxial force vector, typically resulting from a direct impact along the shaft. On the other hand, indirect fractures involve lower-energy loading without a direct impact at the fracture site. Indirect fractures are more common and often occur due to a fall on an outstretched hand (FOOSH) when attempting to prevent a fall from standing height. Sheehan et al (2013) conducted comparison studies between younger and elder populations. Indirect fractures are more common in the elderly due to conditions like osteoporosis and a higher risk of falling. Younger patients, on the other hand, face a higher percentage of direct fractures, frequently because of high-impact sports or vehicular accidents. Less frequent processes include electric shocks or uncontrollable muscle contractions during seizures. Nondisplaced or one-part fractures have no fragment meeting displacement or angulation criteria. Two-part fractures involving the surgical neck and lesser tuberosity can be managed conservatively if the displacement is less than 66% with acceptable functional angulation.[15.17] Fractures involving the greater tuberosity are often associated with anterior glenohumeral dislocations, and significant displacement may indicate an associated rotator cuff tear. A study conducted in Finland on 109 patients with proximal humerus fractures associated with osteoporosis found that 97% of these fractures resulted from simple falls.[16] Among the falls, 54% occurred outdoors, 61% while walking normally, and 72% after slipping or tripping. The impact of the falls was typically on the tip of the shoulder, resulting in visible hematomas.[16] Factors associated with fractures of the proximal humerus included low bone mineral density (BMD), loss of height, a maternal history of hip fracture, previous falls, low physical activity levels, and poor balance. Understanding the different types of proximal humerus fractures and their mechanisms is crucial for appropriate diagnosis, treatment planning, and determining associated injuries and outcomes.

Proximal metaphyseal and diaphyseal fractures in the pediatric population are commonly caused by traumatic events, and it is crucial to rule out pathological and stress fractures.[42] As noted by Ahmed Khedr (2019), nonoperative treatment is the preferred approach in most cases, while operative treatment is required for open fractures, vascular injuries, or when adequate functional reduction cannot be maintained. Percutaneous pinning and flexible intramedullary nailing are viable options for proximal humeral metaphyseal fractures, while elastic intramedullary nailing or plate and screw fixation can be employed for humeral diaphyseal fractures that cannot be managed nonoperatively.[42] These fixation

methods generally have low complication rates, with skin and soft tissue irritation, and radial nerve injury being the main concerns. External fixation can also be utilized for open fractures with extensive soft tissue injury.[42] Notably, postoperative stiffness and non-union are not common complications after fixing pediatric humeral fractures, in contrast to adult cases.[42] Ahmed Khedr highlights that humerus fractures in the pediatric population represent less than 5% of all musculoskeletal injuries, with a higher incidence observed in patients younger than 3 years and older than 12 years. Birth trauma, accidental and nonaccidental injuries, bone diseases, and repetitive traumas are common contributing factors. The diagnosis of these fractures involves a thorough clinical assessment according to the patient's age and the mechanism of injury, including careful neurovascular evaluation. A comprehensive inspection of X-ray views is essential to exclude the possibility of pathological fractures.[42] Further research is needed to explore preventive measures and refine treatment options for proximal humerus fractures, considering the diverse fracture patterns and patient-specific factors involved in their management.

2.3 Medical imaging related to PHFs (DEXA, SEQCT, and DEQCT)

Bone mineral density (BMD) is an important indicator of bone health and fracture risk. There are several methods available to assess BMD in the proximal humerus. Dual-energy x-ray absorptiometry (DEXA) is commonly used clinically to measure areal BMD (aBMD) in the hip/spine and these values are used to determine fracture risk in alternate locations, such as the upper extremity. While DEXA is convenient and accessible, it provides a two-dimensional measurement of aBMD which can be influenced by patient size and shape.

DEXA measurements of BMD have proved helpful in medical care and research to evaluate skeletal health. While DEXA is well known for its use in determining BMD in the hip and spine, its application in determining BMD in the shoulder has drawn more attention as a useful method for determining osteoporosis and tracking the success of treatment in the upper extremities. To establish the usefulness and dependability of DEXA measures for shoulder BMD evaluation, additional research and standardization are needed.

Various skeletal areas, including the shoulder, can now be measured for BMD using DEXA scans. DEXA scans use low-dose X-rays to evaluate the quantity of mineral content in bone. Although DEXA scans are frequently used to assess BMD in the hip and spine, its use in the shoulder has drawn

more interest recently. The shoulder joint is crucial to the function of the upper limbs, and measuring BMD in this area can reveal important information about the health of the bones and the likelihood of fracture. Particular regions of interest (ROIs) inside the shoulder, such as the proximal humerus, greater tuberosity, and surgical neck, can be precisely measured for aBMD using DEXA images. Clinicians can identify possible sites of bone loss or osteoporosis-related degradation by measuring low aBMD in these regions, assisting in early detection and intervention. DEXA scans can also be used to monitor aBMD changes over time, gauge the effectiveness of a treatment, and direct clinical judgment.

A study by Oh et al (2014) also investigated the correlation between aBMD measurements of the hip and lumbar spine using conventional DEXA and the aBMD of the greater tuberosity (GT) in both shoulders.[30] It was found that there was only a moderate correlation between these measurements.[30] Moreover, the aBMD of the hip showed a better correlation with the GT of the proximal humerus compared to the aBMD of the lumbar spine. Gender differences were observed in aBMD values, with significantly higher aBMDs in all ROIs for males compared to females.[30] However, in men aged between 70 and 79 years, there was no significant decrease in aBMD with age.[30] In contrast, for women, T-scores of DEXA (hip and spine) and aBMD values of ROIs in bilateral shoulders were significantly lower compared to male patients.[30] Multiple regression analysis revealed that, apart from gender, no significant correlations were found between other clinical characteristics such as age, symptom duration, tear size, and the aBMD of the GT in the affected shoulder.[30] Furthermore, there were no significant differences in complications between the osteoporosis and non-osteoporosis groups, and the range of motion was comparable in both groups at the one-year follow-up.[30]The findings highlight the gradual decline in aBMD in operated shoulders, the correlation between aBMD measurements and DEXA scans, and the potential benefits of autografts for proximal humerus fracture repairs in osteoporotic bone. Additionally, sex differences and the variations in aBMD across different regions of the proximal humerus were explored, contributing to a better understanding of bone health and the implications for shoulder-related conditions. Furthermore, DEXA measures for shoulder BMD demonstrated excellent reliability and revealed significantly lower aBMD values in the shoulder's that had undergone a procedure (e.g. Arthroplasty) compared to the unaffected shoulder.[30] Moving forward, further research is needed to explore the impact of aBMD changes on functional outcomes and the long-term effects of surgical interventions on bone density.

Single energy quantitative computed tomography (SEQCT) and dual-energy quantitative computed tomography (DEQCT) are three-dimensional imaging techniques that enable the quantitative

assessment of vBMD and material composition within specific regions of interest, such as the proximal humerus. SEQCT utilizes a single X-ray energy spectrum and leverages the differential attenuation properties of various materials to decompose the acquired data into distinct tissue components, such as bone mineral and soft tissue.[41] SEQCT expands on single-energy conventional CT that collects individual voxel (3D pixel) data in Hounsfield Units (HU), by scanning a calibration phantom with rods of known density within the ROI. This provides one of the key advantages of SEQCT, which is its ability to provide accurate vBMD measurements in a three-dimensional (3D) manner, overcoming the limitations of traditional two-dimensional (2D) techniques like dual-energy X-ray absorptiometry (DEXA).[53] By accounting for the volumetric distribution of bone mineral and correcting for the influence of overlying soft tissues, SEQCT offers a more comprehensive assessment of bone health, particularly in complex anatomical regions like the proximal humerus. Due to spatial resolution of SEQCT, each voxel may incorporate bone, marrow, or other tissues, and the amount of each of tissue cannot be determined directly with SEQCT, due to the single-energy spectrum and tissue attenuation properties at the single scan energy.

DEQCT, on the other hand, employs two distinct X-ray energy spectra to further enhance the material decomposition process.[45] By exploiting the energy-dependent attenuation properties of different materials, DEQCT can differentiate and quantify multiple tissue compositions simultaneously, such as cortical and trabecular bone, as well as various soft tissue types.[51] This results in more accurate quantitative voxel data, specifically vBMD, and has been shown to improve correlations between fracture load and density.[3,4] This approach relies on carefully calibrated systems and advanced material decomposition algorithms to quantify the relative concentrations of these components within each voxel of the scanned volume.

In the context of the proximal humerus, SEQCT has demonstrated the potential for accurate vBMD assessment and fracture risk prediction; however, the use of DEQCT in the upper extremity has not been reported. The proximal humerus is a complex anatomical region with a high prevalence of osteoporotic fractures, and these quantitative CT techniques offer a more comprehensive understanding of bone quality and strength compared to traditional BMD measurements.[49,52] Furthermore, the quantitative data obtained from SEQCT and DEQCT can be integrated with advanced computational techniques, such as finite element modeling (FEM), to further enhance the analysis of bone biomechanics and fracture risk assessment. By incorporating patient-specific material properties and geometries derived from these imaging modalities, researchers and clinicians can simulate and predict

the mechanical behavior of the proximal humerus under various loading conditions, ultimately contributing to improved diagnosis, treatment planning, and patient outcomes.

It is important to note that while SEQCT and DEQCT offer significant advantages in bone assessment, they are associated with higher radiation doses compared to conventional techniques like DEXA. Therefore, careful consideration of radiation exposure and adherence to appropriate protocols are essential when utilizing these advanced imaging modalities, particularly for longitudinal or repeated assessments.

To address the limitations of DEXA, volumetric BMD (vBMD) methods have been developed to assess three-dimensional, size-independent density. Single-energy quantitative computed tomography (QCT) can be used to estimate vBMD but requires a calibration standard like a bone mineral phantom to calculate BMD values. More recently, dual-energy QCT (DEQCT) has emerged as an accurate volumetric method to measure vBMD. DEQCT acquires images at two energy levels, allowing differentiation of bone from other tissues to quantify vBMD.

Few studies have directly compared proximal humerus aBMD from DEXA with vBMD from DEQCT and SEQCT QCT. However, DEQCT vBMD has shown higher accuracy and precision compared to DEXA aBMD at other anatomical sites. DEQCT vBMD provides a volumetric measurement and accounts for overlying soft tissue that may improve fracture risk assessment and prediction at the proximal humerus over two-dimensional projections from DEXA. Further research is warranted to directly compare DEXA, SEQCT and DEQCT vBMD at the clinically important proximal humerus site.

Table 2.1: Comparison between DEXA, SEQCT and DEQCT scanning techniques.

Scanning Technique	Parameters	Energy Levels	Strengths	Weakness
DEXA	Areal bone mineral density (aBMD)	Two X-ray beams at different energy levels	Low dose, quantifies bone mineral density	Mostly used for bone density, limited other uses
SEQCT	Volumetric bone mineral density (vBMD)	Single X-ray beam energy	Lower radiation dose, quantifies density in vBMD	Limited material differentiation and density measures
DEQCT	Volumetric bone mineral density (vBMD)	Uses dual X-ray beams at different energy levels	Improved material characterization, can differentiate materials with similar densities	Slightly higher radiation dose, requires specialized equipment

2.4 Proximal humerus bone mineral density measures

To properly diagnose and treat a variety of musculoskeletal diseases, including osteoporosis and fractures, bone mineral density (BMD) must be evaluated. BMD is a key parameter quantified in the proximal humerus due to its implications for fracture risk assessment and prediction. As a material property, BMD correlates with bone's elastic modulus and ultimate strength, describing its stiffness and failure resistance respectively.[36] Loss of BMD in the metaphysis and along the surgical neck renders the proximal humerus more susceptible to fragility fractures.[37] Furthermore, BMD can be readily measured from clinical CT scans and serves as a useful input for FEMs to assign density-dependent mechanical properties.[38] While BMD alone does not fully characterize bone strength, it remains an important predictor of fracture that can be tracked over time. Quantifying and monitoring changes in regional vBMD of the proximal humerus through CT scanning thus provides clinically useful data on the susceptibility of the bone to failure under loading. This motivates the focus on precise BMD measurement in this region.

Particularly in the senior population, proximal humerus fractures can significantly affect a patient's independence, quality of life, and financial burden on the healthcare system. By accurately measuring proximal humeral BMD, doctors can identify patients who are more likely to suffer fractures and launch preventative therapies to stop future incidents. Additionally, measuring proximal humeral

BMD is essential for assessing the efficacy of osteoporosis treatment plans and tracking long-term bone health.[6,16,21] Clinicians can enhance the accuracy of fracture prediction models and improve patient care strategies by including proximal humeral BMD values into fracture risk assessment algorithms.[54] In the setting of proximal humeral fracture, proximal humeral BMD testing also has the ability to evaluate bone healing and treatment success.[54] As a result, the measurement of proximal humeral BMD is a useful tool for assessing the risk of fracture, assessing the effectiveness of treatment, and managing patients on an individual basis. This ultimately improves patient outcomes and musculoskeletal health.

Micro-computed tomography (microCT) is another advanced imaging technique that can assess bone density and microarchitecture in three dimensions. While microCT radiation dose is too high for clinical use, it serves as an excellent reference standard for ex vivo studies. With microCT, tissue mineral density of the bone tissue itself can be quantified, along with trabecular and cortical bone morphological parameters. By comparing DEXA aBMD, QCT vBMD methods, and microCT measures, we can comprehensively evaluate different BMD assessment techniques for the proximal humerus.

Sprecher et al (2015) compared the bone mineral density of cancellous and cortical bone between normal and osteoporotic patients. Their research revealed no statistically significant differences between the osteoporotic and normal groups, as well as among different locations within both groups. However, among normal and osteoporotic donors, differences in the apparent density of the cancellous bone were seen in various subcapital areas of the humeral head. Notably, the humeral head's cancellous region showed the highest bone density readings, excluding the subchondral plate. The initial third of the subcapital region showed the greatest distinction between the osteoporotic and normal groups. People with osteoporosis showed more pronounced differences than their healthy counterparts in a number of proximal humeral areas. A considerable bone loss was seen in particular in the medial metaphyseal area, which resulted in a weakening of the biomechanical structure. These results reveal regional differences in bone density and the effects of osteoporosis on particular regions of the proximal humerus, particularly the medial metaphyseal area.[21]

Furthermore, another study by Blakeney et al (2021) utilized CT imaging and 3D modeling to compare proximal humeral bone mineral density in patients undergoing a shoulder arthroplasty procedure. Additionally, they compared the data from 3D models to 2D and discovered a moderate connection between the values for bone mineral density between these two techniques.[25] Regression

models showed a significant age-related drop in the amount of bone evaluated by DEXA at the proximal humerus. Between the ages of 30 and 80, there was a 29% drop in the modeled areal bone mineral density (aBMD).[22]

Bone mineral density in the proximal humerus was also studied in women during menopause by Wang et al (2022). It was found that the cortical loss of the humeral head associated with menopause primarily manifested in the lateral part of the greater tuberosity. Complex proximal humerus fractures may be strongly influenced by the larger tuberosity's faster rate of bone loss. The results of the study showed significant regional variation in cortical loss caused by estrogen shortage and/or aging, impacting both the larger and minor tuberosities. These findings highlight the need of considering the distinct areas of the proximal humerus when evaluating how aging and estrogen insufficiency affects cortical bone loss. It is possible relevance of fracture susceptibility in menopause-related bone alterations is highlighted by the discovery of the lateral SEQCT of the larger tuberosity as a region of severe cortical loss.[25]

Unbalances in the bone remodeling process cause individuals to gradually lose bone mass and density as they age. The overall integrity and health of the joint may be significantly impacted by this age-related loss in shoulder BMD, potentially making the joint more fracture-prone and decreasing functional ability. Osteoporosis, characterized by a decrease in bone mass and deterioration of bone microarchitecture, is a common condition in older adults, particularly in postmenopausal women. The progressive loss of BMD in osteoporosis weakens the skeletal structure, making the bones more susceptible to fractures, including those occurring within the shoulder joint.

Similarly, osteoarthritis, a degenerative joint disease, can affect the shoulder joint, resulting in cartilage degradation, joint inflammation, and changes in bone structure. The combination of age-related BMD loss and osteoarthritis can further increase joint damage, leading to joint stiffness, chronic pain, and functional impairment. Understanding the dynamic relationship between the anatomy of the shoulder joint, its functional capabilities, and the changes in bone density over time is crucial for diagnosing and managing age-related shoulder conditions.

2.5 Finite Element Modeling

Finite element modeling (FEM) has become a widely used computational tool in the field of biomechanics and orthopedics, allowing researchers to create highly accurate 3D models of complex bone structures, such as the proximal humerus, and simulate their mechanical behavior under various loading conditions.[54] The development of FEM models typically starts with the acquisition of patient-specific imaging data, such as quantitative computed tomography (QCT) or magnetic resonance imaging (MRI), which provide detailed information about the geometry, material properties, and composition of the bone structure being studied.[41] The acquired imaging data is then processed and segmented to create a 3D digital representation of the bone, known as a finite element mesh.[56] Once the finite element mesh is generated, material properties, such as bone mineral density and trabecular architecture, can be assigned to different regions of the mesh based on the imaging data, enabling the creation of highly accurate and patient-specific FE models that closely resemble the actual bone structure and its biomechanical properties.[41]

In the context of the proximal humerus, FEM has been used to study the biomechanics of this complex bone structure, particularly in relation to fractures and implant design.[56] Dahan et al. (2019) utilized FEM to predict anatomical neck fractures in the proximal humerus, demonstrating the potential of this approach in identifying fracture risk and optimizing treatment strategies. The study highlighted the importance of considering patient-specific factors, such as bone geometry and material properties, in the development of accurate FEM models. FEM has also been applied to compare the biomechanical performance of various implant designs for proximal humeral fractures. Razfar et al. (2016) used FEM to compare the bone stresses in the proximal humerus between stemless, short stem, and standard stem length implants, providing valuable insights into the potential advantages and disadvantages of each design. This study underscores the role of FEM in optimizing implant selection and design for improved patient outcomes.

Ye et al. (2017) provided a comprehensive review of the applications of FEM in proximal humeral fractures, highlighting the various ways in which this computational tool can be used to enhance our understanding of fracture biomechanics and guide treatment decisions. The review emphasized the importance of incorporating patient-specific imaging data, such as QCT-derived BMD, into FEM models to improve their accuracy and reliability. The integration of advanced imaging

techniques, such as QCT, with FEM has been a key focus of research in recent years. Knowles et al. (2016) conducted a thorough review of the literature on the use of QCT-derived BMD in finite element studies, highlighting the advantages of this approach in creating patient-specific models with improved accuracy and predictive power. The review also discussed the challenges and limitations associated with the use of QCT-derived BMD in FEM, such as the need for standardized imaging protocols and the potential for errors in the segmentation and assignment of material properties.

As FEM continues to evolve and integrate with advanced imaging techniques, it holds great promise in enhancing our understanding of the biomechanics of the proximal humerus and improving the prevention, diagnosis, and treatment of fractures in this complex bone structure. However, it is crucial to validate and verify FEM models against experimental or clinical data to ensure their reliability and clinical relevance.[54,56] With ongoing advances in computational methods and imaging technologies, FEM is poised to play an increasingly important role in the field of orthopedics and biomechanics, ultimately leading to improved patient care and outcomes.

3. Methodology

This chapter describes the chronological methodology of how the data was collected, analyzed and the statistics that were performed. Figure 3.1 showcases the initial to final steps of generation of models initially obtained from the scanning modalities by DICOM images to obtain vBMD measures and strain analysis. The DICOM images are used as inputs in FEM software creating FE models to obtain strain results for each cadaver. Note that, all figures in the main body text are images captured from specimen 22150 left humerus. Figure 3.2 showcases the same but for minimum principal strain.

Figure 3.3 showcases the general flow of the thesis. Seven pairs of shoulders from cadavers were collected of which there were isolated left and right arms and four full torsos. These cadavers underwent scanning in both SEQCT and DEQCT to produce DICOM images that were used to produce 3D models of the humerus which were used as input for FEM construction.

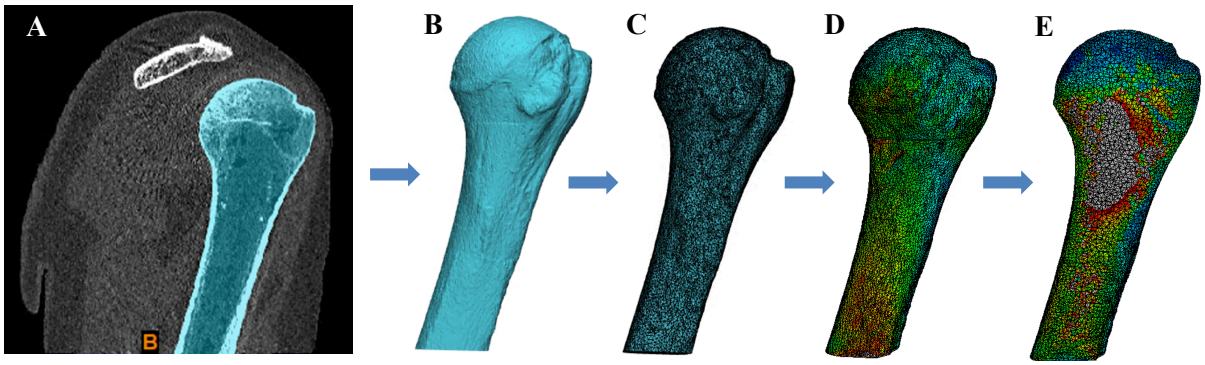


Figure 3.1: Generation of FEM from DICOM images to 3D models to obtain maximum (tensile) principal strain results. (A – MIMICS project; B – Filled humerus; C -Filled humerus with 2 mm mesh length; D – Surface of the humerus; E – Sliced humerus)

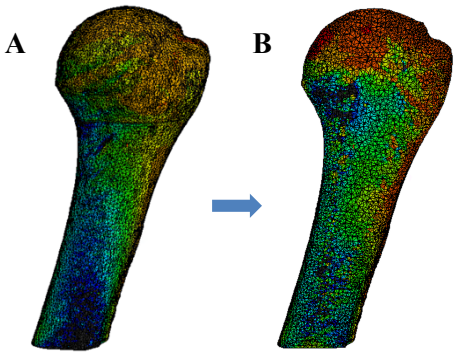


Figure 3.2: FE model of humerus showcasing minimum (compressive) principal strain results. (A – Surface of the humerus; B – Sliced humerus)

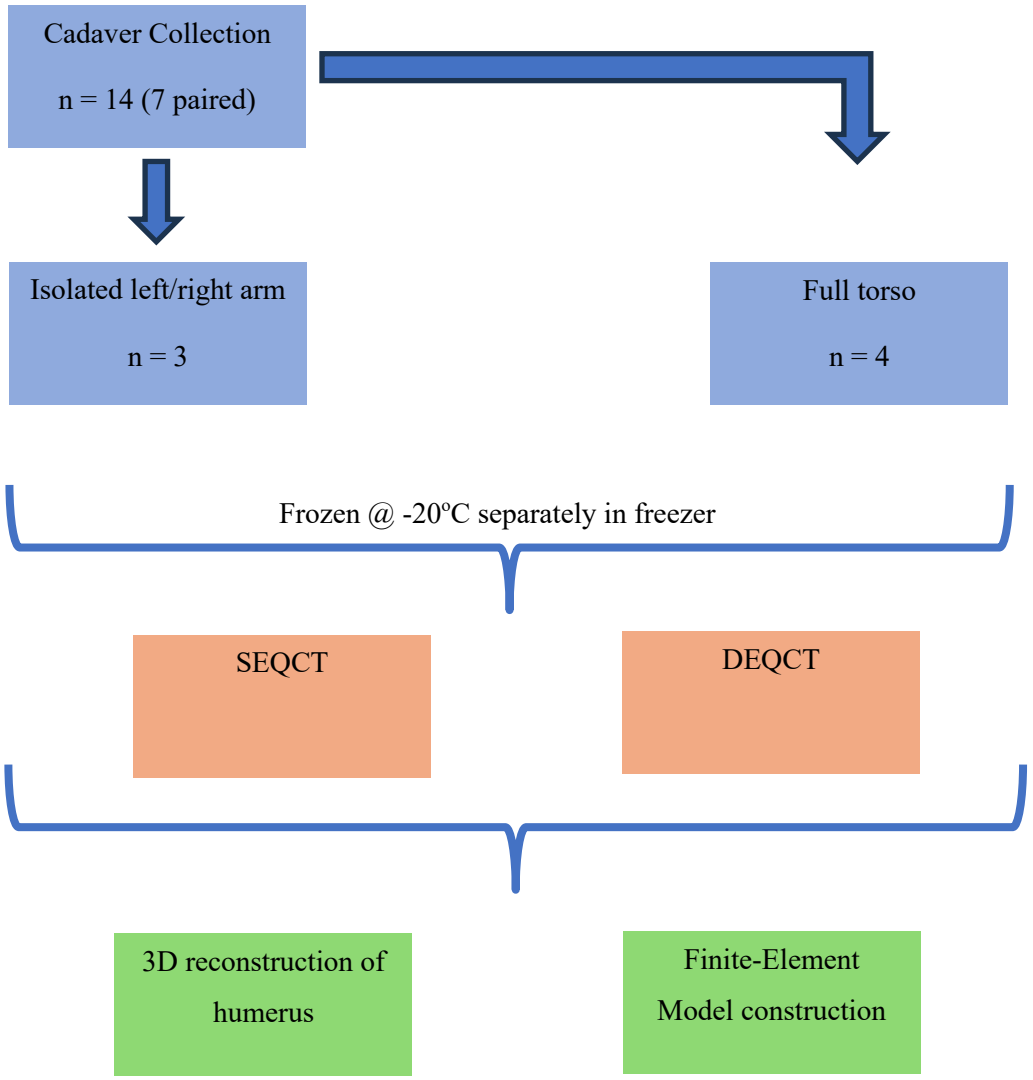


Figure 3.3: Thesis workflow. Cadaver preparation (blue), medical imaging (orange), and finite element modeling (green).

3.1 Cadaver Demographics, Preparation, and Dissection

Newly acquired donors sourced from the University of Waterloo School of Anatomy Body Bequeathal program were used in this study. The cadavers underwent dissection, dividing them into full torsos (comprising the neck to mid-thorax, including the glenohumeral joint to mid-humerus) or isolated proximal humeri connected to the scapula, encompassing the adjacent muscles, skin, and surrounding tissues as depicted in Figure 3.1.1. Smaller donors' full torsos were utilized, while larger donors' isolated shoulder joints (mid-humerus, including scapula, clavicle, and all soft tissues) were used due to restrictions in scanner volume and transportation logistics. All soft tissues were preserved as necessary to replicate in vivo CT scan acquisitions. Isolated shoulders were separated before the initial freezing at -20°C, and full torsos were sectioned post-initial freezing with support from the School of Anatomy's technical staff.

A total of seven sets of bilateral cadaveric shoulder specimens were gathered (n = 7 left, n = 7 right). One donor featured a Proximal Humeral Fracture (PHF) and was not utilized for image analysis or FEM generation. This study incorporates four female and three male cadavers, averaging 85 years of age with a standard deviation of 7 years (Table 3.1). The cadavers remained frozen at -20°C until the scanning day, where they were then transported in specimen coolers with icepacks to the imaging sites. SEQCT and DEQCT scans were conducted at St. Joseph's Hospital, London, ON, in one day with the cadavers spending 7 hours out of the freezer. Notably, no thawing occurred during transportation or scanning and were returned to the freezers. All imaging procedures were executed by certified imaging technologists experienced in the specific imaging protocols.

Table 3.1: Age and sex of cadaver specimens for imaging with the various techniques.

Specimen #	Sex	Age (yrs.)	Anatomy
22150	M	78	Isolated shoulders
22151	F	85	Isolated shoulders
22152	F	78	Isolated shoulders
22153	F	91	Full torso
22155	F	98	Full torso
23156	M	88	Full torso
23157	M	78	Full torso

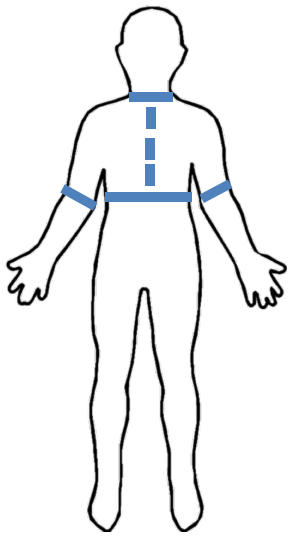


Figure 3.1.1: Frontal plane view of incision to segment the arm and torso.

3.2 Medical Imaging Analysis

All cadavers underwent scanning in both SEQCT and DEQCT without moving the specimen, scanning in two different reconstruction kernels: BONEPLUS and STD. These reconstruction kernels were chosen based on literature review, keeping consistency with other studies. A calibration phantom was incorporated for the SEQCT scanning for calibration purposes to convert from HU to vBMD. DEQCT images were generated in calibrated vBMD directly and did not require additional calibration. Scans produce DICOM images for each cadaver which were input into MIMICS to create humeral masks to calculate vBMD in the region of interest: humeral head, metaphysis, and diaphysis. Appendix D shows a step-by-step flow of how these were created.

Medical Imaging and Image Analysis Workflow:

Density Analysis

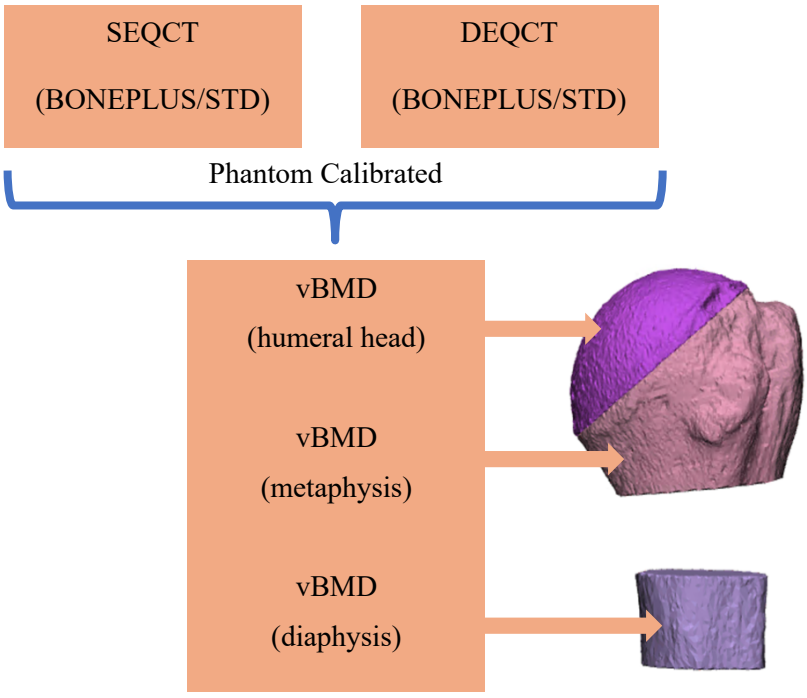


Figure 3.2.1: Density Analysis workflow.

3.2.1 SEQCT and DEQCT Imaging:

Using established best practices in QCT image collection,[27] each glenohumeral joint underwent separate scans following standard clinical procedures using a fast-switching kVp clinical CT scanner (GE Revolution HD GSI, Waukesha, WI, USA). The isolated shoulder and full torso cadavers were positioned so that the entirety of the humerus was in the middle of the scanner. The shoulders were oriented in a supine position, simulating the same position as a scan with an actual patient. The position of the cadavers was not changed between SEQCT and DEQCT scans, ensuring only the imaging modality was changed. A dipotassium phosphate (K_2HPO_4) calibration phantom was utilized and placed below the cadavers, with rods of known density concentrations as seen in Figure 3.2.3,[10] to convert native Hounsfield Units (HU) to equivalent vBMD [mg_{K2HPO4}/cc]. The method was standardized and can be referred to in the manufacturer's documentation. Appendix C shows a step-by-step process of how to create a rod/segmentation through phantom calibration using ITK-SNAP, an open-source image processing software.[28] Each rod was manually identified and highlighted using segmentation properties in ITK-SNAP by using different labelling for each rod (as seen in Figure 3.2.3 in cyan, yellow, blue, green and red) every 25 slices in the axial direction in the area of the CT image containing the phantom rod. The single-energy QCT scans were conducted at 120 kVp, with a pixel size of 0.488 mm, a slice thickness of 0.625 mm, and 79 mA, consistent with standard QCT image parameters used in vBMD analysis and FEA of bone.[29] Dual-energy QCT scans were performed without moving the specimen, making use of the built-in fast switching 80/140 kVp scanner capabilities. A four-stack protocol was applied to encompass the entire scan volume from the SEQCT images. The pixel size and slice thickness matched those of SEQCT images. Reconstruction of all images involved the use of a standard (STD) and bone sharpening (BONEPLUS) reconstruction kernel, leading to two sets of images for comparative analysis (SEQCT STD vs SEQCT BONE and DEQCT STD vs DEQCT BONE).[10,21,22,23,24] Monochromatic images at simulated 40 keV and 90 keV were generated during the reconstruction of DEQCT scans. Custom python code was used for bone analysis, as described previously.[5]

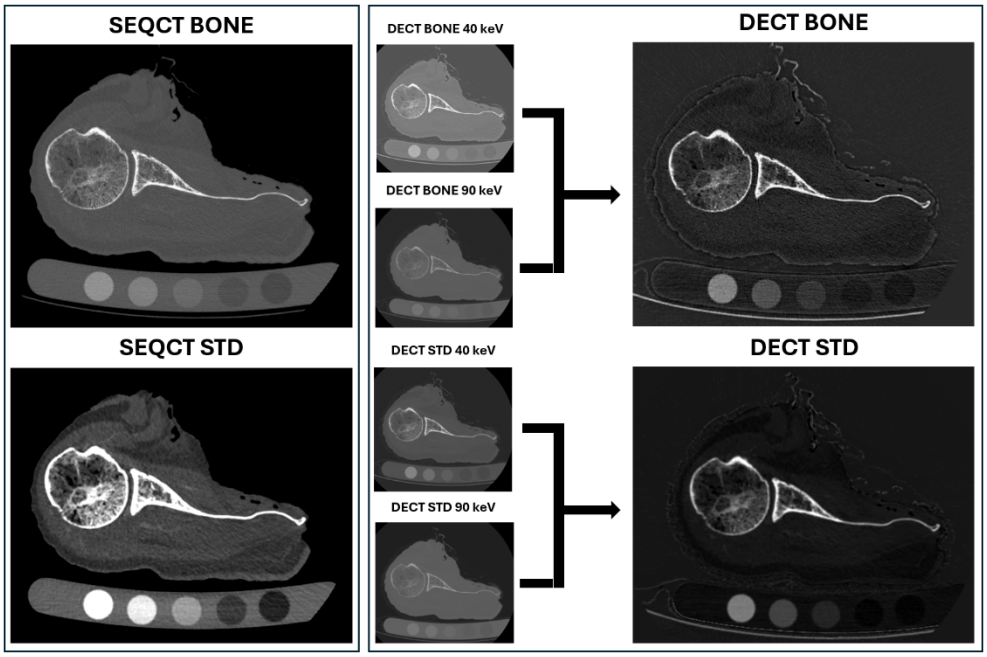


Figure 3.2.2: Axial representation of an isolated cadaveric shoulder from SEQCT and DEQCT images using BONE and STD reconstruction kernels. Note the variation in contrast across images due to range of intensity values.

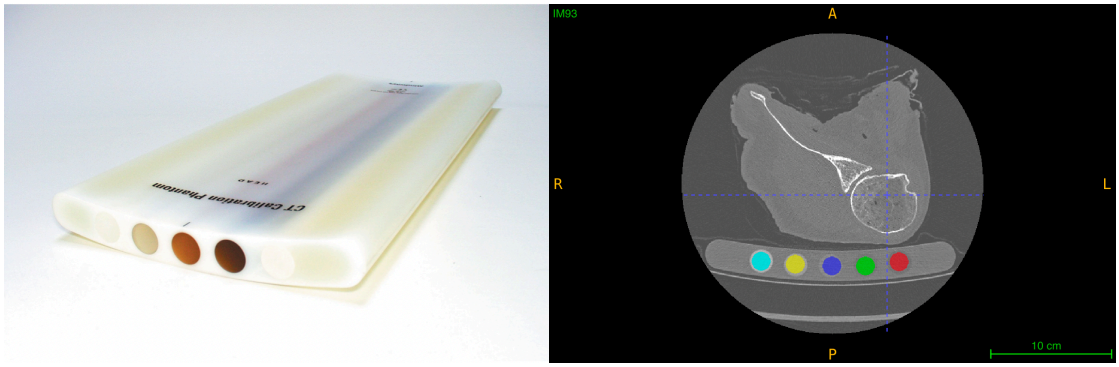


Figure 3.2.3: Phantom rod calibration used during scanning to compute a linear conversion between Hounsfield Units (HU) and an equivalent density (mgK2HPO4/cc) (left). A clinical QCT scan of a cadaveric shoulder and calibration phantom with sampling of rods of known density (QCT Pro. Bone Mineral Density Software CT Calibration Phantom. Version 5.0 - Revision 20110801. Mindways Software. User Guide)

3.2.2 Humerus Mask Creation in MIMICS and 3-MATIC:

SEQCT BONE images were used to generate three-dimensional reconstruction of the humerus for density and morphology calculations and FEM generation (Mimics v. 25.0, Materialise, Leuven, BE). A standard threshold defined the outer periosteal cortex, set at 225 HU threshold and semi-automated morphological operations were used to fill in the entire image mask, as required for density analysis and FEM generation (Appendix D). The 'filled' humeral mask was translated to the SEQCT STD images and was inherently aligned, ensuring a common volume for analysis across both images. The three-dimensional models were transferred to 3-Matic (Materialise, Leuven, BE) and used to separate the humerus into humeral head, metaphysis (defined between the anatomic and surgical necks), and diaphysis (Figure 3.2.4). Custom generated cubes of various sizes were implemented over the humerus at set location. A 75 mm cube was positioned at the anatomical neck to cover the humeral head portion of the humerus, forming the humeral head segment (Figure 3.2.6). Another 75 mm cube was placed at the surgical neck of the humerus so that the humeral head section was encased within this cube (Figure 3.2.6). For the diaphysis, a 20 mm thick cuboid was used and translated down 8.5 cm from the most proximal point of the humerus (Figure 3.2.6). These boxes alongside the 3D-model of the humerus were then transferred back into MIMICS to utilize an operation called the Boolean Operation. This operation allows for designated locations of the humerus to be isolated through the use of the intersection or unite feature to establish the desired regions. The same procedure was performed in DEQCT BONE images like SEQCT BONE where the 'filled' humeral mask was translated to the DEQCT STD image using a threshold at the specimen-specific vBMD value to ensure a common volume for analysis across both images. All 3 regions were matched between BONE and STD within the SEQCT and DEQCT images for consistency in measures.[17] The 3D regions were used to create image masks in MIMICS for density and morphology calculations.

A specimen-specific calibration slope and intercept were determined for each image using rod masks from the K_2HPO_4 phantom (Figure 3.2.5) using ITK-SNAP and custom python scripts. The slope/intercept were used to convert from native HU to equivalent vBMD [mg_{K2HPO4}/cm^3].[10] Density in vBMD was calculated in the humeral head, metaphysis, and diaphysis regions, for images from SEQCT BONE and SEQCT STD.



Figure 3.2.4: 3D model (left) of proximal humerus obtained from SEQCT and DEQCT images translated into 3-MATIC, showing the different regions for calculated vBMD in HU units (blue –humeral head; green – metaphysis; red – diaphysis). HU are obtained choosing highlighted region by reading the average value and converted to vBMD using a specimen-specific calibration slope and intercept.

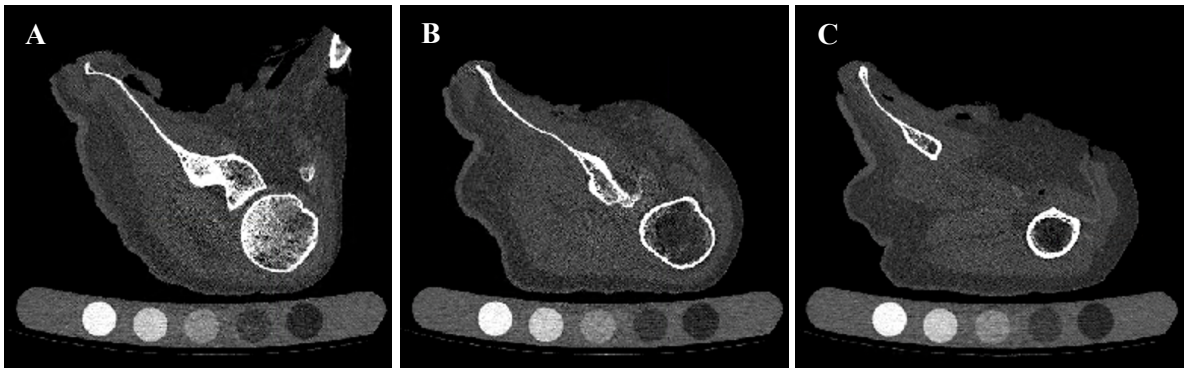


Figure 3.2.5 Representative axial SEQCT BONE image showing a proximal humerus section at the 3 regions (A - humeral head; B - metaphysis; C - diaphysis) for HU and vBMD analysis and input to image-based FEM, highlighting the difference in cortical bone thickness amongst the regions.

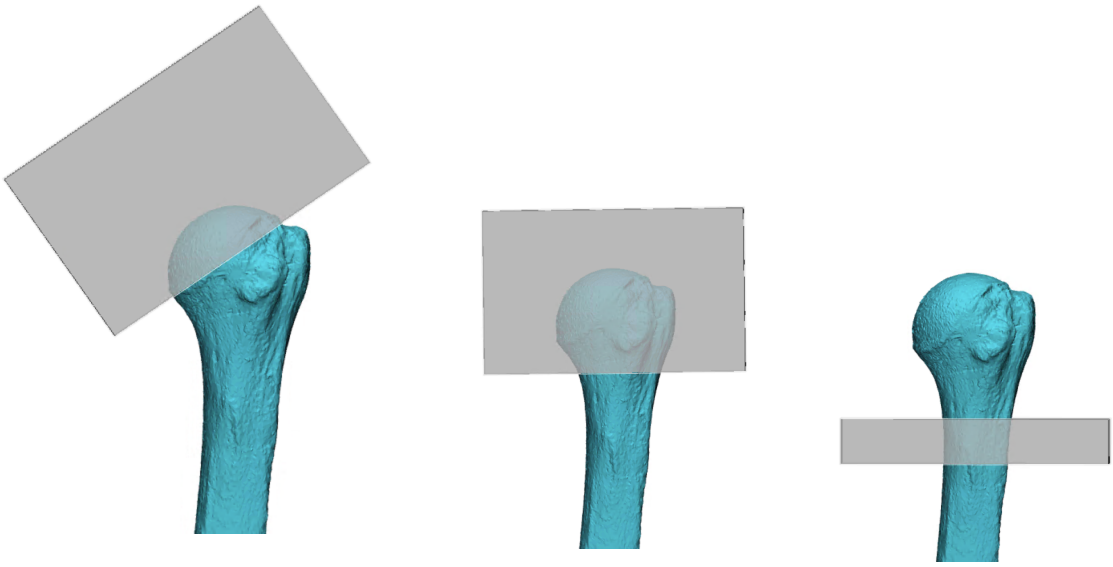


Figure Error! Use the Home tab to apply 0 to the text that you want to appear here.**2.6: Placement of custom-made cubes to form the 3 regions of interest.**

3.3 Finite-Element Generation

3.3.1 Finite Element Mesh Generation

CT DICOM images from SEQCT and DEQCT were imported into MIMICS for segmentation using a combination of thresholding, region growing, and manual editing tools. Identical 3D models generated from vBMD, and morphology analysis above were used as geometrical input to FEMs. A 2mm surface mesh (Figure 3.3.1) was performed in 3-MATIC and mesh geometry was checked using an automated wizard that is incorporated in the software to check for no errors in diagnostics of the model. This model was then exported as a surface mesh to Abaqus (v.2022, Simulia, Providence, RI) and converted to a tetrahedral volume mesh (Figure 1.1). 3D solid models were generated from the mask segments using 10-node quadratic tetrahedral elements (C3D10) (Figure 1.1) with a target edge length of 2 mm based on a mesh convergence study and literature recommendations, done in 3-MATICS.[10,16] Quadratic tetrahedral elements were used because of its advantageous ability to depict the complexity in curvature of the humerus geometry with smoother surfaces, enabling for higher accuracy. [41]

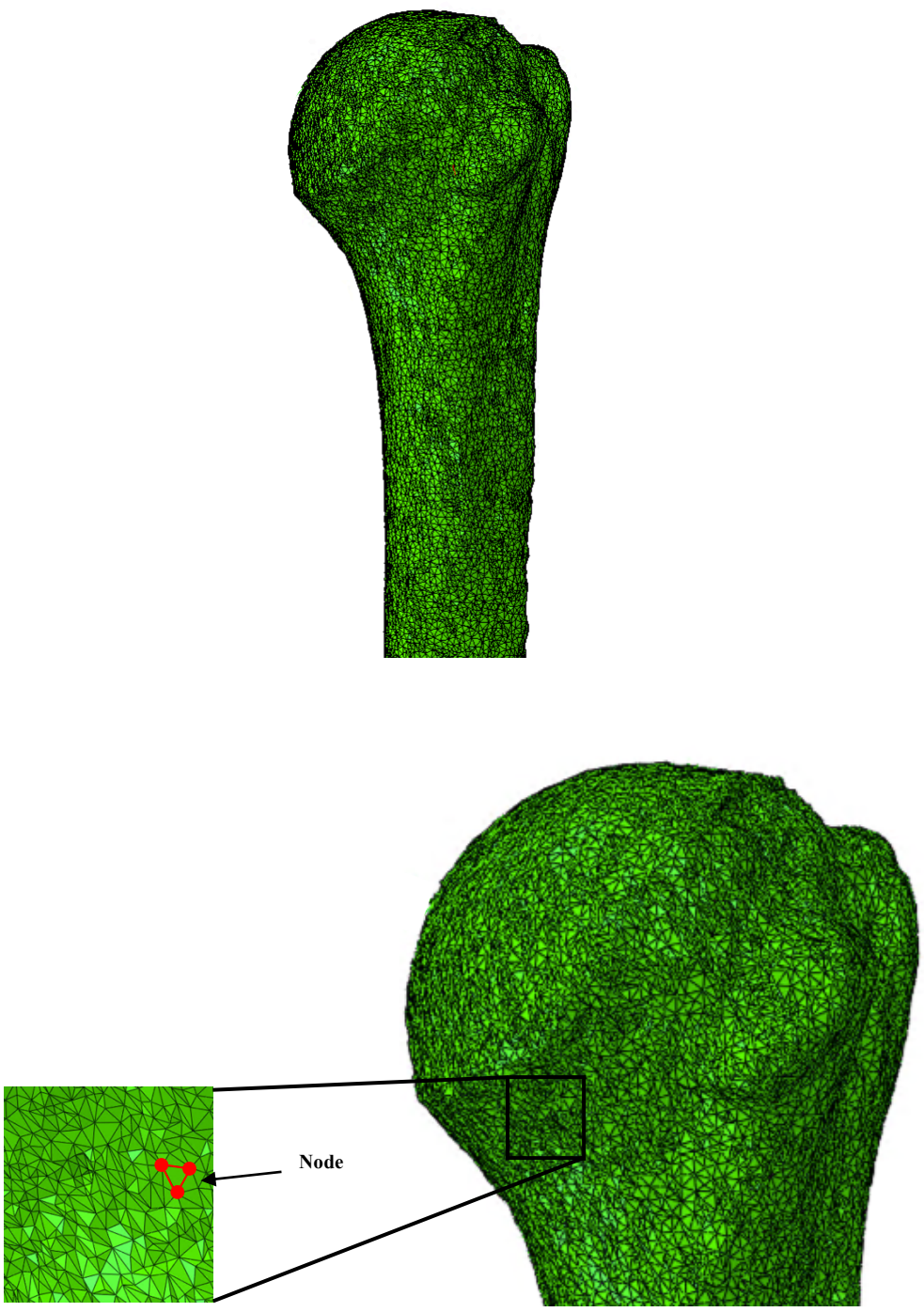


Figure 3.3.1: A finite element model of a humerus, separated into a 10-node quadratic tetrahedral mesh, consisting of nodes and elements.

3.3.2 FEM Material Property Assignment

The volume meshed models were exported to an open-source FEM pre-processing software (BoneMat v.3.2)[64] for material property assignment using validated relationships between vBMD and elastic modulus.[36] The appropriate DICOM images of each cadaver and image type were added allowing BoneMat to apply the appropriate vBMD to modulus conversion. Material was added into the volume mesh models through the CT densitometric calibration calculated through the specimen-specific calibration slope and intercept using the following equation (Equation 3.1). RhoQCT outputs the vBMD. For SEQCT this was set based on the specimen-specific slope/intercept. For DEQCT, this was set at "0" and "1", respectively.

$$RhoQCT = a + b * HU$$ **[Equation 3.1]**

Correction calibration was set at Single Interval and density-elasticity relationship was calculated using the following equation where the variables "a" was set at 0, "b" at 12486, and "c" at 1.16 based on the lowest mean relative error with a minimum elasticity modulus at 1E-06 (Equation 3.2 and Equation 3.3). [41,43,44] A poissons ratio of 0.3 was applied across models. Since the density modulus relationship is in units of dipotassium phosphate, the values of a, b, and c in Equation 3.2 were set to 0, 1, and 1 respectively due to limitation of BoneMat only accepting density as RhoAsh.

$$RhoAsh = 0+1*RhoQCT$$ **[Equation 3.2]**

$$E = 0+12486*RhoQCT^{1.16}$$ **[Equation 3.3]**

3.3.3 Local coordinate system of the humerus

Each humerus was exported from 3-MATIC into Abaqus and 10 random evenly distributed points along the smooth articular head of the humerus were selected to give coordinates in (X,Y,Z). The origin of the humerus head was defined using a least-squares sphere-fit algorithm in MATLAB [39] using the 10 random points, giving a single coordinate point as the origin. MATLAB code was used to calculate the circle-fit, along the shaft[40] 8.5 cm below the most superior point of the humerus head. Eight random points were chosen along the edges of the shaft for input as coordinates into the code.

The vector between the origin and the circle-fit center point was defined as the X-axis (+inferior). The vector between the origin and the most medial point of the humerus head was defined as the Y-axis (+medial). The Z-axis (+posterior) was the cross-product of the X- and Y-axes.

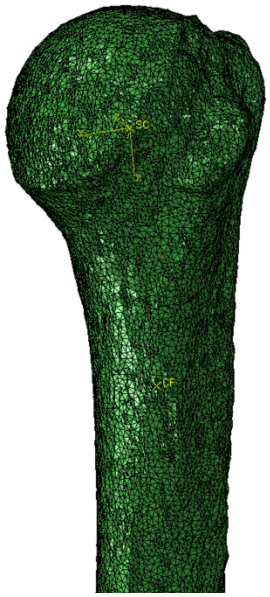


Figure 3.3.2: Coordinate system (SC - Sphere Centre; CF - Circle Fit)

Abaqus CAE (Dassault Systems, Providence, RI) was used to apply boundary conditions simulating a fall on an outstretched arm, with applied loads of 2500 N, simulating the average proximal humerus fracture load across populations.[54] Load direction was applied over specimen-specific contact areas defined between the humeral head and glenoid, with the arm rotated at 90 degrees of abduction (Figure 3.3.3). This was consistent with validated cadaveric experimental modeling of the proximal humerus, simulating a fall on an outstretched hand.[54] The distal humeral shaft was constrained in all degrees of freedom.

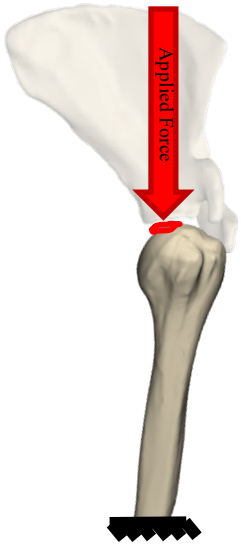


Figure 3.3.3: 3D model of proximal humerus showing humerus at 90 degrees abduction with the scapula. Red area marked indicates the glenoid contact area between the humerus and scapula.

3.3.4 Finite-Element Analysis

The FEMs underwent quasi-static analysis using Abaqus Standard linear analysis. The maximum principal (tensile) and minimum principal (compressive) strains were extracted for the entire proximal humerus model and gathered in the humeral head, metaphysis, and diaphysis regions using custom MATLAB code. In the humeral head and metaphysis, where the thin cortical shell is considered to play a minor role in fracture propagation, emphasis was placed on crack propagation through the trabecular bone.[10,13] For the humeral head and metaphysis, the focus was on determining the percentage of total elemental strains surpassing 4100 (tensile) and 8300 (compressive) microstrain for trabecular bone.[65] Conversely, in the diaphysis cortical bone region, the aim was to ascertain the percentage of total elemental strains exceeding 6700 (tensile) and 9800 (compressive) microstrain for cortical bone.[66] Total elemental strains surpassing fracture threshold in each region was similar to existing studies for consistency. The regions exhibiting the largest distribution of elemental strains surpassing these thresholds were used to help predict where fractures may occur under the given loading conditions. Percentage of strained volume thresholds are a well-established measure for determining the likely site of bone fractures.[65,66]

3.4 Data Collection Errors

Every study encounter problem that can impact the data collection process. This section will describe issues that were encountered throughout this study and the reasoning for not including models for data analysis.

Both cadavers 22151R and 22155R were not used for the entirety of this research. Cadaver 22155R possessed a fracture and obtaining vBMD data by performing masks for this cadaver would not have been accurate. Cadaver 22155R had phantom errors. During scanning, the rods of the phantom were not in scope of the scan and hence, no calibration was able to be performed and therefore was not used in this study. All other cadavers (n = 12) were used for calculated vBMD. For SEQCT, the Humeral Head only had eleven models due to an anomaly that cannot be accounted for (cadaver 22155L) and was omitted from analysis (n = 11).

For models created from images obtained by SEQCT, cadavers 22153L, 22153R, 23157L and 23157R were not created. For cadaver 22153L, material properties of this specimen were not loading and could not add specific materials to this specimen, causing the software to crash. For the other three cadavers, transforming the surface mesh models into volume mesh were not working. This left me with eight different models of humeri obtained from SEQCT images.

For models created from images obtain by DEQCT, cadavers 22150R, 22151L, 22153L, 23157L and 23157R were not created. Cadavers 22150R and 22151L had problems with loading the images and processing. As for the other three models, they all failed the auto wizard check for ensuring no errors in diagnostics of the model in the initial phase. This left me with seven different models of humeri obtained from DEQCT images.

3.5 Statistical Analysis

3.5.1 Specimens

Descriptive statistics were used to report the age, sex, anatomy of how the cadavers were harvested and cause of death (if available) for all cadavers.

3.5.2 Density and morphology

The density of each specimen was reported as HU and vBMD [mg_{K2HPO4}/cm^3] within the anatomical neck, metaphysis, and diaphysis, regions for SEQCT. The vBMD measurements obtained from each scanning parameters are presented for each cadaver and as the mean value with +/- standard deviation and compared utilizing a paired t-test, within each of the SEQCT BONE/STD. DEQCT BONE/STD produce calibrated images in vBMD, and thus only vBMD was reported and compared in these models. Again, the vBMD measurements obtained from each scanning parameters are presented for each cadaver and as the mean value with +/- standard deviation and compared utilizing a paired t-test, within each of the DEQCT BONE/STD.

3.5.3 FEM Strain Correlations

Full frontal, uncut view of the humerus and a sliced humerus are presented for each cadaver alongside a histogram for each region for each the maximum and minimum principal strain. Strain colourmap thresholds were consistent amongst cadavers with a range of 0 to 4100 for maximum principal and 0 to -8300 for minimum principal. Reasons for using these thresholds was to be consistent with literature review.[65,66] Regions where the largest number of elements exceeded the thresholds indicated the location that will likely exhibit a fracture. This was confirmed by the FE models of each cadaver and where the areas of largest strain elements are present. No statistical comparisons were made but a qualitative comparison was done between visual representations of the FEM and strains that exceeded the threshold from the histograms for each cadaver individually. X-axis for the histograms were set to capture all the bars that were visible. Total number of elements that are not visible are reported as part of the figure caption. This was done for ease of visualization of the histograms.

4. Results

4.1 Bone Mineral Density

The specimen-specific density in HU and vBMD for the eleven models derived from the two SEQCT reconstruction kernels are presented in Table 4.1, and the twelve models presented in Table 4.2 and 4.3 representing each region chosen, respectively (Humeral Head, Metaphysis and Diaphysis). All the models reconstructed from the BONE kernel images from SEQCT exhibited higher HU and vBMD compared to those derived from the STD kernel images. This was consistent amongst the three different regions. For all three regions, Humeral Head, Metaphysis and Diaphysis, significant differences occurred between SEQCT BONE and STD in both the average HU and the average vBMD. Across the models compared, the results demonstrate that the BONE reconstruction kernel yield higher vBMD and HU values in SEQCT compared to the STD reconstruction kernel, with a significant difference observed in all the regions.

Table 4.1: Density measures in HU and vBMD in humeral head region (n = 11) derived from SEQCT scans of both BONE and STD reconstruction kernels.

Model	SEQCT HU		SEQCT vBMD [mg_{K2HPO4}/cc]	
	BONE	STD	BONE	STD
22150L	307.61	303.68	238.07	235.11
22150R	279.81	275.54	212.76	209.50
22151L	356.51	351.57	270.77	266.87
22152L	175.62	169.91	129.59	125.08
22152R	180.87	175.01	137.16	132.38
22153L	209.54	206.59	155.54	152.96
22153R	271.59	266.69	206.55	202.59
23156L	228.53	226.80	171.23	169.61
23156R	203.58	199.18	151.87	146.19
23157L	288.88	286.51	224.72	222.24
23157R	276.89	275.01	214.82	213.58
Average ± SD	**252.68 ± 57.22[a]**	**248.77 ± 57.55[a]**	**192.10 ± 45.65[b]**	**188.74 ± 46.16[b]**

Average values sharing a common letter are significantly different using a Paired T-Test ($p < 0.05$). SEQCT – single energy CT; BONE – boneplus reconstruction kernel; STD – standard reconstruction kernel; HU – Hounsfield Unit; vBMD – Volumetric Bone Mineral Density

Table 4.2: Density measures in HU and vBMD in Metaphysis region (n = 12) derived from SEQCT scans of both BONE and STD reconstruction kernels.

Model	SEQCT HU		SEQCT vBMD [mg_{K2HPO4}/cc]	
	BONE	STD	BONE	STD
22150L	122.88	119.41	96.52	93.76
22150R	146.34	142.04	110.29	107.03
22151L	149.39	143.68	111.80	107.30
22152L	145.57	139.03	106.35	101.23
22152R	148.06	141.91	111.39	106.35
22153L	140.25	136.03	102.22	98.64
22153R	151.43	148.42	113.04	110.62
22155L	131.62	127.11	94.28	90.52
23156L	128.61	124.52	94.11	90.65
23156R	118.18	113.66	85.56	80.67
23157L	215.70	211.87	168.27	166.24
23157R	185.31	182.42	142.23	140.14
Average ± SD	**148. 61 ± 27.33[a]**	**144.18 ± 27.61[a]**	**111.34 ± 22.92[b]**	**107.76 ± 23.57[b]**

Average values sharing a common letter are significantly different using a Paired T-Test ($p < 0.05$). SEQCT – single energy CT; BONE – boneplus reconstruction kernel; STD – standard reconstruction kernel; HU – Hounsfield Unit; vBMD – Volumetric Bone Mineral Density

Table 4.3: Density measures in HU and vBMD in Diaphysis region (n = 12) derived from SEQCT scans of both BONE and STD reconstruction kernels.

Model	SEQCT HU		SEQCT vBMD [mg_{K2HPO4}/cc]	
	BONE	STD	BONE	STD
22150L	351.07	341.17	271.37	263.87
22150R	375.15	365.64	285.96	278.67
22151L	564.95	549.38	430.76	418.70
22152L	517.60	497.24	394.01	378.00
22152R	476.07	458.68	369.04	355.44
22153L	370.07	362.30	279.05	272.83
22153R	385.91	377.37	295.51	288.67
22155L	532.44	518.01	404.75	392.91
23156L	299.96	288.72	226.37	217.41
23156R	314.02	303.64	237.61	226.22
23157L	514.90	507.55	399.06	389.87
23157R	474.58	468.23	371.51	366.85
Average ± SD	**431.39 ± 91.85[a]**	**419.83 ± 89.89[a]**	**330.42 ± 71.53[b]**	**320.79 ± 70.15[b]**

Average values sharing a common letter are significantly different using a Paired T-Test ($p < 0.05$). SEQCT – single energy CT; BONE – boneplus reconstruction kernel; STD – standard reconstruction kernel; HU – Hounsfield Unit; vBMD – Volumetric Bone Mineral Density

The regression parameters (Table 4.4) show strong correlations ($R^2 = 0.99$) between BONE and STD image-based density (HU and vBMD) by bone region (Humeral head, Metaphysis, and Diaphysis). Significant differences were not observed between the slopes differing from 1 in all three regions in both HU and vBMD respectively besides for vBMD in the metaphysis. On the other hand, all the intercepts are significantly different from 0 in HU and vBMD respectively in all three regions. The coefficient of determination (R-squared) in all regions in vBMD is lower than HU across the two different reconstruction kernels (BONE vs STD) in all three regions.

Table 4.4: Regression parameters (BONE vs STD) obtained from 3D humeral models using HU and vBMD [mg_{K2HPO4}/cc] in SEQCT.

Region	Measurement	Regression parameters		r^2
		slope	intercept	
Humeral head	HU	1.0054	5.2707[b]	0.9994
	vBMD	1.0108	5.4315[b]	0.9992
Metaphysis	HU	1.0095	5.8408[b]	0.9983
	vBMD	1.1402[a]	18.243[b]	0.993
Diaphysis	HU	0.9778	1.9688[b]	0.9981
	vBMD	1.0107	11.056[b]	0.9874

Average values sharing a common letter of 'a' are significantly different from 1 and 'b' are significantly different from 0 using linear regression ($p < 0.05$).

The specimen-specific vBMD values for the ten humeri models derived from the two different image input types for DEQCT are presented in Table 4.6, 4.7 and 4.8, representing each region chosen, respectively (Humeral Head, Metaphysis and Diaphysis). All the models reconstructed from the BONE kernel images of DEQCT acquisitions exhibited higher vBMD compared to those derived from the standard (STD) kernel images in the humeral head, besides for 1 model (Model - 22152R). In the metaphysis, all models experienced higher BMD in the BONE than STD reconstruction kernel (Table 4.7). In the diaphysis, 60% of the models showcased higher BMD in the BONE than STD reconstruction kernel. Notably, the average vBMD values derived from DEQCT BONE kernel, which is considered the most accurate representation of vBMD, exhibited statistically significant differences when compared to the average vBMD values obtained from the STD kernel image in all three regions (Humeral Head, Metaphysis and Diaphysis). This finding suggests that for longitudinal monitoring of vBMD, it was imperative to maintain consistency in the reconstruction kernel (BONE or STD) employed. Failure to do so may introduce artificial variations in the vBMD measurements, potentially confounding the assessment of bone mineral density changes over time.

Table 4.5: Density measures in vBMD in Humeral head region (n = 10) derived from DEQCT scans of both BONE and STD reconstruction kernels.

	Model	DEQCT	
		BONE	STD
vBMD [mg_{K2HPO4}/cc]	22150L	224.0110	213.8588
	22152L	130.3394	128.9908
	22152R	153.6663	154.2201
	22153L	160.2898	156.5091
	22153R	191.4757	181.7831
	22155L	175.1898	171.0679
	23156L	161.0219	152.2474
	23156R	139.6318	132.4322
	23157L	211.1145	209.7667
	23157R	196.5638	195.5844
	Average ± SD	**174.33 ± 30.82[a]**	**169.65 ± 30.07[a]**

Average values sharing a common letter are significantly different using a Paired T-Test ($p < 0.05$). DEQCT – dual energy CT; BONE – boneplus reconstruction kernel; STD – standard reconstruction kernel; vBMD – Volumetric Bone Mineral Density. Red highlighted values indicate a STD vBMD measurement larger than BONE

Table 4.6: Density measures in vBMD in Metaphysis region (n = 10) derived from DEQCT scans of both BONE and STD reconstruction kernels.

	Model	DEQCT	
		BONE	STD
vBMD [mg_{K2HPO4}/cc]	22150L	104.3941	93.9138
	22152L	114.5372	108.4242
	22152R	114.0505	111.6892
	22153L	127.9324	114.3357
	22153R	111.5342	98.6204
	22155L	118.8395	107.8170
	23156L	106.5977	95.7445
	23156R	91.8467	83.1433
	23157L	179.1821	163.5500
	23157R	153.8473	140.7112
	Average ± SD	**122.28 ± 25.85[a]**	**111.79 ± 23.85[a]**

Average values sharing a common letter are significantly different using a Paired T-Test ($p < 0.05$). DEQCT – dual energy CT; BONE – boneplus reconstruction kernel; STD – standard reconstruction kernel; vBMD – Volumetric Bone Mineral Density

Table 4.7: Density measures in vBMD in Diaphysis region (n = 10) derived from DEQCT scans of both BONE and STD reconstruction kernels.

	Model	DEQCT	
		BONE	STD
vBMD [mg_{K2HPO4}/cc]	22150L	**209.3295**	**225.2200**
	22152L	**327.7620**	**343.8271**
	22152R	**296.3244**	**308.7152**
	22153L	272.2926	248.1529
	22153R	254.0117	236.0199
	22155L	**351.1186**	**361.0535**
	23156L	251.7380	217.6278
	23156R	265.8246	232.7840
	23157L	422.6804	379.1334
	23157R	403.8521	355.8322
	Average ± SD	**305.49 ± 69.55[a]**	**290.84 ± 64.93[a]**

Average values sharing a common letter are significantly different using a Paired T-Test ($p < 0.05$). DEQCT – dual energy CT; BONE – boneplus reconstruction kernel; STD – standard reconstruction kernel; vBMD – Volumetric Bone Mineral Density. Red highlighted values indicate a STD vBMD measurement larger than BONE

The regression parameters (Table 4.9) show strong correlations ($R^2 = 0.98$) between BONE and STD image-based vBMD in the humeral head and metaphysis, respectively. The r-squared was lower in the diaphysis region (0.86). Only the diaphysis reported significant differences in the slopes compared to 1 whereas there were significant differences seen in the intercept in both the humeral head and diaphysis only.

Table 4.8: Regression parameters (BONE vs STD) obtained from 3D humeral models using vBMD [mg_{K2HPO4}/cc] in DEQCT.

Region	Regression Parameters		r2
	Slope	Intercept	
Humeral head	0.9675	0.9812[b]	0.9836
Metaphysis	0.9143	0.00006	0.9817
Diaphysis	0.8671[a]	25.94[b]	0.8627

Average values sharing a common letter of 'a' are significantly different from 1 and 'b' are significantly different from 0 using linear regression ($p < 0.05$).

4.2 Strain

Note that strain model results below refer to cadaver 23156R. All other models are shown in the Appendix A and Appendix B and follow similar explanations to model 23156R. Fracture location predictions are possible through the combination use of visual data from the color thresholds obtained from Abaqus and both maximum (tensile) and minimum (compressive) principal strain data within the three different regions from the histograms. Based on Figure 4.2.1 and Figure 4.2.2, the sliced images display high level of failure in the middle region (metaphysis region) indicated by the grey elements (indicating maximum or minimum tensile or compressive strain values, respectively) in both the BONE and STD reconstruction kernel. This was supported by Figure.4.2.4 where maximum tensile in the metaphysis was recorded to be higher in this region in comparison to both humeral head and diaphysis. DEQCT data showcase similar results of strain indication that the metaphysis displays high level of failure. The bigger the maximum (tensile) principal strain, the more these voxels are deformed hence, the higher the risk a fracture occurs. The smaller the minimum (compressive) principal strain, the more these voxels are deformed hence, the higher the risk a fracture occurs. Important thing to note between different reconstruction kernels, the images generated from STD reconstruction kernels always display more grey elements (more likelihood of fracture) compared to the ones from BONE. This was supported by the histograms as well where the STD bars exceed and therefore showcase predicted fracture compared to BONE.

The histograms showcase differences in reconstruction kernels and the influence on strain measurement. Most of the higher strains are recorded higher in the STD compared to the BONE reconstruction kernel when looking at maximum (tensile) principal strain. There was an overestimation to strain data when using STD reconstruction kernel. This was consistent in both SEQCT and DEQCT. This can influence the diagnosis of best implant choice and can also mislead to fracture location predictions. To add to that, more elements are recorded in higher end strains in STD than BONE, showcased by the blue bars exceeding. This was similarly reported in minimum principal but in the opposite direction. Note that, results vary independently for each cadaver, reasons due to different comorbidities, bone quality, age but, all follow the same trend. Strain distributions are also load magnitude and load direction dependent.

For SEQCT, 7 of the 7 specimens had strains that exceeded the thresholds the largest in the metaphysis region compared to the other two regions. For DEQCT, 7 of the 7 specimens also had strains that exceeded the thresholds the largest in the metaphysis region compared to the other two regions.

This indicates that the metaphysis region was most likely to experience fracture under the simulated loading conditions performed.

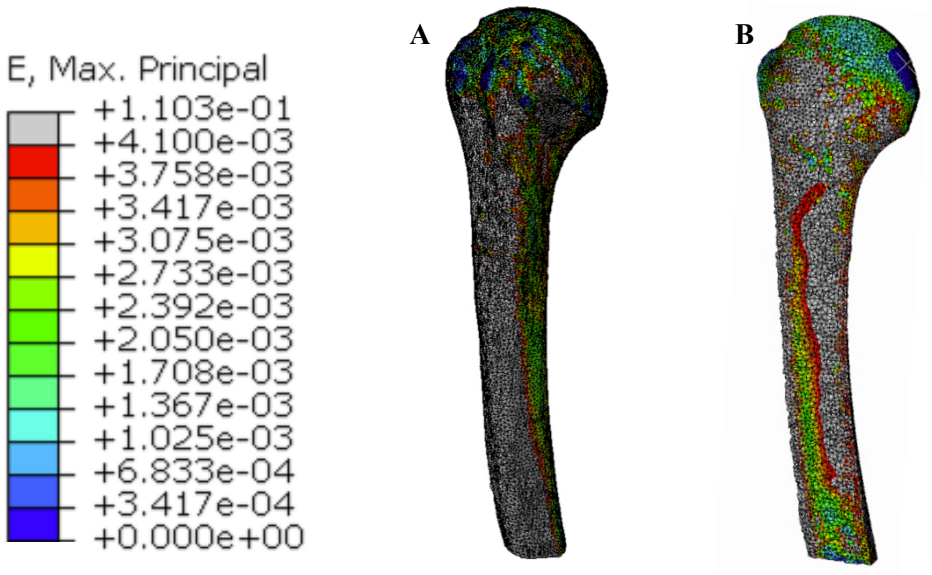


Figure 4.2.1: 23156R SEQCT maximum (tensile) principal strain with a microstrain set at 4100 for BONE reconstruction kernel (A - Surface of the humerus; B - Sliced humerus)

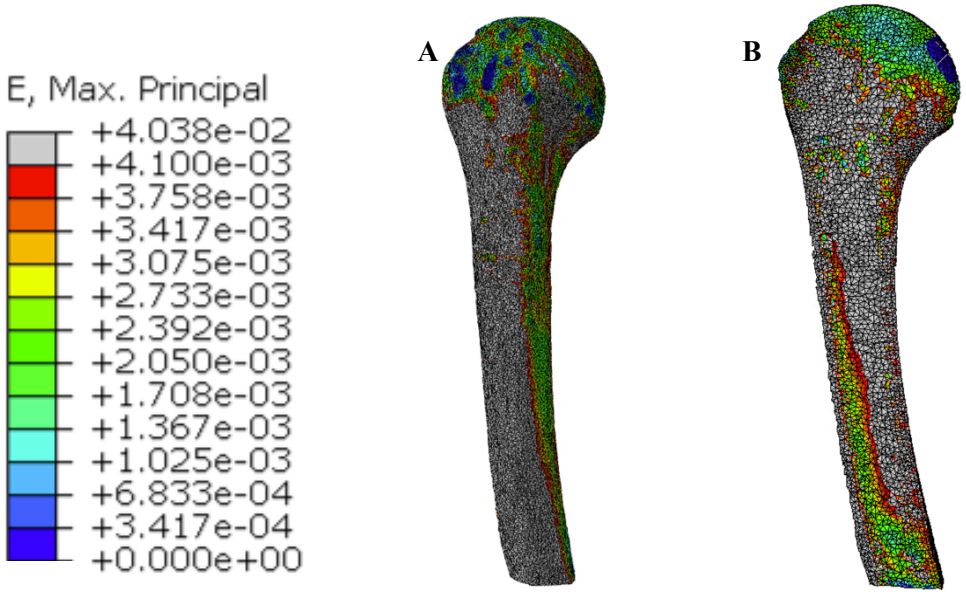


Figure 4.2.2: 23156R SEQCT maximum (tensile) principal strain with a microstrain set at 4100 for STD reconstruction kernel (A - Surface of the humerus; B - Sliced humerus)

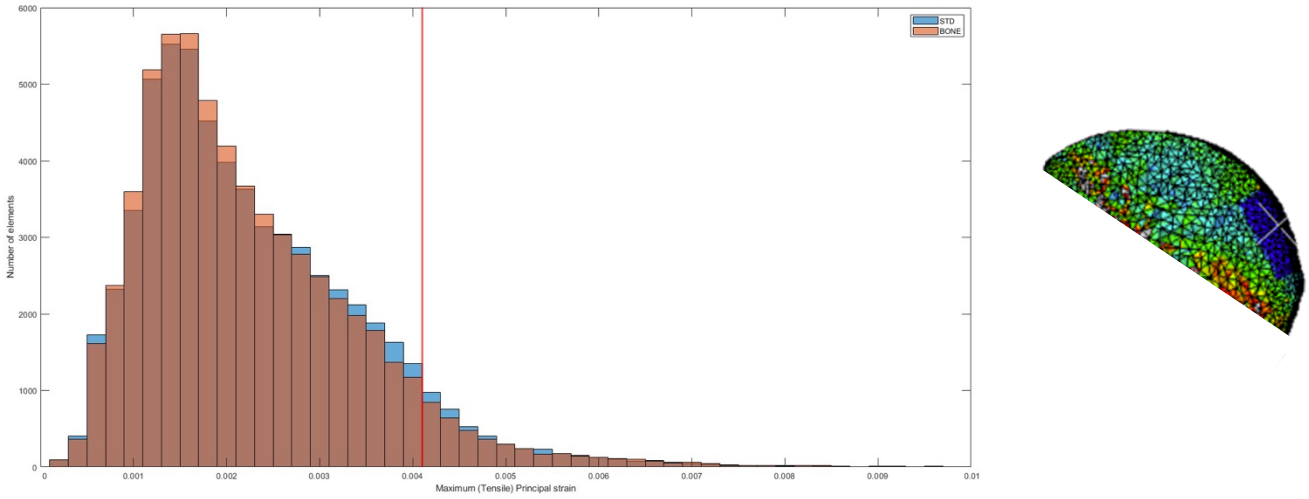


Figure 4.2.3: 23156R Humeral Head maximum principal differences between BONE and STD reconstruction kernel in SEQCT. The highest reported strain in each reconstruction kernel: BONE = 0.0148; STD = 0.0162. Number of elements exceeding 0.01 strain: BONE = 24; STD = 33. Red line indicates elemental strains of 4100 (tensile) microstrain for trabecular bone.

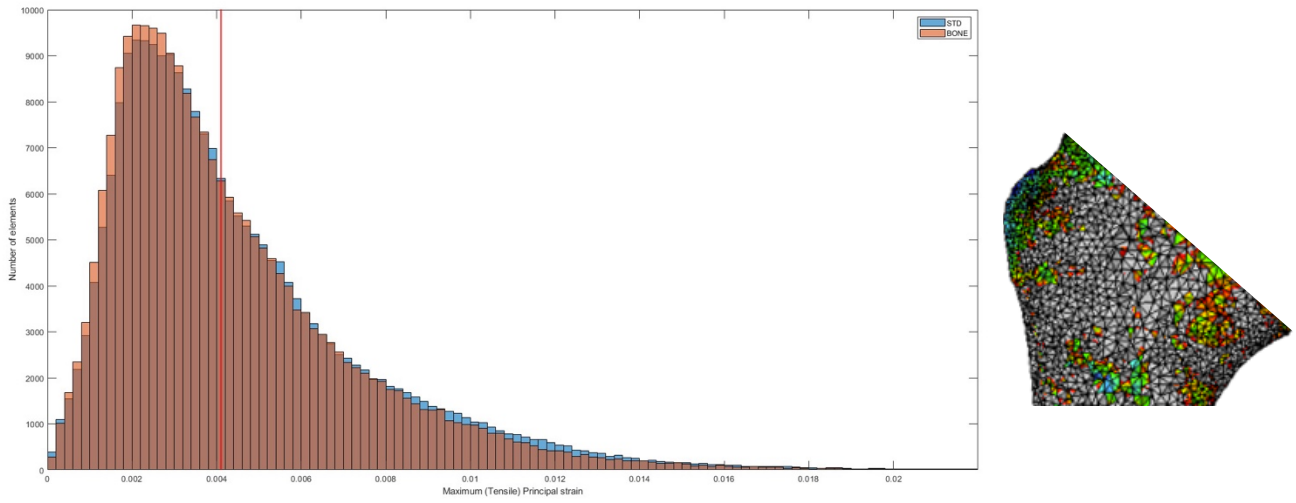


Figure 4.2.4: 23156R Metaphysis maximum principal differences between BONE and STD reconstruction kernel in SEQCT. The highest reported strain in each reconstruction kernel: BONE = 0.0784; STD = 0.0457. Number of elements exceeding 0.022 strain: BONE = 145; STD = 17. Red line indicates elemental strains of 4100 (tensile) microstrain for trabecular bone.

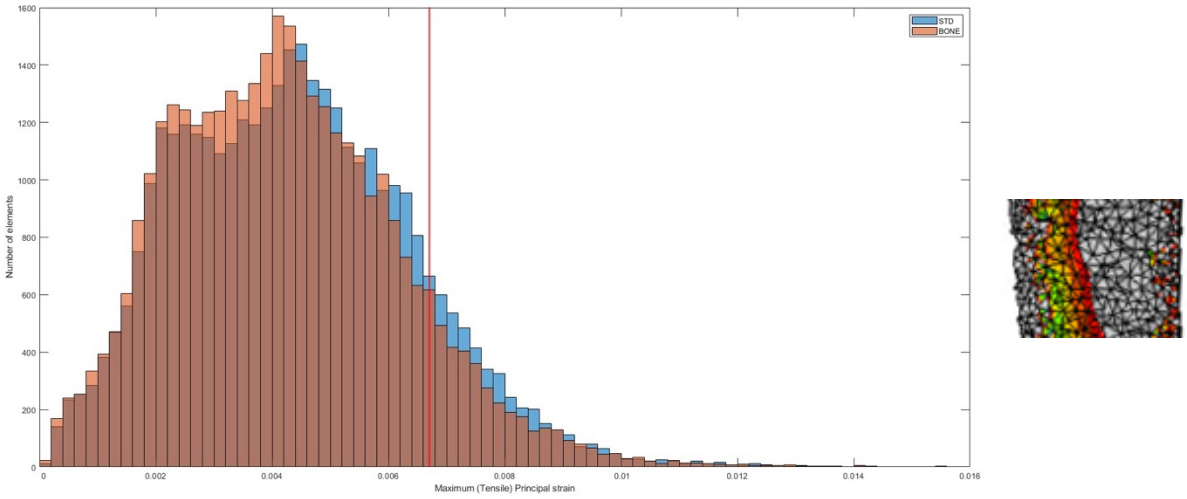


Figure 4.2.5: 23156R Diaphysis maximum principal differences between BONE and STD reconstruction kernel in SEQCT. The highest reported strain in each reconstruction kernel: BONE = 0.0186; STD = 0.0181. Number of elements exceeding 0.016 strain: BONE = 3 STD = 2. Red line indicates elemental strains of 6700 (tensile) microstrain for cortical bone.

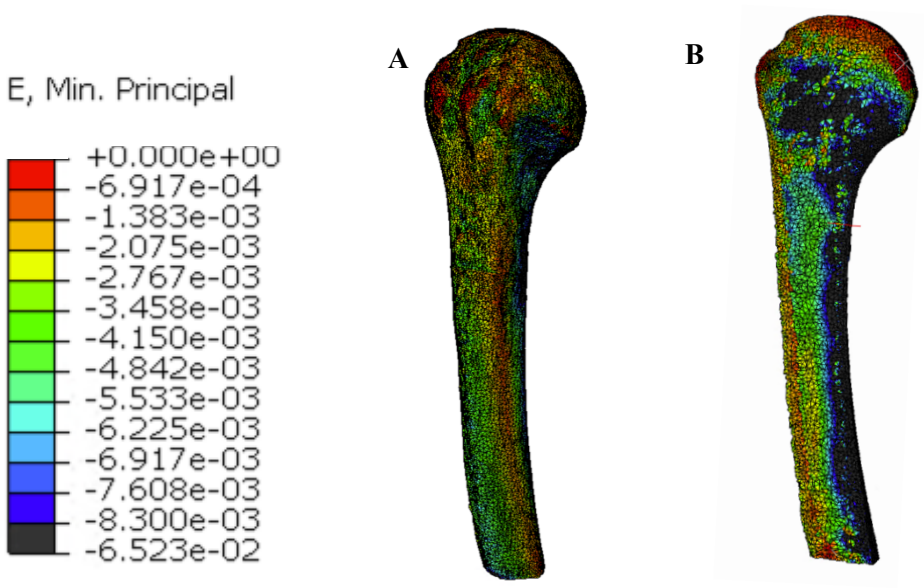


Figure 4.2.6: 23156R SEQCT minimum (compressive) principal strain with a microstrain set at 8300 for BONE reconstruction kernel (A - Surface of the humerus; B - Sliced humerus)

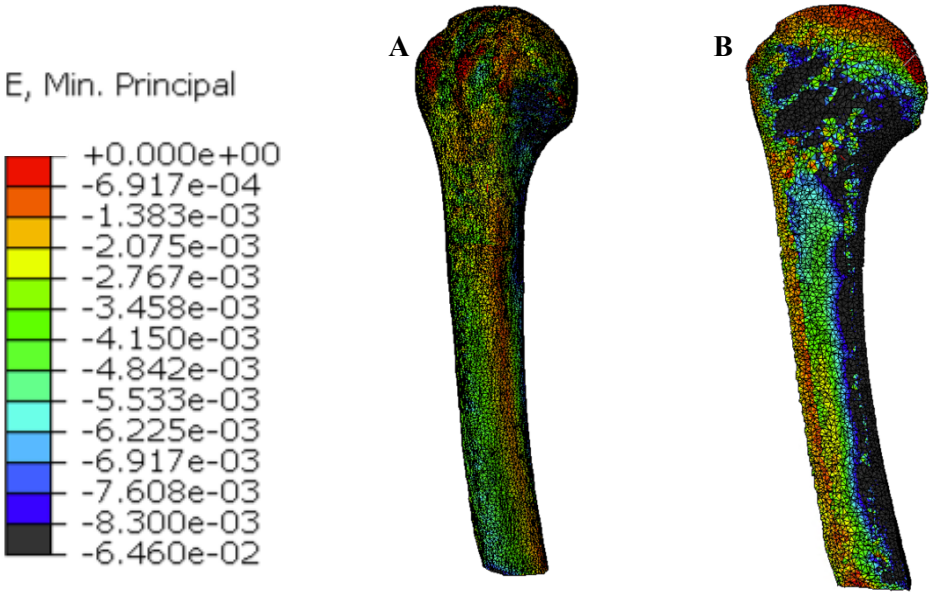


Figure 4.2.7: 23156R SEQCT minimum (compressive) principal strain with a microstrain set at 8300 for STD reconstruction kernel (A - Surface of the humerus; B - Sliced humerus)

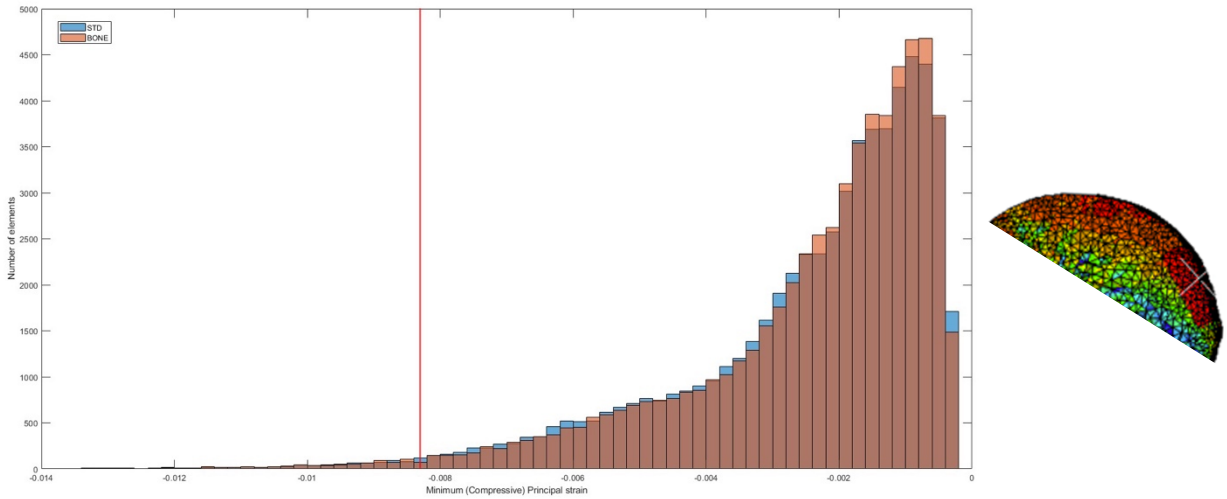


Figure 4.2.8: 23156R Humeral Head minimum principal differences between BONE and STD reconstruction kernel in SEQCT. The lowest reported strain in each reconstruction kernel: BONE = -0.0182; STD = -0.0213. Number of elements less than -0.014 strain: BONE = 20; STD = 33. Red line indicates elemental strains of 8300 (compressive) microstrain for trabecular bone.

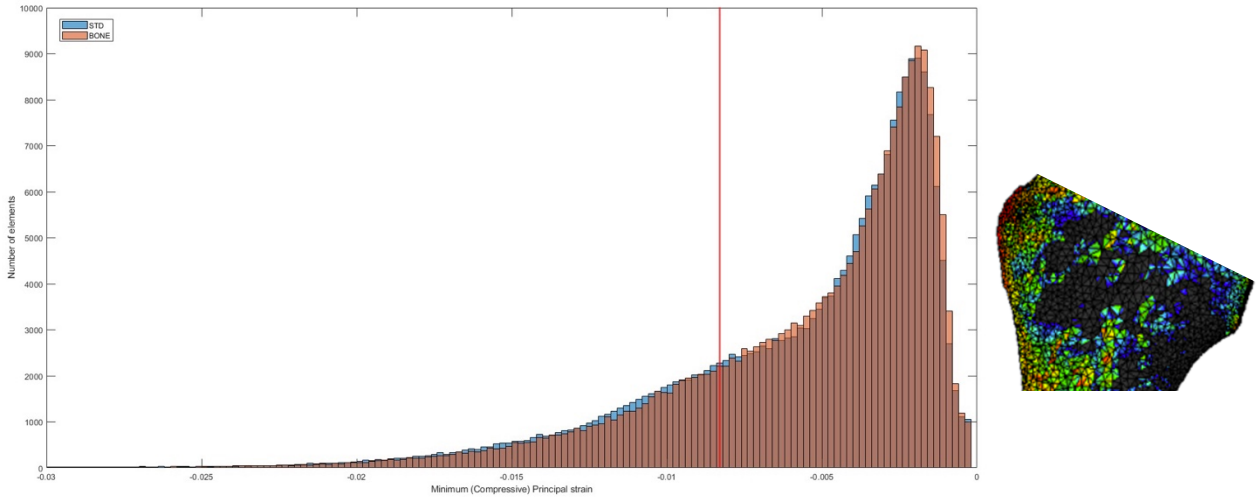


Figure 4.2.9: 23156R Metaphysis minimum principal differences between BONE and STD reconstruction kernel in SEQCT. The lowest reported strain in each reconstruction kernel: BONE = -0.0674; STD = -0.0556. Number of elements exceeding -0.03 strain: BONE = 275; STD = 3. Red line indicates elemental strains of 8300 (compressive) microstrain for trabecular bone.

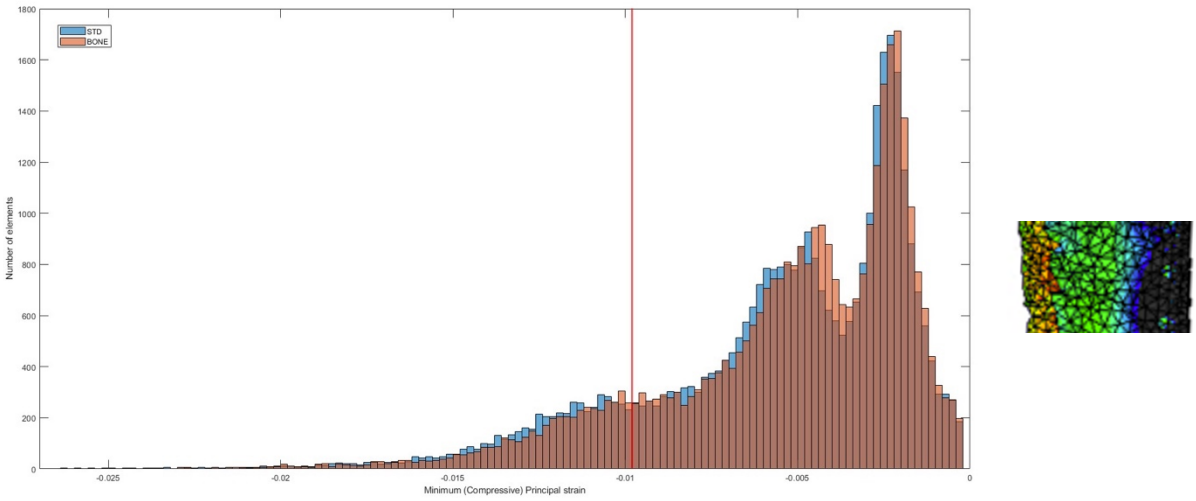


Figure 4.2.10: 23156R Diaphysis minimum principal differences between BONE and STD reconstruction kernel in SEQCT. The lowest reported strain in each reconstruction kernel: BONE = -0.0420; STD = -0.0421. Number of elements less than -0.027 strain: BONE = 36; STD = 29. Red line indicates elemental strains of 9800 (compressive) microstrain for cortical bone.

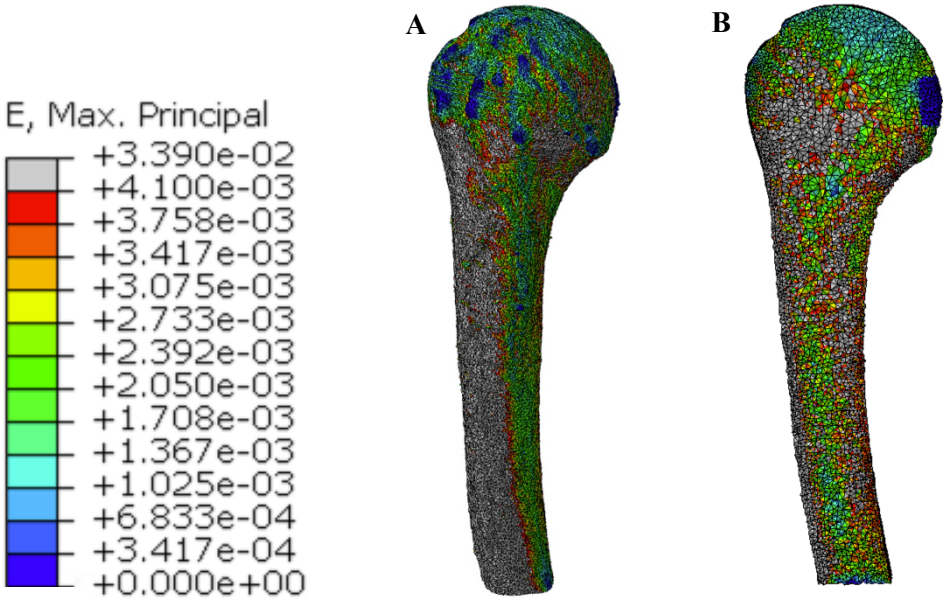


Figure 4.2.11: 23156R DEQCT maximum (tensile) principal strain with a microstrain set at 4100 for BONE reconstruction kernel (A - Surface of the humerus; B - Sliced humerus)

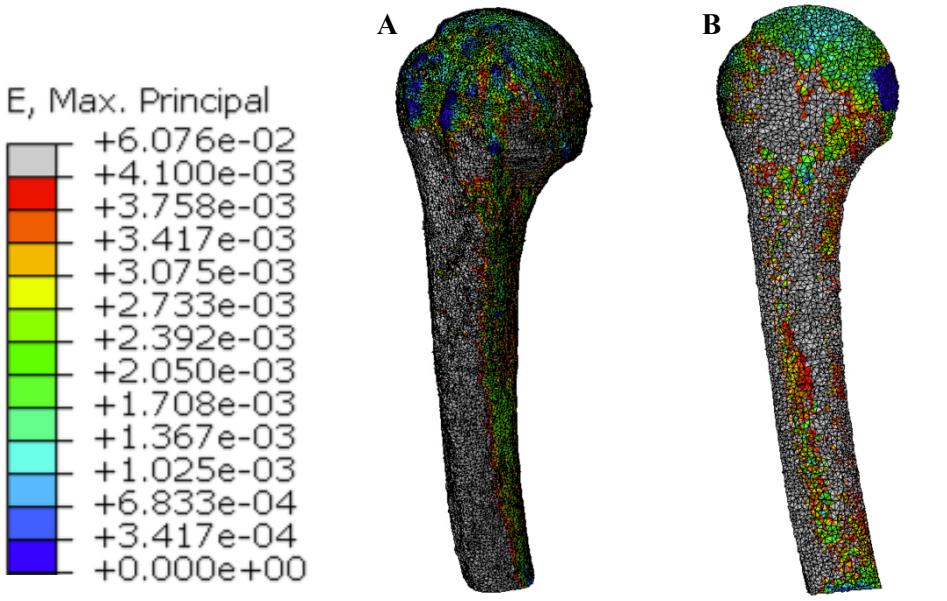


Figure 4.2.12: 23156R DEQCT maximum (tensile) principal strain with a microstrain set at 4100 for STD reconstruction kernel (A - Surface of the humerus; B - Sliced humerus)

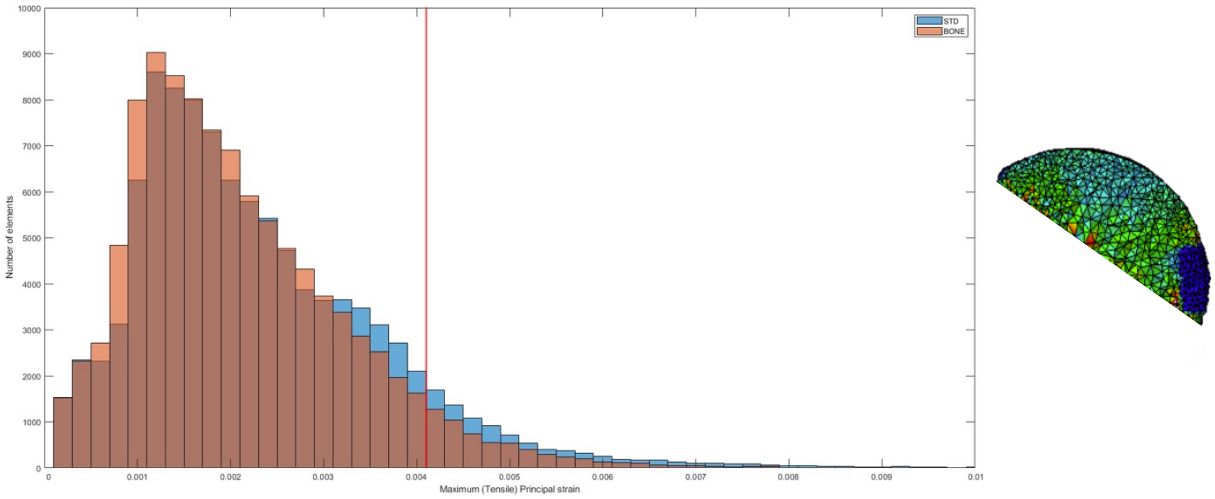


Figure 4.2.13: 23156R Humeral Head maximum principal differences between BONE and STD reconstruction kernel in DEQCT. The highest reported strain in each reconstruction kernel: BONE = 0.0145; STD = 0.0168. Number of elements exceeding 0.01 strain: BONE = 15; STD = 120. Red line indicates elemental strains of 4100 (tensile) microstrain for trabecular bone.

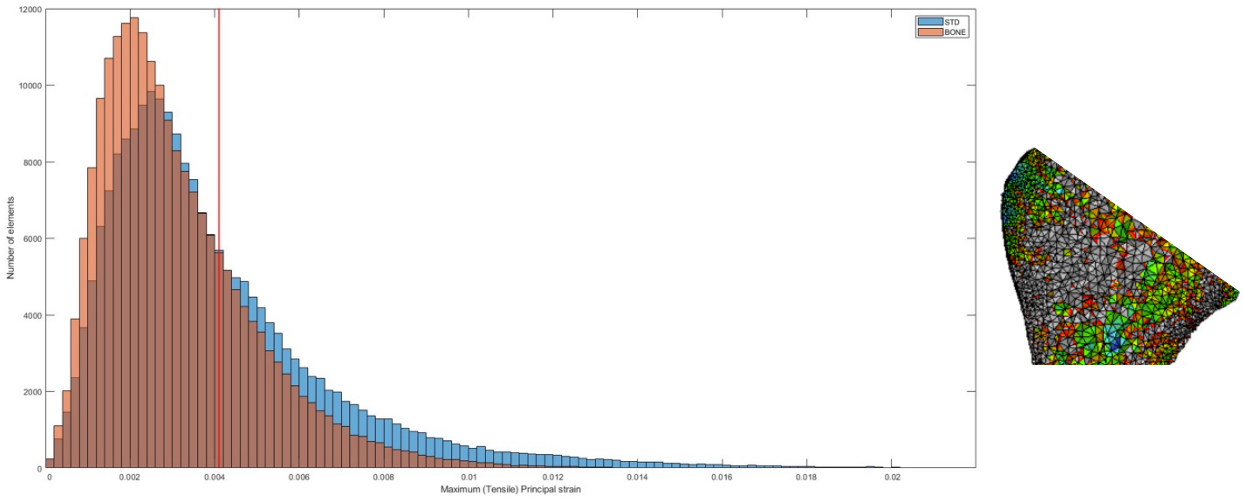


Figure 4.2.14: 23156R Metaphysis maximum principal differences between BONE and STD reconstruction kernel in DEQCT. The highest reported strain in each reconstruction kernel: BONE = 0.0267; STD = 0.0396. Number of elements exceeding 0.022 strain: BONE = 2; STD = 140. Red line indicates elemental strains of 4100 (tensile) microstrain for trabecular bone.

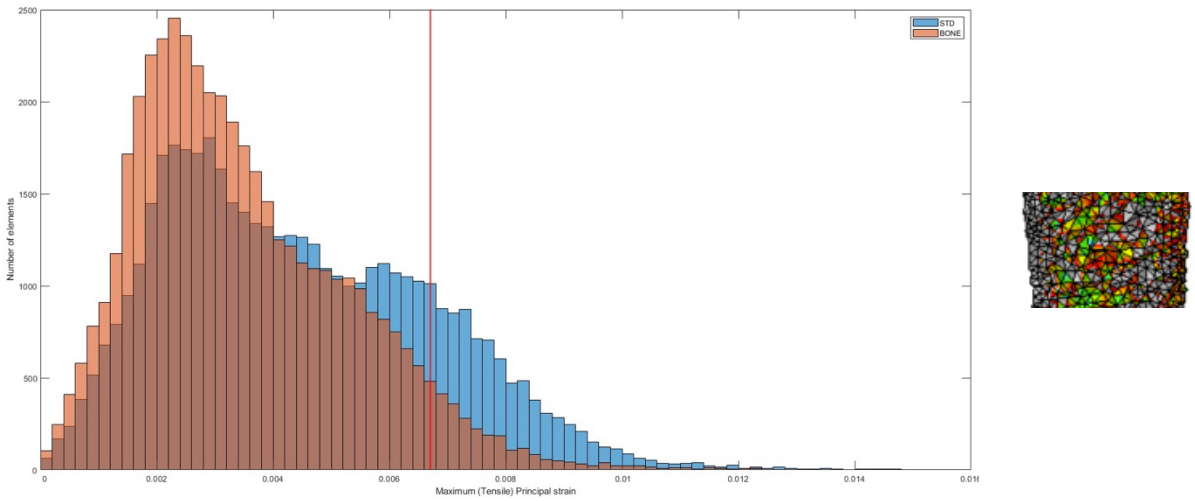


Figure 4.2.15: 23156R Diaphysis maximum principal differences between BONE and STD reconstruction kernel in DEQCT. The highest reported strain in each reconstruction kernel: BONE = 0.0268; STD = 0.0192. Number of elements exceeding 0.016 strain: BONE = 5; STD = 10. Red line indicates elemental strains of 6700 (tensile) microstrain for cortical bone.

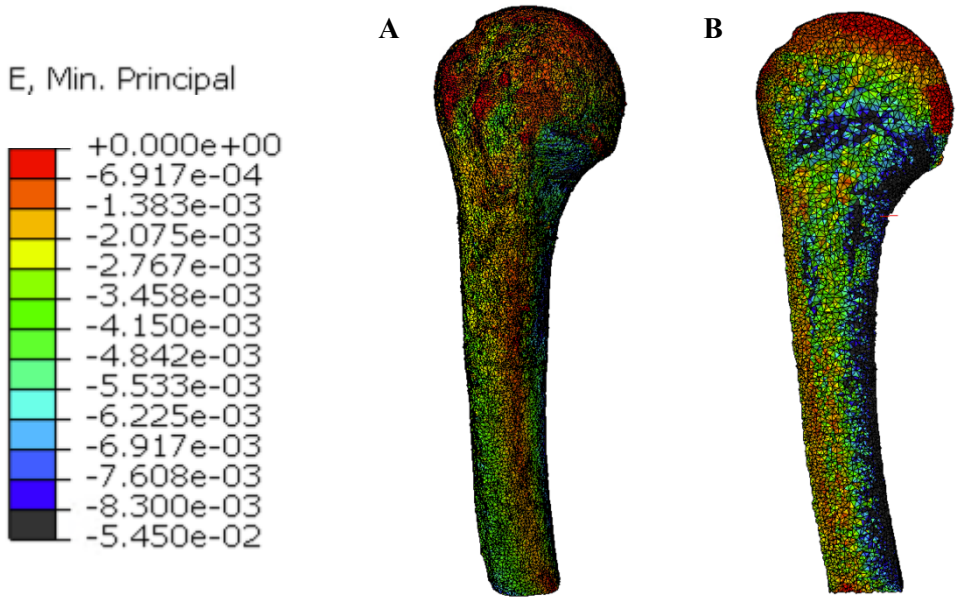


Figure 4.2.16: 23156R DEQCT minimum (compressive) principal strain with a microstrain set at 8300 for BONE reconstruction kernel (A - Surface of the humerus; B - Sliced humerus)

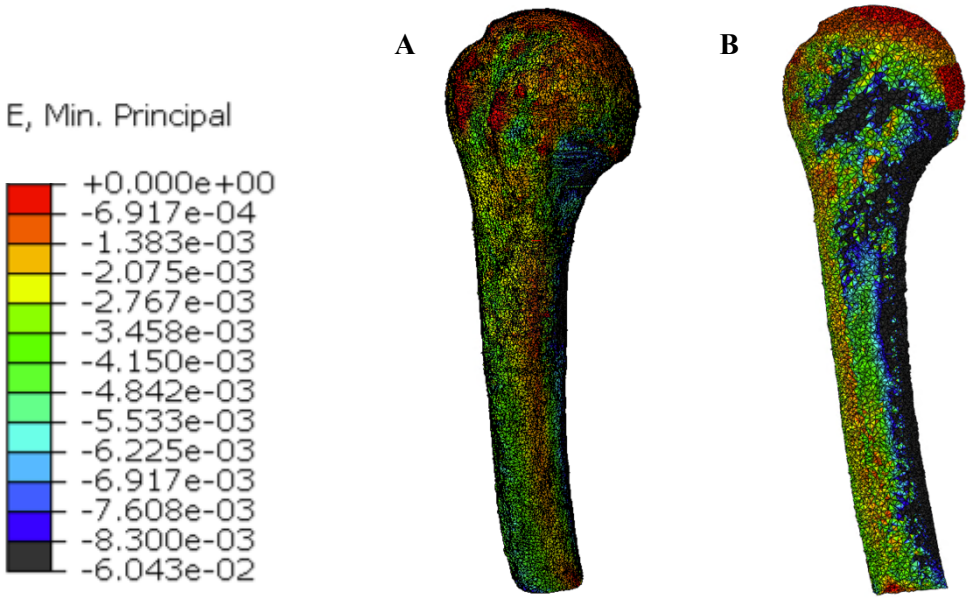


Figure 4.2.17: 23156R DEQCT minimum (compressive) principal strain with a microstrain set at 8300 for STD reconstruction kernel (A - Surface of the humerus; B - Sliced humerus)

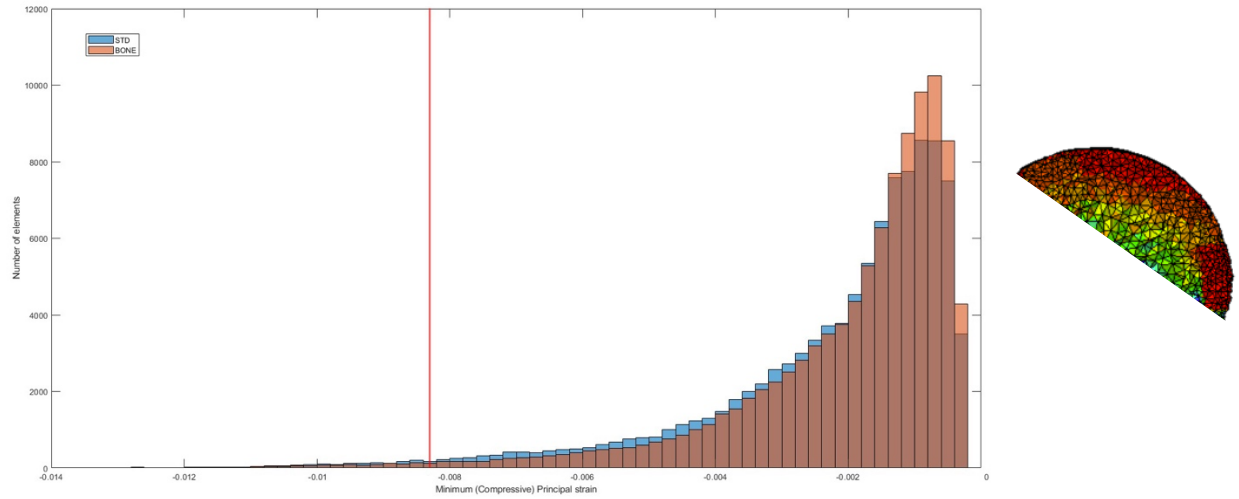


Figure 4.2.18: 23156R Humeral Head minimum principal differences between BONE and STD reconstruction kernel in DEQCT. The lowest reported strain in each reconstruction kernel: BONE = -0.0240; STD = -0.0249. Number of elements less than -0.014 strain: BONE = 30; STD = 50. Red line indicates elemental strains of 8300 (compressive) microstrain for trabecular bone.

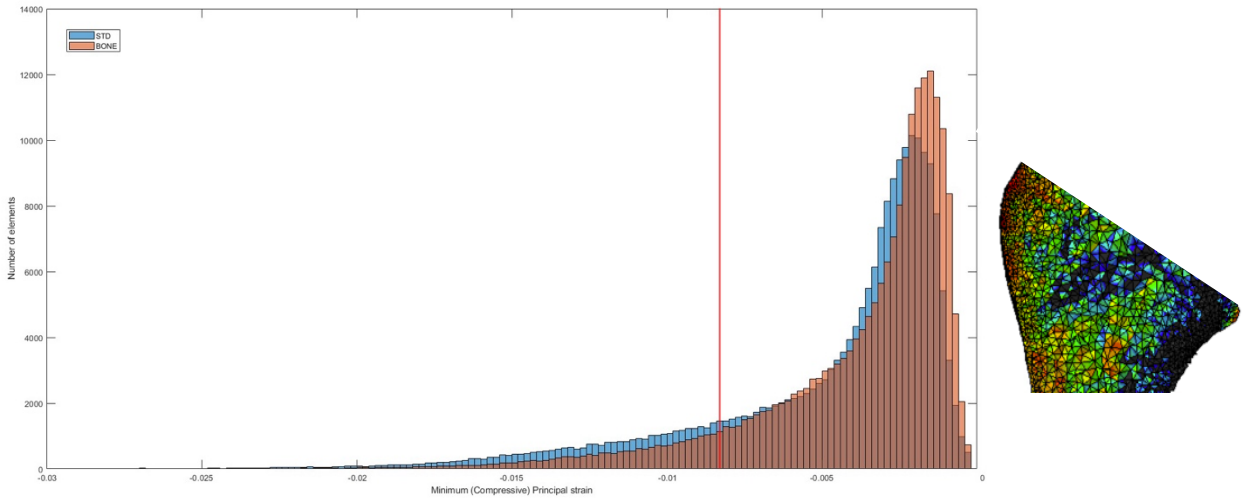


Figure 4.2.19: 23156R Metaphysis minimum principal differences between BONE and STD reconstruction kernel in DEQCT. The lowest reported strain in each reconstruction kernel: BONE = -0.0443; STD = -0.0535. Number of elements less than -0.03 strain: BONE = 46; STD = 24. Red line indicates elemental strains of 8300 (compressive) microstrain for trabecular bone.

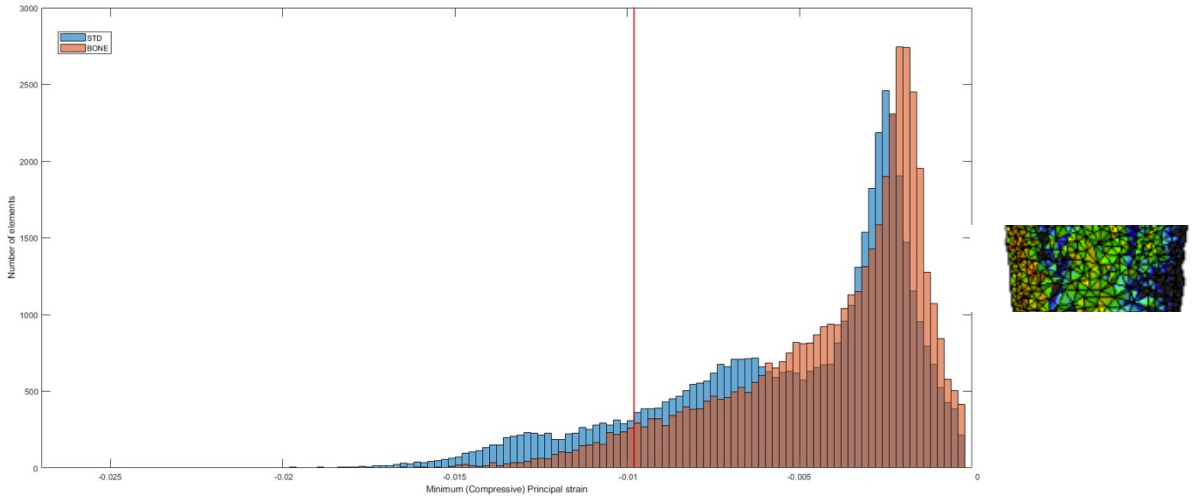


Figure 4.2.20: 23156R Diaphysis minimum principal differences between BONE and STD reconstruction kernel in DEQCT. The lowest reported strain in each reconstruction kernel: BONE = -0.0213; STD = -0.0278. Number of elements less than -0.027 strain: BONE = 0; STD = 1. Red line indicates elemental strains of 9800 (compressive) microstrain for cortical bone.

5. Discussion

This study compared four CT image inputs (SEQCT with BONE and STD reconstruction kernels, and DEQCT with BONE and STD reconstruction kernels) utilized for vBMD measurement and as inputs to image based FEMs to estimate strain in models derived from cadaveric proximal humeri specimens to predict fracture location.

5.1 vBMD in SEQCT

Across the twelve samples evaluated, the results demonstrate that the BONE reconstruction kernel yielded higher HU and vBMD values compared to the STD reconstruction kernel when acquired via SEQCT, with a statistically significant difference observed between BONE and STD in average HU and average vBMD of all cadavers, respectively, across all three anatomical regions examined. Although percentage differences between the respective BONE and STD images within each model was not as large (<4%), the aim of this study was to showcase that differences are evident when changing imaging modalities and even when changing parameters within the same imaging modality. To address whether this is a clinically relevant difference, future work is to be concluded to tackle this issue.

The comparison between reconstruction kernel within density measures demonstrates the importance of having a specimen-specific calibration slope and intercept for the conversion of HU into vBMD as the standard deviation in the models are smaller when measuring in vBMD than HU. The variability among the specimens decreases when using subject-specific values in comparison to HU measurements in the context of this study for SEQCT. In the three regions, the humeral head consists of mostly trabecular bone, the metaphysis, both trabecular and cortical bone, and the diaphysis, mostly cortical bone. Observing significant differences in the regions with cortical bone in SEQCT makes sense because these regions are less influenced by voxels that have trabecular marrow space that alters the “true” measure of density. The significant difference observed in the metaphysis region, could be driven by higher cortical elements on the periphery. Reconstruction kernels enhance the optimization of images post-processing to improve the quality of the images and the BONE kernel alters the frequency content of image data thereby increasing the quantitative voxel data.[45]

Bone content morphology amongst the regions was different. Regions where humeral cortical bone thickness is lower compared to trabecular bone is associated with a low BMD.[57,48] The difference in the humeral head between the amount of trabecular bone compared to cortical bone was higher in

this region.[48] As for diaphysis, there was more of a significant difference to the metaphysis because of the thicker layer of cortical bone in the periphery present and hence why the BONE reconstruction kernel shows more BMD data compared to the STD reconstruction kernel due to the higher spatial resolution and sharpening of the image (specifically the bone) because the cortical bone is a thicker bone layer compared to the trabecular hence, influencing the BONE reconstruction kernel data.[48] Although this is could be a potential reasoning, it was hard to conclude this due to the vBMD measurements in each region being an average of all the voxels within each individual sample region. Hence, it was hard to determine how much is influenced by number of cortical/trabecular voxels, and how much its influenced by the vBMD and HU of each of those voxels. The average statistical comparison was not enough to conclude this. Figure 3.2.5 showcases the differences in cortical and trabecular bone thickness in each region and how the results obtained are supported by morphological differences between the regions.

Although measuring BMD in HU is a well-established technique, a phantom calibration was used as phantom-less calibration is still not widely used. Adding the specimen-specific calibration is beneficial as it allows us to obtain subject specific BMD measurement. In this study, a density-modulus relationship specific to K_2HPO_4 was adopted to mitigate potential sources of error. However, it is recommended that future research to investigate the sensitivity of density-modulus relationships and/or establish anatomical location and vBMD inputs. The exponential characteristics of density-modulus relationships, may significantly impact the accuracy of vBMD assessments, thus introducing potential errors in FEM analyses.[58]

5.2 vBMD in DEQCT

This study utilizes monochromatic images that were simulated at 40 keV and 90 keV during the reconstruction of DEQCT scans. It was expected to see that all BONE reconstruction kernel values to be higher than those compared to the STD kernel. With DEQCT, although the average vBMD in all three regions was higher in BONE than STD reconstruction kernel, with significant differences across the regions, not all cadavers followed the trend. The diaphysis region neglects this trend. Gluer et al (1988) suggest that the presence of large osteophytes in this region is hard to be isolated with these scans and could contribute to these differences in the vBMD.[60] Although only 40 keV and 90 keV monochromatic images were generated by reconstruction kernel, future studies should utilize monochromatic images at higher energy pairs for better vBMD estimates due to differences in material

decomposition.[3] Different tissues have varying attenuation properties at different energy levels. The proposed energies used in this study may favor the visualization of certain tissue types over others, potentially affecting vBMD measurements differently in the diaphysis region compared to the other regions. DEQCT produces 3D images by rotating the CT gantry around the specimen and collecting multiple projection views. Based on Table 4.5 and 4.7, we can see the cadavers that were isolated for the shoulder had lower vBMD in the BONE compared to STD reconstruction kernel. For isolated shoulder specimens, the lack of surrounding soft tissues results in higher beam attenuation compared to full torso specimens with more surrounding soft tissue attenuation.[41,51] This differential attenuation between air and soft tissue can lead to beam hardening artifacts that affect vBMD measurements.[51] Specifically, the BONE kernel, optimized for high resolution bone imaging, is more susceptible to beam hardening from the high attenuation differences present in isolated specimens. Conversely, the softer STD kernel blends information across projections, mitigating beam hardening impact, having a more accurate attenuation measurements.[51] Consequently, isolated shoulder specimens exhibited lower vBMD in BONE compared to STD, contrary to expectations that the higher resolution BONE kernel would yield increased vBMD measurements optimized for bone mineralization assessment. Attenuation differences arising from specimen positioning highlight the importance of consistent soft tissue accounting during DEQCT scanning.

5.3 Strain in SEQCT

Finite element analysis that has been conducted in this study provides important information into the strain distribution and potentially identifying where the location of a fracture in the proximal humerus under simulated fall conditions could be. A force of 2500 N was loaded onto the humeral head to mimic an outstretch arm fall which contacts with the glenoid fossa, allowing for a comprehensive evaluation of strain patterns across the three regions of interest of the humerus. The results revealed a consistent pattern of high strain concentration in the metaphysis region, which was evident by both visual color threshold of grey elements in the models and quantitative strain measurements showcased in the histograms. Although some models are fully grey in both the metaphysis and diaphysis, knowing where the fracture starts is not feasible by just looking at the model. However, the histograms show more elements that exceed the threshold in the metaphysis region, displaying that more of the strain was going through that region which means this region is most likely to fail. Some fractures may have started at the articular surface where the point of impact was, but it translates through the rest of the

bone and instead, these models showcase where strain propagates through the bone. Razfar et al (2016) concluded that the area of highest fracture in the humerus is in the surgical neck.[55] This makes sense with the results obtained as areas of highest element deformation, indicated by the grey elements are located within the metaphysis region. This was further agreed by looking at the histograms where the number of elements that surpass the threshold for fracture based on each location is in the metaphysis region. The higher maximum tensile strain recorded in the metaphysis, compared to the humeral head and diaphysis, suggests that this region may be particularly susceptible to failure under the simulated loading conditions. To add to that, most fracture classification models like the Neer classification, AO/OTA classification and HGLS system classification are three- or four-part fractures in the metaphysis as shown in Figure 2.2.1, 2.2.2 and 2.2.3. However, these fracture types clinically do not tell us anything about where the fracture location is or how many elements failed.

Furthermore, the results that the histograms demonstrate differences between the BONE and STD reconstruction kernels in strain measurement. The STD kernel consistently showed more elements in the higher strain values compared to the BONE kernel, particularly for maximum (tensile) principal strain. This overestimation of strain data was observed in both SEQCT and DEQCT models. These findings are important for accurately determining fracture location and hence, clinical decision-making prior to surgical procedures. The observed difference between reconstruction kernels emphasizes how crucial it is to choose imaging parameters depending on the aim of the study. Michalski et al (2019) concluded that a small difference of 0.3% of vBMD between reconstruction kernels resulted in significant differences in FE bone stiffness and failure load estimates.[50] The differences observed of more elements presented at higher strains in STD than BONE reconstruction kernel was supported by Michalski et al (2019)'s work.

Consistency of strain patterns that will indicate the metaphysis being common area for fracture location will be apparent, but it is important to note that individual variations in bone quality, age, and comorbidities will influence these results. This indicates for the need of personalized assessments to be made in clinical applications by surgeon to clinically predict the location of a fracture based on data presented to them. FE analysis gives opportunities clinically for osteoporosis screening, drug efficacy, and the ability to evaluate internal fixation postoperatively.

5.4 Strain in DEQCT

The differences observed between the STD and BONE reconstruction kernels highlights the importance of consideration to choose imaging parameters carefully as per the aim of the study. As highlighted by de Bakker et al. (2022), accurate assessment of bone mineral density and stiffness requires advanced imaging techniques such as dual-energy or high-resolution computed tomography. The result in this study further emphasizes this point, demonstrating that the choice of reconstruction kernel and use of DEQCT can influence strain measurements and potentially affect fracture risk assessments. It was important to note that when looking at DEQCT, it was evident that strain varied much more between STD and BONE than it did in SEQCT, and this will become important in the future when it comes to reporting DEQCT parameters as input to FEMs. This large difference was concerning if you are using a single strain threshold as the initiation to strain. This shows that just based on what the FE models are made of whether it was SEQCT or DEQCT and even choosing BONE or STD, showcases the huge difference between these choices. This does not take into consideration material properties or loading conditions, but the choice of imaging parameters alone has a significant impact on BMD readings. DEQCT is more accurate than SEQCT and hence, vBMD will be more accurate in DEQCT. Slight variations in vBMD between SEQCT and DEQCT will largely influence strain analysis as the quantitative data of these elements change. This change will lead to more accurate assessment and better fracture location prediction. To add to that, since DEQCT gives out more accurate data than SEQCT, the consequent data in BONE reconstruction kernels will be even more accurate and will also lead to bigger differences in strain data to those obtained from STD reconstruction kernel.

Here again, consistency of strain patterns that will indicate the region of being most likely to fracture is dependent on individual variations in bone quality, age, and comorbidities that will influence these results. This indicates for the need of personalized assessments to be made in clinical applications by surgeon to clinically predict the location of a fracture based on data presented to them.

5.5 Limitations

A primary limitation of this study was that comparison between SEQCT and DEQCT was not performed directly. Initial plans were to keep cadavers situated in the same position without moving them and to have both SEQCT and DEQCT scans to be performed. The issue lays during post-processing where it was found that images in the DEQCT were shifted in the z-axis, differently in each cadaver. Unlike other studies, this study planned on comparing the differences between reconstruction

kernels within cadavers between both SEQCT and DEQCT respectively, keeping the volume of the models the same to ensure that only vBMD values were changed according to different scanning modalities and reconstruction kernel choices. Registration techniques were attempted to re-align the DEQCT images to match those of SEQCT to ensure overlapping of both images but due to time constraints and longevity of this process, this was not performed. If performed in future studies, this would allow direct comparisons between SEQCT and DEQCT and compare differences in reconstruction kernels whilst keeping model volumes that other studies have not done. Another limitation was that the analysis using n = 12 shoulders from seven cadaveric donors (3:4 m:f) may not fully represent the range of bone densities and strain across the population. The analysis was constrained to the given number of specimens due to the substantial quantity of images necessitated for comparative evaluations across kernel types (BONE/STD) and image modalities (SEQCT/DECT), amounting to a total of 48 images. A cadaver (22151R) possessed a fracture but was not utilized as part of the data acquisition. This cadaver was a clinically relevant fracture that can be used to compare to strain fracture patterns that are obtained from other cadavers and models.

The resolution limitations of SEQCT and DEQCT result in the presence of voxels within bone that contain both bone and marrow, as well as voxels at the periosteal border of bone that contain both soft tissue and bone. These voxel-specific variations cannot be accounted for within SEQCT images and may be further influenced using different reconstruction kernels. In contrast, DEQCT has the capability to account for these differences using voxel-specific material variations through the utilization of material decomposition techniques. In this study, we employed an established method based on simulated monochromatic images, which has demonstrated good results within trabecular bone.[3,60] This approach, originally described by Gluer et al. (1988), generally resulted in vBMD values derived from DEQCT that were greater than those obtained from SEQCT. However, in models where vBMD was found to be lower in DEQCT, the presence of large osteophytes within the measurement region that could not be isolated was observed. Due to the composition of these osteophytes, this may be a contributing factor to the observed differences in vBMD in these models.

5.6 Relevance and clinical implications

This study was the first to present comparisons of different reconstruction kernels from DEQCT and its effect on vBMD and FEM input. Previous studies have already reported the effects by SEQCT reconstruction kernel on vBMD and stiffness/strain.[49,50] Changing the reconstruction kernel

influences vBMD measurement as per Michalski et al (2019) showing similar results to this study, with decreased vBMD in the smooth (U30) kernel models which is the same as the STD reconstruction kernel in this study.[49] STD reconstruction reduces the contrast in these images, making it more difficult to segment the geometry and distinguish any bone tissue local abnormalities.[49,59] With the BONE (sharper) reconstruction kernel, noise was introduced to the image as perceived by the increase of speckles compared to the STD reconstruction kernel.[49,59] Variations in trabecular and cortical vBMD have also been identified due to differences in choice of reconstruction kernel.[48] Giambini et al (2015), shows this in a study looking at a single rabbit femur that was cleaned of all soft tissues.[48] It was shown that when using a hard kernel (B70), HU and vBMD values obtained for cortical bones were higher when compared to the soft kernel (B30).[48] The opposite was observed when cancellous bone BMD was measured where the soft kernel showcased higher HU and vBMD values compared to the hard kernel.[48]

This study kept the volume of the models consistent when obtaining the BMD of the selected regions between each image input (BONE vs STD). Michalski et al (2019) instead recreated a new model hence, new volumes for comparison.[50] It was unknown if common volumes were used across image types in the other reported studies. Keeping the same volume for the models for comparison reduces changes in vBMD. Changing the volume of the models will essentially alter both the vBMD reading and consequently the strain/stiffness when inputting in FEM. Differences in volume could influence the average vBMD significantly since these values are affected by the partial volume averaging of low-density voxels that are present in the border of the humerus.

This research allows for a parametric evaluation for a lot of parameters. These FE models created allow for the adjustment of loading situations and see the effects it has on strain or even stiffness. To add to that, this study improves the input to computational FE modeling in the context of proximal humerus fractures.

5.7 Future directions

Future studies should focus on the use of alternative monochromatic energy pairs and may need to adapt material decomposition methods to optimize vBMD estimates at different material interfaces. Use of 40 keV and 90 keV and 140 keV will help to further improve the accuracy and reliability of vBMD measurements obtained using DEQCT in the presence of complex anatomical structures and variations in bone composition. Future studies will include individuals who have experienced a PHF to assess fracture healing in both non-surgical and surgical situations given the expected success.

Another future direction to consider is experimentally validating the models for proximal humerus fractures. Small sample sizes and controlled loading conditions have been previously researched.[54,] This research shows that a single force does not predict where a fracture location is because of many other variables that influence it. A need for better methods for validating proximal humerus fractures so that we can get to the stage of being predictive is needed to know the effects of the other parameters in addition to the choice of imaging modality. Fracturing a real-life humerus using biomechanical testing using the same parameters in this study to validate if fracture does occur in the metaphysis as predicted by simulations in this study.

6. Conclusion

This study has advanced imaging input and simulated loading to better understand of proximal humerus fractures through the innovative combination of advanced imaging techniques and finite element modeling. By comparing different reconstruction kernels within SEQCT and DEQCT, I have displayed the complex relationships between bone mineral density, fracture characteristics, and biomechanical properties of the proximal humerus.

The findings demonstrate the importance of reconstruction kernel selection in imaging analysis. In SEQCT, the BONE kernel consistently provided higher values in both Hounsfield Units (HU) and Volumetric Bone Mineral Density (vBMD) compared to the STD kernel across all regions of interest. Significant differences were observed between BONE and STD kernels for HU and vBMD in all three regions. In DEQCT, the results were more distinct. While the BONE kernel generally showcased higher vBMD values, this trend was not consistent across all specimens and regions. Notably, statistically significant differences were observed between the average BONE and average STD kernels in all three regions, underscoring the importance of maintaining consistency in reconstruction kernel selection for longitudinal vBMD monitoring.

The integration of FEM with these imaging techniques has allowed for more accurate predictions of fracture locations based on strain distributions. The simulations, applying a 2500 N force to mimic an outstretched arm fall, revealed that the metaphysis region consistently showed the highest risk of failure across both SEQCT and DEQCT models. This was evidenced by higher maximum tensile and minimum compressive principal strains in this region compared to the humeral head and diaphysis. Importantly, the results highlight a tendency for the STD reconstruction kernel to overestimate strain data compared to the BONE kernel. This overestimation was consistent across both SEQCT and DEQCT modalities and could potentially lead to inaccuracies in fracture location predictions and implant choice decisions. These findings have significant clinical implications. FEM has showcased to be an important tool to display how changes in parameters can lead to significant differences in how a humerus might be perceived to change under proposed loading conditions. This is an instant visual representation to how changes in imaging modalities and parameters influence the qualitative and the associated quantitative data with it. The choice of reconstruction kernel and imaging modality can substantially influence the assessment of bone quality and fracture risk. Therefore, clinicians must be aware of these factors when interpreting imaging results and making treatment decisions.

In conclusion, this research represents a significant advancement in the field of orthopedic imaging and biomechanics. The FE model representation of the humerus obtained serves a quick and simple way for surgeons to make a surgical decision in a clinical scenario for the benefit of the patient. This can be important when it comes to choosing an implant design for a patient where every assessment must be specific to that patient and not generalized amongst a population. By bridging the gap between advanced imaging techniques and computational modeling, a developed and more vigorous framework for understanding and predicting proximal humerus fractures is possible. This approach has the potential to improve diagnostic accuracy, inform treatment decisions, and ultimately enhance patient outcomes. Ultimately, this work lays the foundation for more personalized and effective management of proximal humerus fractures, promising to reduce the burden of these challenging injuries on patients and healthcare systems alike. It showcases that just due to different input parameters, there are a lot of variabilities that arise. The insights gained from this study will contribute to more informed decision-making in clinical practice, potentially leading to improved surgical outcomes and patient care.

References

[1] de Bakker, C. M. J., Peedikayil, T., Walker, R. E. A., Neeteson, N. J., Manske, S. L., & Boyd, S. K. (2022). Diagnostic accuracy of a dual-energy computed tomography-based post-processing method for imaging bone marrow edema following an acute ligamentous knee injury. *Skeletal Radiology*, *51*(9), 1817–1827. https://doi.org/10.1007/s00256-022-04023-7

[2] de Bakker, C. M. J., Walker, R. E. A., Besler, B. A., Tse, J. J., Manske, S. L., Martin, C. R., French, S. J., Dodd, A. E., & Boyd, S. K. (2021). A quantitative assessment of dual energy computed tomography-based material decomposition for imaging bone marrow edema associated with acute knee injury. *Medical Physics*, *48*(4), 1792–1803. https://doi.org/10.1002/mp.14791

[3] de Bakker, C. M. J., Knowles, N. K., Walker, R. E. A., Manske, S. L., & Boyd, S. K. (2022). Independent changes in bone mineralized and marrow soft tissues following acute knee injury require dual-energy or high-resolution computed tomography for accurate assessment of bone mineral density and stiffness. *Journal of the Mechanical Behavior of Biomedical Materials*, *127*. https://doi.org/10.1016/j.jmbbm.2022.105091

[4] Cataño Jimenez, S., Saldarriaga, S., Chaput, C. D., & Giambini, H. (2020). Dual-energy estimates of volumetric bone mineral densities in the lumbar spine using quantitative computed tomography better correlate with fracture properties when compared to single-energy BMD outcomes. *Bone*, *130*, 115100. https://doi.org/10.1016/j.bone.2019.115100

[5] Mallinson, P. I., Coupal, T. M., McLaughlin, P. D., Nicolaou, S., Munk, P. L., & Ouellette, H. A. (2016). Dual-Energy CT for the Musculoskeletal System. *Radiology*, *281*(3), 690–707. https://doi.org/10.1148/radiol.2016151109

[6] Gruenewald, L. D., Koch, V., Martin, S. S., Yel, I., Eichler, K., Gruber-Rouh, T., Lenga, L., Wichmann, J. L., Alizadeh, L. S., Albrecht, M. H., Mader, C., Huizinga, N. A., D'Angelo, T., Mazziotti, S., Wesarg, S., Vogl, T. J., & Booz, C. (2022). Diagnostic accuracy of quantitative dual-energy CT-based volumetric bone mineral density assessment for the prediction of osteoporosis-associated fractures. *European Radiology*, *32*(5), 3076–3084. https://doi.org/10.1007/s00330-021-08323-9

[7] Dabirrahmani, D., Magnussen, J., & Appleyard, R. C. (2015). Dual-Energy Computed Tomography—How Accurate Is Gemstone Spectrum Imaging Metal Artefact Reduction? Its Application to Orthopedic Metal Implants. *Journal of Computer Assisted Tomography*, *39*(6), 925–935. https://doi.org/10.1097/RCT.0000000000000300

[8] Takrouri, H. S., Alnassar, M. M., Amirabadi, A., Babyn, P. S., Moineddin, R., Padfield, N. L., BenDavid, G., & Doria, A. S. (2015). Metal Artifact Reduction: Added Value of Rapid-Kilovoltage-Switching Dual-Energy CT in Relation to Single-Energy CT in a Piglet Animal

Model. *American Journal of Roentgenology*, *205*(3), W352–W359. https://doi.org/10.2214/AJR.14.12547

[9] Majed, A., Thangarajah, T., Southgate, D. F., Reilly, P., Bull, A., & Emery, R. (2019). The biomechanics of proximal humeral fractures: Injury mechanism and cortical morphology. *Shoulder & Elbow*, *11*(4), 247–255. https://doi.org/10.1177/1758573218768535

[10] Lenz, M., Kahmann, S., Behbahani, M., Pennig, L., Hackl, M., Leschinger, T., Müller, L. P., & Wegmann, K. (2022). Influence of rotator cuff preload on fracture configuration in proximal humerus fractures: a proof of concept for fracture simulation. *Archives of Orthopaedic and Trauma Surgery*, *143*(5), 2467–2474. https://doi.org/10.1007/s00402-022-04471-9

[11] Baron, J. A., Barrett, J. A., & Karagas, M. R. (1996). The epidemiology of peripheral fractures. *Bone*, *18*(3), S209–S213. https://doi.org/10.1016/8756-3282(95)00504-8

[12] Halder, A. M., Itoi, E., & An, K.-N. (2000). Anatomy and biomechanics of the shoulder. *Orthopedic Clinics of North America*, *31*(2), 159–176. https://doi.org/10.1016/S0030-5898(05)70138-3

[13] Culham, E., & Peat, M. (1993). Functional Anatomy of the Shoulder Complex. *Journal of Orthopaedic & Sports Physical Therapy*, *18*(1), 342–350. https://doi.org/10.2519/jospt.1993.18.1.342

[14] Fox, A. J. S., Fox, O. J. K., Schär, M. O., Chaudhury, S., Warren, R. F., & Rodeo, S. A. (2021). The glenohumeral ligaments: Superior, middle, and inferior: Anatomy, biomechanics, injury, and diagnosis. *Clinical Anatomy*, *34*(2), 283–296. https://doi.org/10.1002/ca.23717

[15] Sheehan, S. E., Gaviola, G., Sacks, A., Gordon, R., Shi, L. L., & Smith, S. E. (2013). Traumatic Shoulder Injuries: A Force Mechanism Analysis of Complex Injuries to the Shoulder Girdle and Proximal Humerus. *American Journal of Roentgenology*, *201*(3), W409–W424. https://doi.org/10.2214/AJR.12.9987

[16] Guggenbuhl, P., Meadeb, J., & Chalès, G. (2005). Osteoporotic fractures of the proximal humerus, pelvis, and ankle: epidemiology and diagnosis. *Joint Bone Spine*, *72*(5), 372–375. https://doi.org/10.1016/j.jbspin.2004.04.002

[17] Sanchez-Sotelo, J. (2006). Proximal humerus fractures. *Clinical Anatomy*, *19*(7), 588–598. https://doi.org/10.1002/ca.20281

[18] Majed, A., Thangarajah, T., Southgate, D. F., Reilly, P., Bull, A., & Emery, R. (2019). The biomechanics of proximal humeral fractures: Injury mechanism and cortical morphology. *Shoulder & Elbow*, *11*(4), 247–255. https://doi.org/10.1177/1758573218768535

[19] Ganta, A., Solasz, S., Drake, J., Littlefield, C., Konda, S., & Egol, K. (2022). Does mechanism of injury impact the outcome of operative fixation of geriatric proximal humerus fractures. *Archives of Orthopaedic and Trauma Surgery*, *143*(7), 4095–4098. https://doi.org/10.1007/s00402-022-04616-w

[20] Alidousti, H., Giles, J. W., Emery, R. J. H., & Jeffers, J. (2017). Spatial mapping of humeral head bone density. *Journal of Shoulder and Elbow Surgery*, *26*(9), 1653–1661. https://doi.org/10.1016/j.jse.2017.03.006

[21] Sprecher, C. M., Schmidutz, F., Helfen, T., Richards, R. G., Blauth, M., & Milz, S. (2015). Histomorphometric Assessment of Cancellous and Cortical Bone Material Distribution in the Proximal Humerus of Normal and Osteoporotic Individuals. *Medicine*, *94*(51), e2043. https://doi.org/10.1097/MD.0000000000002043

[22] Mantila Roosa, S. M., Hurd, A. L., Xu, H., Fuchs, R. K., & Warden, S. J. (2012). Age-related changes in proximal humerus bone health in healthy, white males. *Osteoporosis International*, *23*(12), 2775–2783. https://doi.org/10.1007/s00198-012-1893-1

[23] Jeong, H. J., Ahn, J. M., & Oh, J. H. (2021). Trabecular Bone Score Could Not Predict the Bone Mineral Density of Proximal Humerus. *Journal of Bone Metabolism*, *28*(3), 239–247. https://doi.org/10.11005/jbm.2021.28.3.239

[24] Blakeney, W. G., Urvoy, M., Chaoui, J., Raiss, P., Athwal, G. S., & Walch, G. (2021). Development and assessment of 3-dimensional computed tomography measures of proximal humeral bone density: a comparison to established 2-dimensional measures and intraoperative findings in patients undergoing shoulder arthroplasty. *JSES International*, *5*(6), 1008–1013. https://doi.org/10.1016/j.jseint.2021.07.015

[25] Wang, Y., Li, J., Men, Y., & Wei, W. (2022). Menopause-related cortical loss of the humeral head region mainly occurred in the greater tuberosity. *Frontiers in Endocrinology*, *13*. https://doi.org/10.3389/fendo.2022.942803

[26] Jabran, A., Peach, C., Zou, Z., & Ren, L. (2018). Biomechanical comparison of screw-based zoning of PHILOS and Fx proximal humerus plates. *BMC Musculoskeletal Disorders*, *19*(1), 253. https://doi.org/10.1186/s12891-018-2185-5

[27] Kim, H., Shin, M. J., Kholinne, E., Seo, J., Ahn, D., Kim, J. W., & Koh, K. H. (2021). How Many Proximal Screws Are Needed for a Stable Proximal Humerus Fracture Fixation? *Geriatric Orthopaedic Surgery & Rehabilitation*, *12*, 215145932199274. https://doi.org/10.1177/2151459321992744

[28] Bue, M., Bright, E., Thillemann, T. M., Mosegaard, S. B., Hansen, T. B., Klebe, T., Mechlenburg, I., & Stilling, M. (2023). Osteoporosis does not affect bone mineral density change in the proximal

humerus or the functional outcome after open reduction and internal fixation of unilateral displaced 3- or 4-part fractures at 12-month follow-up. *Journal of Shoulder and Elbow Surgery*, *32*(2), 292–301. https://doi.org/10.1016/j.jse.2022.07.008

[29] Oh, J. H., Song, B. W., Kim, S. H., Choi, J.-A., Lee, J. W., Chung, S. W., & Rhie, T.-Y. (2014). The measurement of bone mineral density of bilateral proximal humeri using DXA in patients with unilateral rotator cuff tear. *Osteoporosis International*, *25*(11), 2639–2648. https://doi.org/10.1007/s00198-014-2795-1

[30] Bahrs, C., Rolauffs, B., Dietz, K., Eingartner, C., & Weise, K. (2010). Clinical and radiological evaluation of minimally displaced proximal humeral fractures. *Archives of Orthopaedic and Trauma Surgery*, *130*(5), 673–679. https://doi.org/10.1007/s00402-009-0975-9

[31] Hertel, R., Hempfing, A., Stiehler, M., & Leunig, M. (2004). Predictors of humeral head ischemia after intracapsular fracture of the proximal humerus. *Journal of Shoulder and Elbow Surgery*, *13*(4), 427–433. https://doi.org/10.1016/j.jse.2004.01.034

[32] Court-Brown, C. M., Garg, A., & McQueen, M. M. (2001). The translated two-part fracture of the proximal humerus. *The Journal of Bone and Joint Surgery*, *83*(6), 799–804. https://doi.org/10.1302/0301-620X.83B6.11401

[33] Robinson, C. M., Page, R. S., Hill, R. M. F., Sanders, D. L., Court-Brown, C. M., & Wakefield, A. E. (2003). Primary hemiarthroplasty for treatment of proximal humeral fractures. *The Journal of Bone and Joint Surgery-American Volume*, *85*(7), 1215–1223. https://doi.org/10.2106/00004623-200307000-00006

[34] Court-Brown, C. M., & Caesar, B. (2006). Epidemiology of adult fractures: A review. *Injury*, *37*(8), 691–697. https://doi.org/10.1016/j.injury.2006.04.130

[35] Sukthankar, A. v., Leonello, D. T., Hertel, R. W., Ding, G. S., & Sandow, M. J. (2013). A comprehensive classification of proximal humeral fractures: HGLS system. *Journal of Shoulder and Elbow Surgery*, *22*(7), e1–e6. https://doi.org/10.1016/j.jse.2012.09.018

[36] Augat, P., & Schorlemmer, S. (2006). The role of cortical bone and its microstructure in bone strength. *Age and Ageing*, *35*(suppl_2), ii27–ii31. https://doi.org/10.1093/ageing/afl081

[37] Tingart, M. J., Apreleva, M., von Stechow, D., Zurakowski, D., & Warner, J. J. P. (2003). The cortical thickness of the proximal humeral diaphysis predicts bone mineral density of the proximal humerus. *The Journal of Bone and Joint Surgery. British Volume*, *85-B*(4), 611–617. https://doi.org/10.1302/0301-620X.85B4.12843

[38] Helgason, B., Perilli, E., Schileo, E., Taddei, F., Brynjólfsson, S., & Viceconti, M. (2008). Mathematical relationships between bone density and mechanical properties: A literature review. *Clinical Biomechanics*, *23*(2), 135–146. https://doi.org/10.1016/j.clinbiomech.2007.08.024

[39] Jennings A. Sphere fit (least squared) [software]. Available at: http://www.mathworks.com/matlabcentral/fileexchange/34129. MATLAB Central File Exchange. Accessed February 26, 2024.

[40] Bucher I. Circle fit [software]. Available at: https://www.mathworks.com/matlabcentral/fileexchange/5557-circle-fit?s_tid=srchtitle_site_search_1_circl%20fit. MATLAB Central File Exchange. Accessed March 15, 2024.

[41] Knowles, N. K., Reeves, J. M., & Ferreira, L. M. (2016). Quantitative Computed Tomography (QCT) derived Bone Mineral Density (BMD) in finite element studies: a review of the literature. *Journal of Experimental Orthopaedics*, *3*(1), 36. https://doi.org/10.1186/s40634-016-0072-2

[42] Khedr, A., & Mendelson, S. (2019). Proximal Metaphyseal and Diaphyseal Humerus Fractures. *Operative Techniques in Orthopaedics*, *29*(1), 2–10. https://doi.org/10.1053/j.oto.2018.12.002

[43] Taddei, F., Schileo, E., Helgason, B., Cristofolini, L., & Viceconti, M. (2007). The material mapping strategy influences the accuracy of CT-based finite element models of bones: An evaluation against experimental measurements. *Medical Engineering & Physics*, *29*(9), 973–979. https://doi.org/10.1016/j.medengphy.2006.10.014

[44] Eberle, S., Göttlinger, M., & Augat, P. (2013). Individual density–elasticity relationships improve accuracy of subject-specific finite element models of human femurs. *Journal of Biomechanics*, *46*(13), 2152–2157. https://doi.org/10.1016/j.jbiomech.2013.06.035

[45] Borges, A. P., Antunes, C., & Curvo-Semedo, L. (2023). Pros and Cons of Dual-Energy CT Systems: "One Does Not Fit All." *Tomography*, *9*(1), 195–216. https://doi.org/10.3390/tomography9010017

[46] Yan, L., Zhong, Z., Gao, H., He, Y., Li, P., Shen, H., Zhou, S., Guo, Y., Liao, L., & Zhang, K. (2021). Fast kilovoltage (KV)-switching dual-energy CT virtual noncalcium technique using different reconstruction kernels for identifying acute and chronic vertebral compression fractures. *Archives of Osteoporosis*, *16*(1), 85. https://doi.org/10.1007/s11657-021-00948-z

[47] Troy, K. L., & Edwards, W. B. (2018). Practical considerations for obtaining high quality quantitative computed tomography data of the skeletal system. *Bone*, *110*, 58–65. https://doi.org/10.1016/j.bone.2018.01.013

[48] Giambini, H., Dragomir-Daescu, D., Huddleston, P. M., Camp, J. J., An, K.-N., & Nassr, A. (2015). The Effect of Quantitative Computed Tomography Acquisition Protocols on Bone Mineral Density Estimation. *Journal of Biomechanical Engineering*, *137*(11). https://doi.org/10.1115/1.4031572

[49] Giambini, H., Dragomir-Daescu, D., Nassr, A., Yaszemski, M. J., & Zhao, C. (2016). Quantitative Computed Tomography Protocols Affect Material Mapping and Quantitative Computed Tomography-Based Finite-Element Analysis Predicted Stiffness. *Journal of Biomechanical Engineering*, *138*(9). https://doi.org/10.1115/1.4034172

[50] Michalski, A. S., Edwards, W. B., & Boyd, S. K. (2019). The Influence of Reconstruction Kernel on Bone Mineral and Strength Estimates Using Quantitative Computed Tomography and Finite Element Analysis. *Journal of Clinical Densitometry*, *22*(2), 219–228. https://doi.org/10.1016/j.jocd.2017.09.001

[51] Chatzaraki, V., Born, C., Kubik-Huch, R. A., Froehlich, J. M., Thali, M. J., & Niemann, T. (2021). Influence of Radiation Dose and Reconstruction Kernel on Fat Fraction Analysis in Dual-energy CT: A Phantom Study. *In Vivo*, *35*(6), 3147–3155. https://doi.org/10.21873/invivo.12609

[52] Yu, Q., Yang, J., Zhou, C., Xu, Z., Liu, C., Luo, Q., & Zhang, L. (2023). Quantification of bone quality and distribution of the proximal humerus with dual-energy computed tomography. *Quantitative Imaging in Medicine and Surgery*, *13*(9), 5676–5687. https://doi.org/10.21037/qims-22-927

[53] Link, T. M. (2012). This Month in *Radiology*. *Radiology*, *263*(3), 3A-4A. https://doi.org/10.1148/radiol.2633201203

[54] Dahan, G., Trabelsi, N., Safran, O., & Yosibash, Z. (2019). Finite element analyses for predicting anatomical neck fractures in the proximal humerus. *Clinical Biomechanics*, *68*, 114–121. https://doi.org/10.1016/j.clinbiomech.2019.05.028

[55] Razfar, N., Reeves, J. M., Langohr, D. G., Willing, R., Athwal, G. S., & Johnson, J. A. (2016). Comparison of proximal humeral bone stresses between stemless, short stem, and standard stem length: a finite element analysis. *Journal of Shoulder and Elbow Surgery*, *25*(7), 1076–1083. https://doi.org/10.1016/j.jse.2015.11.011

[56] Ye, Y., You, W., Zhu, W., Cui, J., Chen, K., & Wang, D. (2017). The Applications of Finite Element Analysis in Proximal Humeral Fractures. *Computational and Mathematical Methods in Medicine*, *2017*, 1–9. https://doi.org/10.1155/2017/4879836

[57] Mather, J., MacDermid, J. C., Faber, K. J., & Athwal, G. S. (2013). Proximal humerus cortical bone thickness correlates with bone mineral density and can clinically rule out osteoporosis. *Journal of Shoulder and Elbow Surgery*, *22*(6), 732–738. https://doi.org/10.1016/j.jse.2012.08.018

[58] Winsor, C., Li, X., Qasim, M., Henak, C. R., Pickhardt, P. J., Ploeg, H., & Viceconti, M. (2021). Evaluation of patient tissue selection methods for deriving equivalent density calibration for femoral bone quantitative CT analyses. *Bone*, *143*, 115759. https://doi.org/10.1016/j.bone.2020.115759

[59] Jang, K. J., Kweon, D. C., Lee, J.-W., Choi, J., Goo, E.-H., Dong, K.-R., Lee, J.-S., Jin, G. H., & Seo, S. (2011). Measurement of Image Quality in CT Images Reconstructed with Different Kernels. *Journal of the Korean Physical Society*, *58*(2), 334–342. https://doi.org/10.3938/jkps.58.334

[60] Glüer, C.-C., Reiser, U. J., Davis, C. A., Rutt, B. K., & Genant, H. K. (1988). Vertebral Mineral Determination by Quantitative Computed Tomography (QCT). *Journal of Computer Assisted Tomography*, *12*(2), 242–258. https://doi.org/10.1097/00004728-198803000-00013

[61] Wilson, C Available at: https://www.shoulder-pain-explained.com/shoulder-ligaments.html

[62] Rouleau, D. M., Laflamme, G. Y., & Mutch, J. (2016). Fractures of the greater tuberosity of the humerus: a study of associated rotator cuff injury and atrophy. *Shoulder & Elbow*, *8*(4), 242–249. https://doi.org/10.1177/1758573216647896

[63] Cifuentes, A. O., & Kalbag, A. (1992). A performance study of tetrahedral and hexahedral elements in 3-D finite element structural analysis. *Finite Elements in Analysis and Design*, *12*(3–4), 313–318. https://doi.org/10.1016/0168-874X(92)90040-J

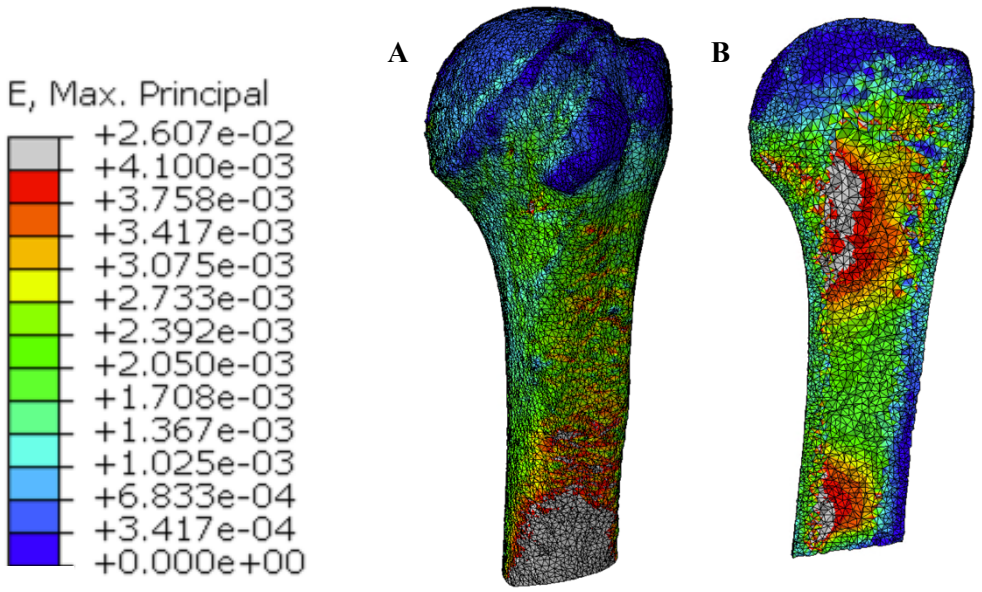
[64] Bonemat, Available at: https://ior-bic.github.io/software/bonemat/index.html

[65] Bayraktar, H. H., Morgan, E. F., Niebur, G. L., Morris, G. E., Wong, E. K., & Keaveny, T. M. (2004). Comparison of the elastic and yield properties of human femoral trabecular and cortical bone tissue. *Journal of Biomechanics*, *37*(1), 27–35. https://doi.org/10.1016/S0021-9290(03)00257-4

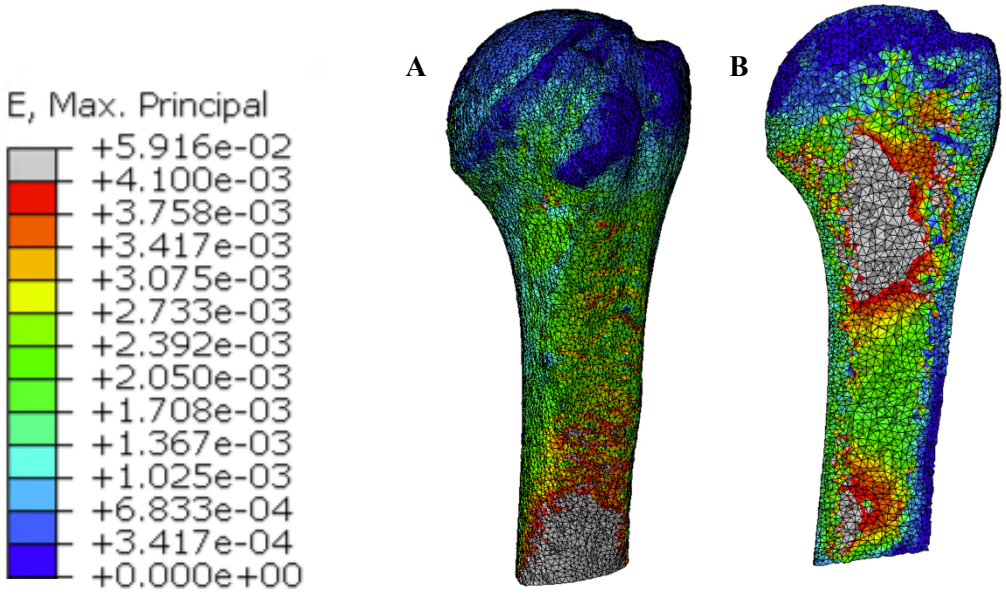
[66] Mirzaali, M. J., Schwiedrzik, J. J., Thaiwichai, S., Best, J. P., Michler, J., Zysset, P. K., & Wolfram, U. (2016). Mechanical properties of cortical bone and their relationships with age, gender, composition and microindentation properties in the elderly. *Bone*, *93*, 196–211. https://doi.org/10.1016/j.bone.2015.11.018

Appendix A

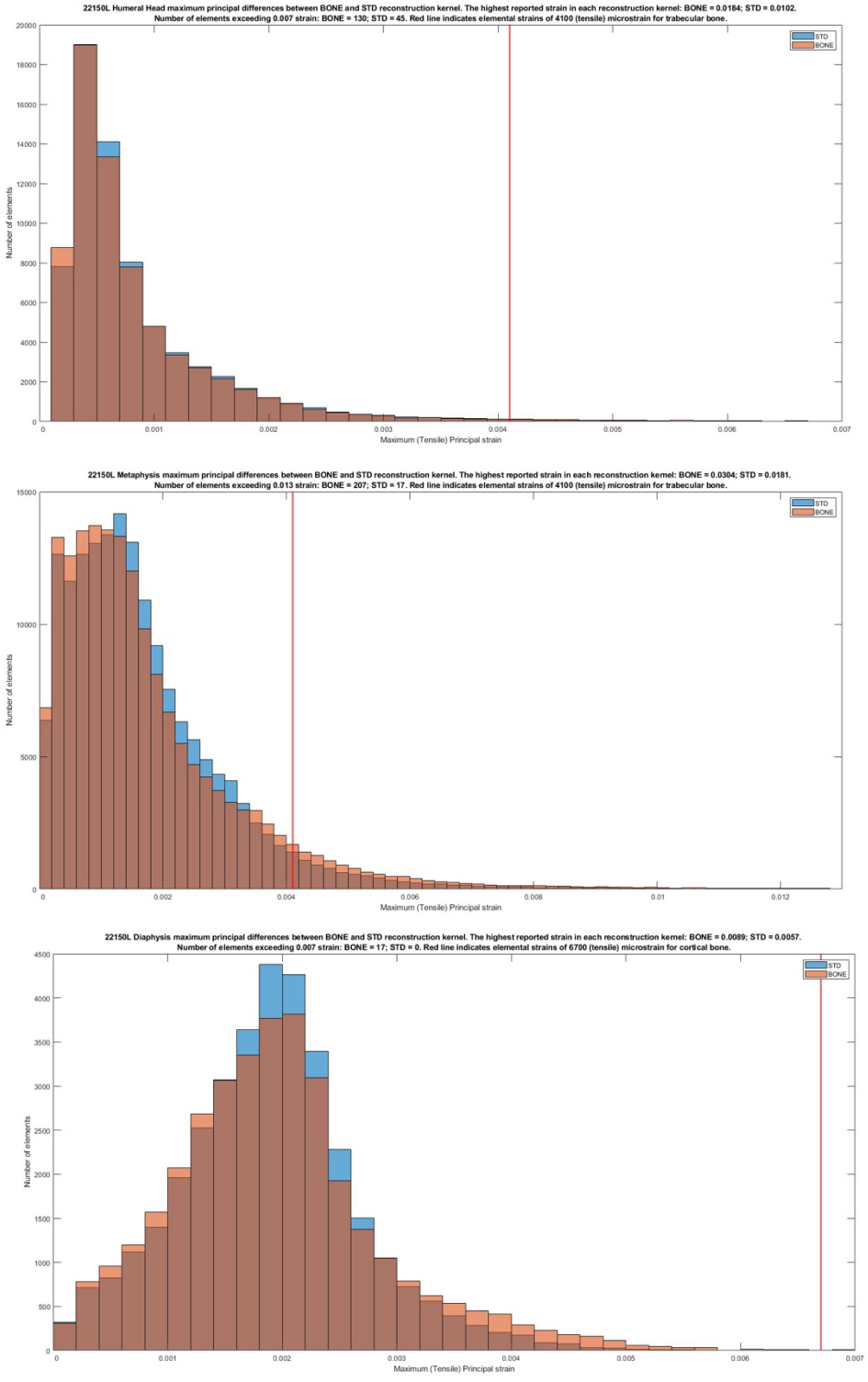
FE models and Histograms from SEQCT for the rest of the models.



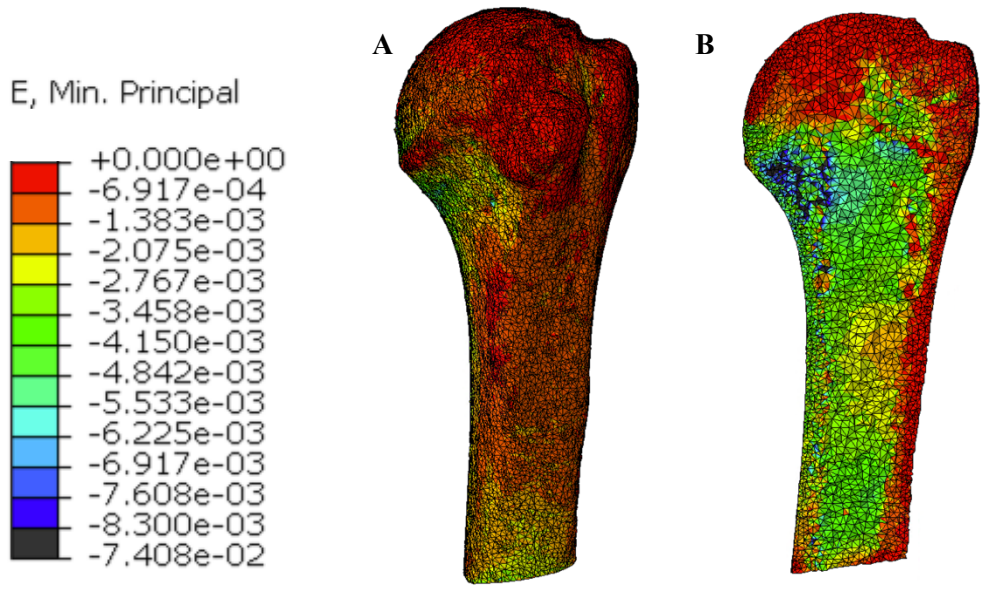
22150L SEQCT maximum (tensile) principal strain with a microstrain set at 4100 for BONE reconstruction kernel (A - Surface of the humerus; B - Sliced humerus)



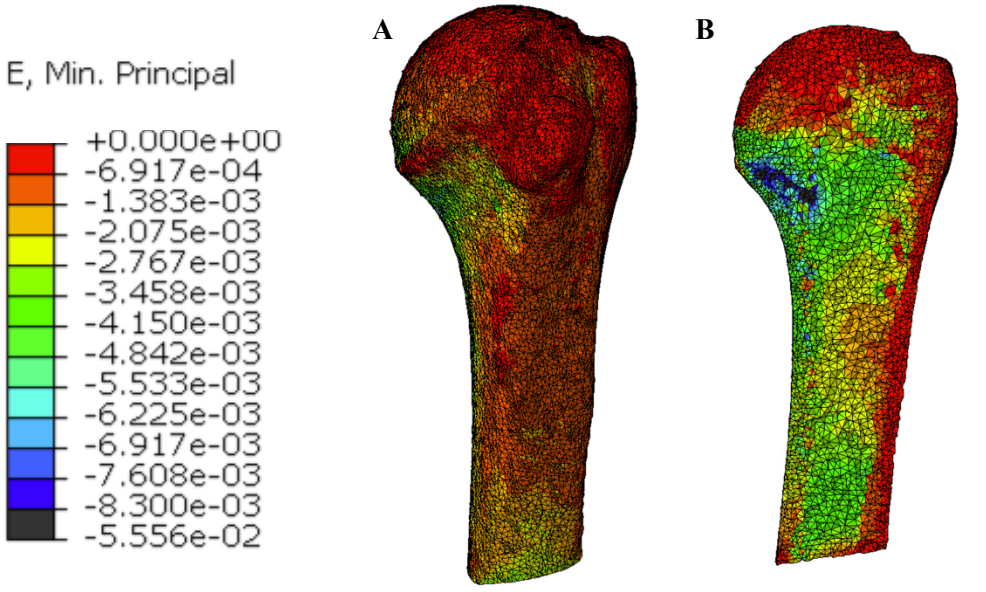
22150L SEQCT maximum (tensile) principal strain with a microstrain set at 4100 for STD reconstruction kernel (A - Surface of the humerus; B - Sliced humerus)



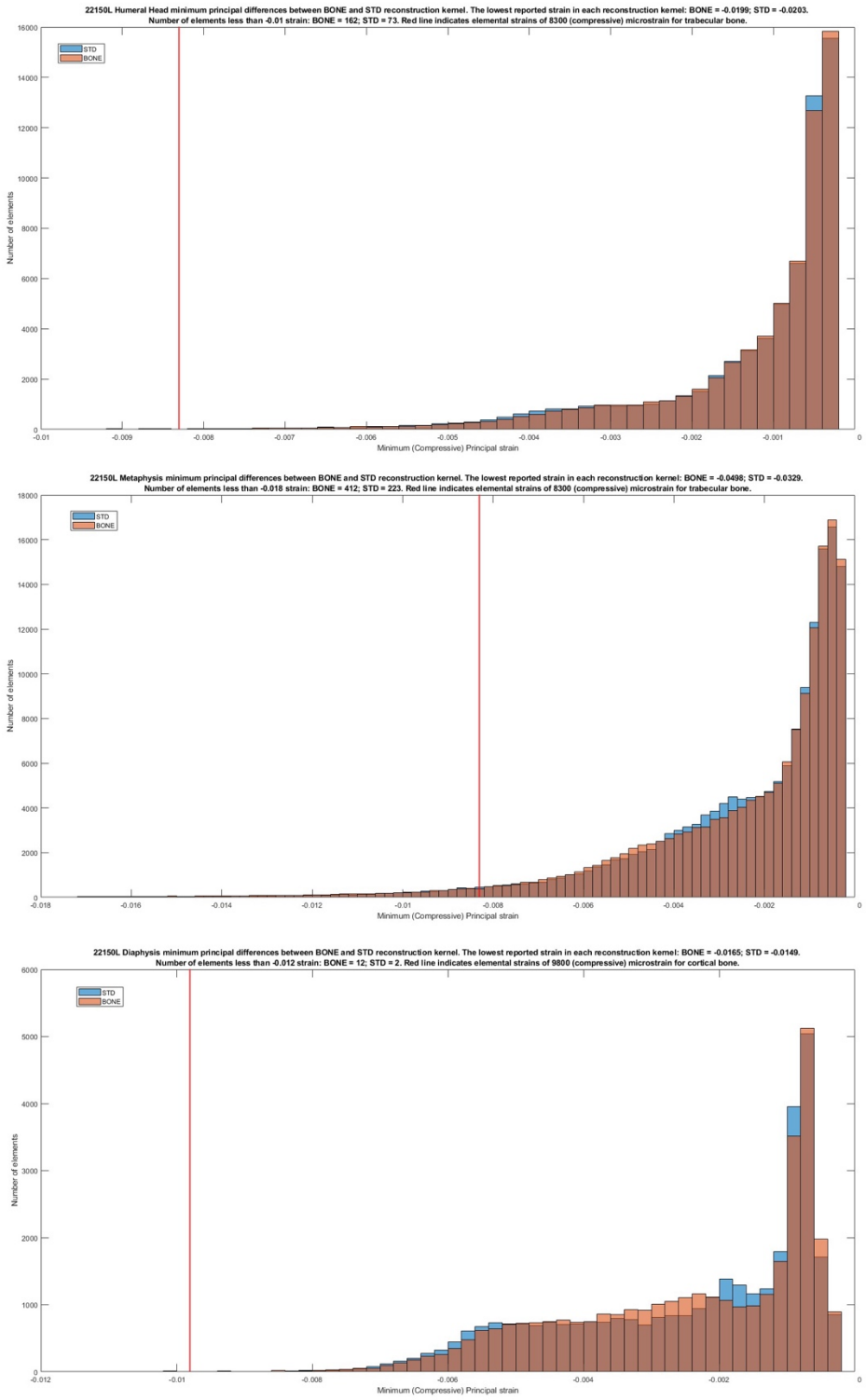
Maximum (tensile) principal strain for cadaver 22150L in SEQCT in the three regions.



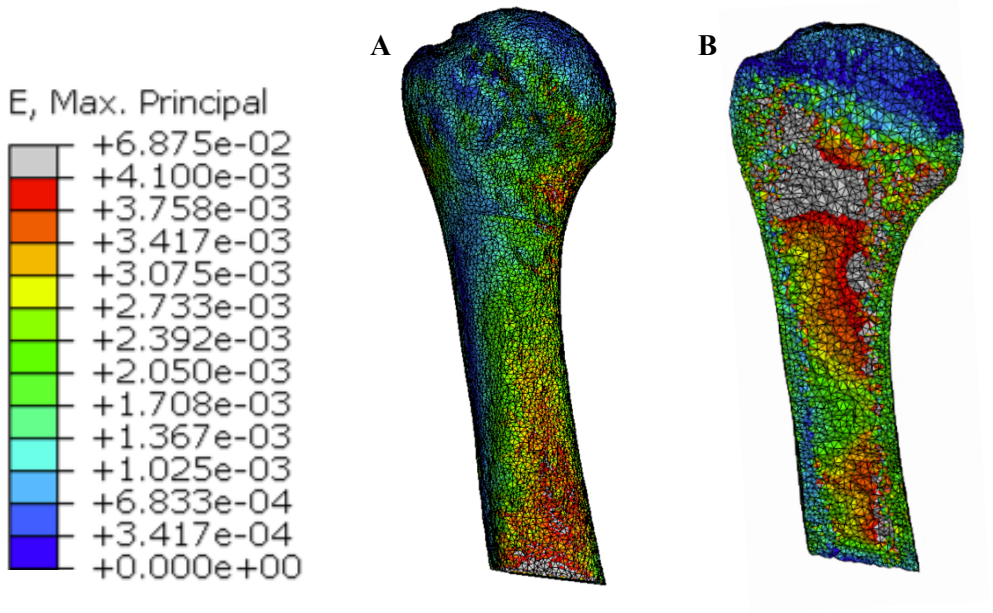
22150L SEQCT minimum (compressive) principal strain with a microstrain set at 8300 for BONE reconstruction kernel (A - Surface of the humerus; B - Sliced humerus)



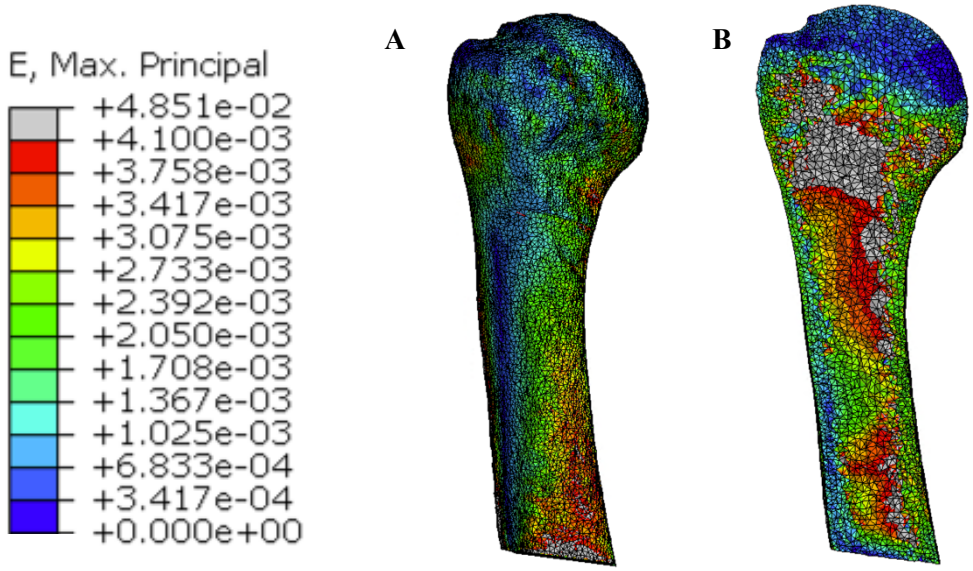
22150L SEQCT minimum (compressive) principal strain with a microstrain set at 8300 for STD reconstruction kernel (A - Surface of the humerus; B - Sliced humerus)



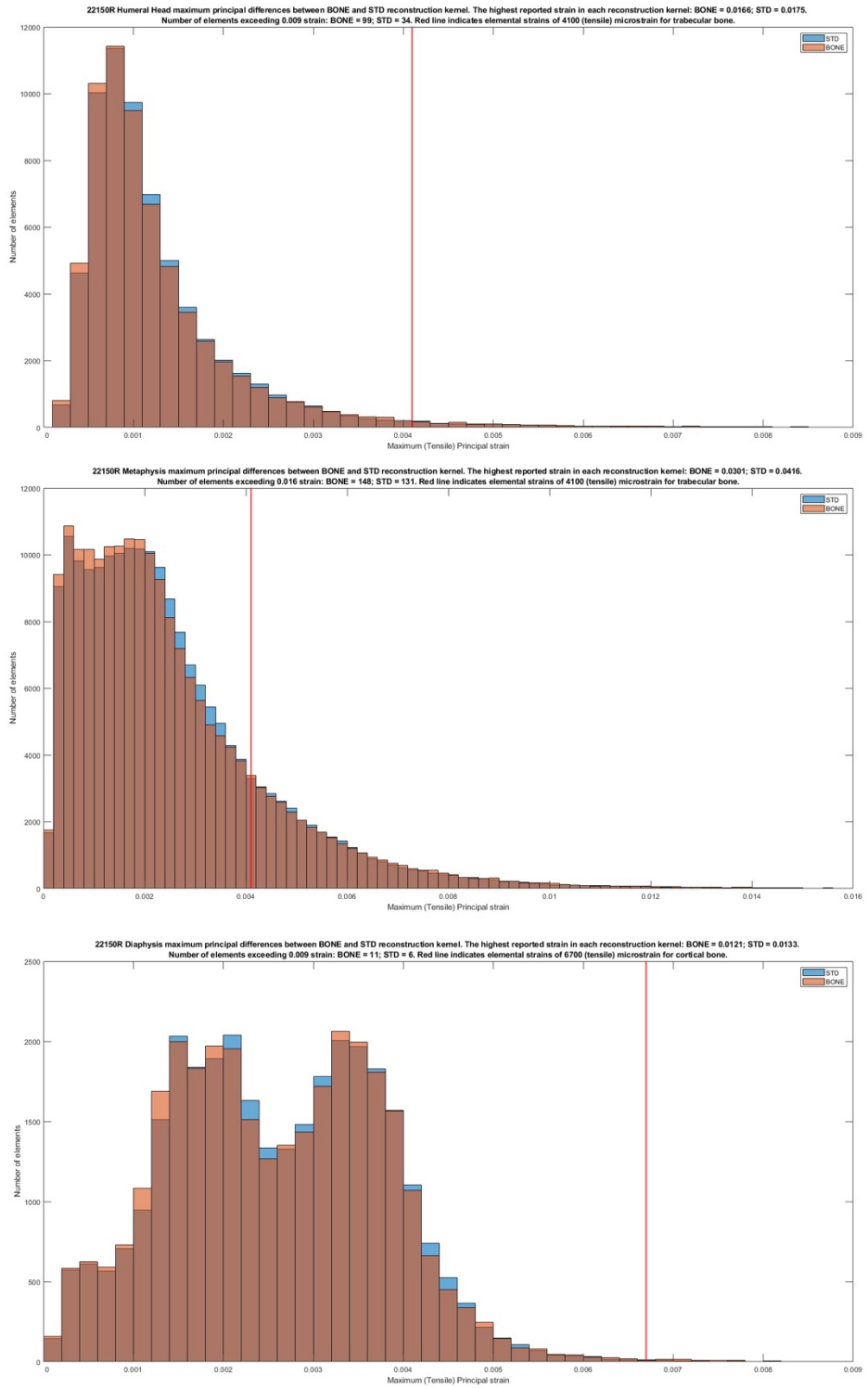
Minimum (compressive) principal strain for cadaver 22150L in SEQCT in the three regions.



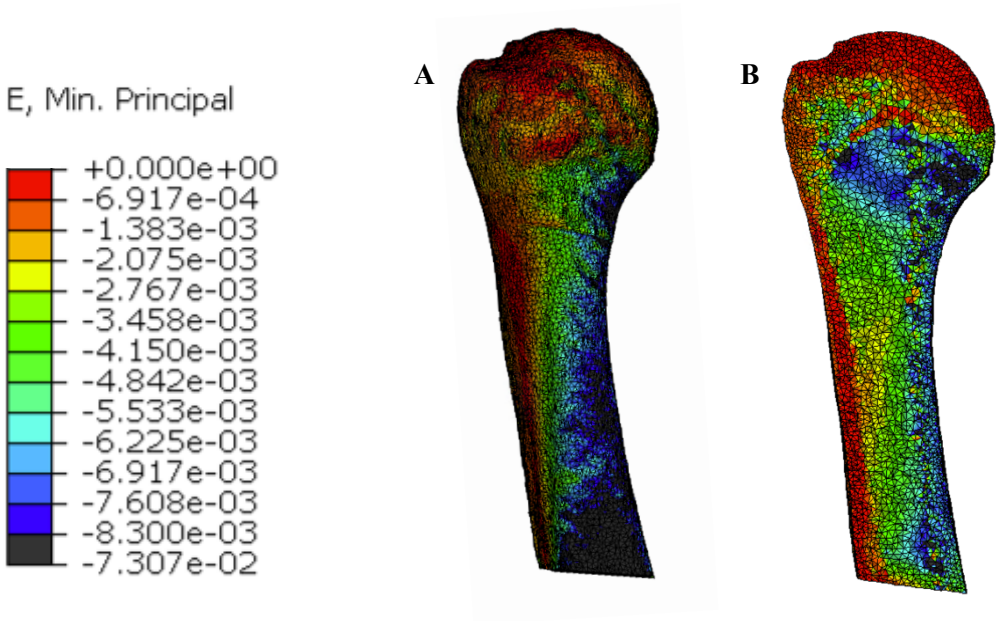
22150R SEQCT maximum (tensile) principal strain with a microstrain set at 4100 for BONE reconstruction kernel (A - Surface of the humerus; B - Sliced humerus)



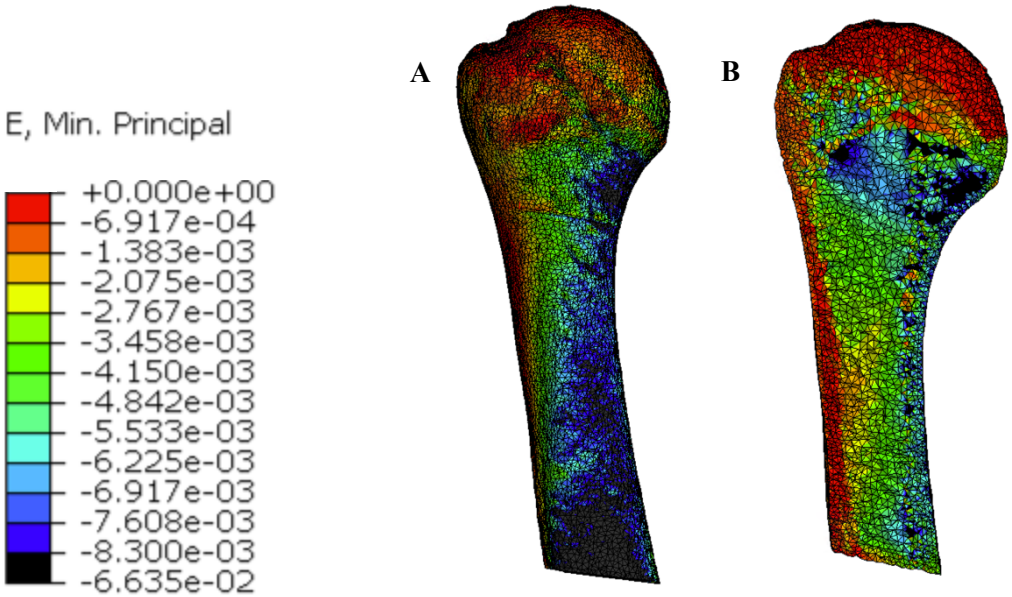
22150R SEQCT maximum (tensile) principal strain with a microstrain set at 4100 for STD reconstruction kernel (A - Surface of the humerus; B - Sliced humerus)



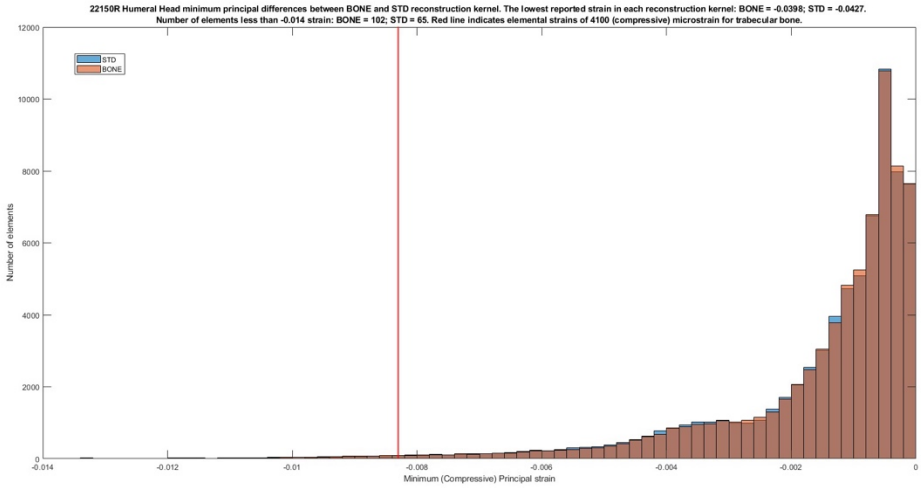
Maximum (tensile) principal strain for cadaver 22150R in SEQCT in the three regions.

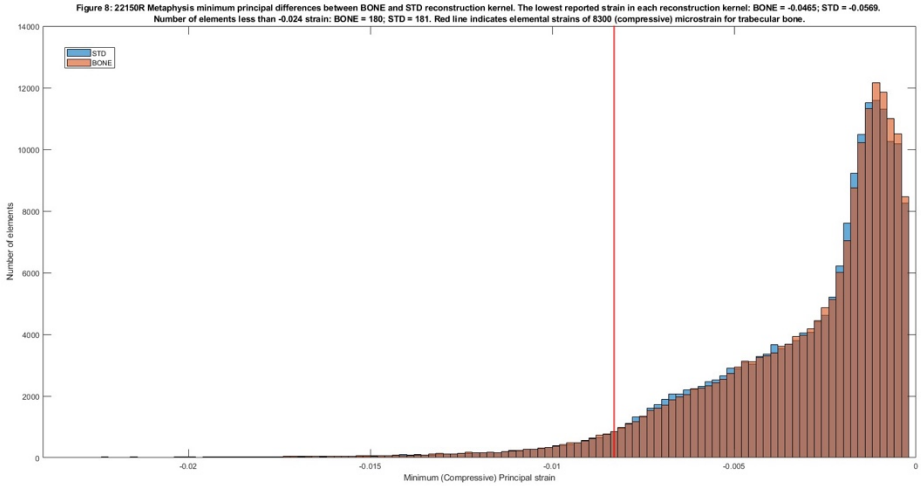


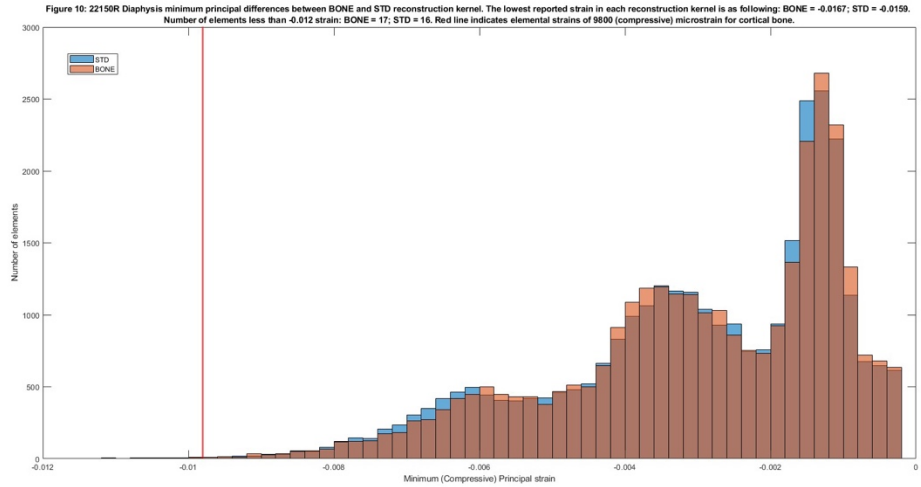
22150R SEQCT minimum (compressive) principal strain with a microstrain set at 8300 for BONE reconstruction kernel (A - Surface of the humerus; B - Sliced humerus)



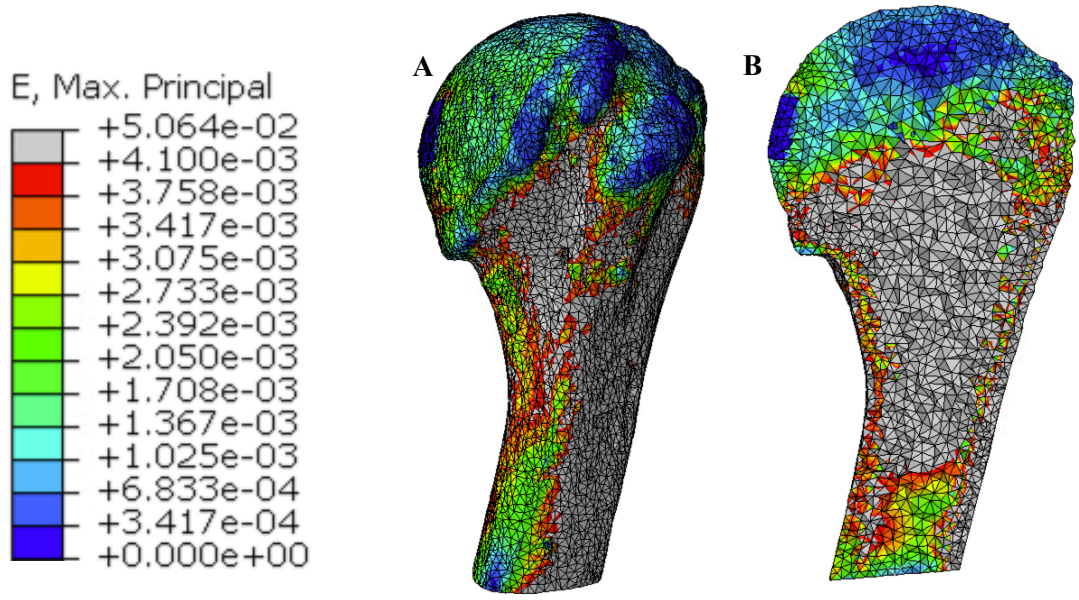
22150R SEQCT minimum (compressive) principal strain with a microstrain set at 8300 for STD reconstruction kernel (A - Surface of the humerus; B - Sliced humerus)



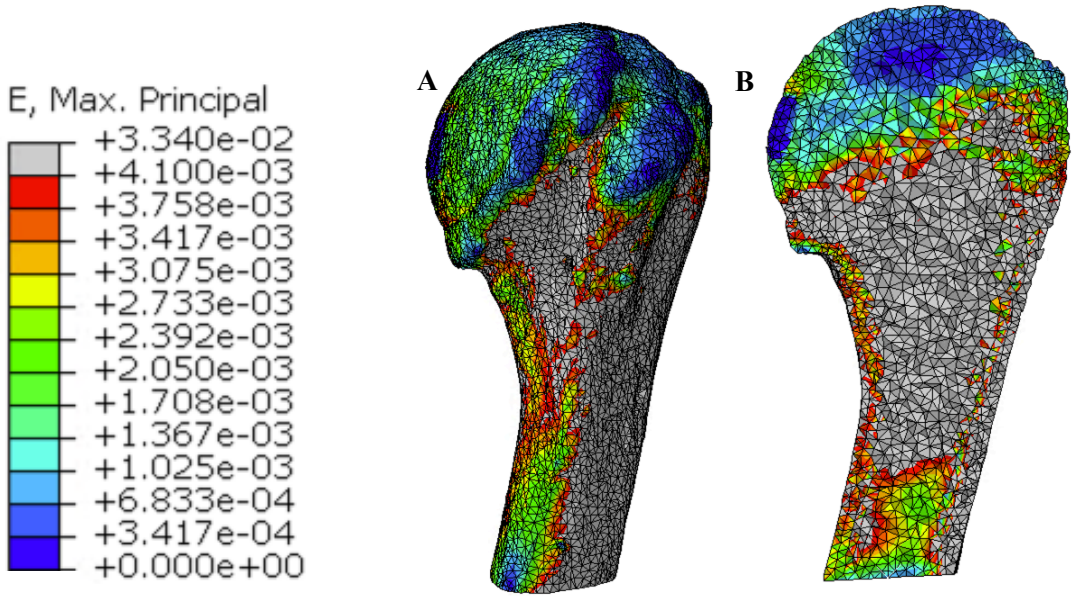




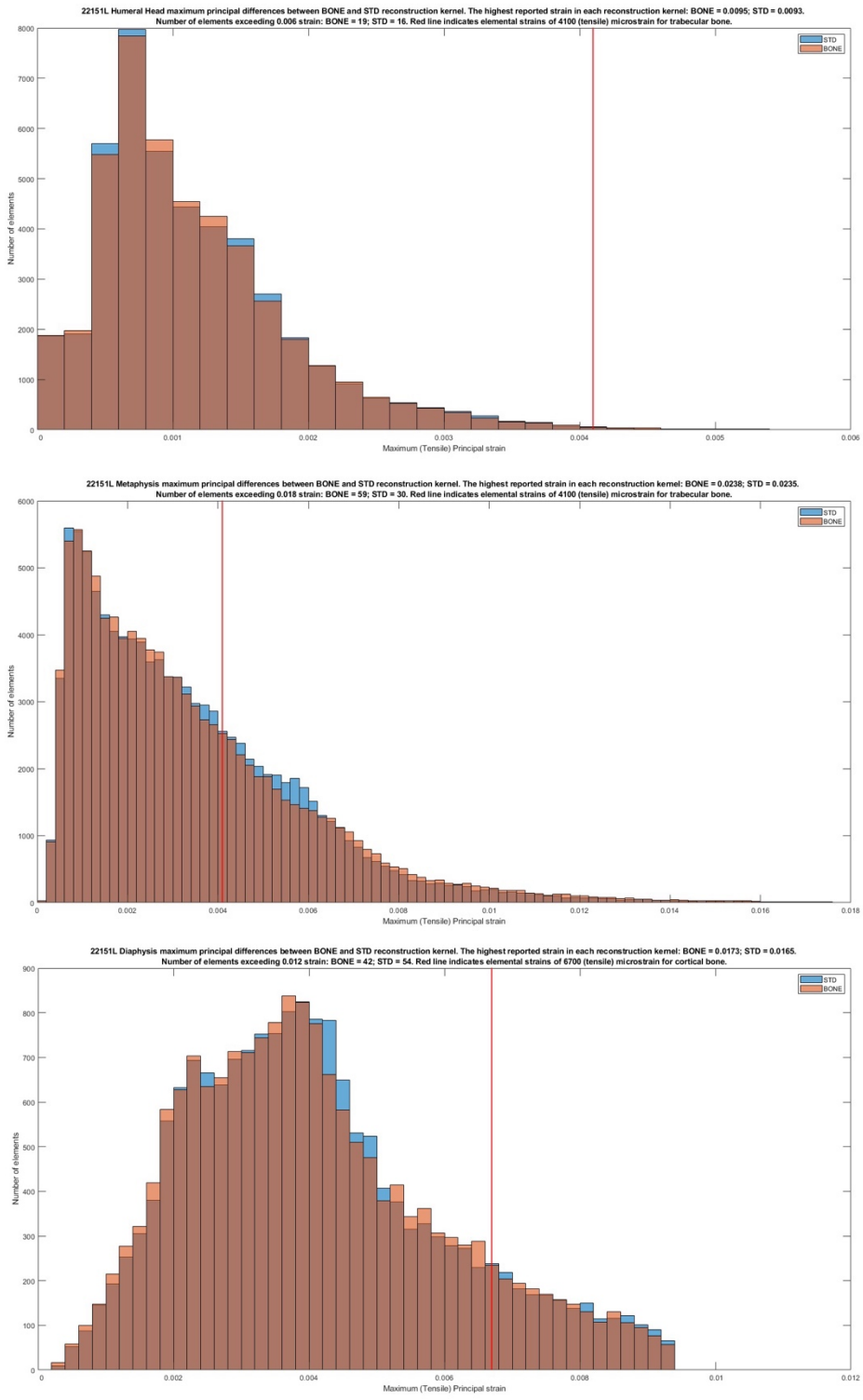
Minimum (compressive) principal strain for cadaver 22150R in SEQCT in the three regions.



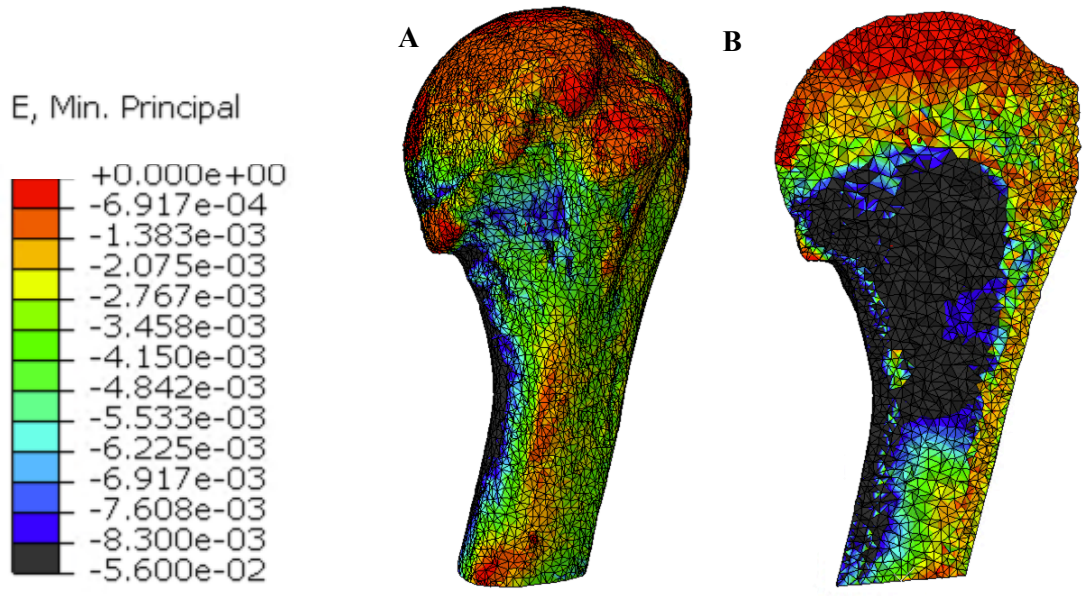
22151L SEQCT maximum (tensile) principal strain with a microstrain set at 4100 for BONE reconstruction kernel (A - Surface of the humerus; B - Sliced humerus)



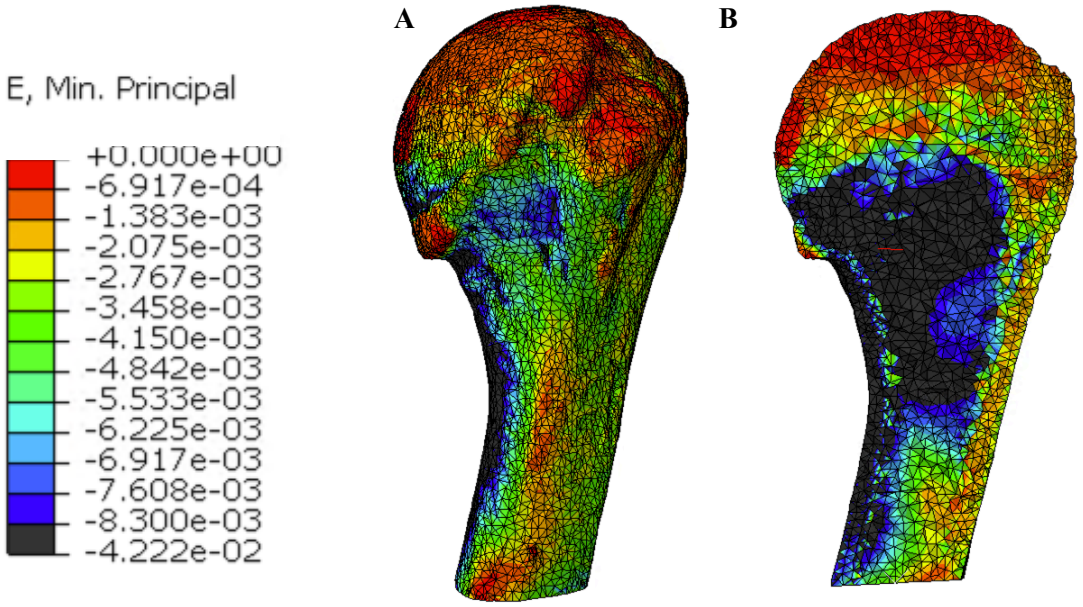
22151L SEQCT maximum (tensile) principal strain with a microstrain set at 4100 for STD reconstruction kernel (A - Surface of the humerus; B - Sliced humerus)



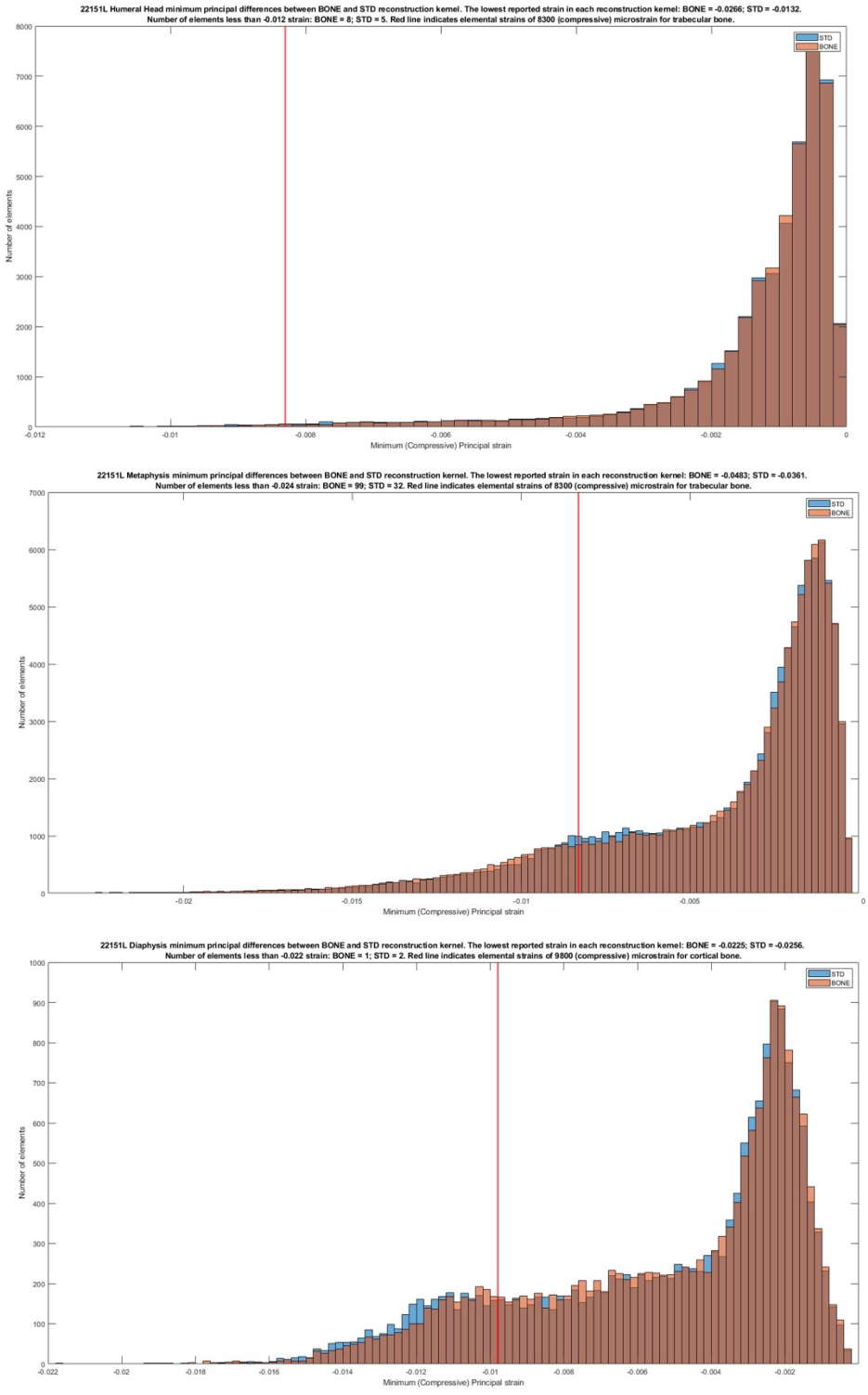
Maximum (tensile) principal strain for cadaver 22151L in SEQCT in the three regions.



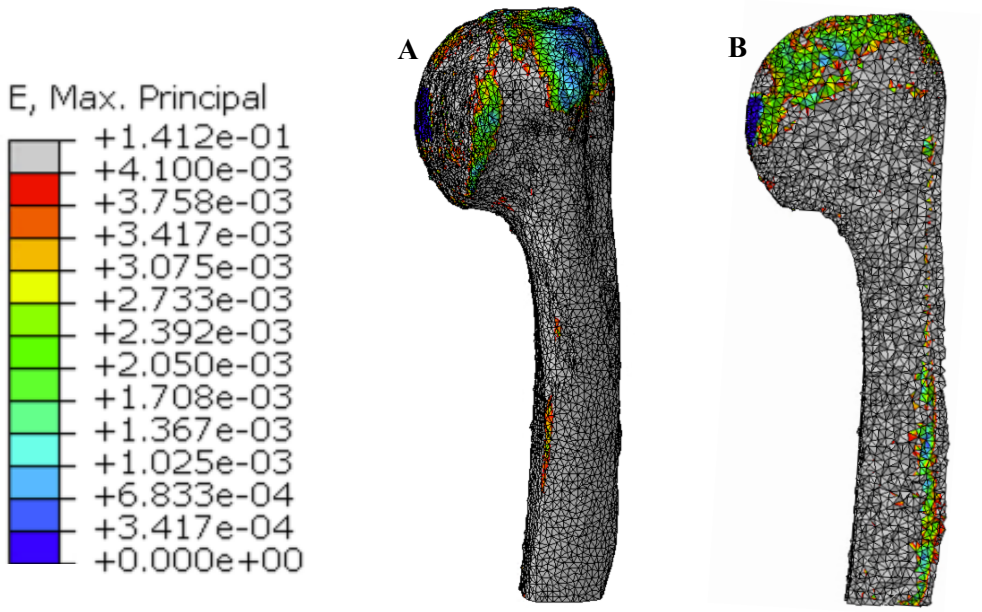
22151L SEQCT minimum (compressive) principal strain with a microstrain set at 8300 for BONE reconstruction kernel (A - Surface of the humerus; B - Sliced humerus)



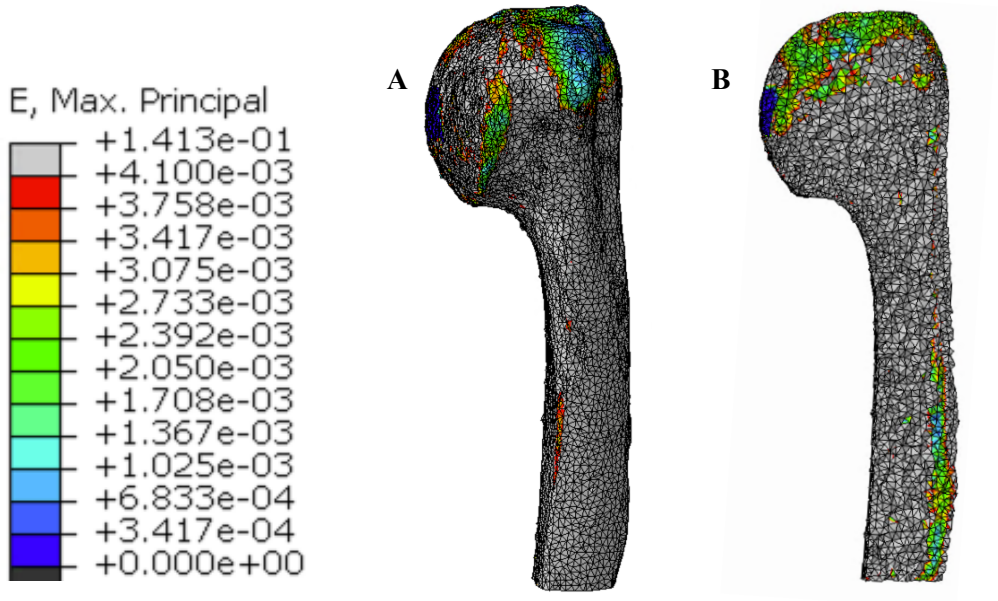
22151L SEQCT minimum (compressive) principal strain with a microstrain set at 8300 for STD reconstruction kernel (A - Surface of the humerus; B - Sliced humerus)



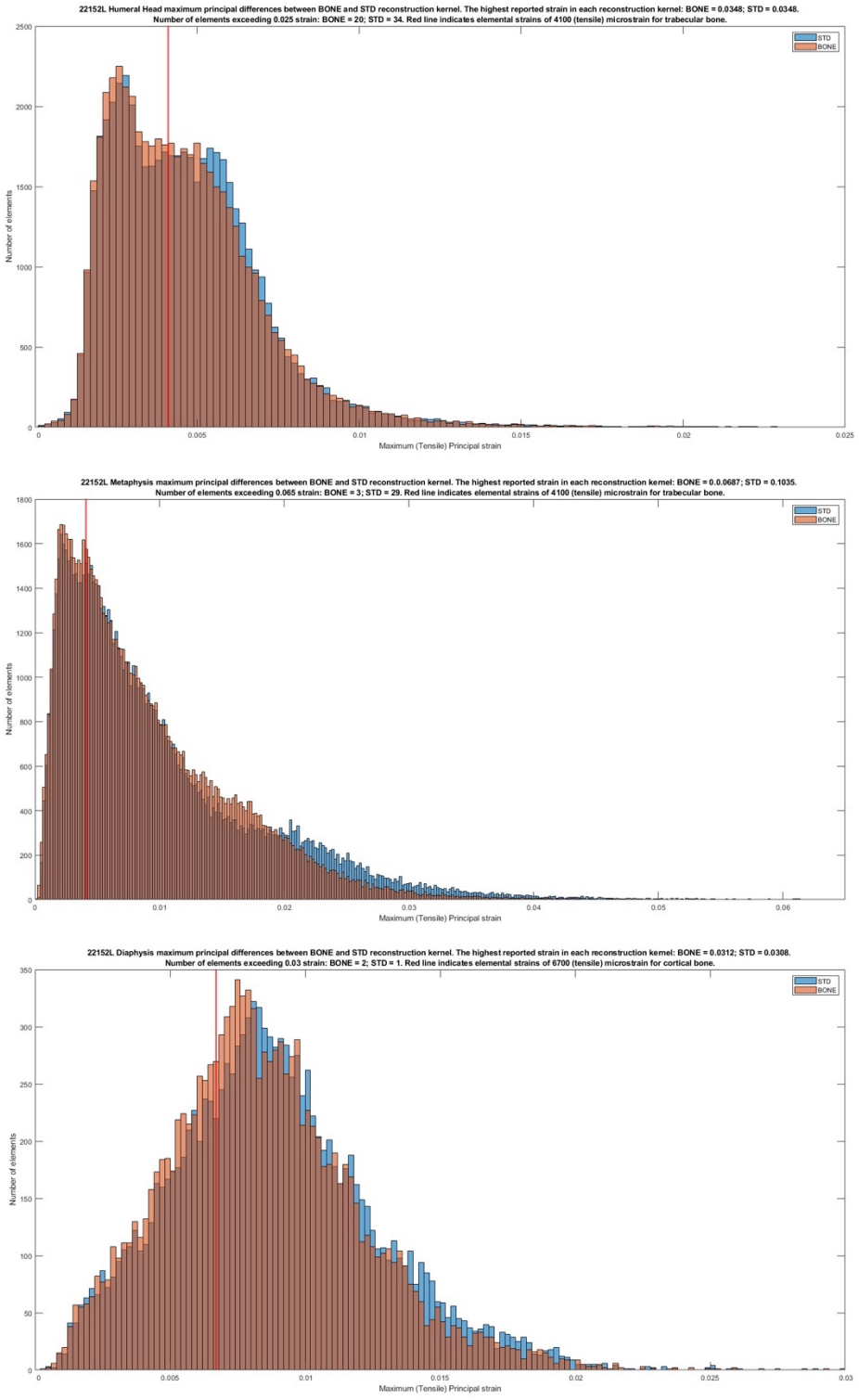
Minimum (compressive) principal strain for cadaver 22151L in SEQCT in the three regions.



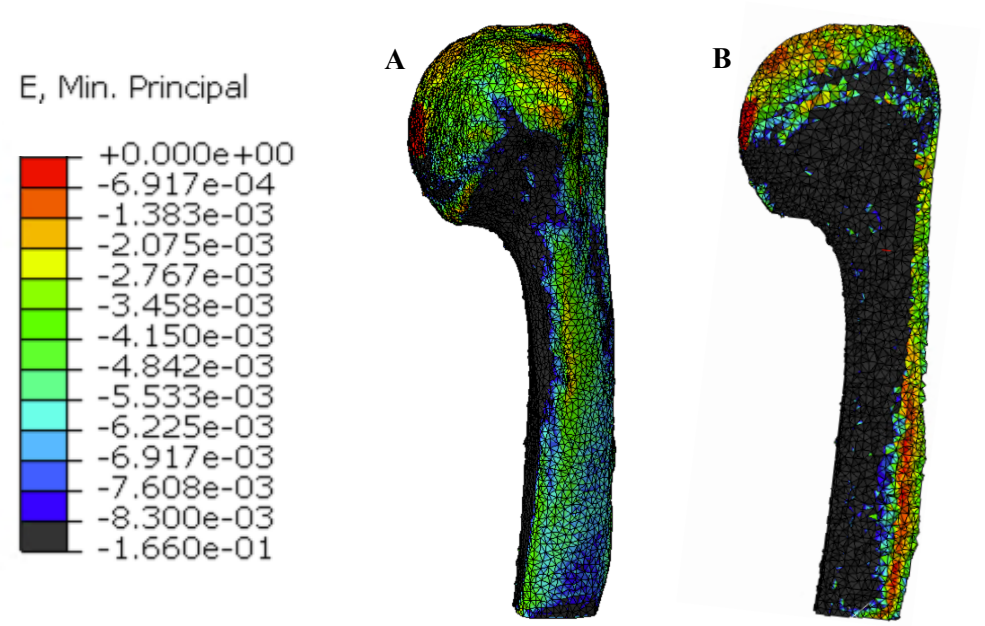
22152L SEQCT maximum (tensile) principal strain with a microstrain set at 4100 for BONE reconstruction kernel (A - Surface of the humerus; B - Sliced humerus)



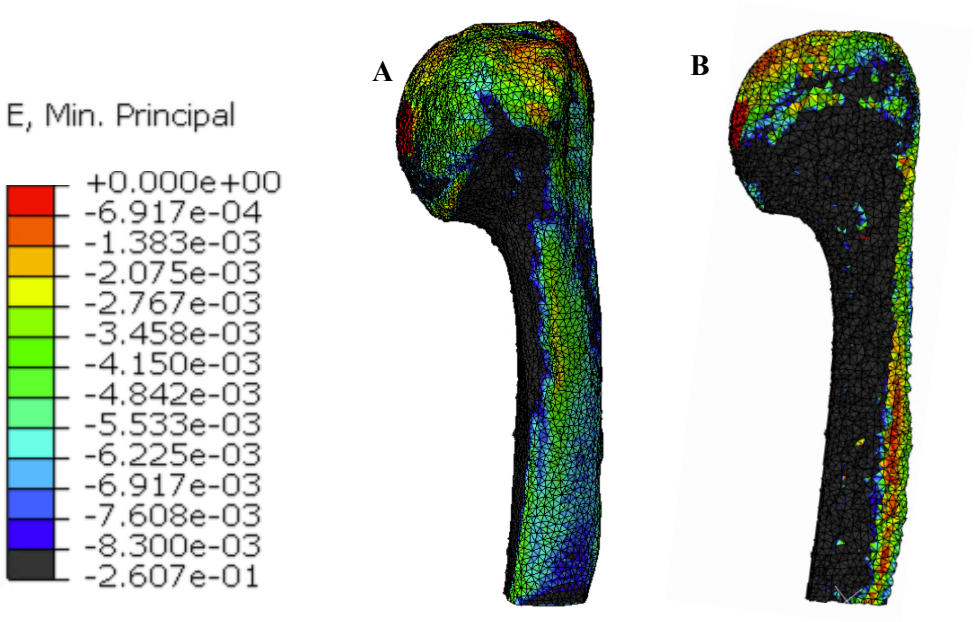
22152L SEQCT maximum (tensile) principal strain with a microstrain set at 4100 for STD reconstruction kernel (A - Surface of the humerus; B - Sliced humerus)



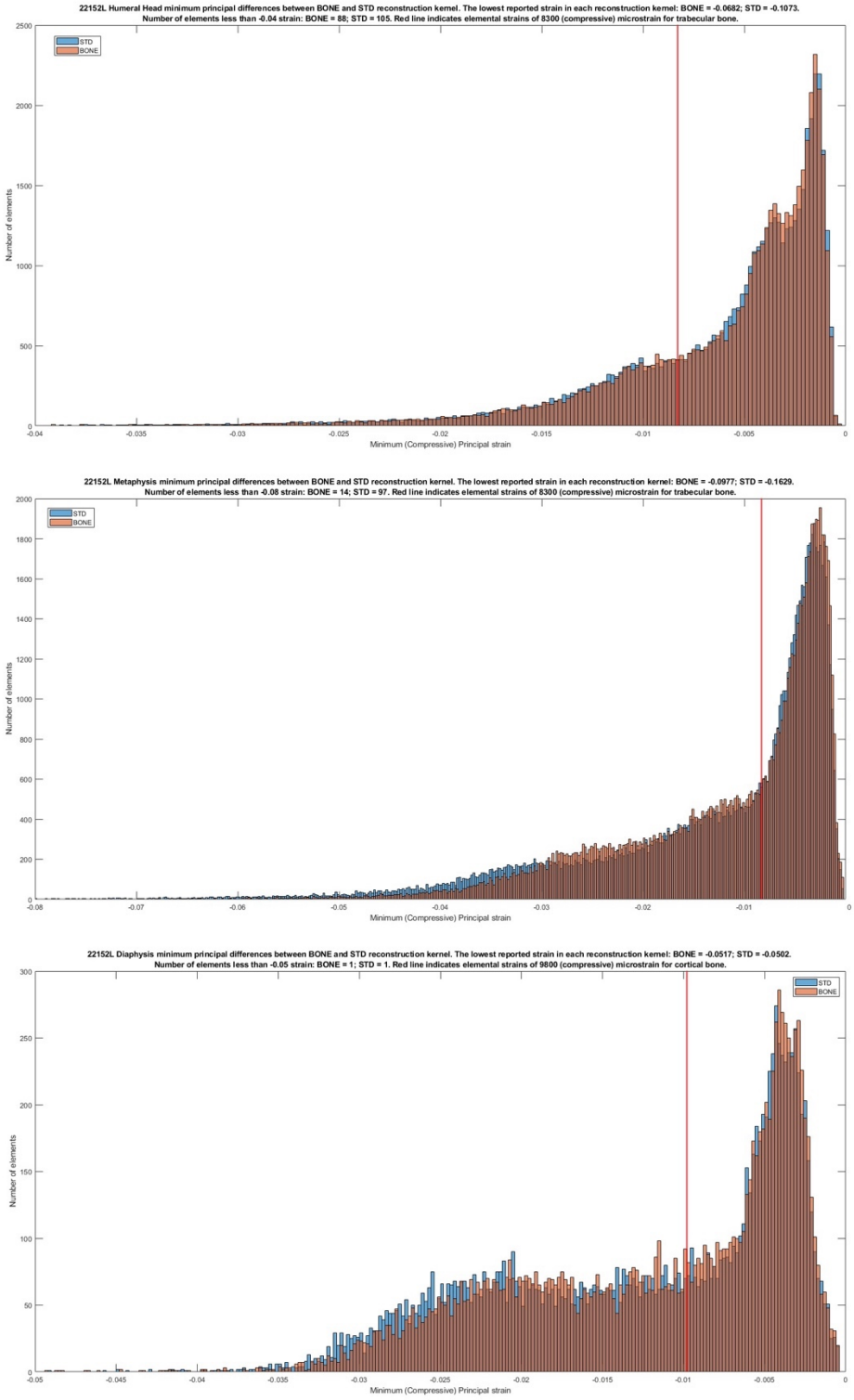
Maximum (tensile) principal strain for cadaver 22152L in SEQCT in the three regions.



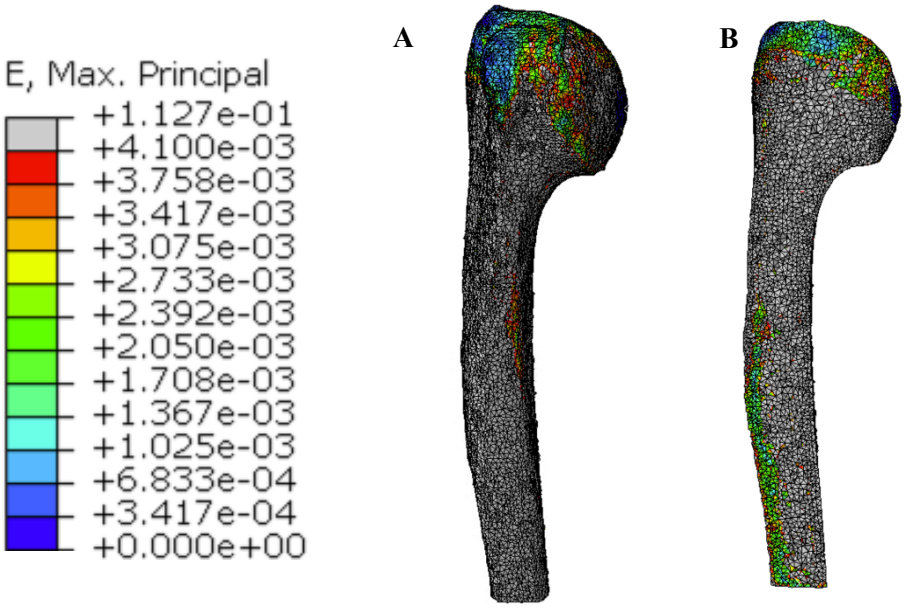
22152L SEQCT minimum (compressive) principal strain with a microstrain set at 8300 for BONE reconstruction kernel (A - Surface of the humerus; B - Sliced humerus)



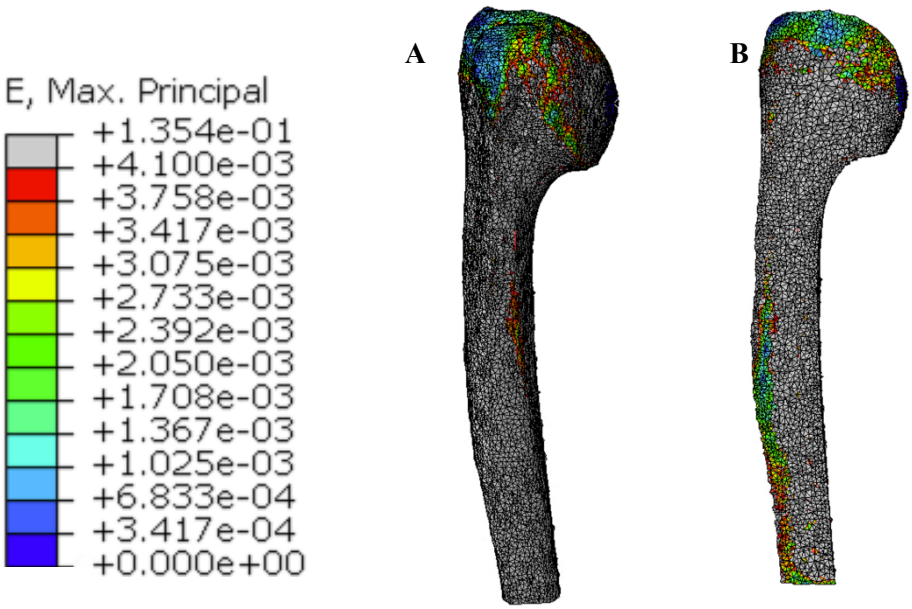
22152L SEQCT minimum (compressive) principal strain with a microstrain set at 8300 for STD reconstruction kernel (A - Surface of the humerus; B - Sliced humerus)



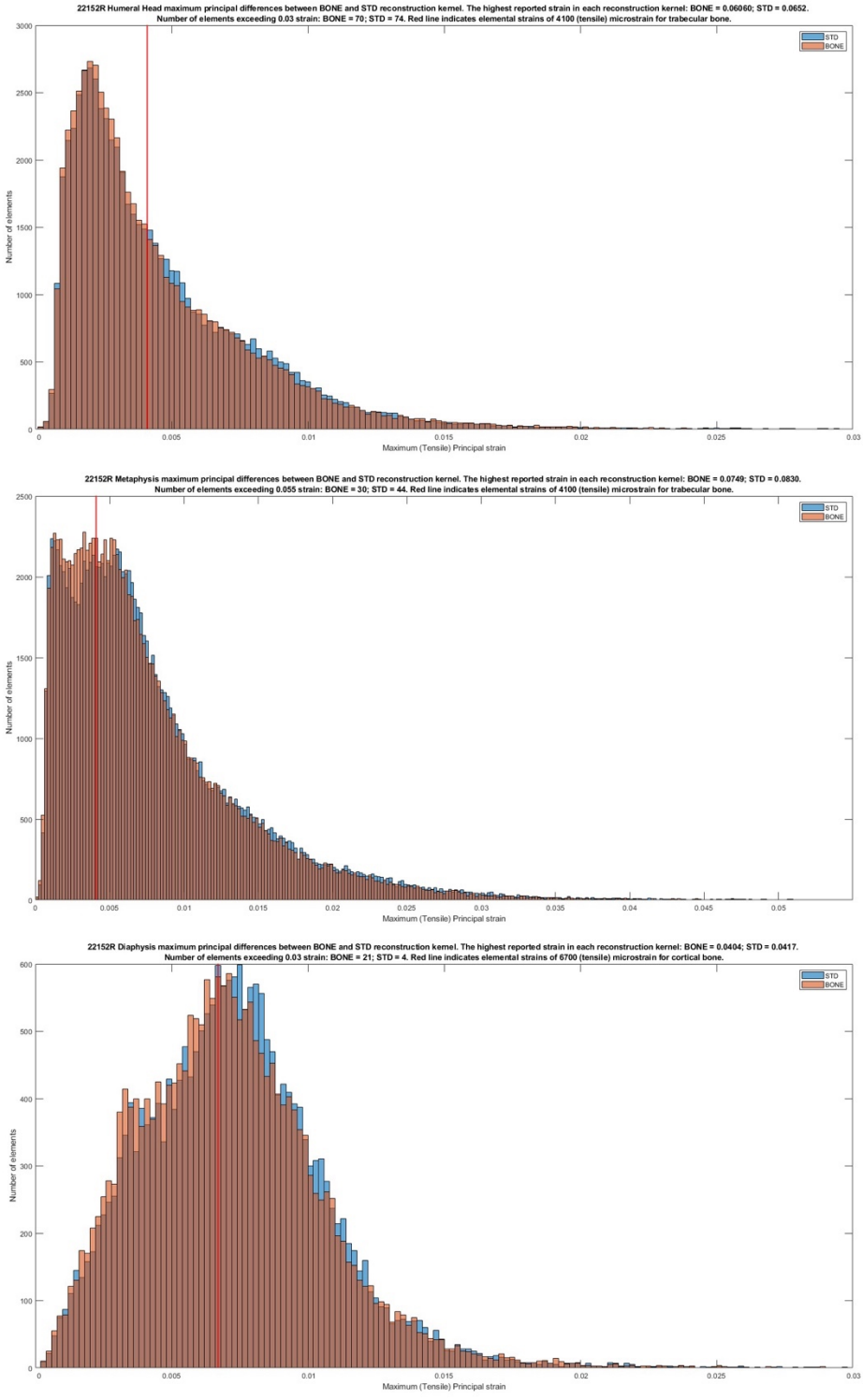
Minimum (compressive) principal strain for cadaver 22152L in SEQCT in the three regions.



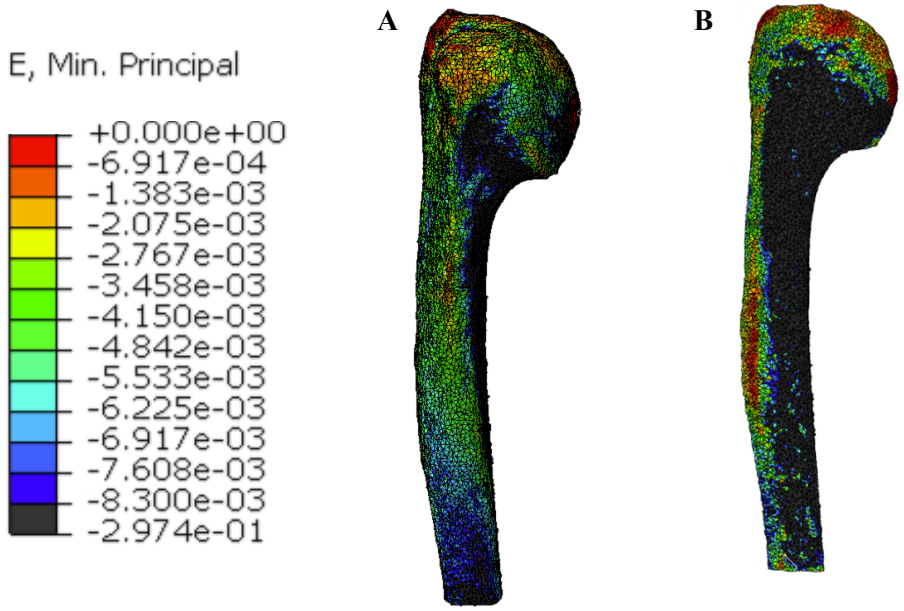
22152R SEQCT maximum (tensile) principal strain with a microstrain set at 4100 for BONE reconstruction kernel (A - Surface of the humerus; B - Sliced humerus)



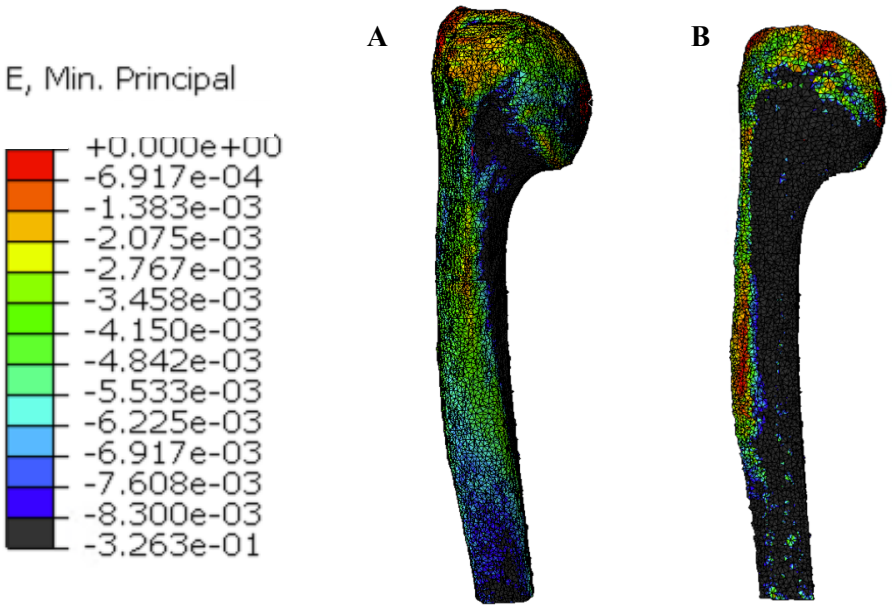
22152R SEQCT maximum (tensile) principal strain with a microstrain set at 4100 for STD reconstruction kernel (A - Surface of the humerus; B - Sliced humerus)



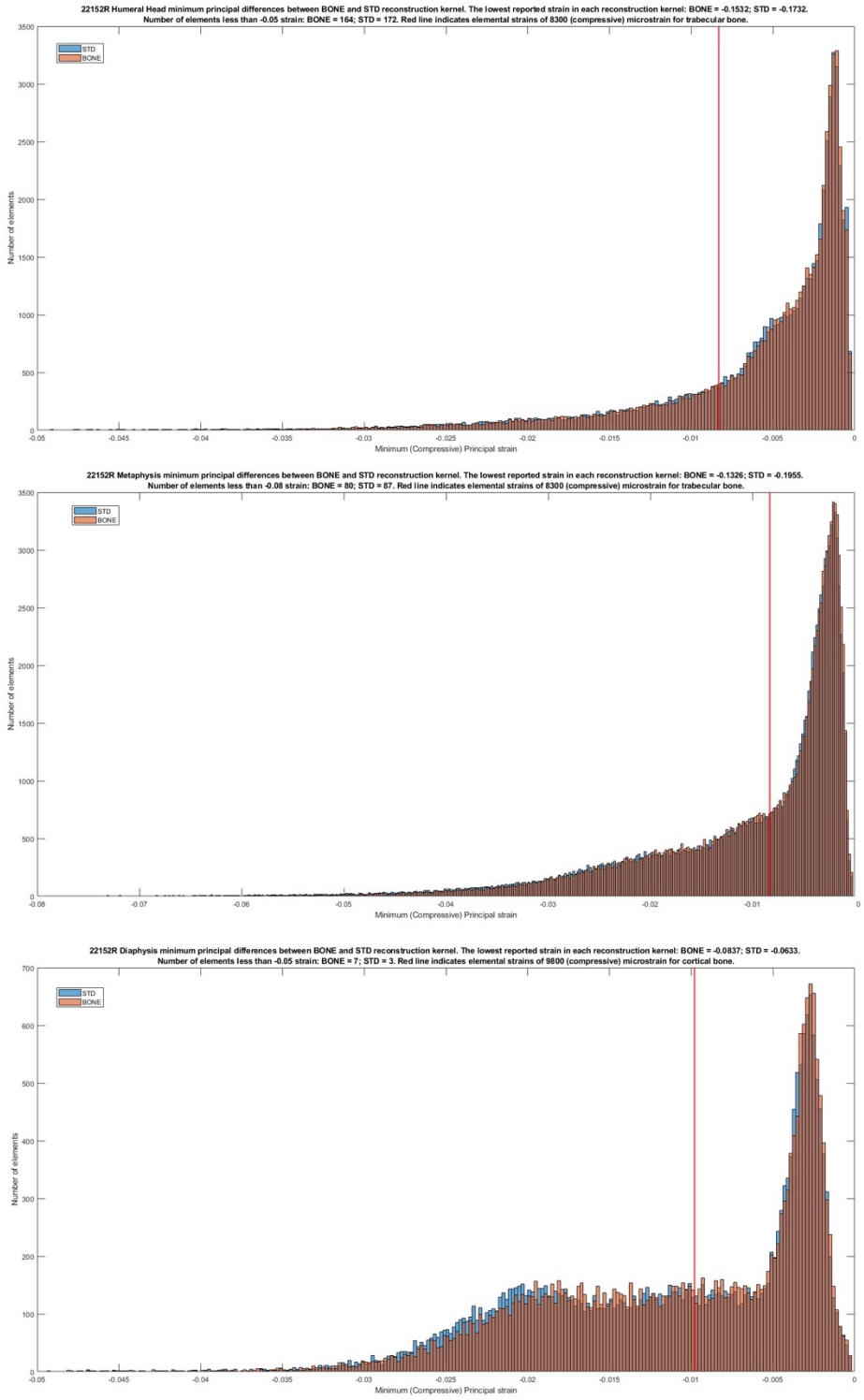
Maximum (tensile) principal strain for cadaver 22152R in SEQCT in the three regions.



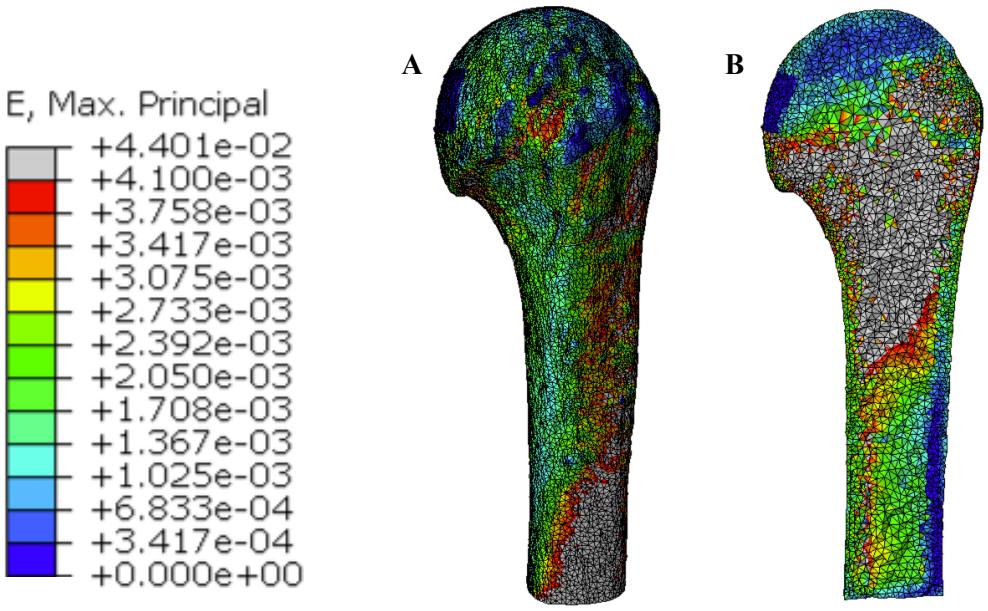
22152R SEQCT minimum (compressive) principal strain with a microstrain set at 8300 for BONE reconstruction kernel (A - Surface of the humerus; B - Sliced humerus)



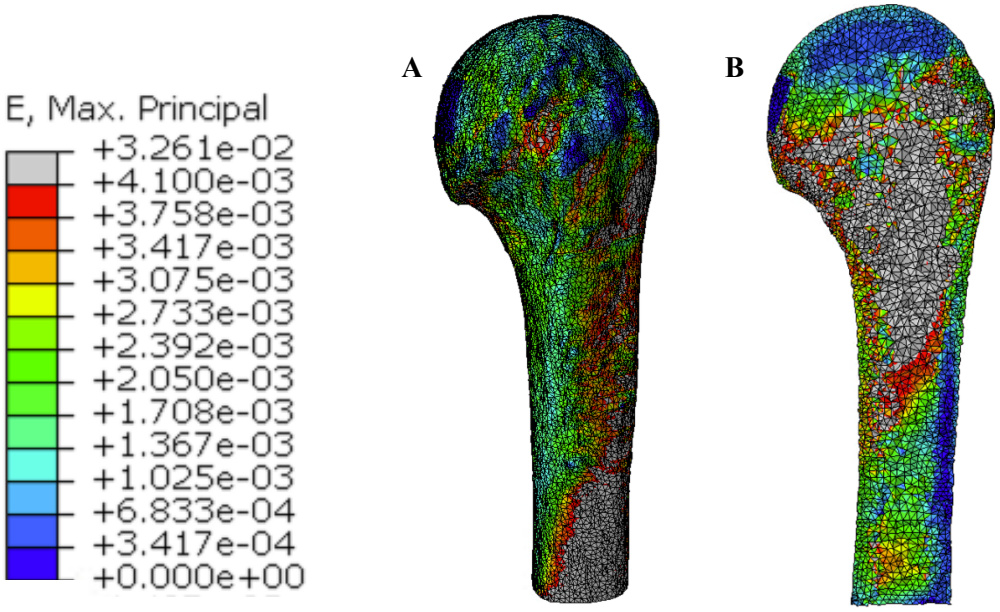
22152R SEQCT minimum (compressive) principal strain with a microstrain set at 8300 for STD reconstruction kernel (A - Surface of the humerus; B - Sliced humerus)



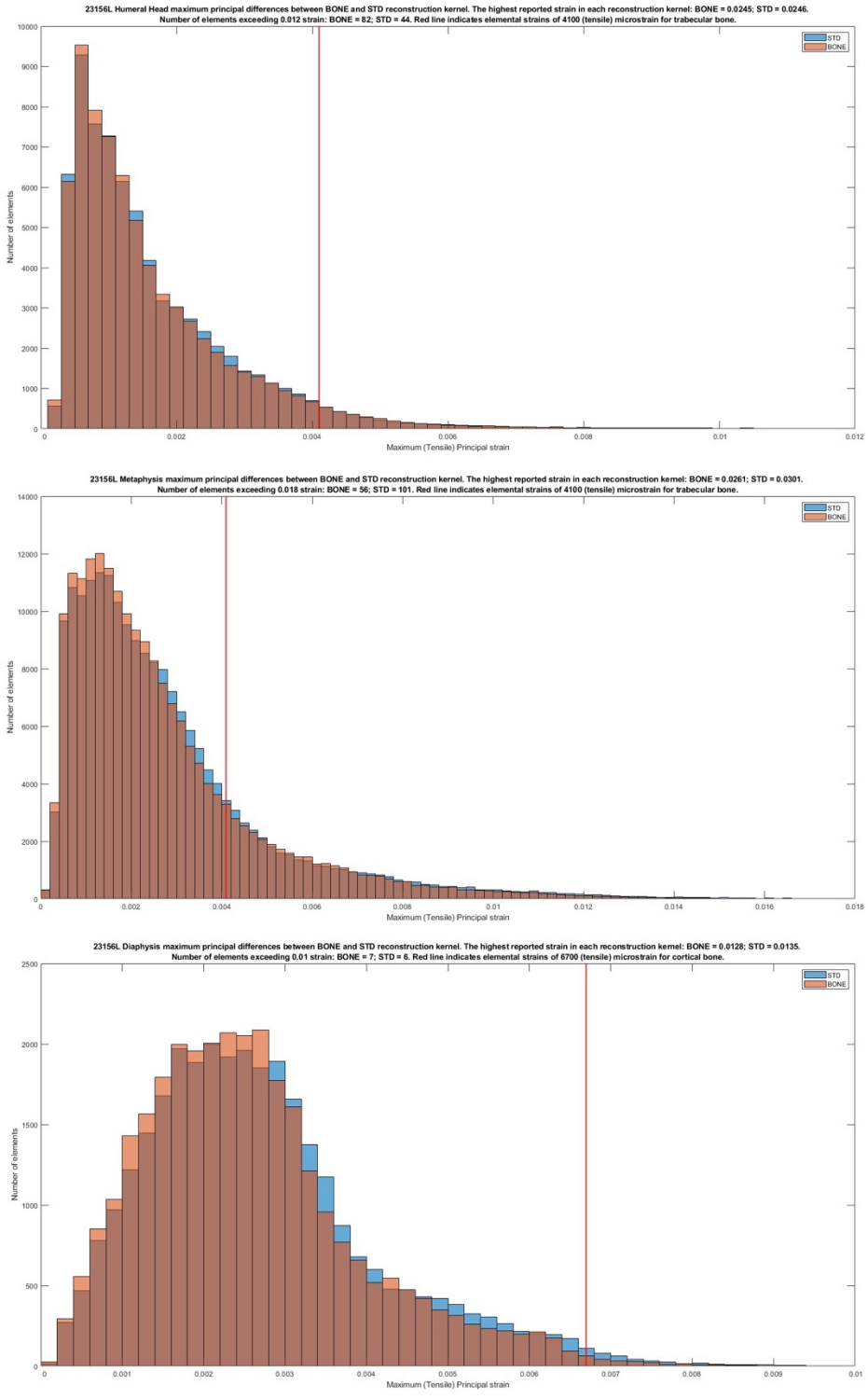
Minimum (compressive) principal strain for cadaver 22152R in SEQCT in the three regions.



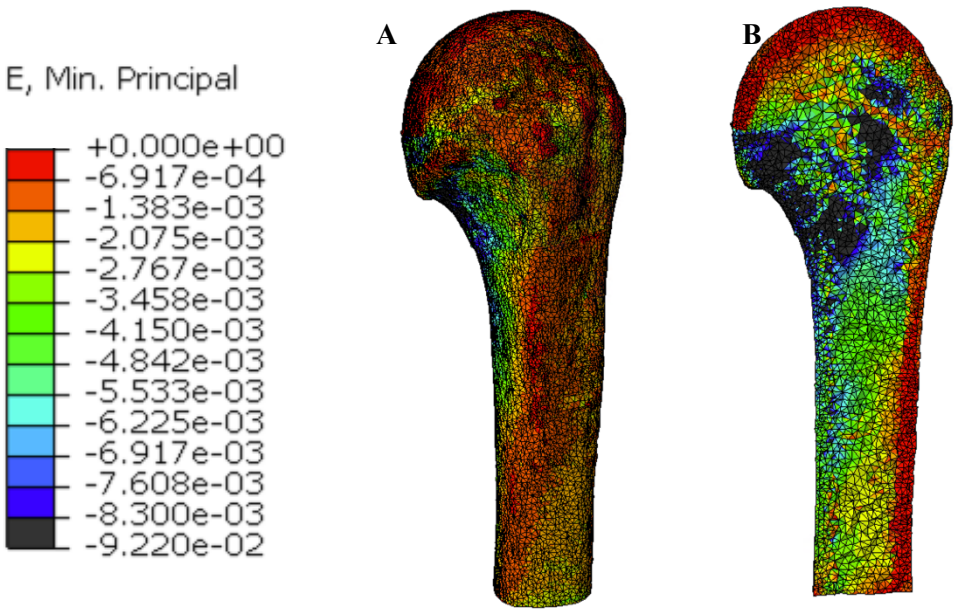
23156L SEQCT maximum (tensile) principal strain with a microstrain set at 4100 for BONE reconstruction kernel (A - Surface of the humerus; B - Sliced humerus)



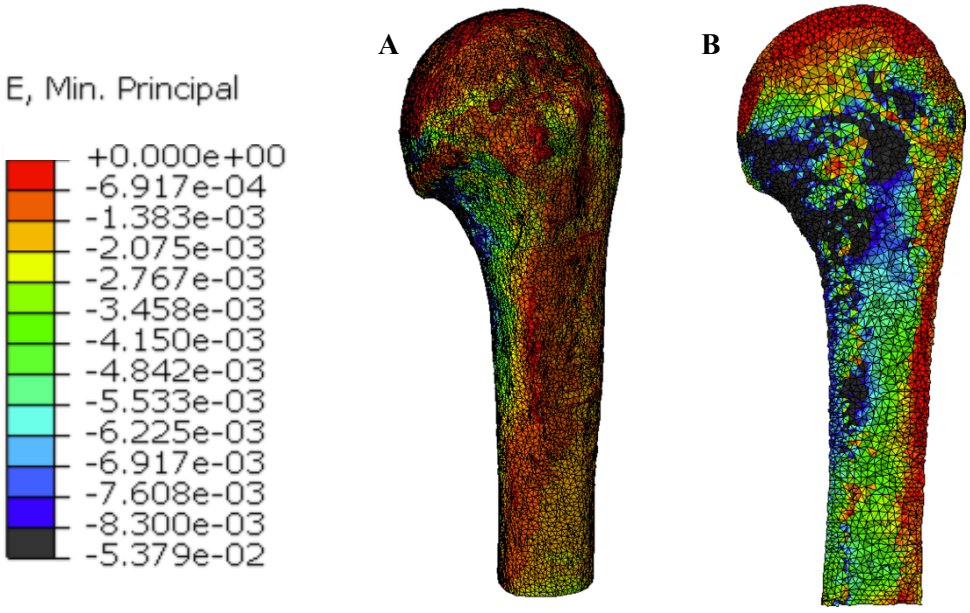
23156L SEQCT maximum (tensile) principal strain with a microstrain set at 4100 for STD reconstruction kernel (A - Surface of the humerus; B - Sliced humerus)



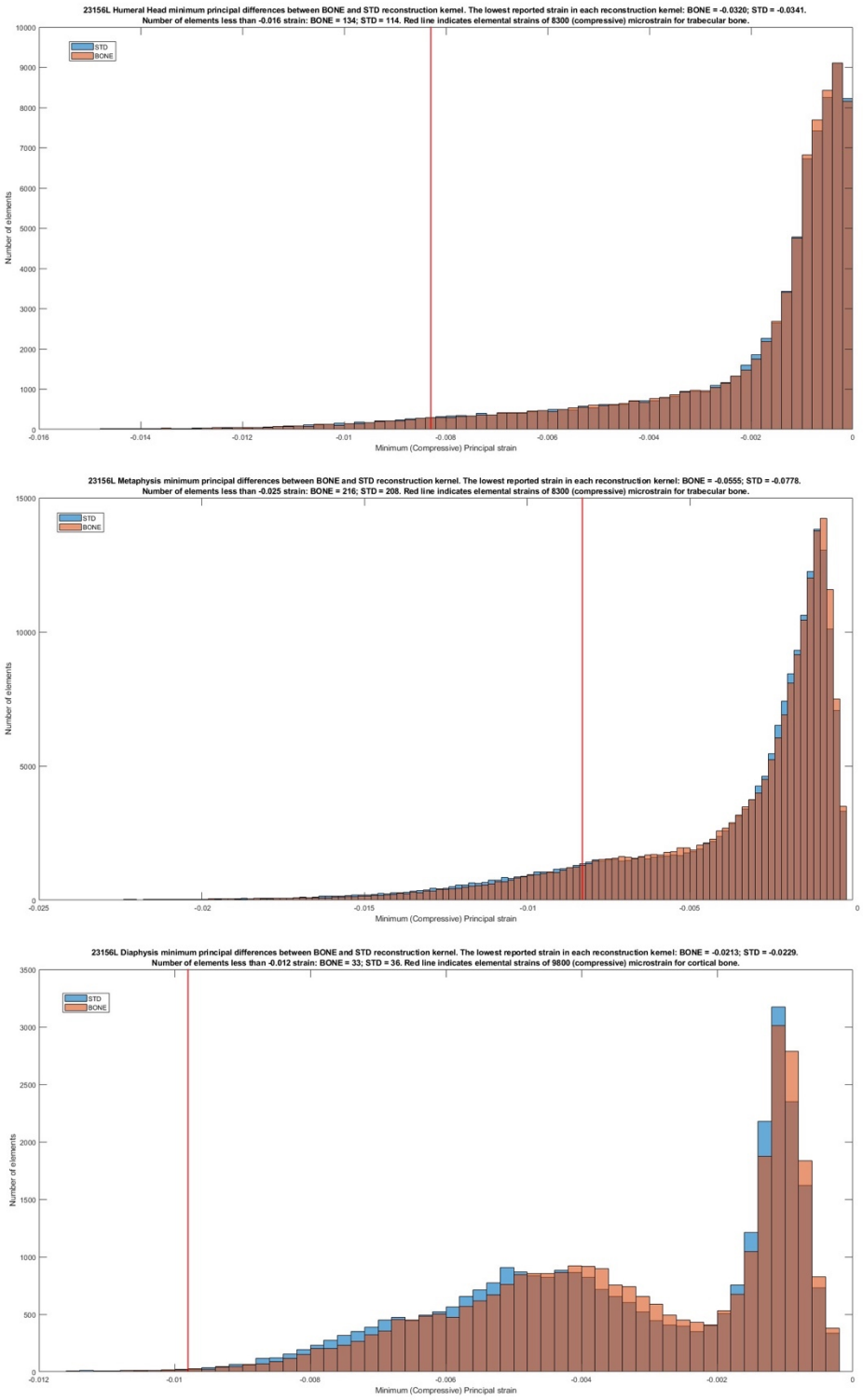
Maximum (tensile) principal strain for cadaver 23156L in SEQCT in the three regions.



23156L SEQCT minimum (compressive) principal strain with a microstrain set at 8300 for BONE reconstruction kernel (A - Surface of the humerus; B - Sliced humerus)



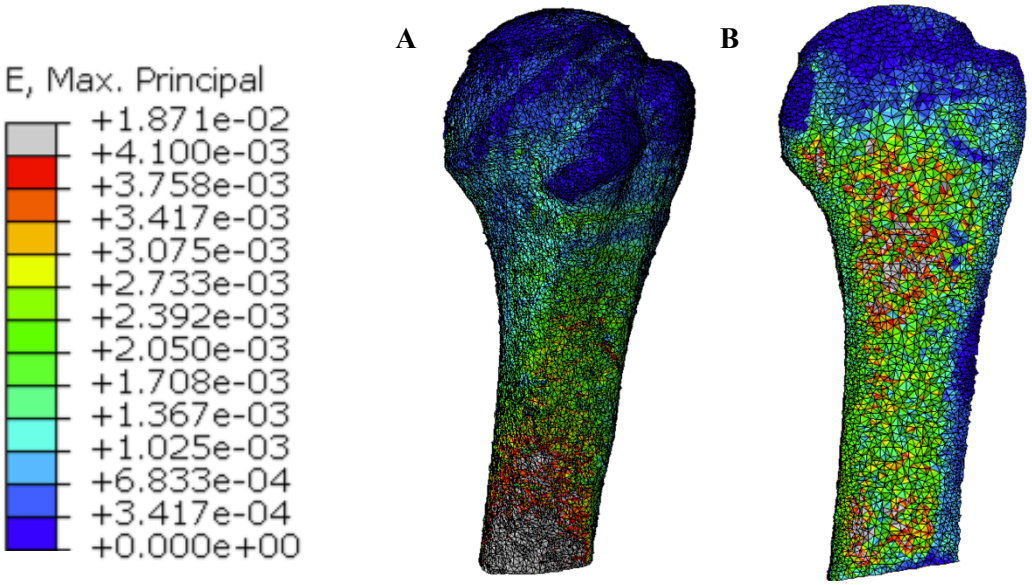
23156L SEQCT minimum (compressive) principal strain with a microstrain set at 8300 for STD reconstruction kernel (A - Surface of the humerus; B - Sliced humerus)



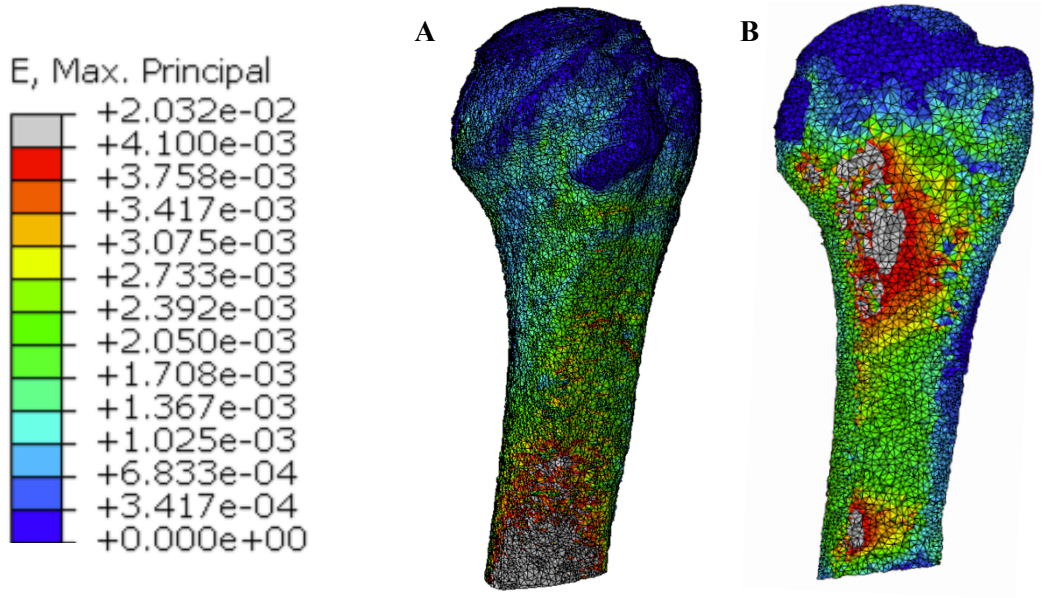
Minimum (compressive) principal strain for cadaver 23156L in SEQCT in the three regions.

Appendix B

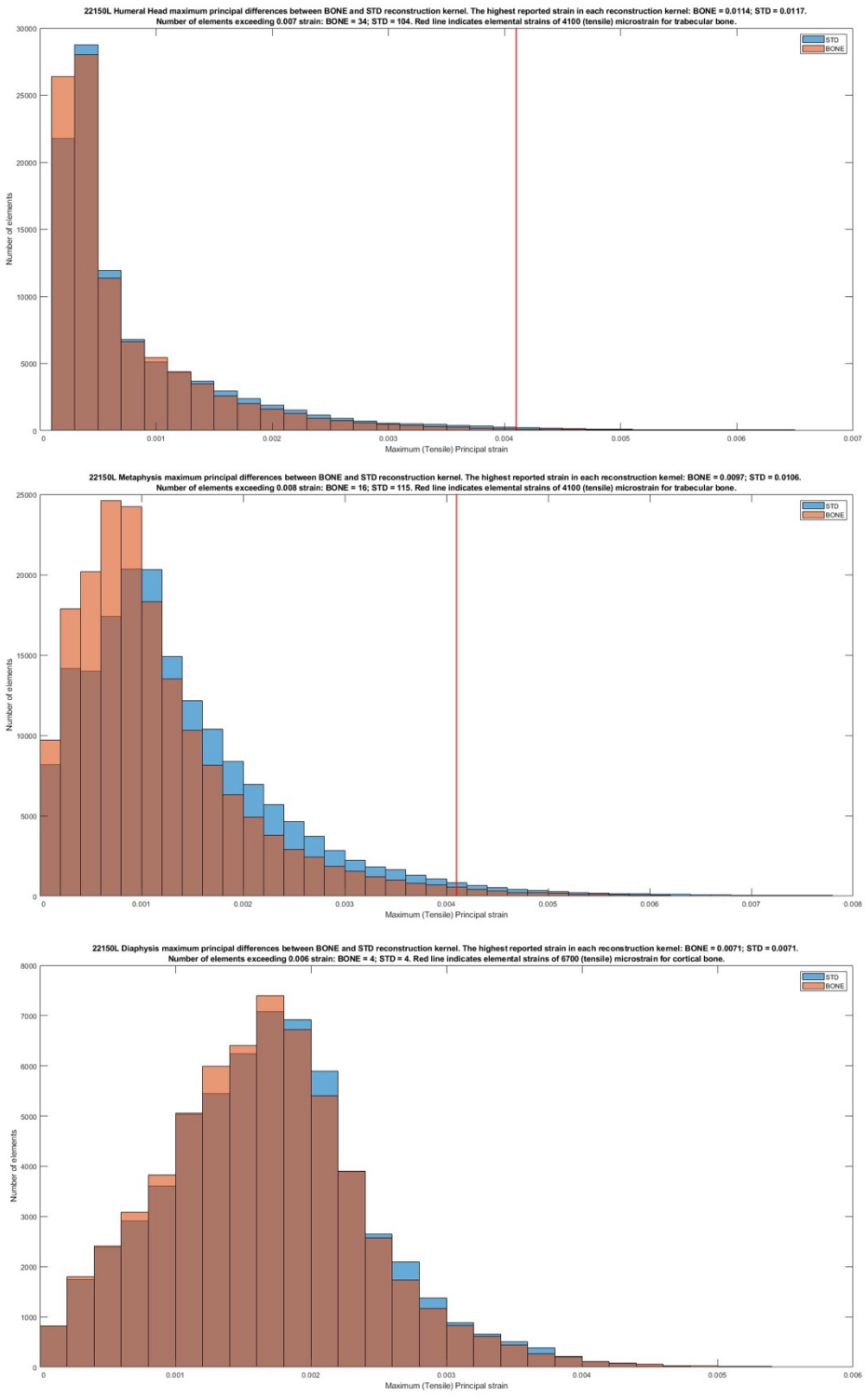
FE models and Histograms from DEQCT for the rest of the models



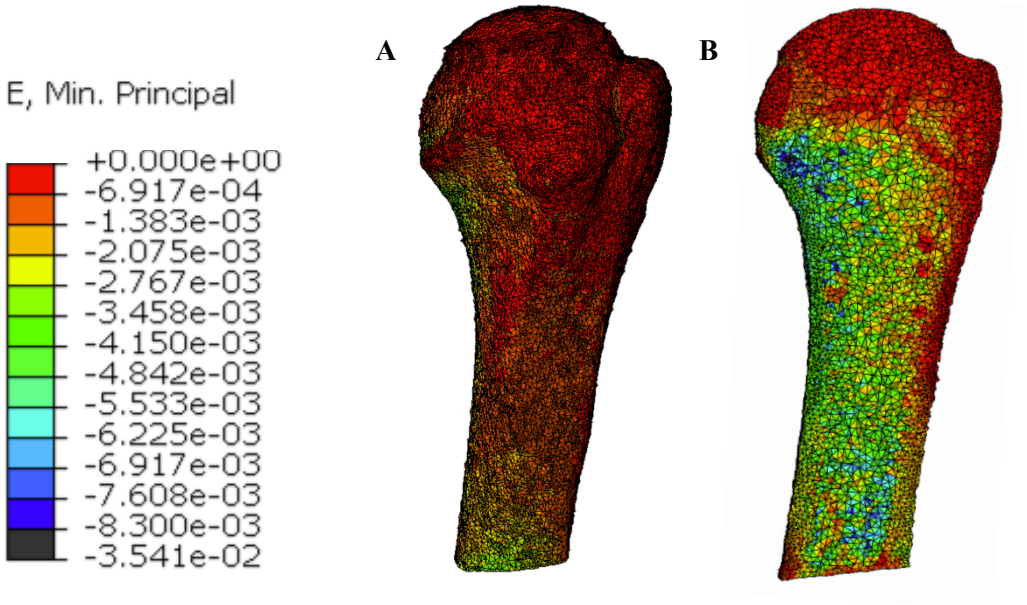
22150L DEQCT maximum (tensile) principal strain with a microstrain set at 4100 for BONE reconstruction kernel (A - Surface of the humerus; B - Sliced humerus)



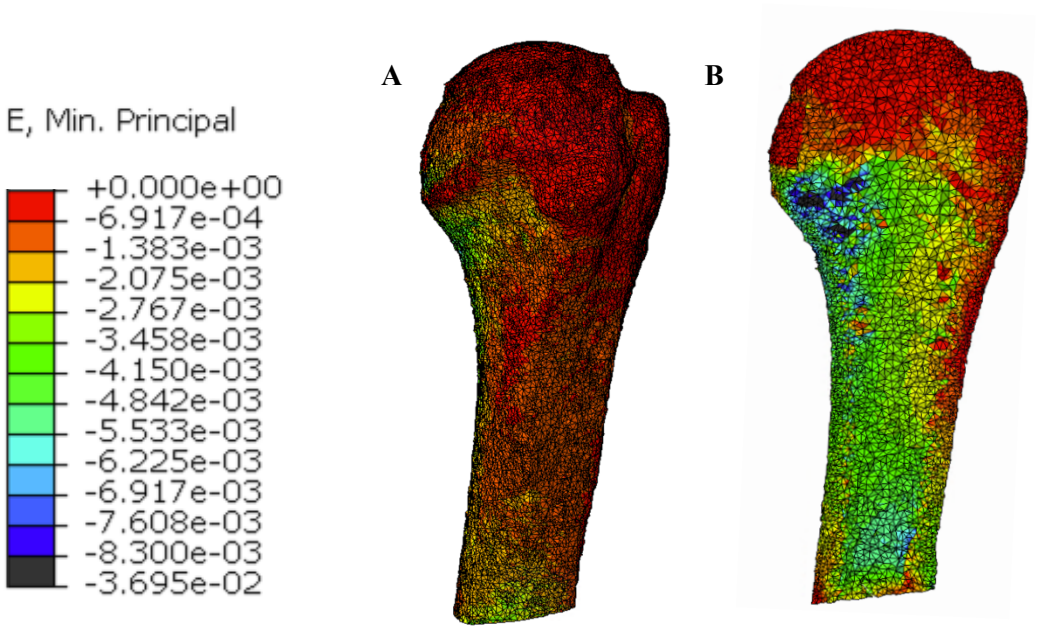
22150L DEQCT maximum (tensile) principal strain with a microstrain set at 4100 for STD reconstruction kernel (A - Surface of the humerus; B - Sliced humerus)



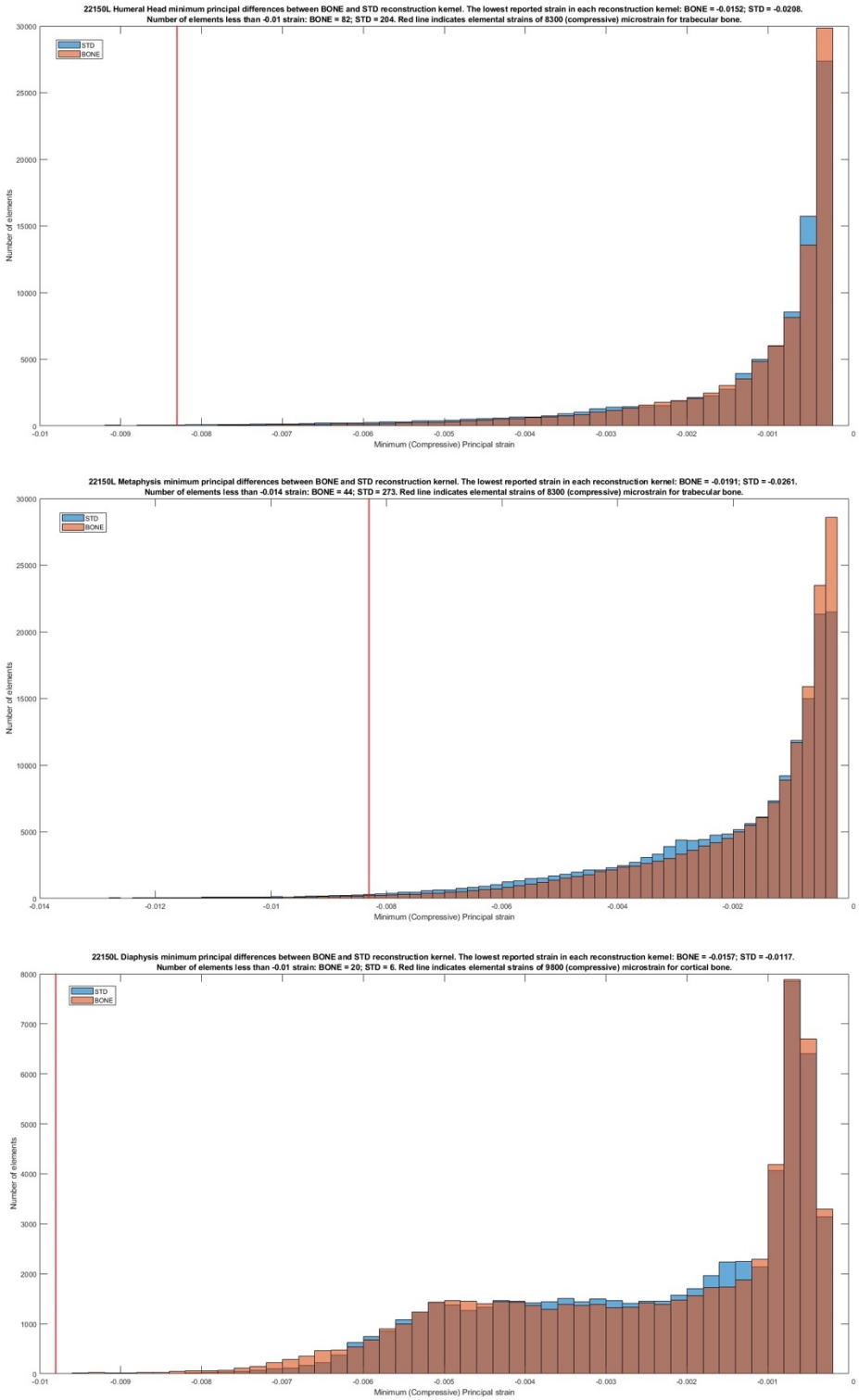
Maximum (tensile) principal strain for cadaver 22150L in DEQCT in the three regions.



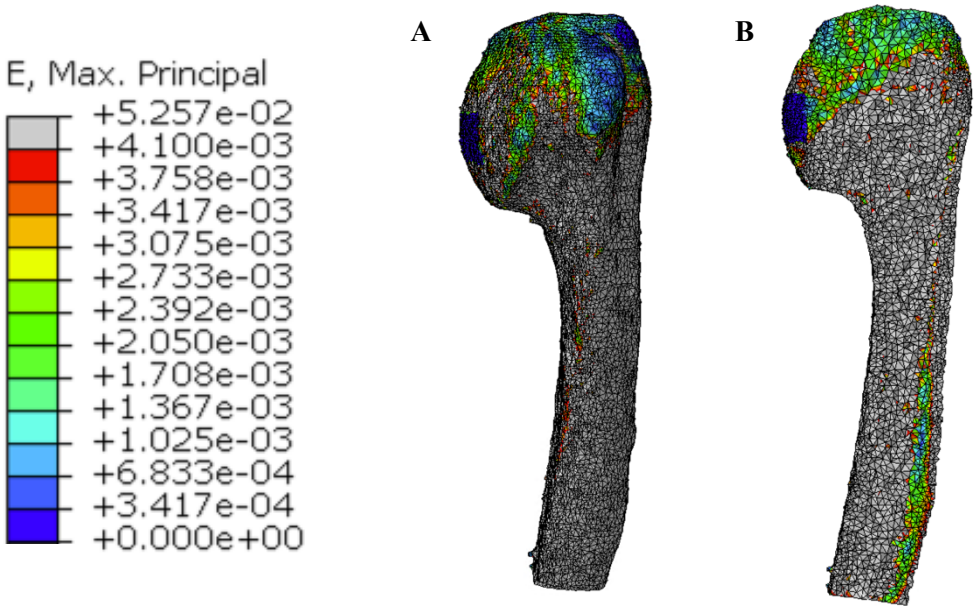
22150L DEQCT minimum (compressive) principal strain with a microstrain set at 8300 for BONE reconstruction kernel (A - Surface of the humerus; B - Sliced humerus)



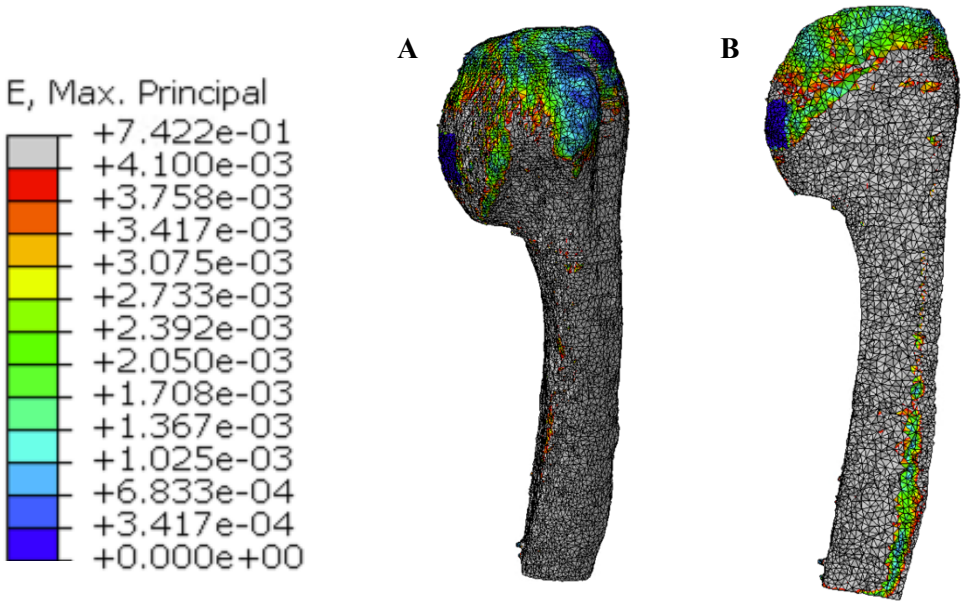
22150L DEQCT minimum (compressive) principal strain with a microstrain set at 8300 for STD reconstruction kernel (A - Surface of the humerus; B - Sliced humerus)



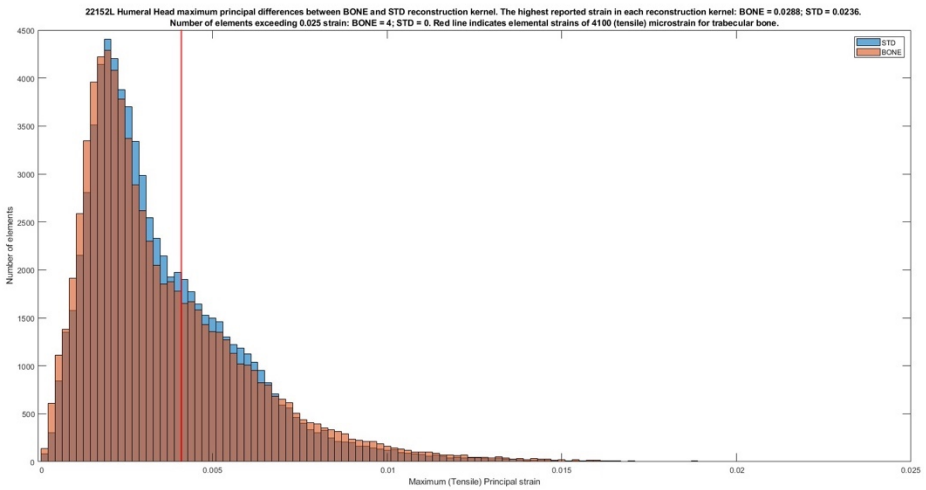
Minimum (compressive) principal strain for cadaver 22150L in DEQCT in the three regions.

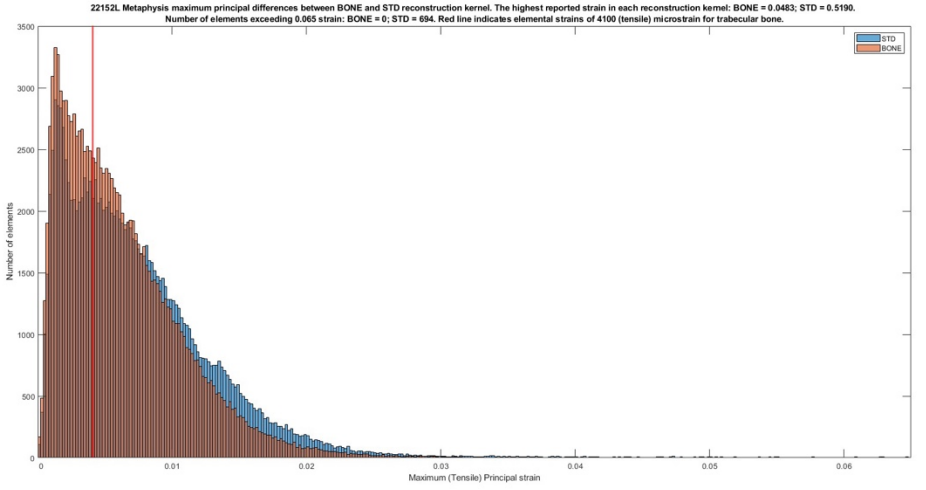


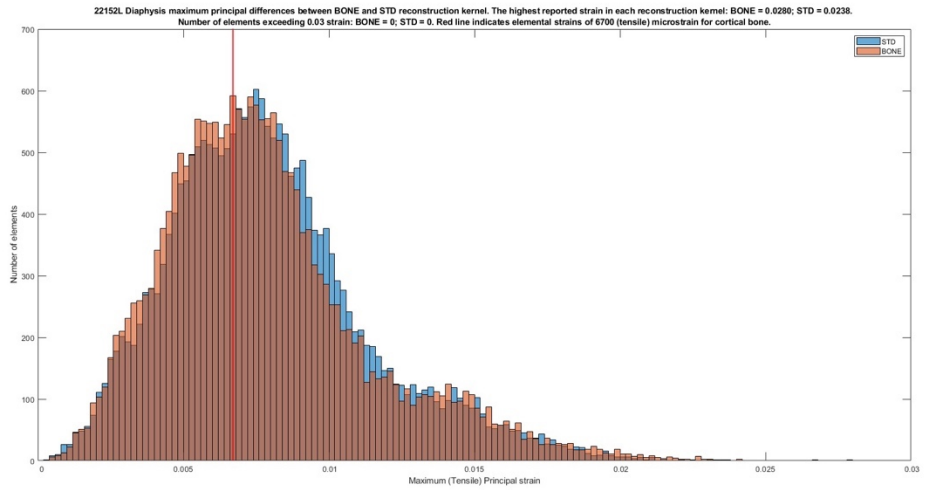
22152L DEQCT maximum (tensile) principal strain with a microstrain set at 4100 for BONE reconstruction kernel (A - Surface of the humerus; B - Sliced humerus)



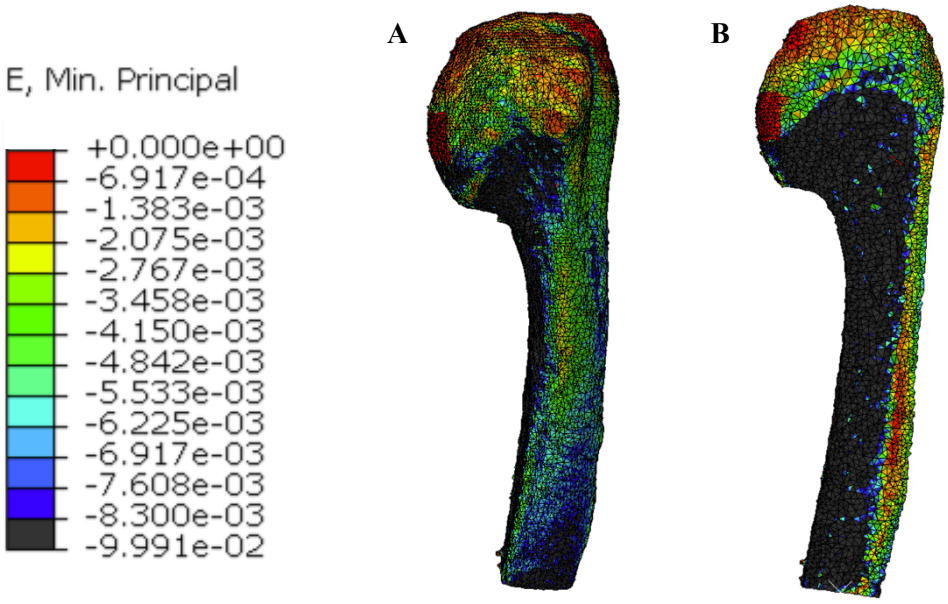
22152L DEQCT maximum (tensile) principal strain with a microstrain set at 4100 for STD reconstruction kernel (A - Surface of the humerus; B - Sliced humerus)



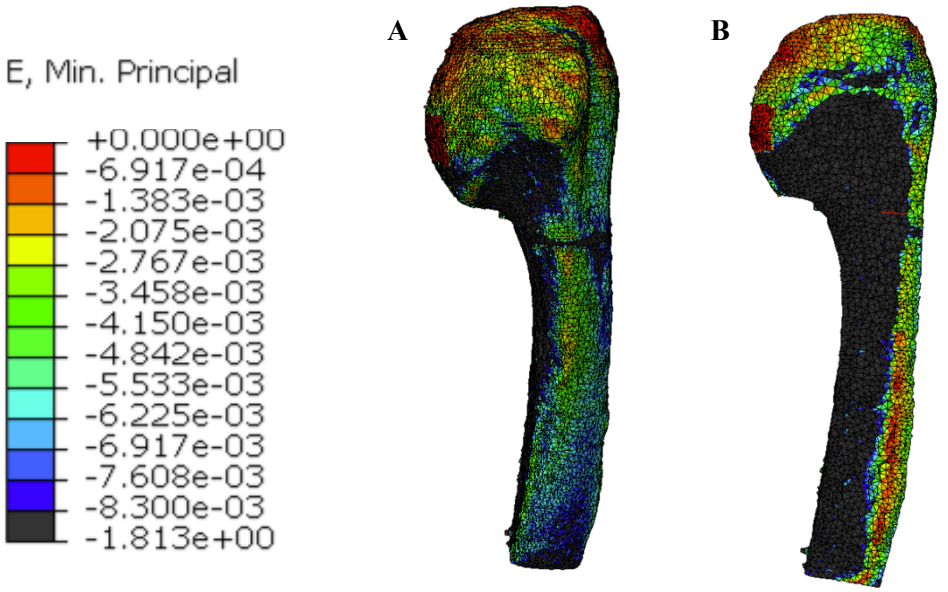




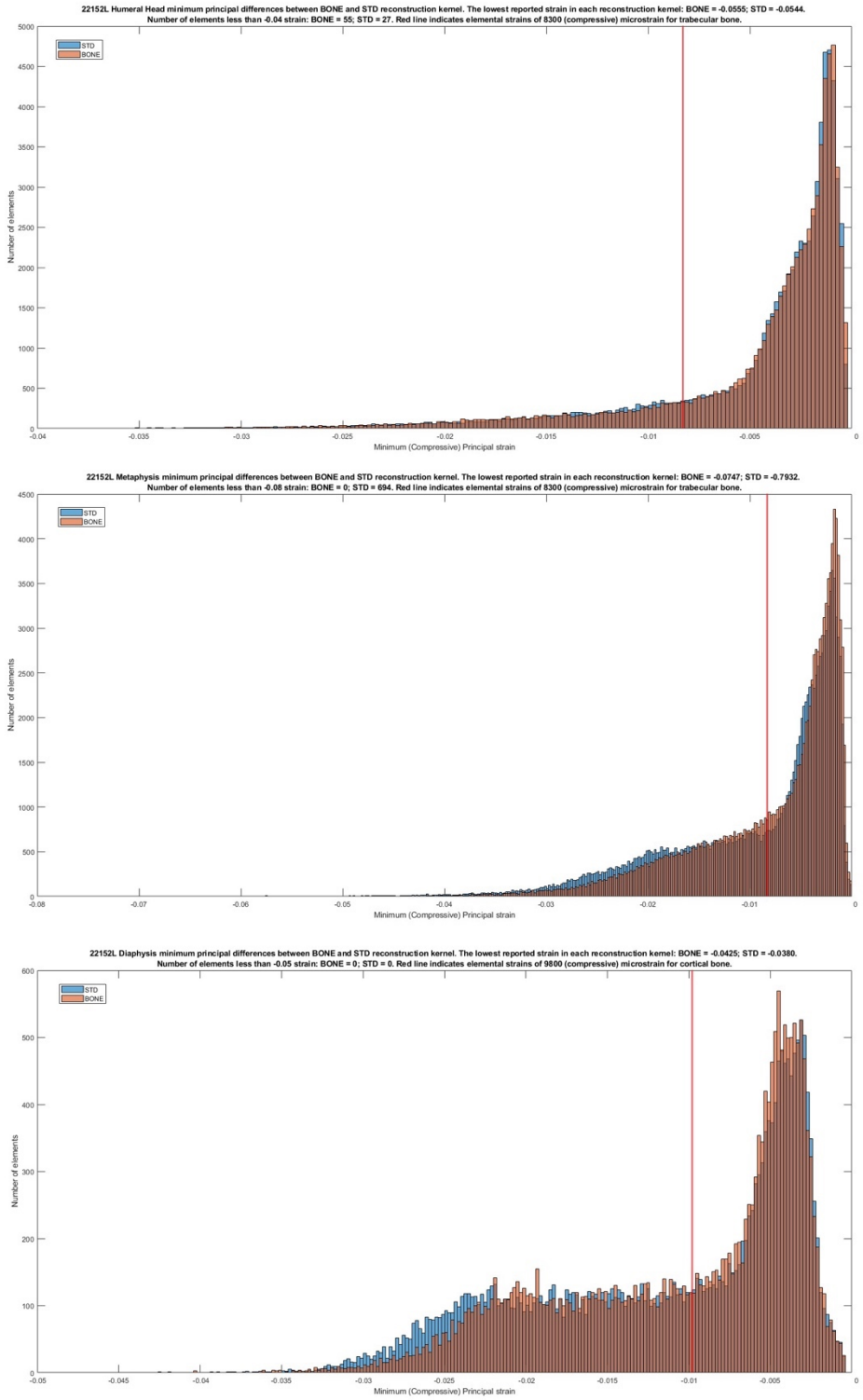
Maximum (tensile) principal strain for cadaver 22152L in DEQCT in the three regions.



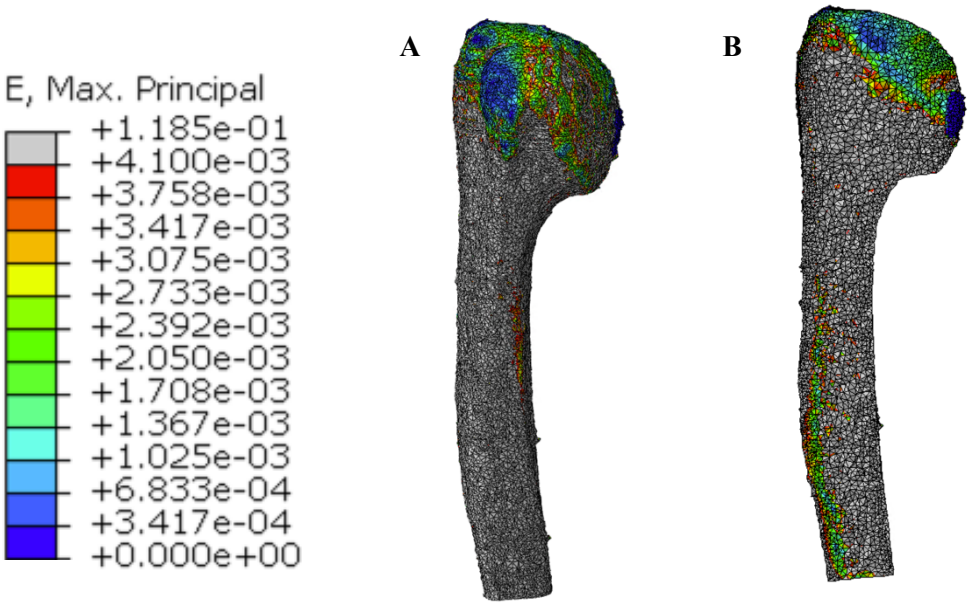
22152L DEQCT minimum (compressive) principal strain with a microstrain set at 8300 for BONE reconstruction kernel (A - Surface of the humerus; B - Sliced humerus)



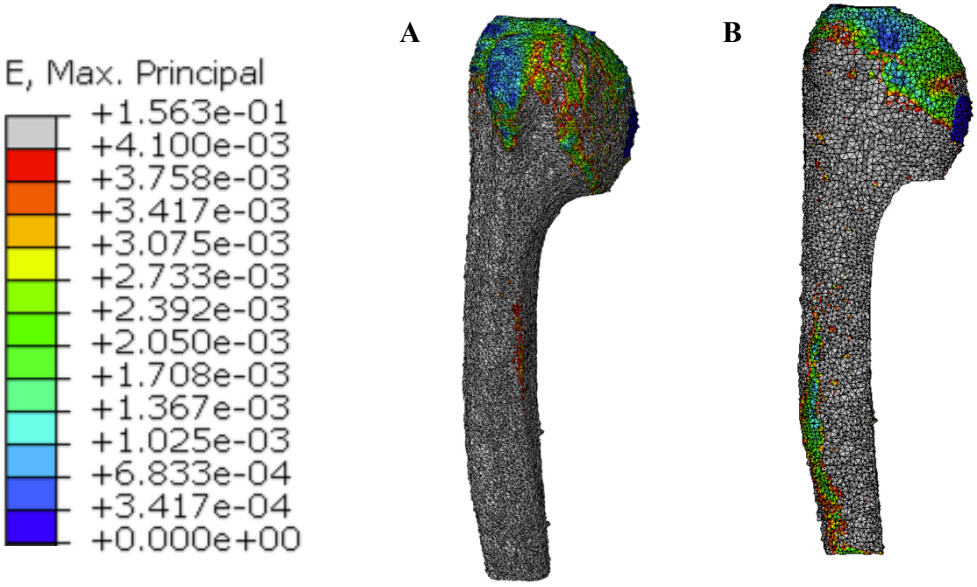
22152L DEQCT minimum (compressive) principal strain with a microstrain set at 8300 for STD reconstruction kernel (A - Surface of the humerus; B - Sliced humerus)



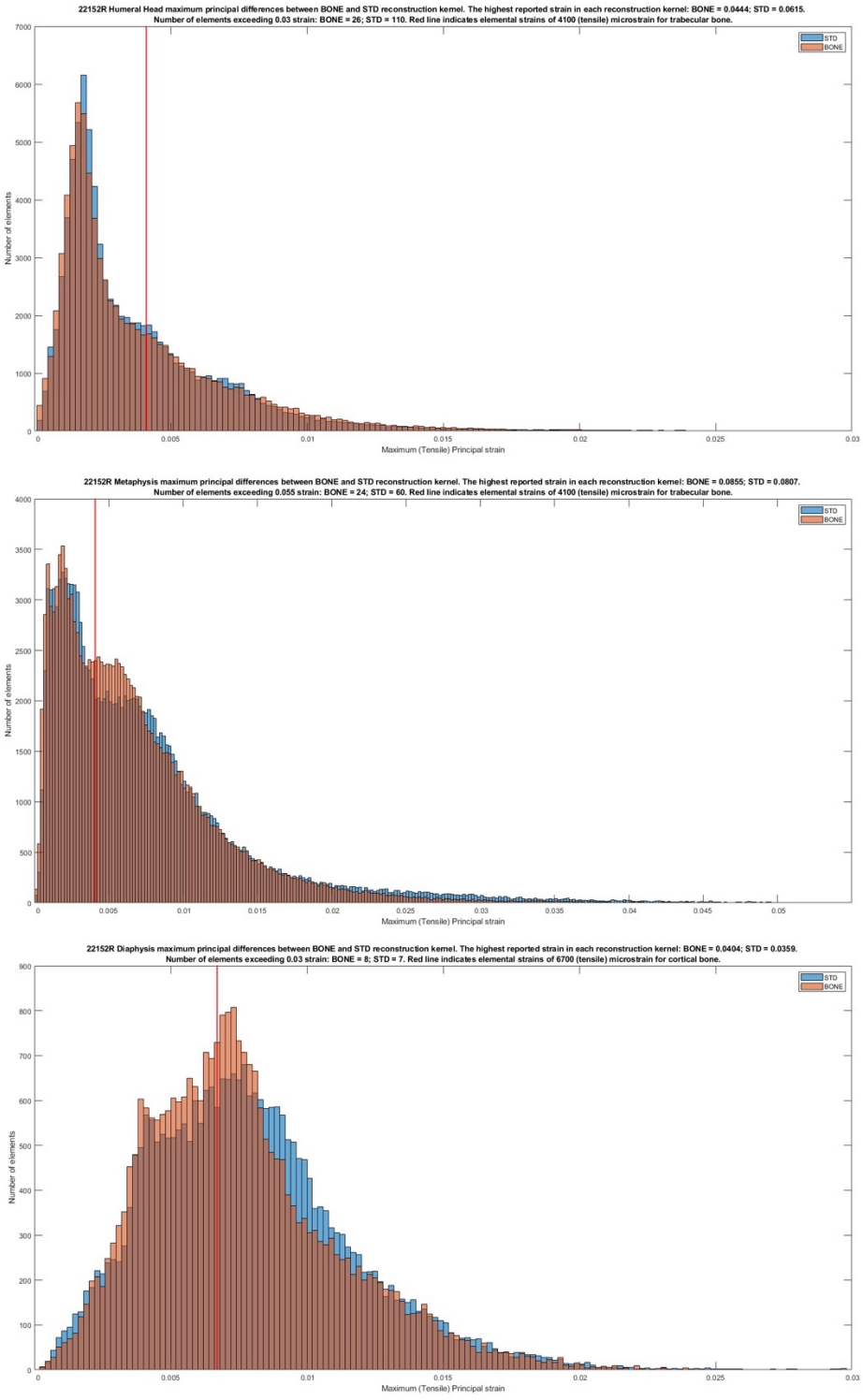
Minimum (compressive) principal strain for cadaver 22152L in DEQCT in the three regions.



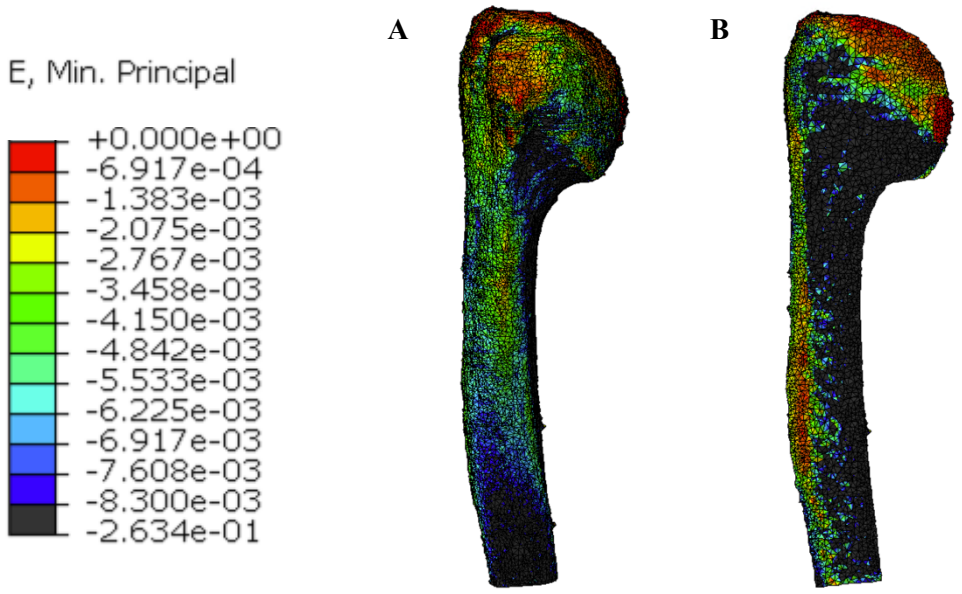
22152R DEQCT maximum (tensile) principal strain with a microstrain set at 4100 for BONE reconstruction kernel (A - Surface of the humerus; B - Sliced humerus)



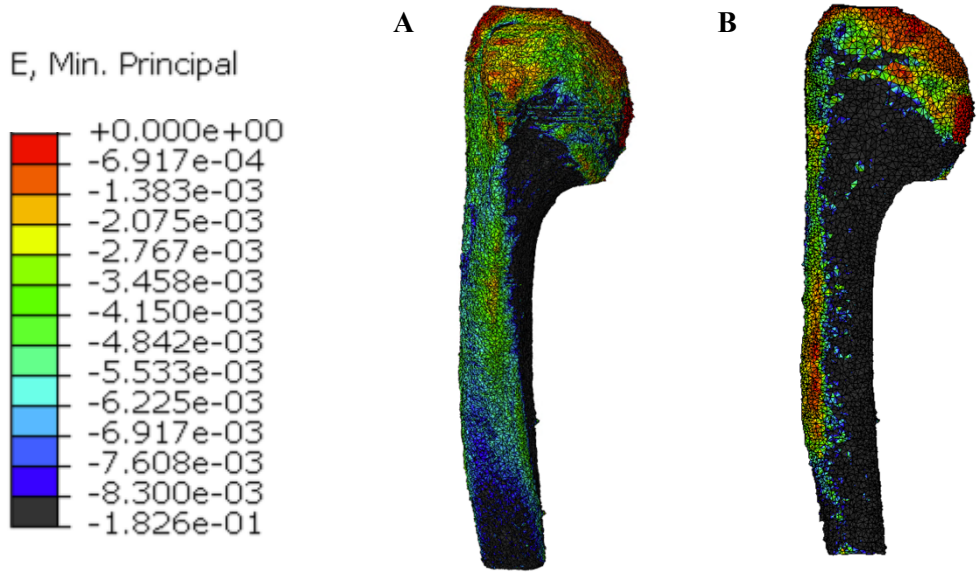
22152R DEQCT maximum (tensile) principal strain with a microstrain set at 4100 for STD reconstruction kernel (A - Surface of the humerus; B - Sliced humerus)



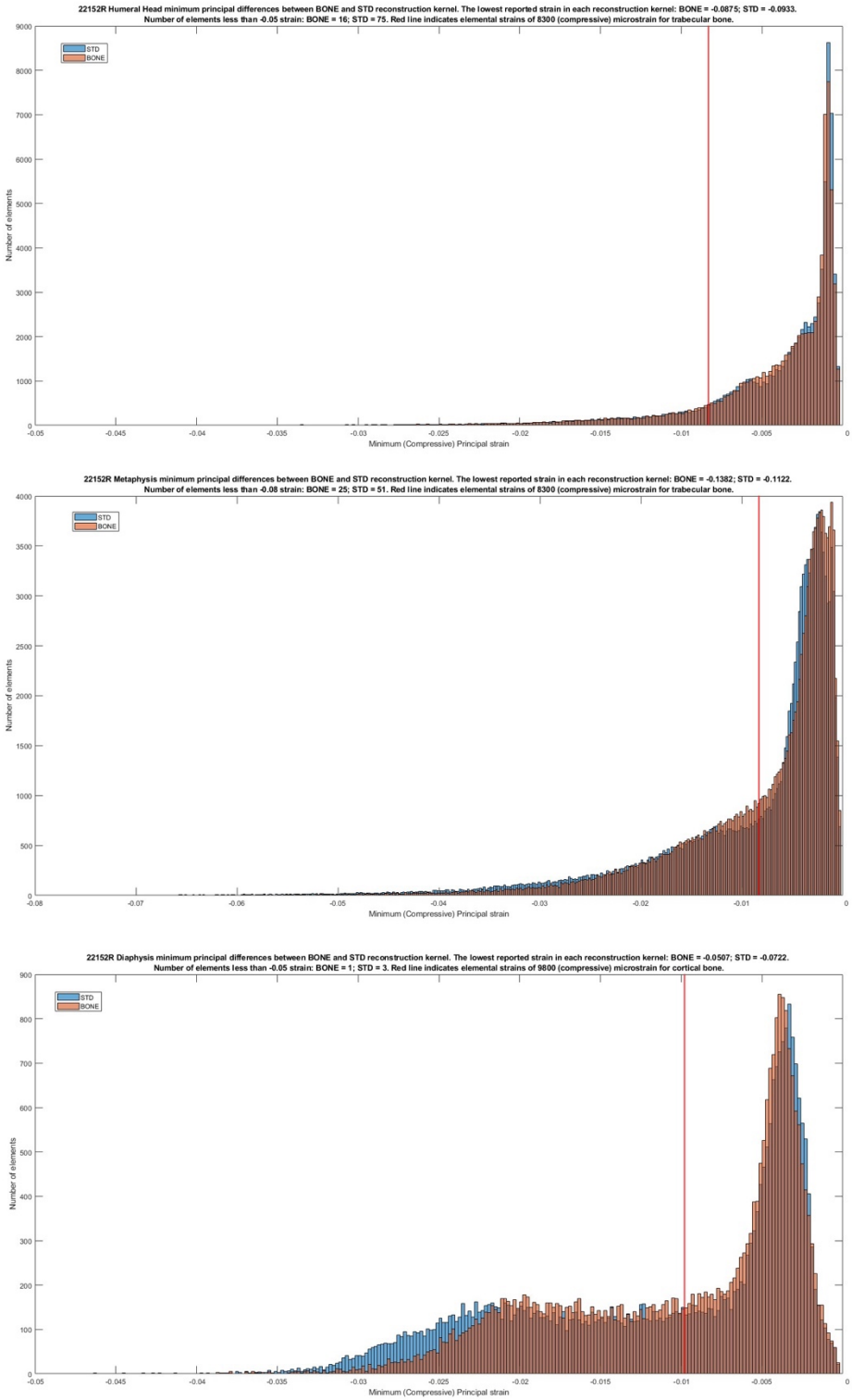
Maximum (tensile) principal strain for cadaver 22152R in DEQCT in the three regions.



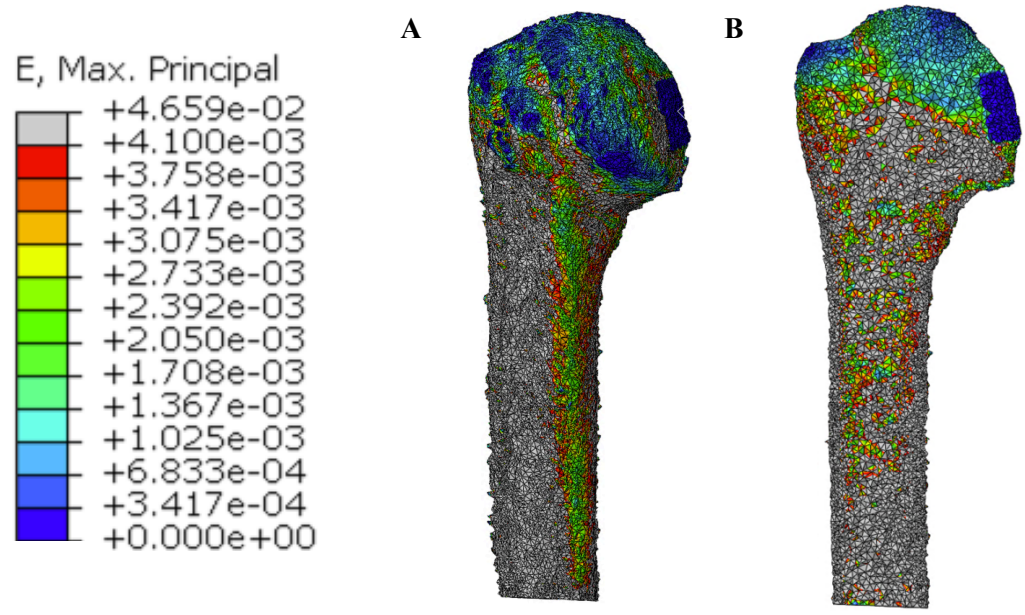
22152R DEQCT minimum (compressive) principal strain with a microstrain set at 8300 for BONE reconstruction kernel (A - Surface of the humerus; B - Sliced humerus)



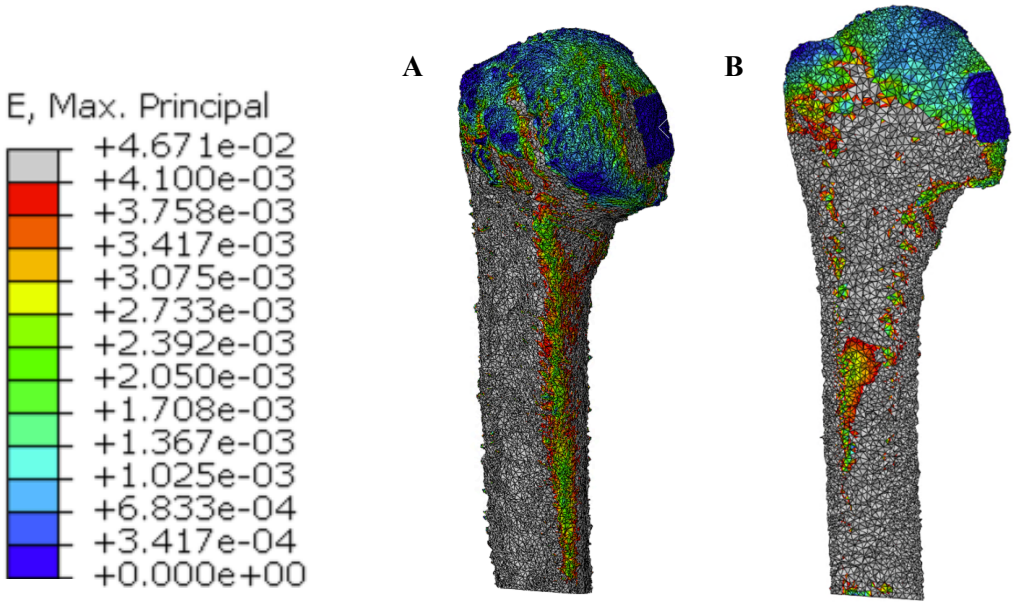
22152R DEQCT minimum (compressive) principal strain with a microstrain set at 8300 for STD reconstruction kernel (A - Surface of the humerus; B - Sliced humerus)



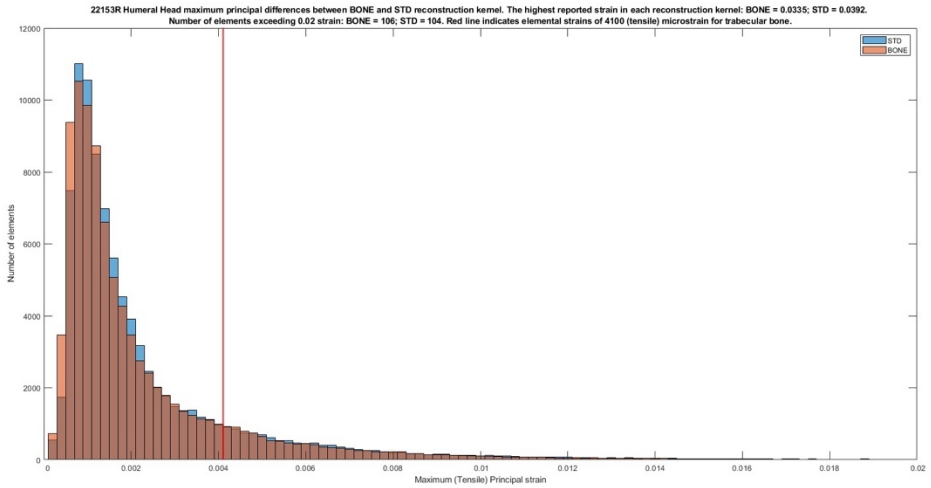
Minimum (compressive) principal strain for cadaver 22152R in DEQCT in the three regions.

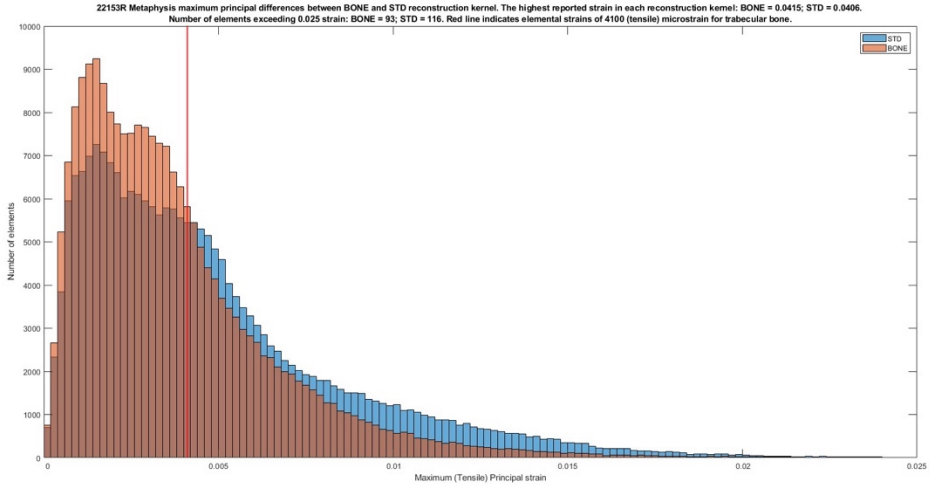


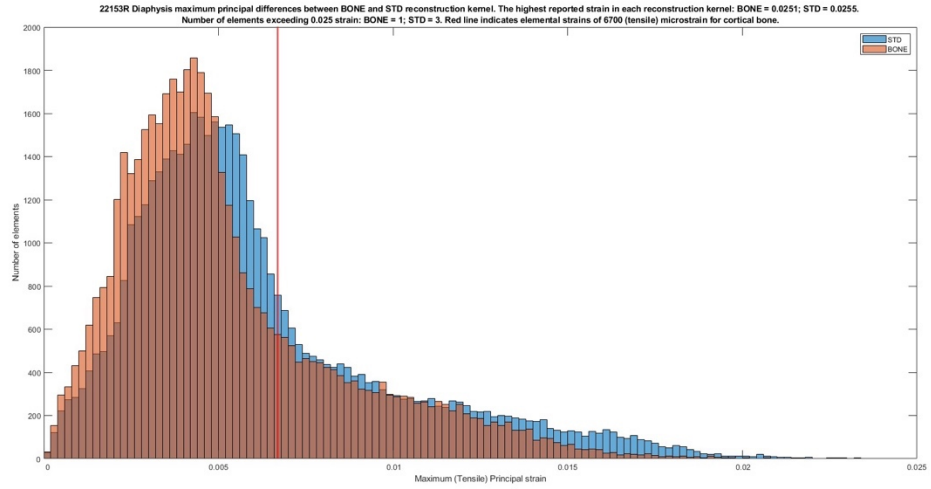
22153R DEQCT maximum (tensile) principal strain with a microstrain set at 4100 for BONE reconstruction kernel (A - Surface of the humerus; B - Sliced humerus)



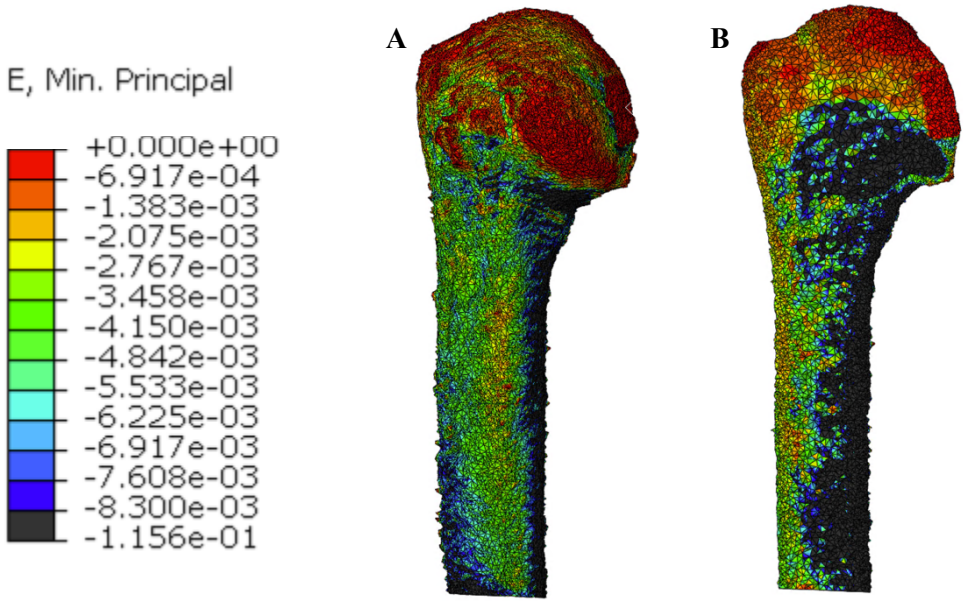
22153R DEQCT maximum (tensile) principal strain with a microstrain set at 4100 for STD reconstruction kernel (A - Surface of the humerus; B - Sliced humerus)



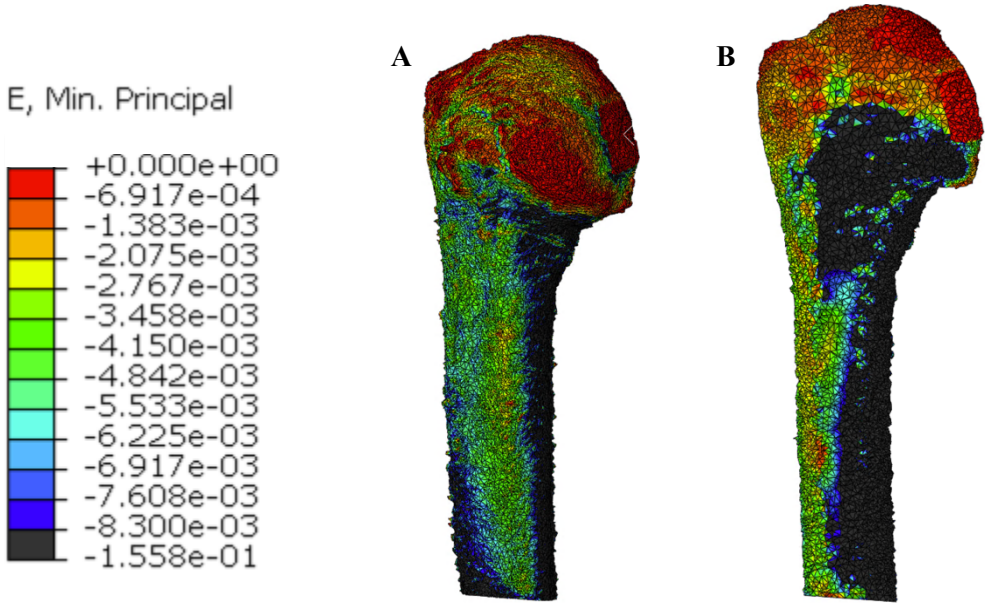




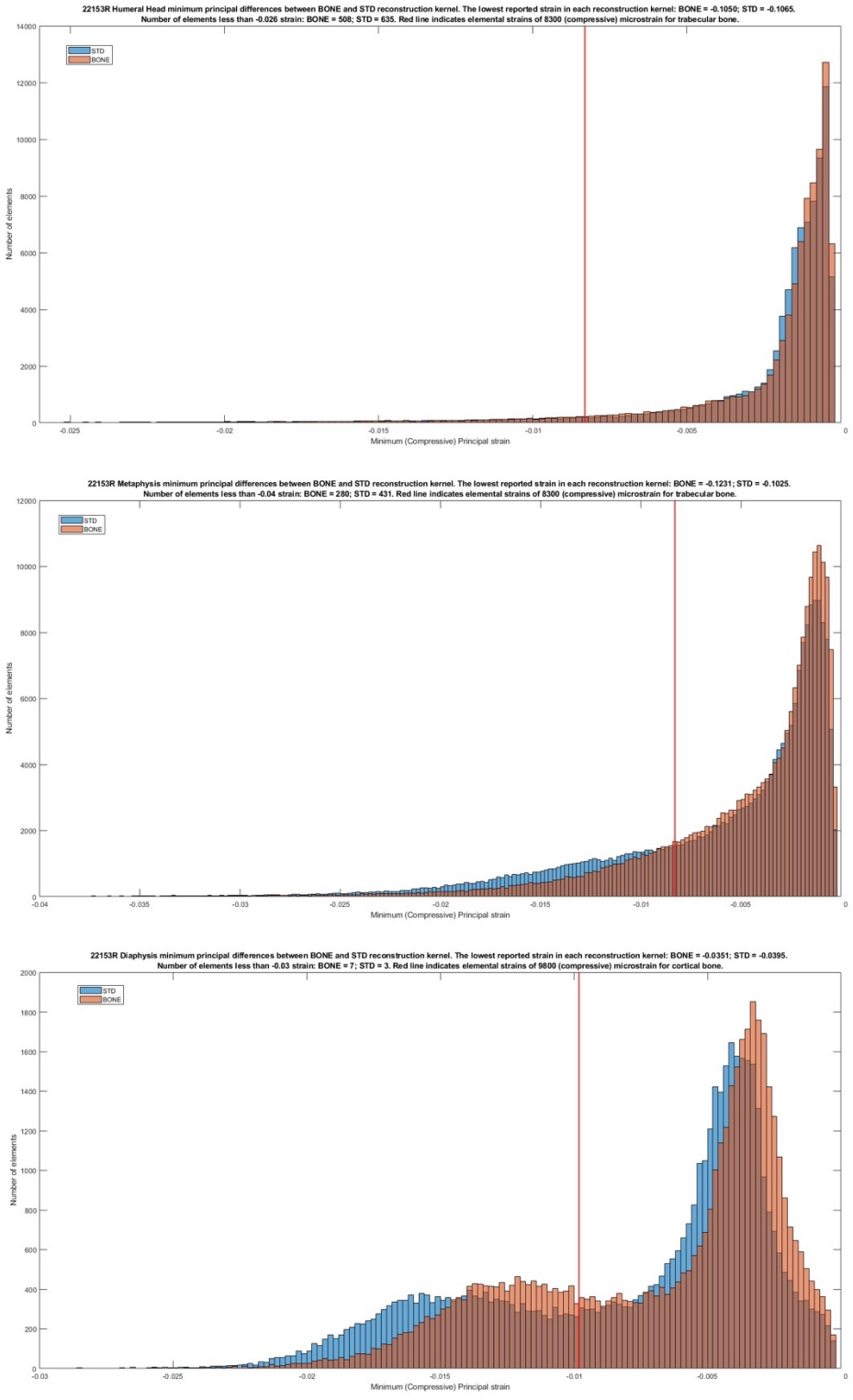
Maximum (tensile) principal strain for cadaver 22153R in DEQCT in the three regions.



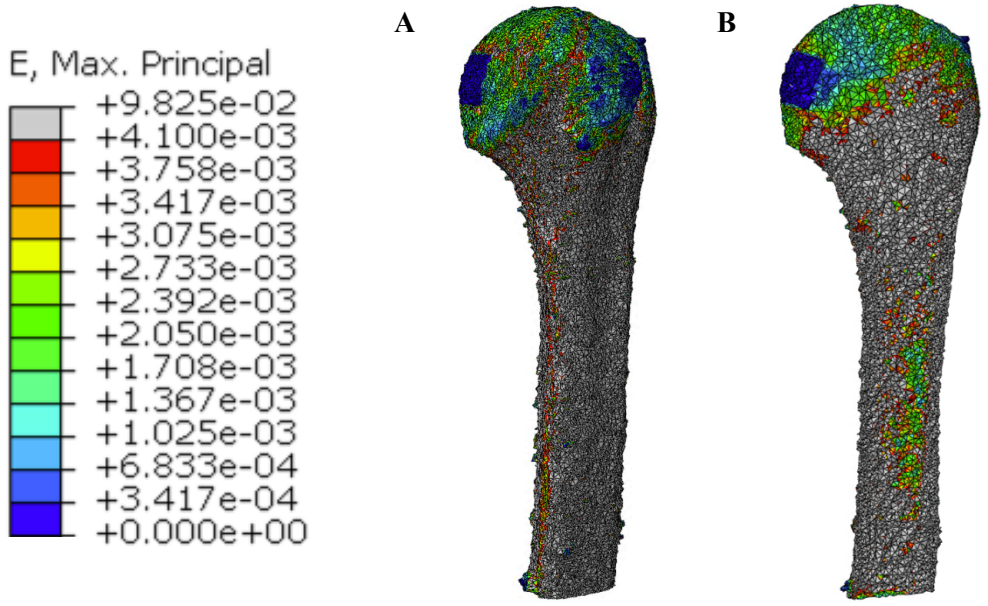
22153R DEQCT minimum (compressive) principal strain with a microstrain set at 8300 for BONE reconstruction kernel (A - Surface of the humerus; B - Sliced humerus)



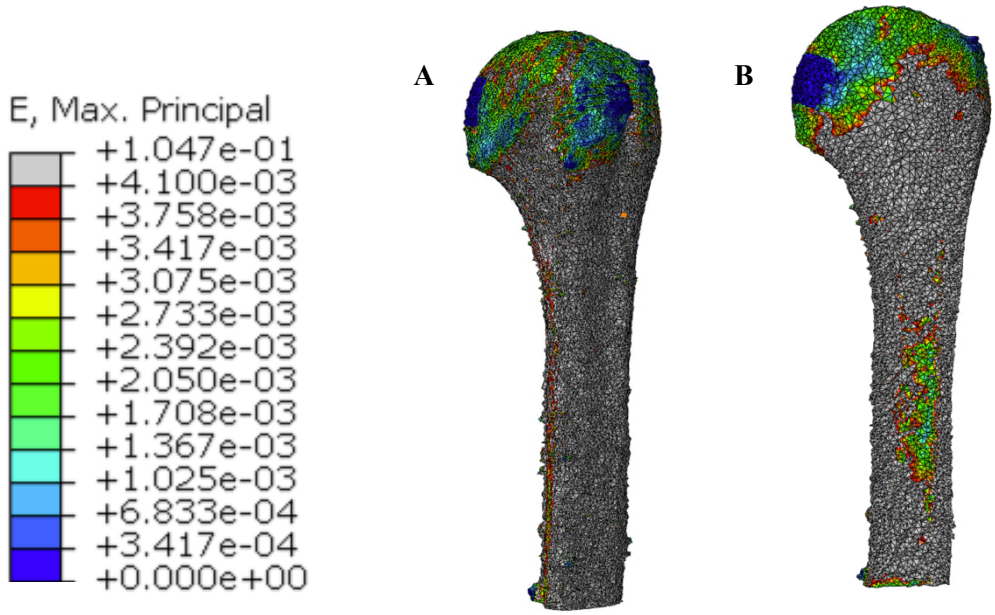
22153R DEQCT minimum (compressive) principal strain with a microstrain set at 8300 for STD reconstruction kernel (A - Surface of the humerus; B - Sliced humerus)



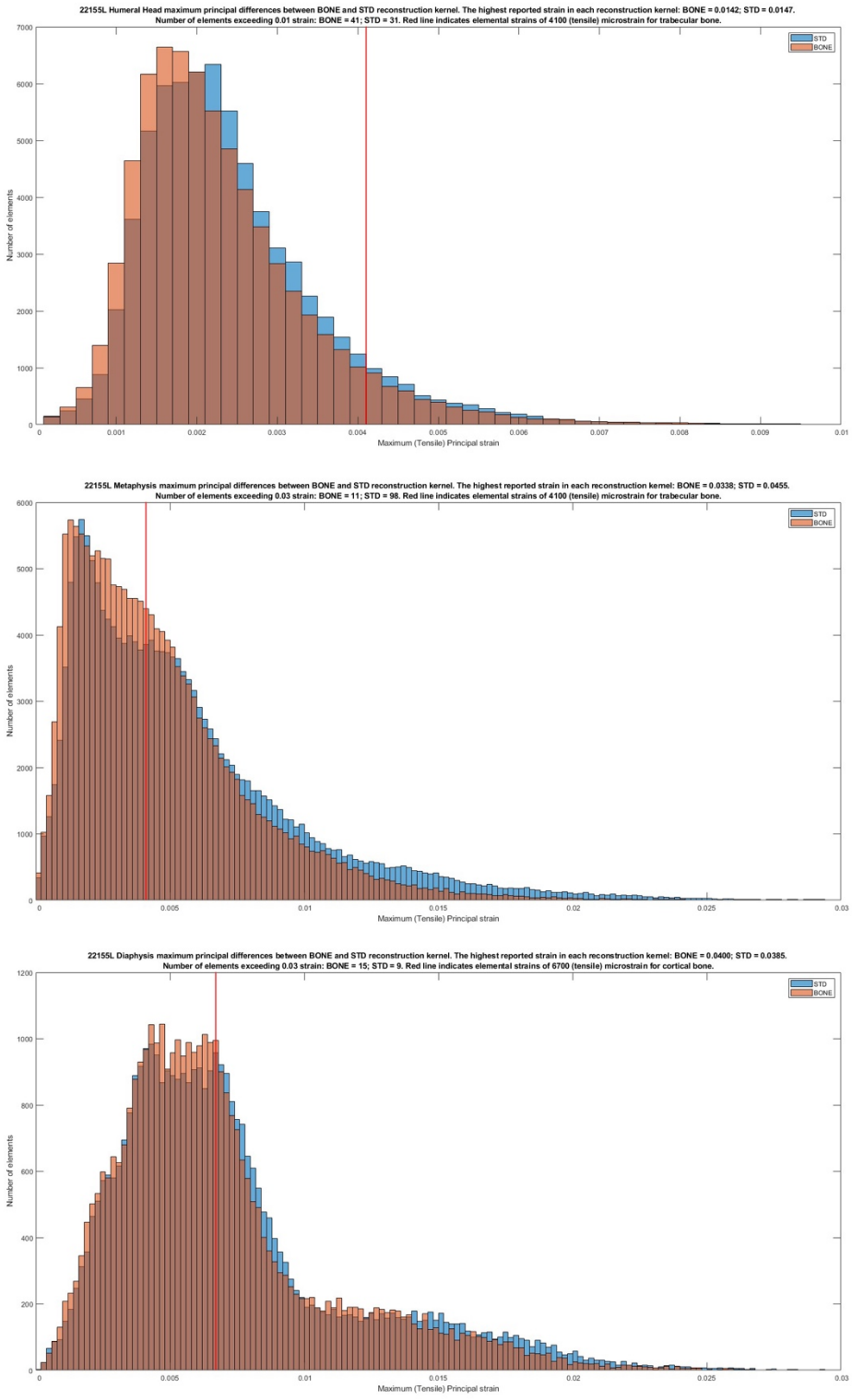
Minimum (compressive) principal strain for cadaver 22153R in DEQCT in the three regions.



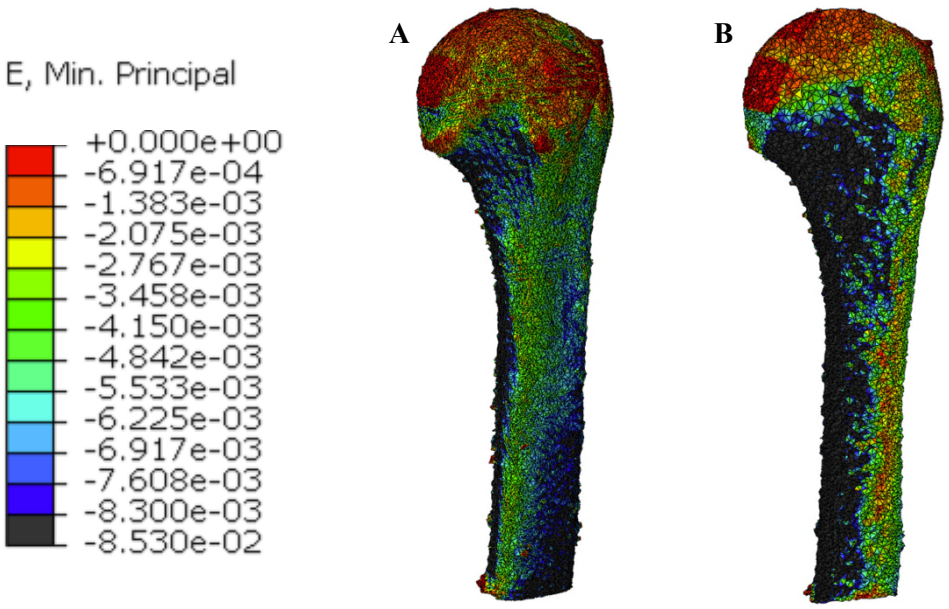
22155L DEQCT maximum (tensile) principal strain with a microstrain set at 4100 for BONE reconstruction kernel (A - Surface of the humerus; B - Sliced humerus)



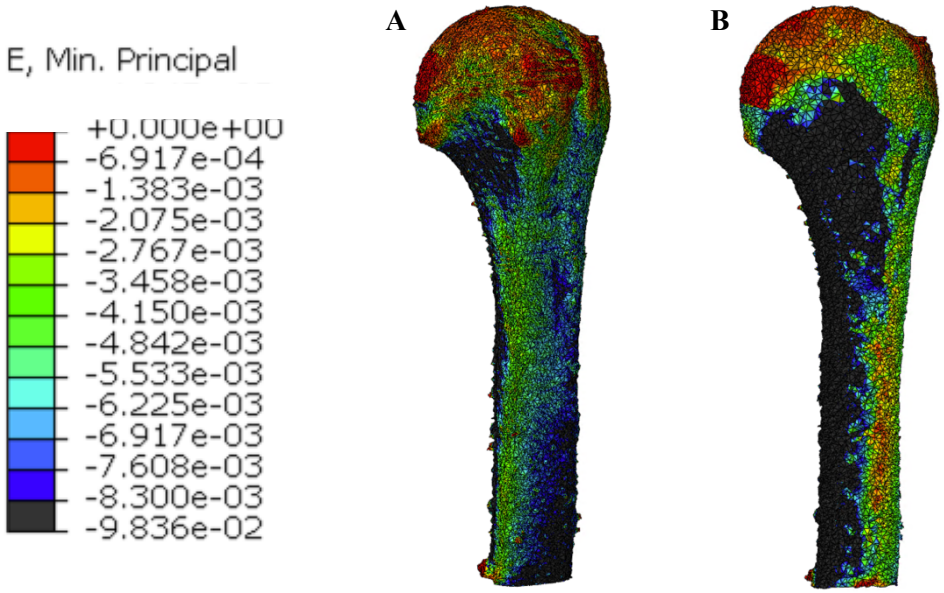
22155L DEQCT maximum (tensile) principal strain with a microstrain set at 4100 for STD reconstruction kernel (A - Surface of the humerus; B - Sliced humerus)



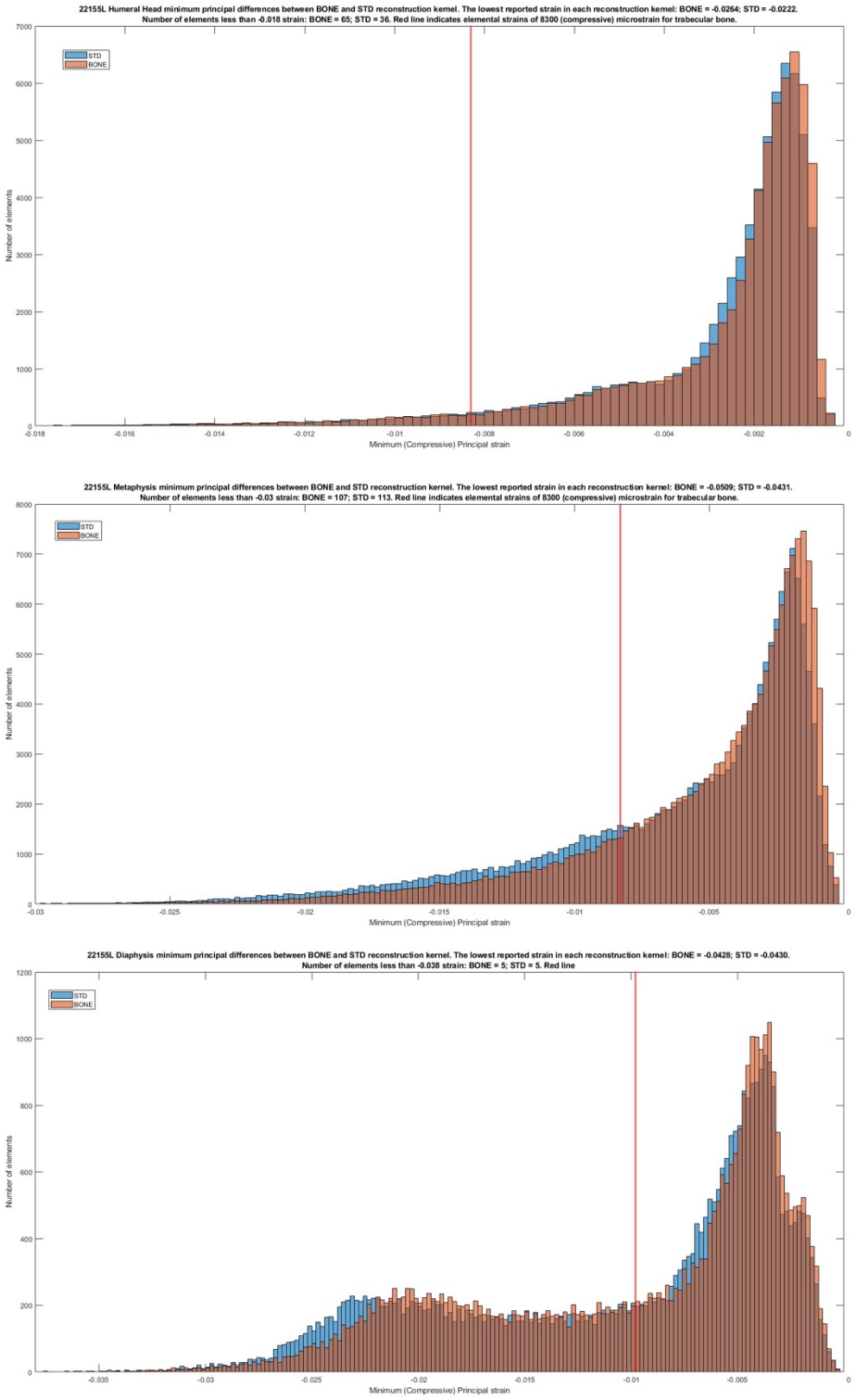
Maximum (tensile) principal strain for cadaver 22155L in DEQCT in the three regions.



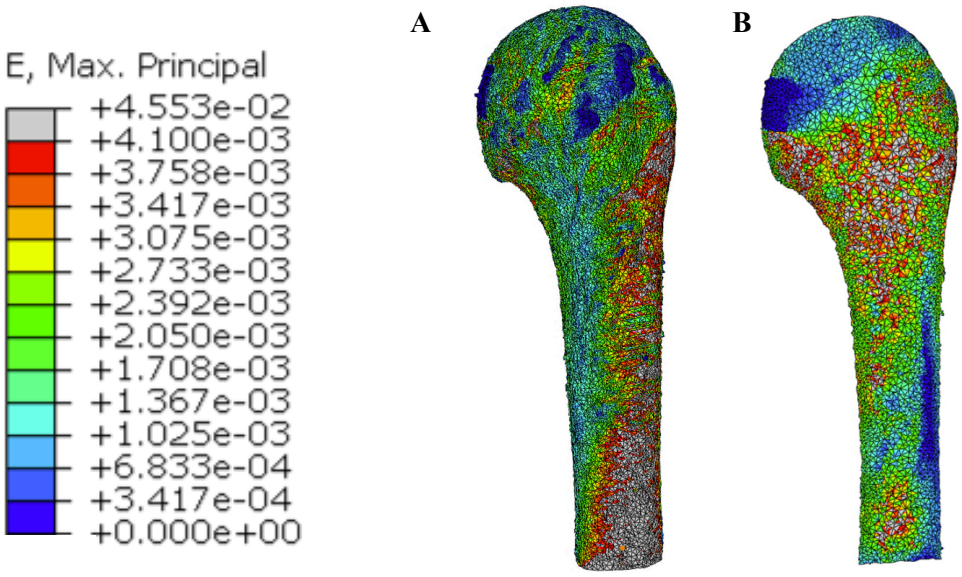
22155L DEQCT minimum (compressive) principal strain with a microstrain set at 8300 for BONE reconstruction kernel (A - Surface of the humerus; B - Sliced humerus)



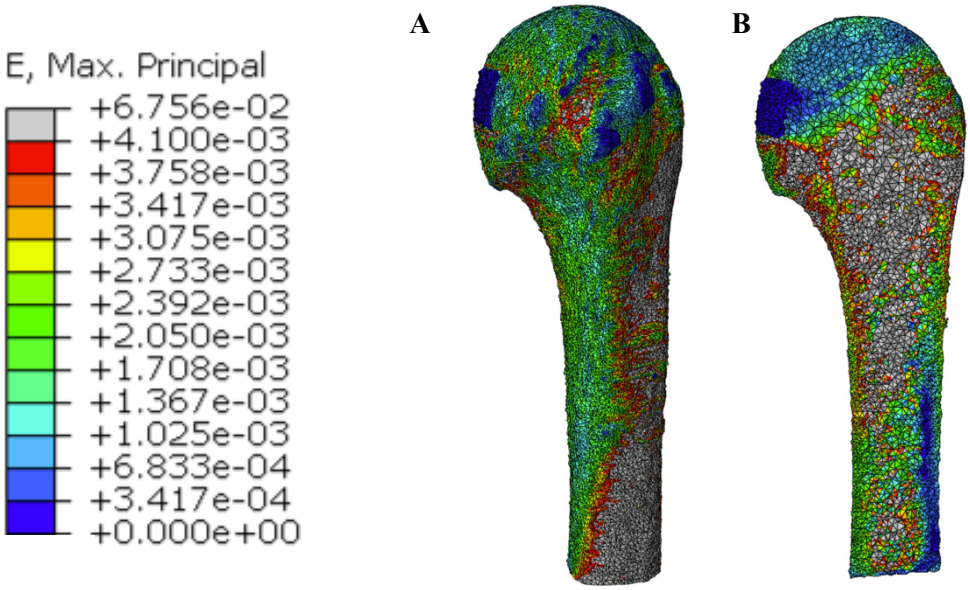
22155L DEQCT minimum (compressive) principal strain with a microstrain set at 8300 for STD reconstruction kernel (A - Surface of the humerus; B - Sliced humerus)



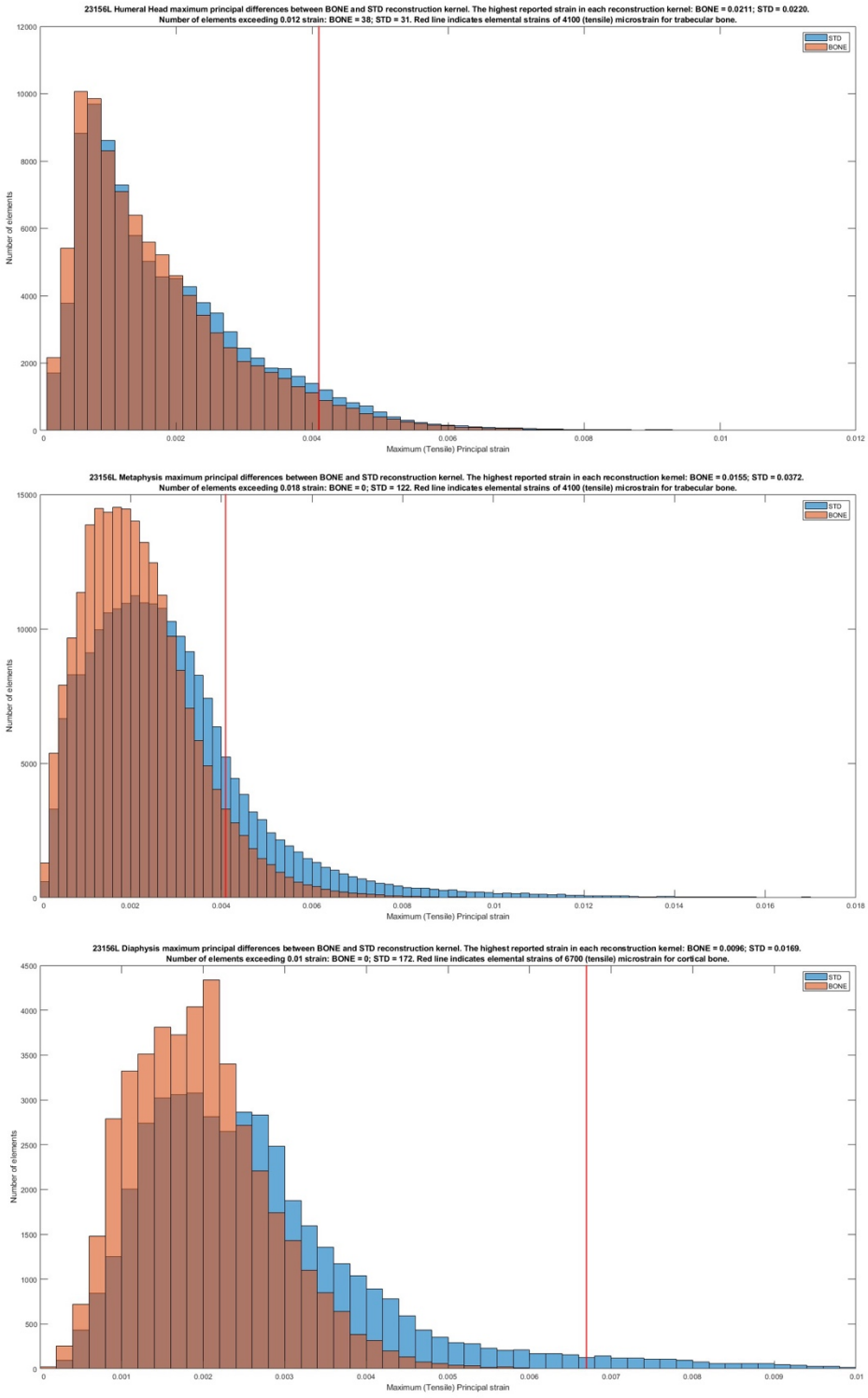
Minimum (compressive) principal strain for cadaver 22155L in DEQCT in the three regions.



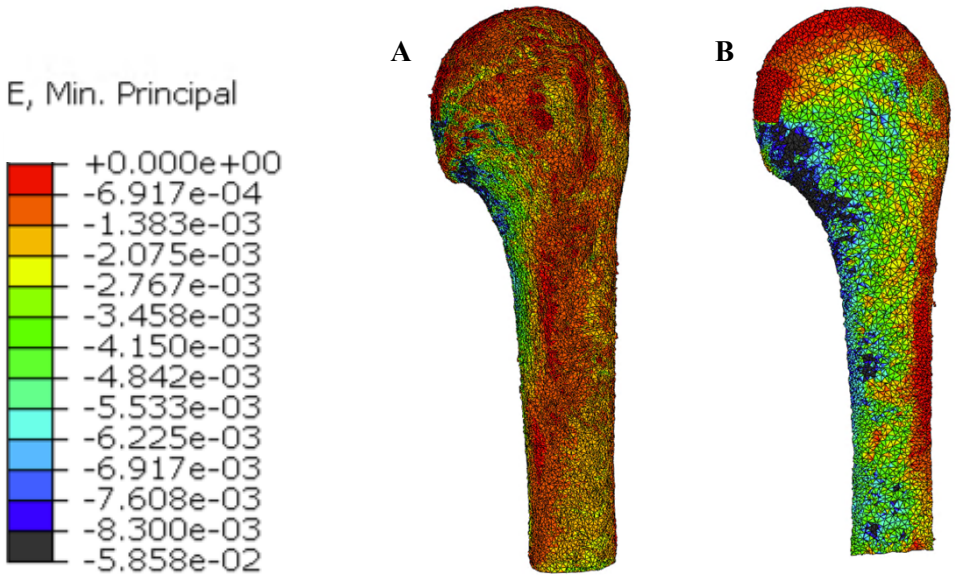
23156L DEQCT maximum (tensile) principal strain with a microstrain set at 4100 for BONE reconstruction kernel (A - Surface of the humerus; B - Sliced humerus)



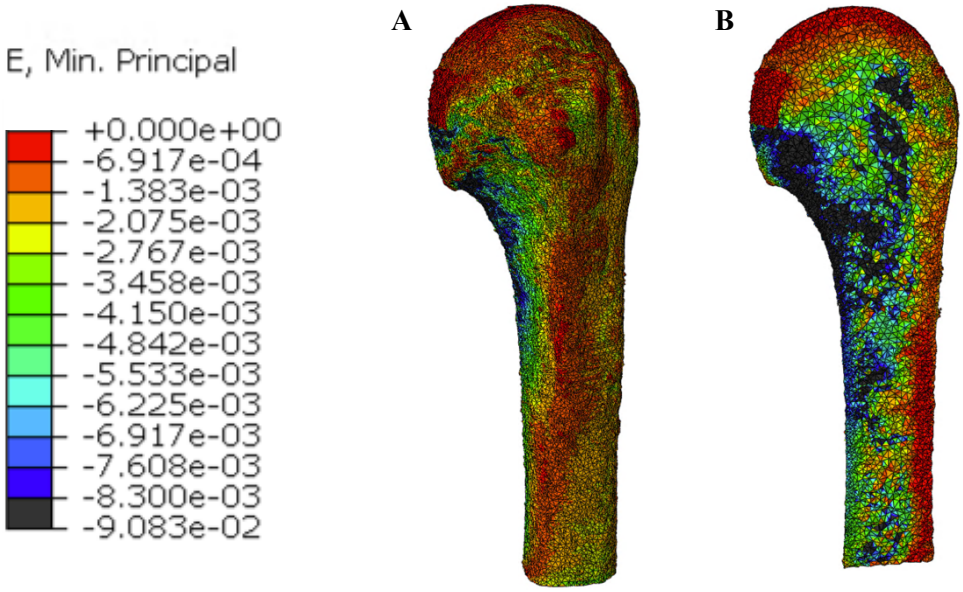
23156L DEQCT maximum (tensile) principal strain with a microstrain set at 4100 for STD reconstruction kernel (A - Surface of the humerus; B - Sliced humerus)



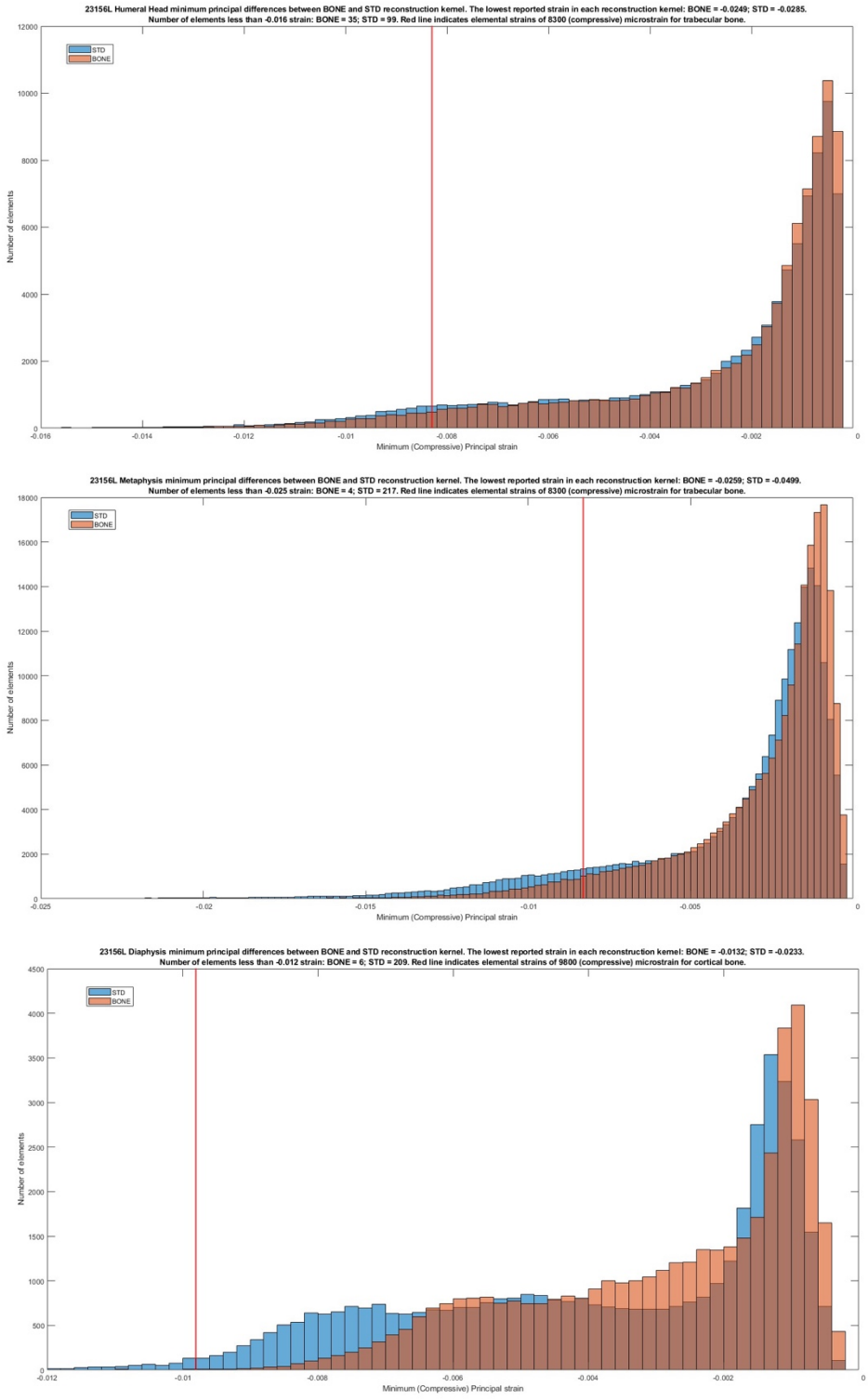
Maximum (tensile) principal strain for cadaver 23156L in DEQCT in the three regions.



23156L DEQCT minimum (compressive) principal strain with a microstrain set at 8300 for BONE reconstruction kernel (A - Surface of the humerus; B - Sliced humerus)



23156L DEQCT minimum (compressive) principal strain with a microstrain set at 8300 for STD reconstruction kernel (A - Surface of the humerus; B - Sliced humerus)

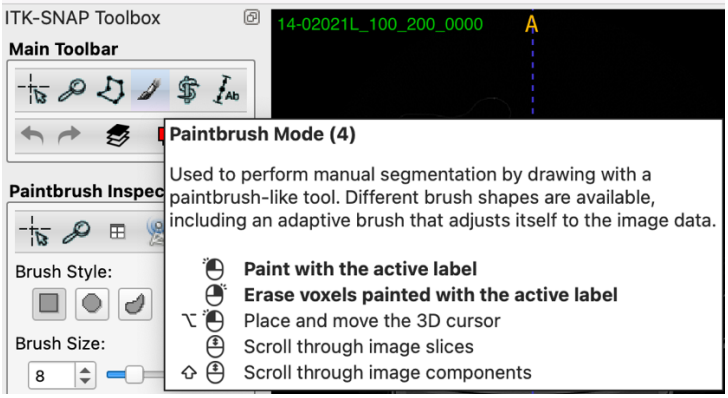


Minimum (compressive) principal strain for cadaver 23156L in DEQCT in the three regions.

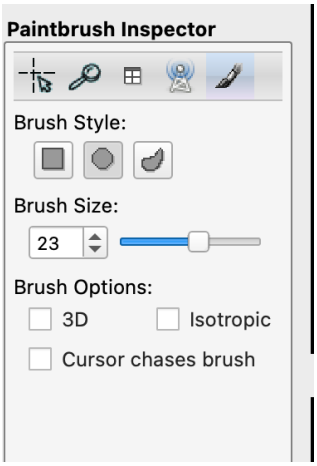
Appendix C

Creating the rod mask/segmentation through phantom calibration using ITK-SNAP

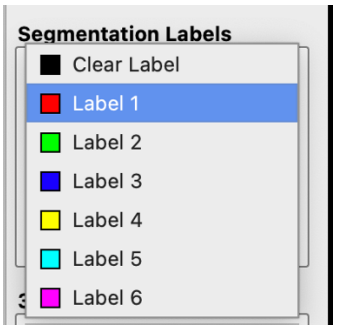
- Open DICOM image in ITK-SNAP
- Select **Paintbrush Mode** from the **Main Toolbar**



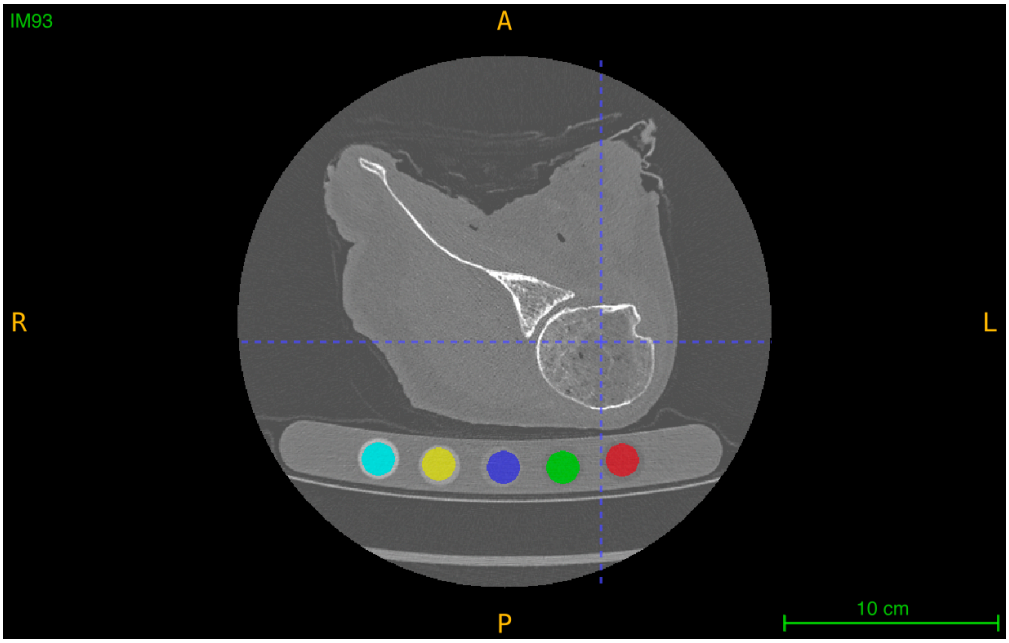
- Under **Paintbrush Inspector**, select the circle brush style and set **Brush Size** to **32**.



- Choose **Segmentation Labels** depending on the intensity of the rod.
  - Lightest rod = **Label 5**
  - Darkest rod = **Label 1**

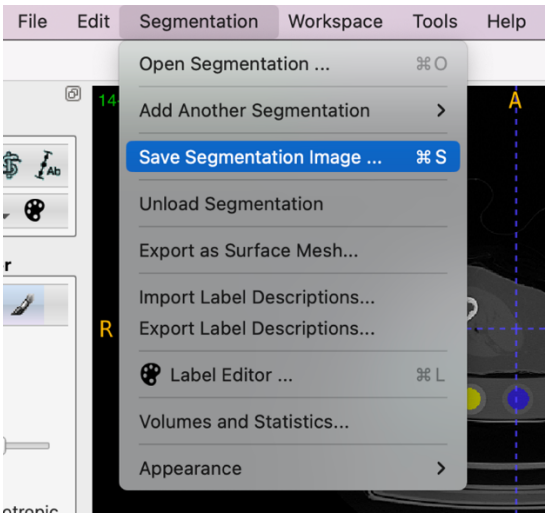


- Click on each rod to create a mask/segmentation label. Ensure the masks are not too close to the edges and cover at least ¾ of the diameter of the rod (see example below).

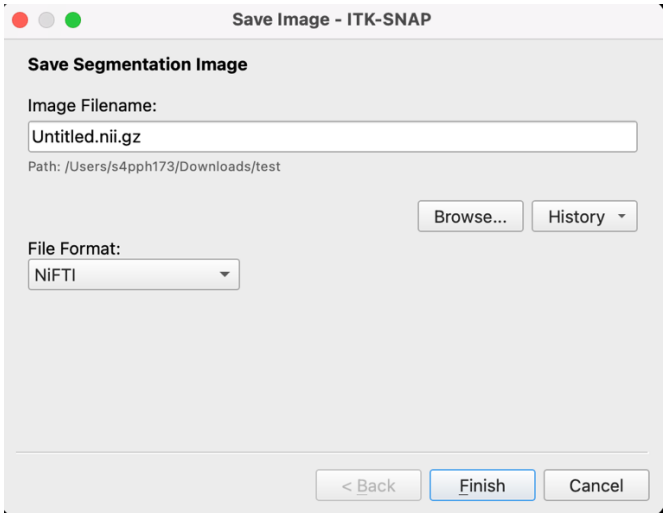


- Collect the mask over the entire length of the phantom to ensure that the variations in the image intensity across the imaged region is accounted for.
    - Scroll to each end of the image sliced that includes the entire rod and isn't 'blurred'.
    - Create the mask for rods 1-5 every 30th axial slice.

- Select **Save Segmentation Image** under **Segmentation** in the Menu Bar



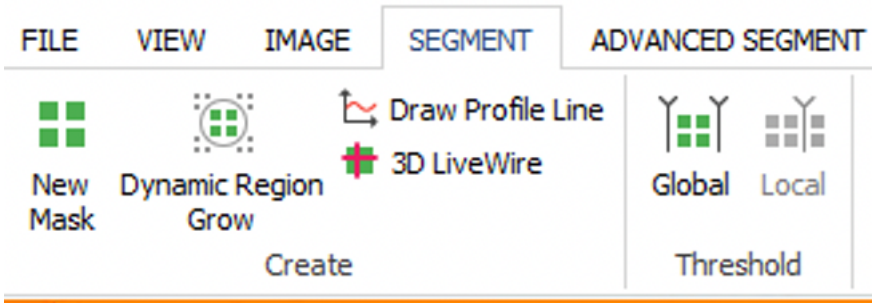
- **Save Image** in **NiFTI format (.nii)** in the correct file folder.



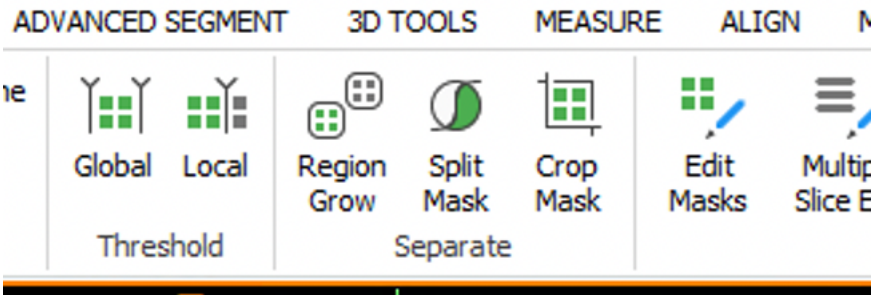
Appendix D

Creating Masks using Mimics and 3-Matic

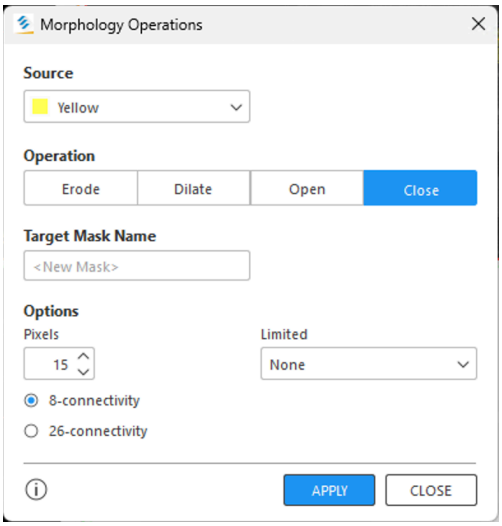
- Open DICOM image on Mimics by making a **New Project.**
- Select **New Mask** from the **Segment** toolbar.



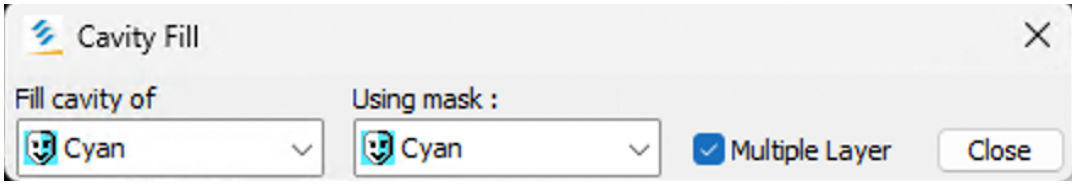
- Set the minimum threshold to 225 and press **OK.**
- Select **Region Grow** from the **Segment** toolbar.

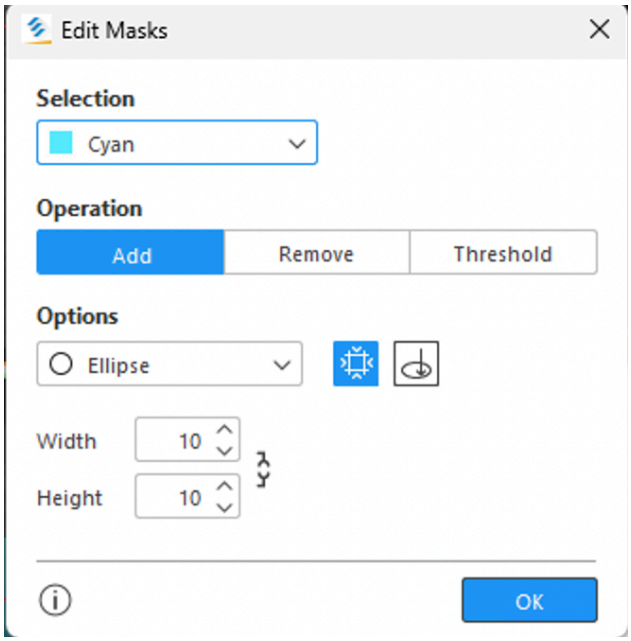


- Select the Humerus to highlight it as the unfilled humerus.
- Select **Morphology Operations** from the **Segment** toolbar
- In the **Operations** Section, select **Close** and set the pixels in the **Options** to 15.

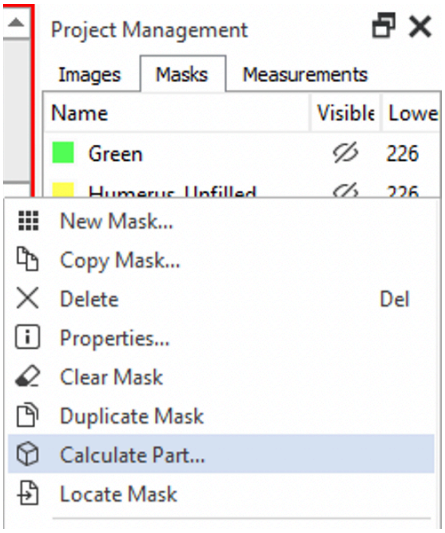


- Select **Cavity Fill** and brush over the humerus to fill it.
- If humerus cannot be filled, select **Edit Masks** and add over areas with openings to close the humerus, adjusting the brush size appropriately.

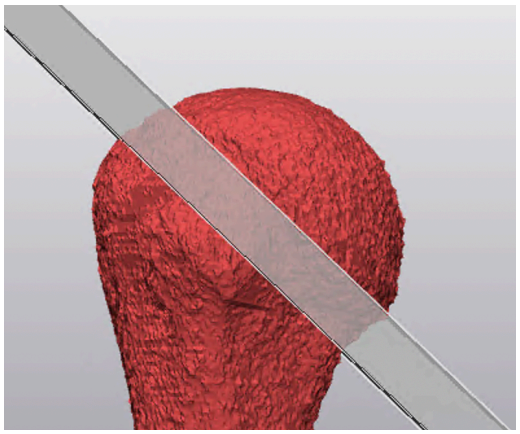


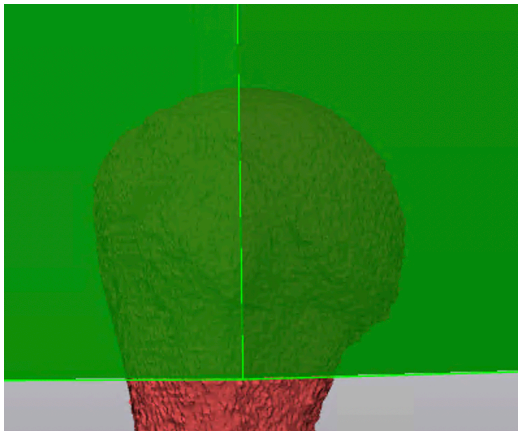


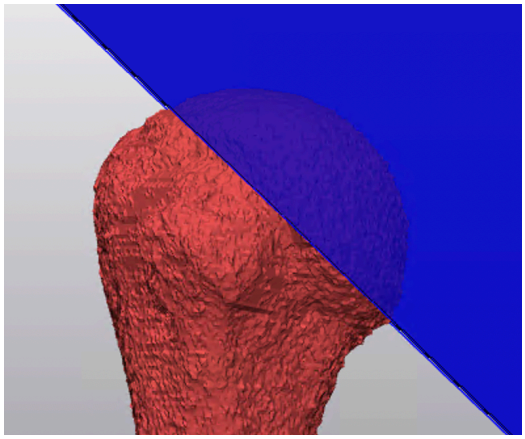
- Keep filling the humerus using the **Cavity Fill**, checking each pixel until entire humerus is filled.
- Once humerus is filled, right click the filled humerus in the project manager and click on **Calculate Part**.



- Open **3-Matic** and past the calculated part humerus from **Mimics**
- A customized 10 mm and 75 mm box was added.
    - 10 mm placed in the ridge of the proximal humerus head.
    - 75 mm placed in the neck of the humerus head.



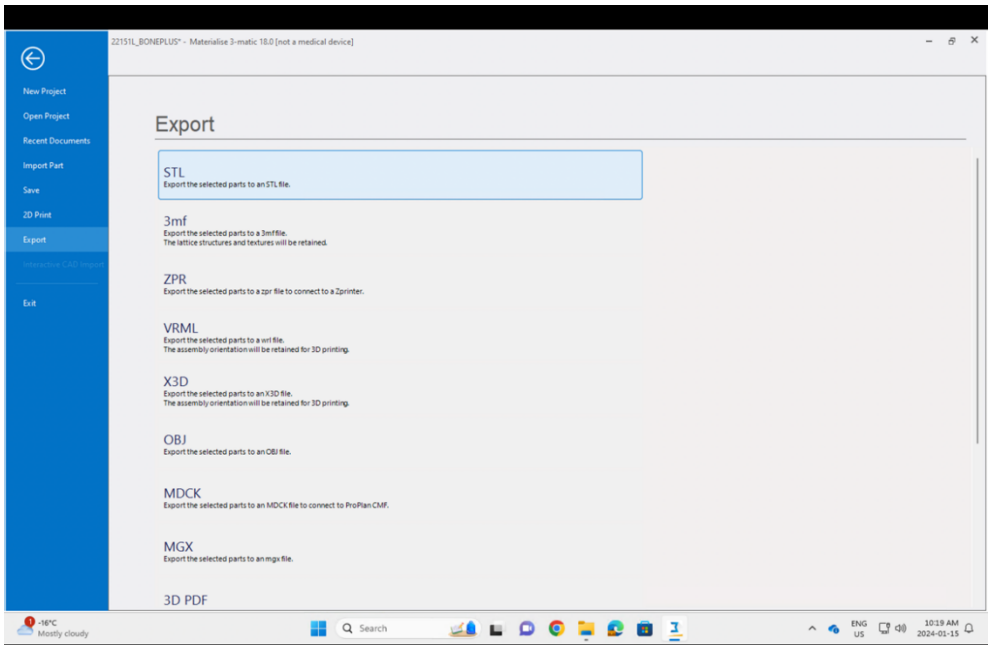




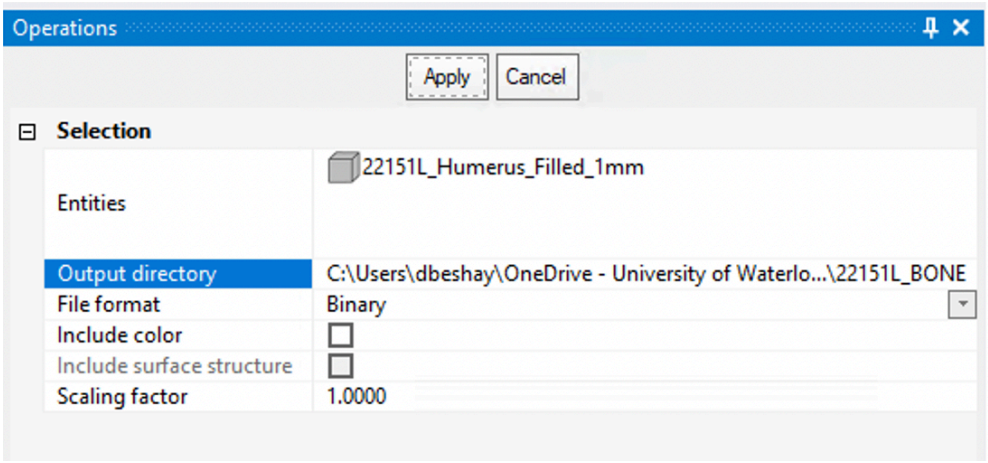
Appendix E

Creating Finite Element Models with Material in Abaqus CAE.

1. Save the 3D model as an STL file.



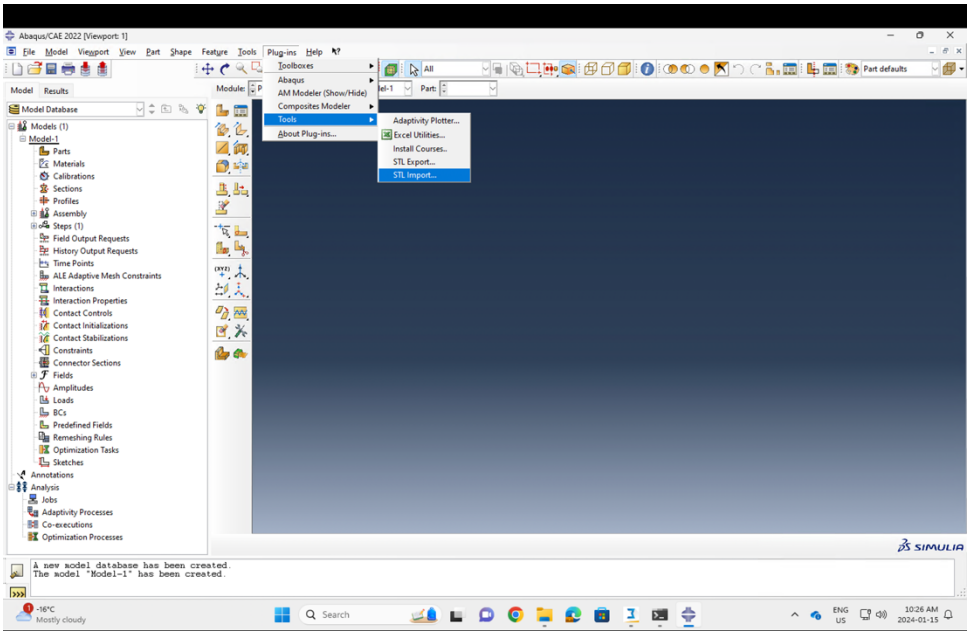
2. Change Output directory to an appropriate file and name then click **Apply**.



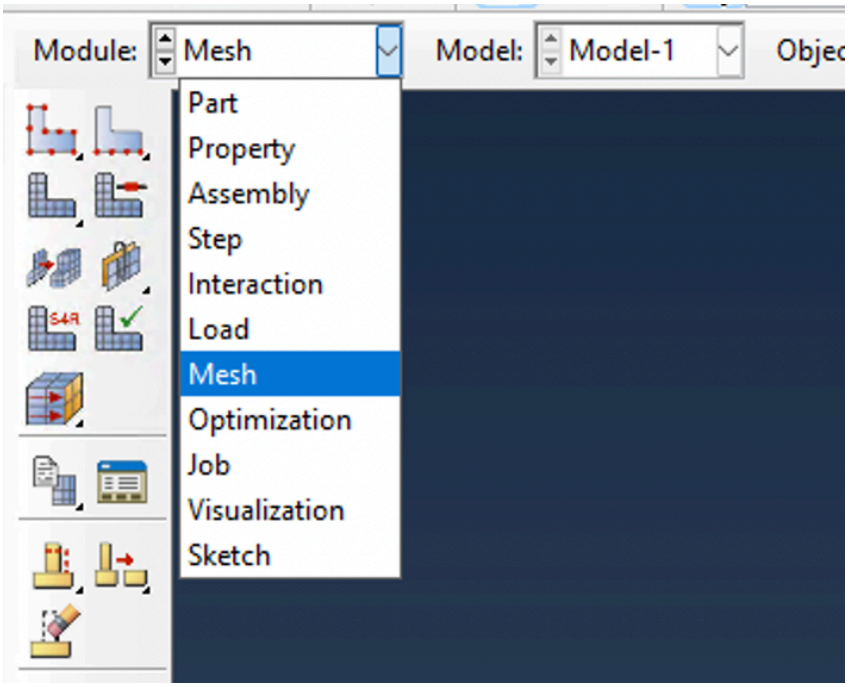
3. Open Abaqus CAE and click on **With Standard/Explicit Model**.



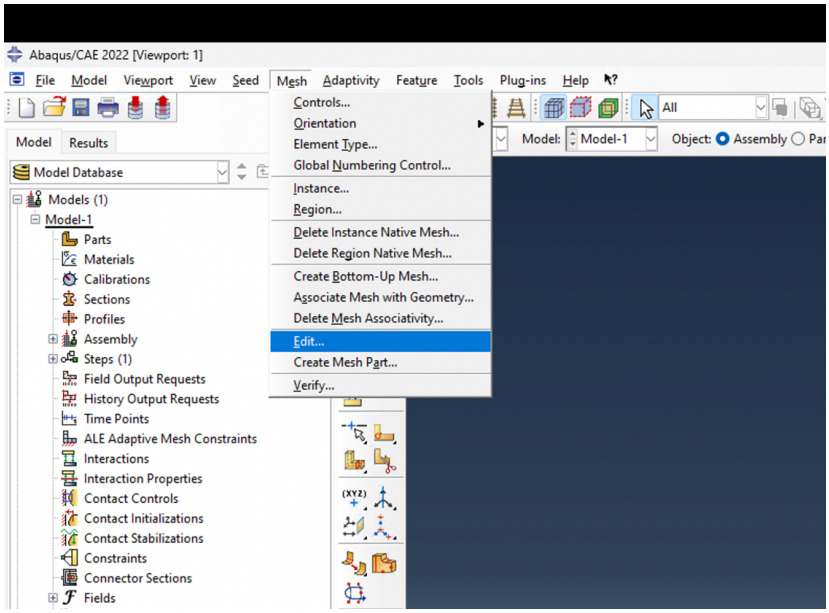
4. Load saved STL file from 3-MATIC by going on **Plug-ins** then **Tools** then **STL import.**



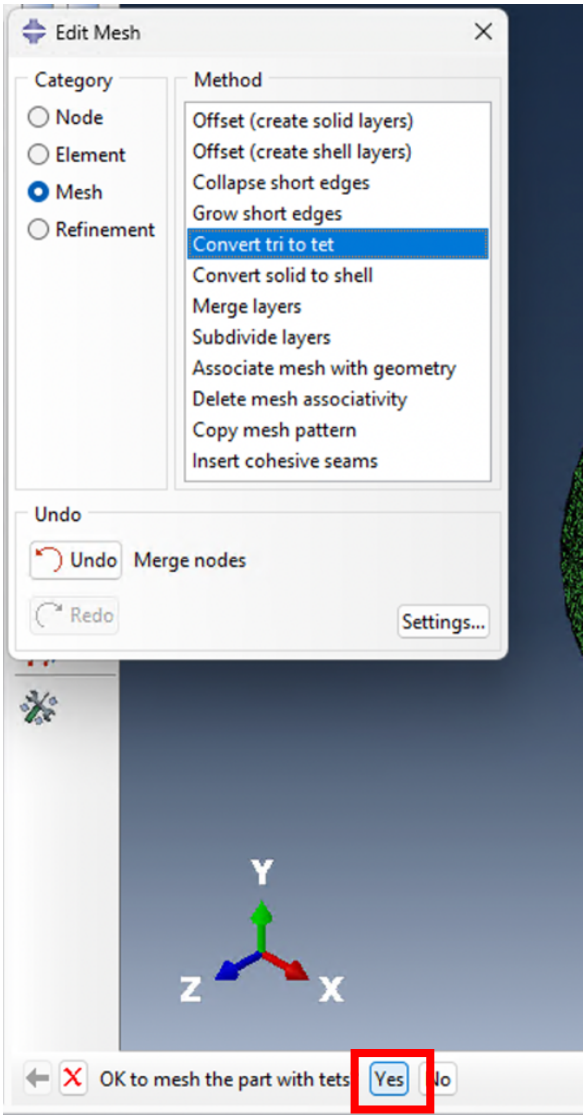
5. Convert this to a volume mesh so that it has insides.
    - Change **Module** from **Part** to **Mesh** (changes toolbar on top).



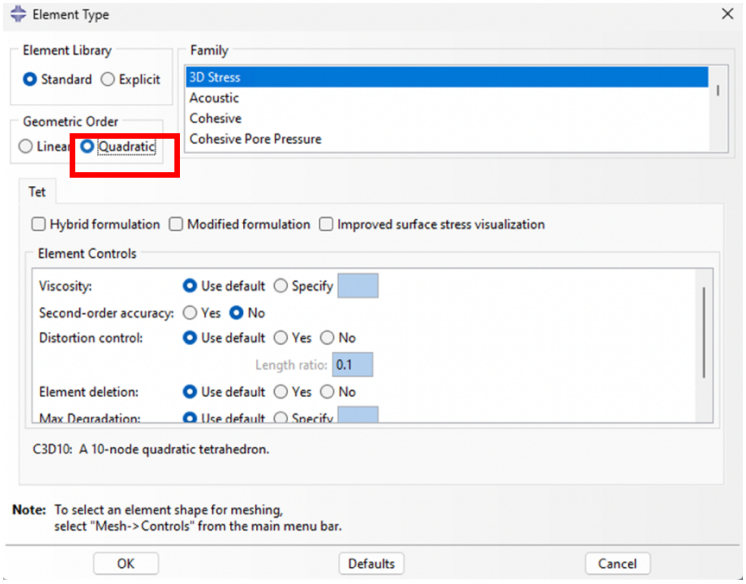
6. Go on **Mesh** on the toolbar and hit **Edit**.



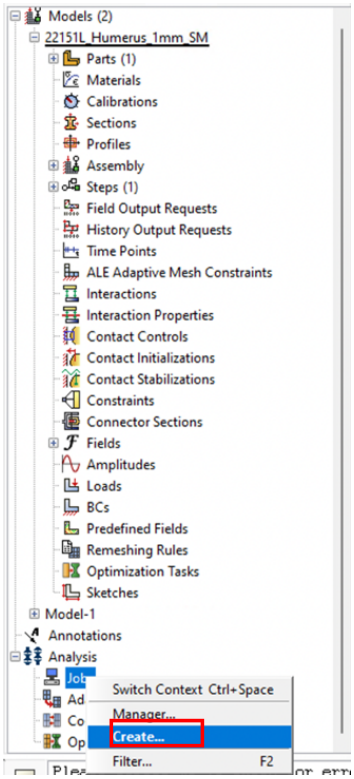
7. Once on Edit Mesh page, click on **Mesh** then select **Convert tri to tet** and **Yes** on the bottom.
    - This changes all the triangles into a tetrahedral, making them linear having 4 nodes (filling them in).



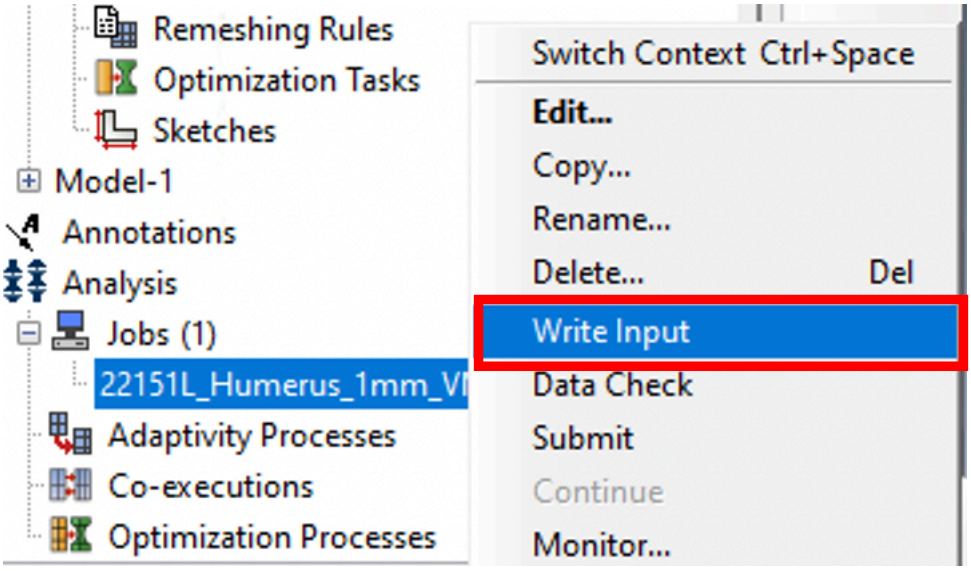
8. Converting from linear to quadratic.
    - Click **Mesh** then **Element Type** and then highlight the whole bone**.**
    - Hit **Done** on the bottom window panel.
    - Change Geometric order from **Linear** to **Quadratic.**



9. Right click on **Job** in the Analysis Tree on the left panel and hit **Create.**
    - Change file name to appropriate name.
    - This model now is a volume mesh.



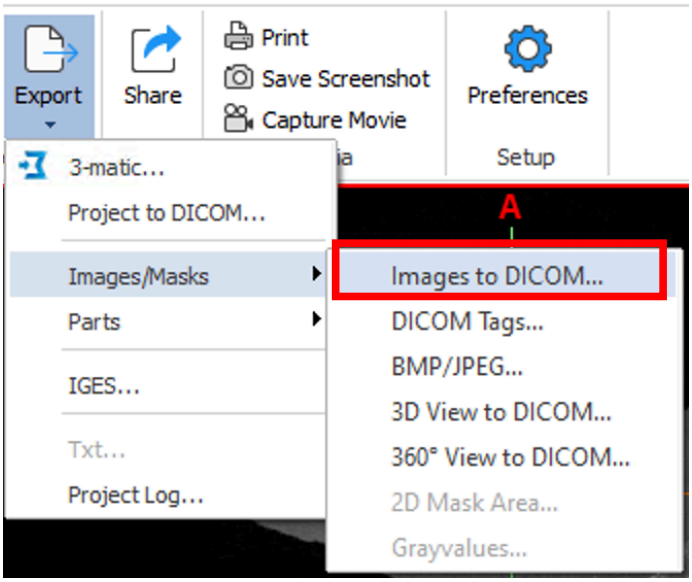
10. Extend the Jobs tree and right click the new file and select **Write Input.**
    - This will save a new file as .inp in your temp directory.



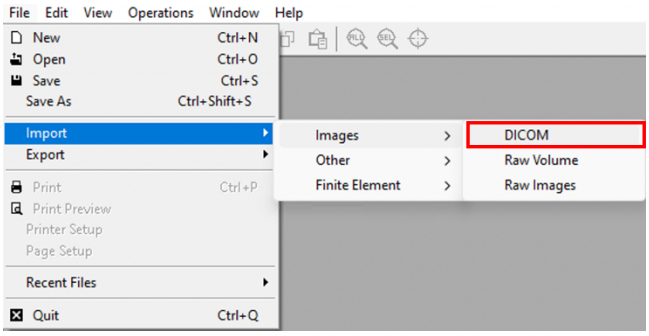
Appendix F

Adding Materials to the 3D model

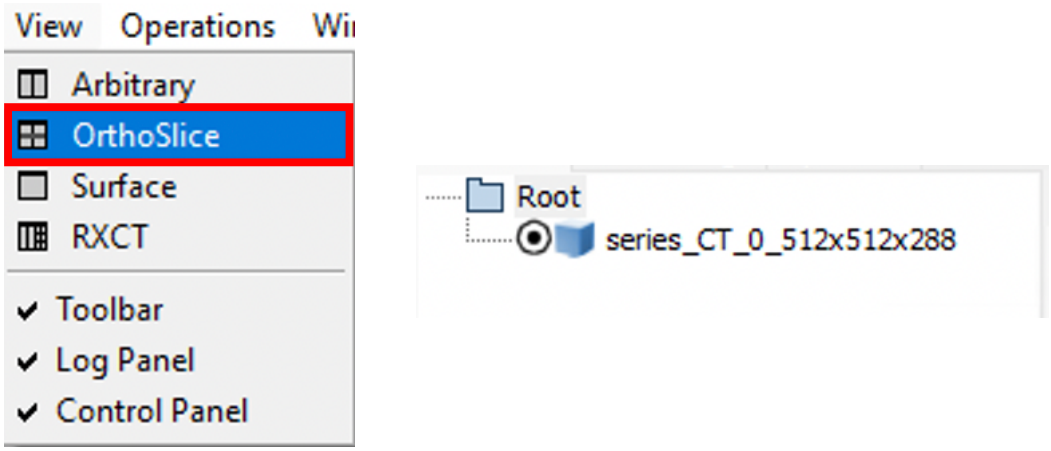
1. Open appropriate DICOM images in MIMICS.
    - Save Images to DICOM by clicking **Export**, **Images/Masks** and then selecting **Images to DICOM**.
    - Save to an appropriate Output Directory.
    - This step is necessary because however they were saved from the CT scanner, BoneMat cannot read. However MIMICS outputs the Meta data, all the information is saved can be read by BoneMat.



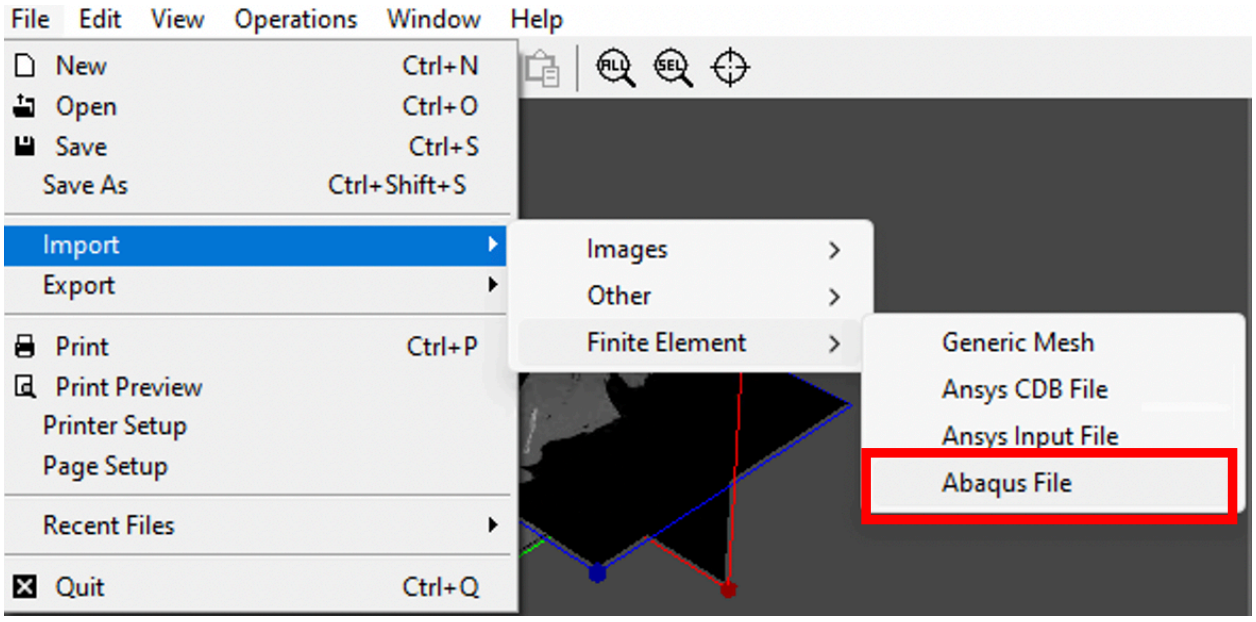
2. Import the DICOM images in BoneMat by clicking **File**, **Import**, **Images**, **DICOM** and opening the appropriate DICOM images saved from MIMICS.



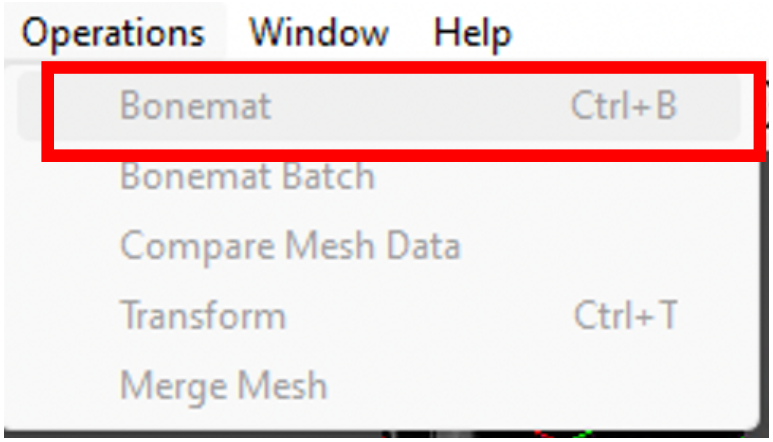
3. Click on **Crop**, **Build** and **Finish** as nothing needs to be changed.
4. Click **View** and select **OrthoSlice** and then click on the tree in the right panel.
    - This is the link between quantitative data and the FE model.



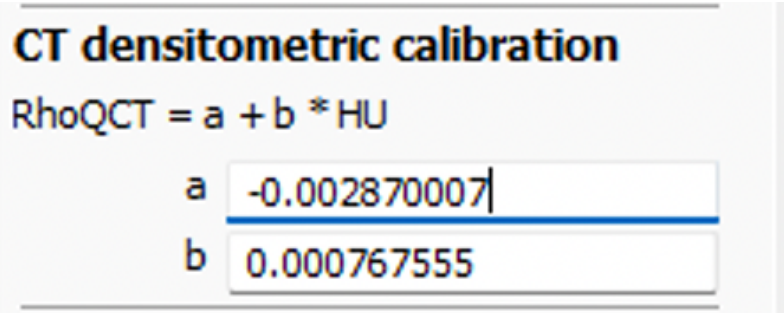
5. Import Abaqus File now as seen below.
6. Upload the Volume Mesh STL file from D:/temp.



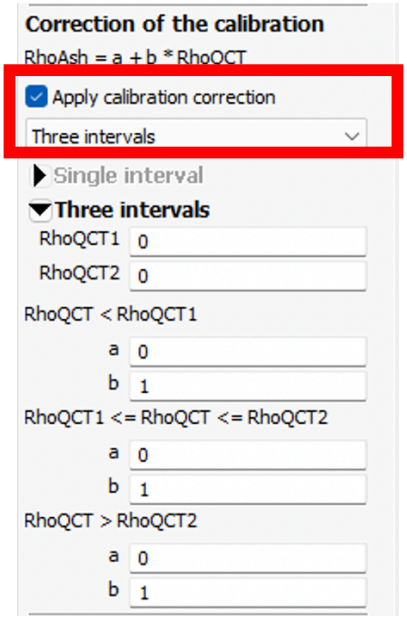
7. Highlight the Volume Mesh file from the Data Tree window panel on the right and then click **Operations** and select **Bonemat**



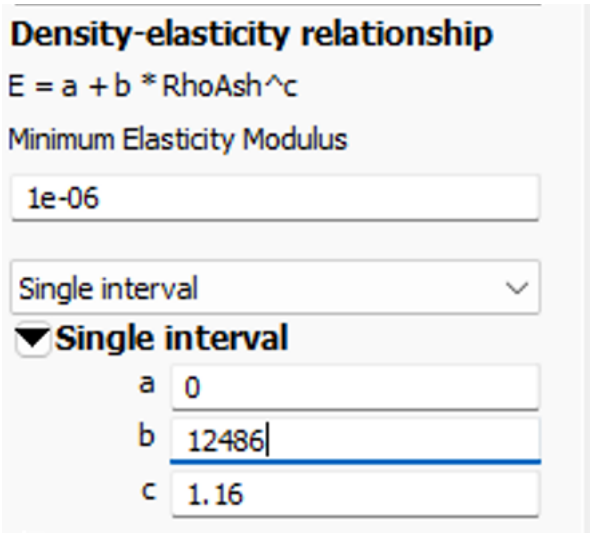
8. In the CT densitometric calibration, add the slope and intercept that have been calculated prior.
    - Make sure to divide both the **slope (b)** and **intercept (a)** by **1000** for conversion in BoneMat (example below).
    - RhoQCT is your volumetric bone mineral density.



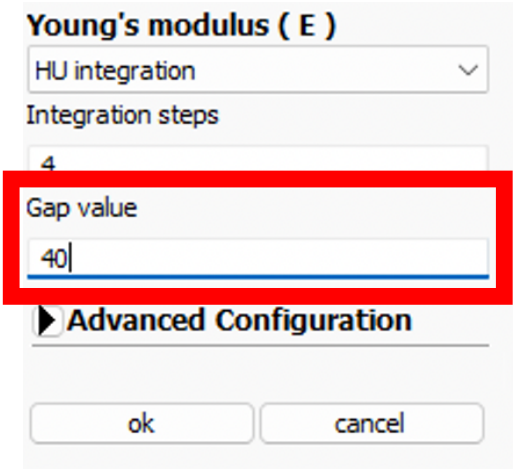
9. In **Correction of the calibration**, click on **Apply calibration correction** and change it to **Three intervals**.
    - Add appropriate data based on calculations and literature.



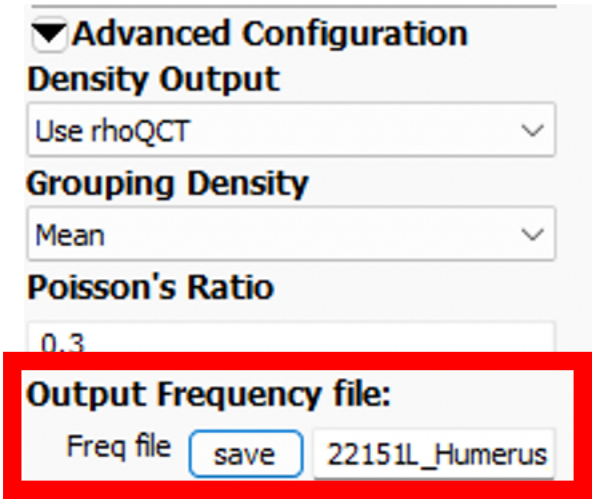
10. In **Density-elasticity relationship**, change "b" and "c" values appropriately (example below).



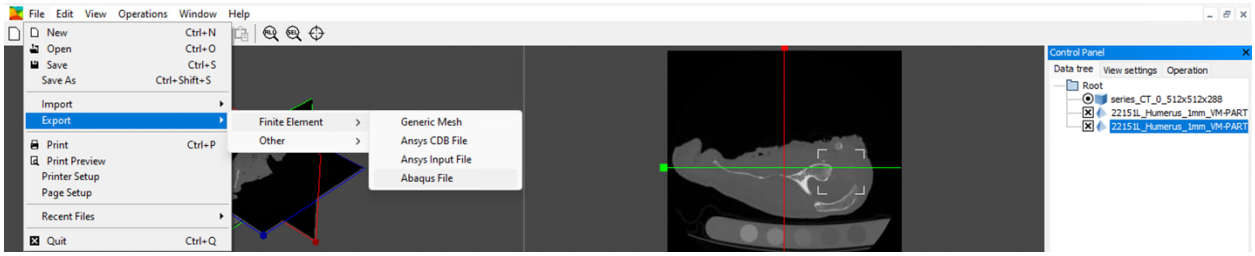
11. In **Young's modulus**, change **Gap Value** to "40"
    - Anything between 40 megapascals in modulus will be assigned the same material.



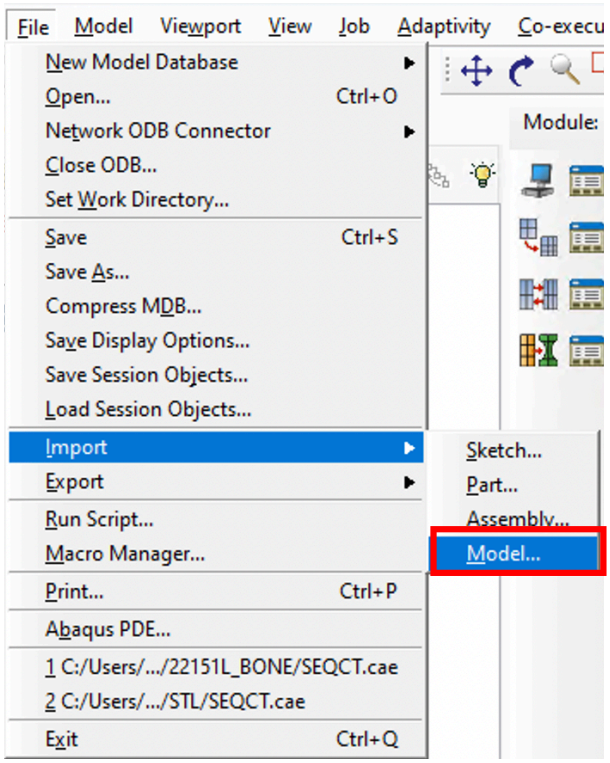
12. Click on **Advanced Configuration** and save it in an appropriate directory.



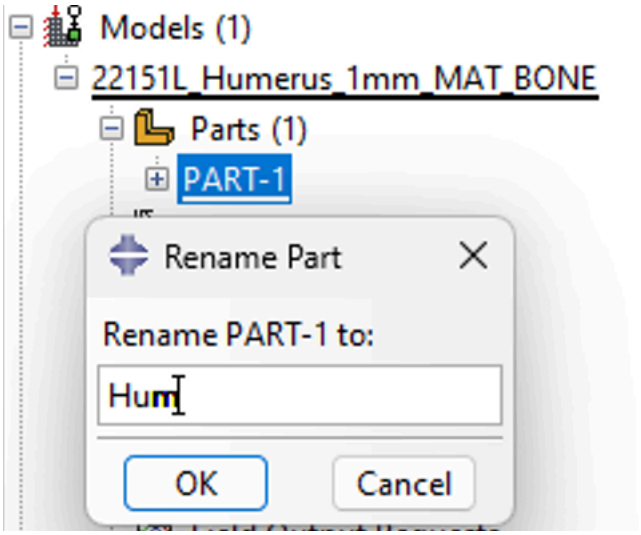
11. A new tree will appear.
12. Highlight the new tree and export as an **Abaqus File**.



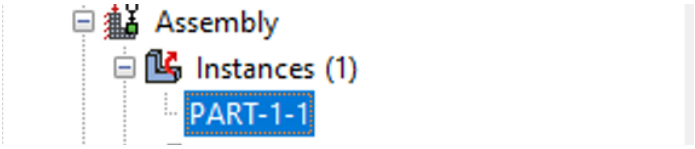
13. Save where SM file is and change file name.
14. Reopen Abaqus CAE and save the file as "SEQCT" with other files.
15. Delete SM tree (and any other tree)
16. Import **BONE_MAT file** by finding the right folder and changing **File Filter** to .inp

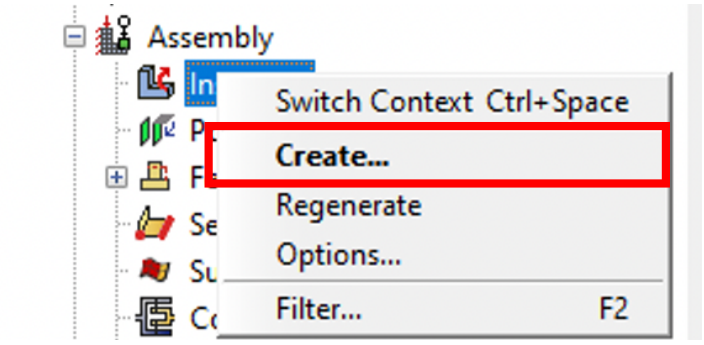


17. Under the "**Parts (1)**" tree, rename "**PART-1**" into **Hum**
    - The reason for this is now when we bring a new model, and rename it Hum as well, everything else will stay the same since the mesh doesn't change.

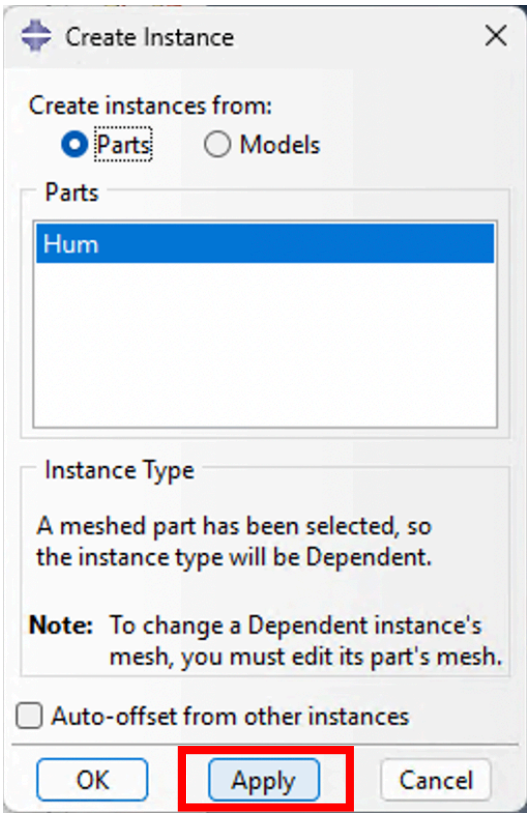


18. Delete the Part-1-1 **Instance** and create a new one.

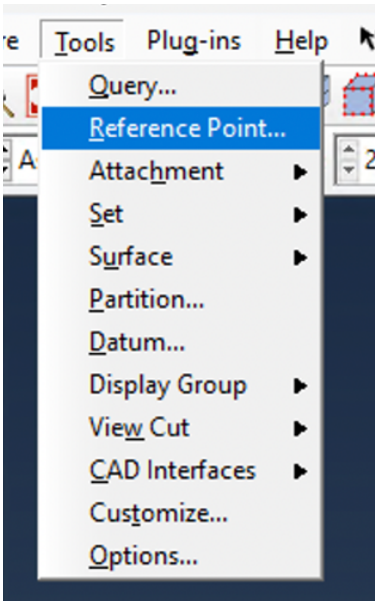




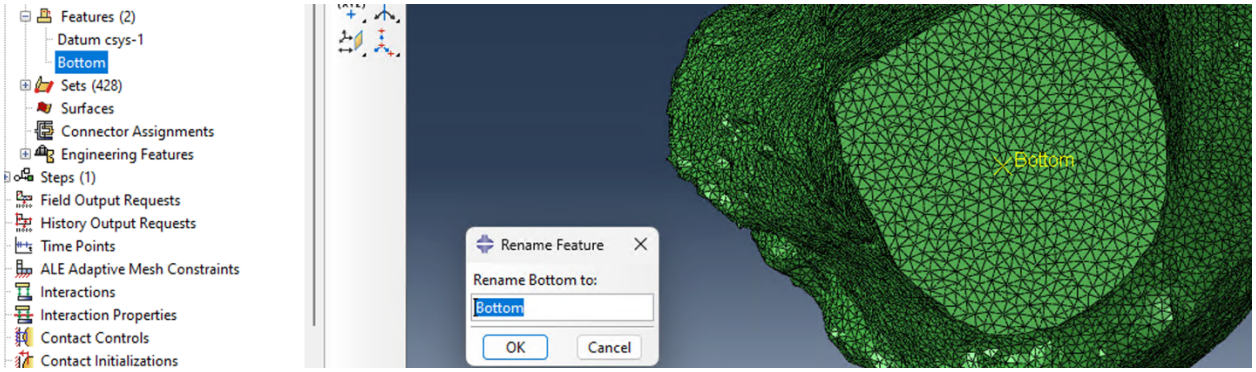
19. Select the **Hum** Instance and click **Apply**, then **Cancel**.



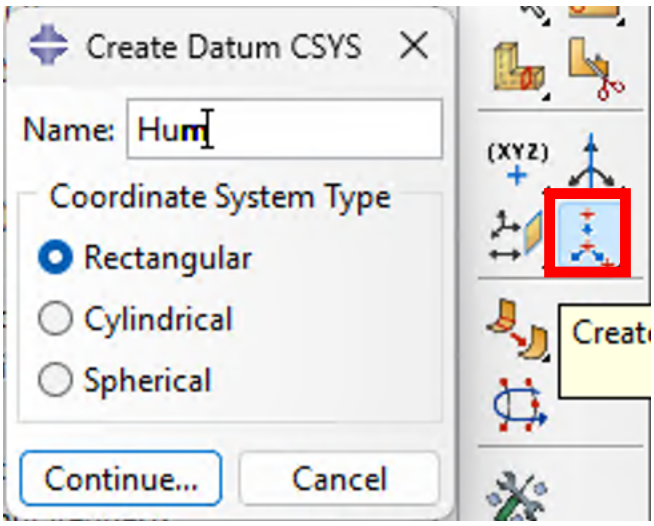
20. In the toolbar, select **Tools** and click on **Reference Point.**



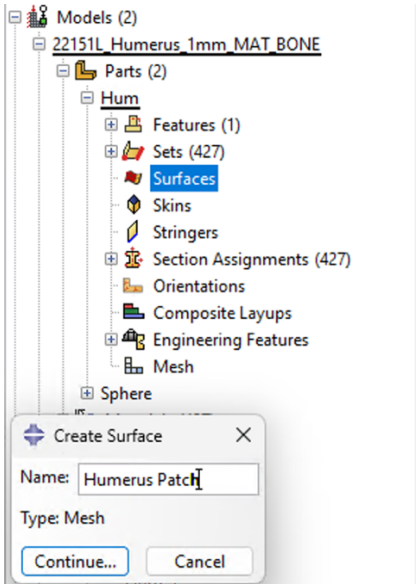
21. Rotate the Humerus so that you are looking at it from the bottom and select a node that is in the middle.
22. This will show up under **Assembly → Features** tree.
    - Edit into an appropriate name.



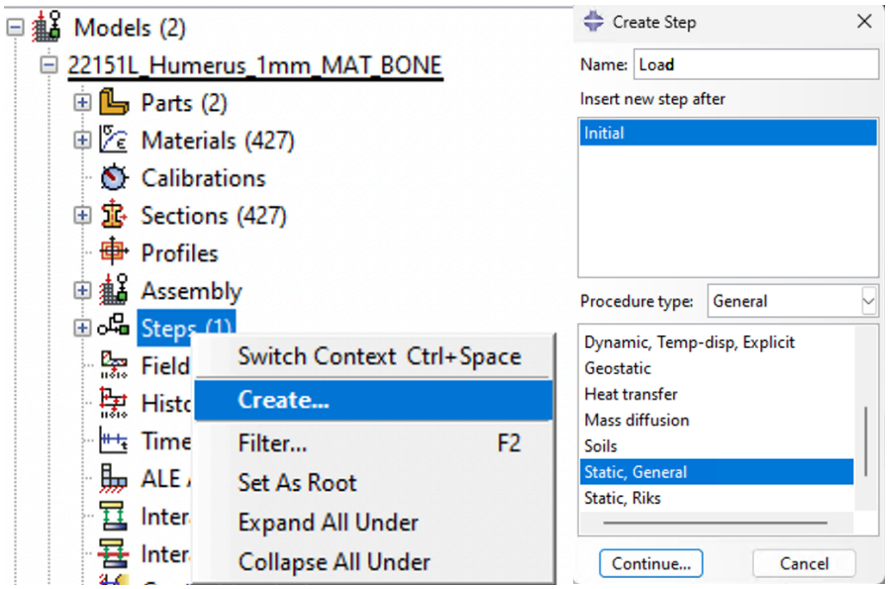
23. Do the same on the top of the humerus.
24. Create coordinates system by clicking the button in red below.
    - Rename it to **Hum**.
    - Select **Rectangular**.
    - The origin will be the center of the sphere of the humeral head.
    - The load will be applied based on the coordinate system.



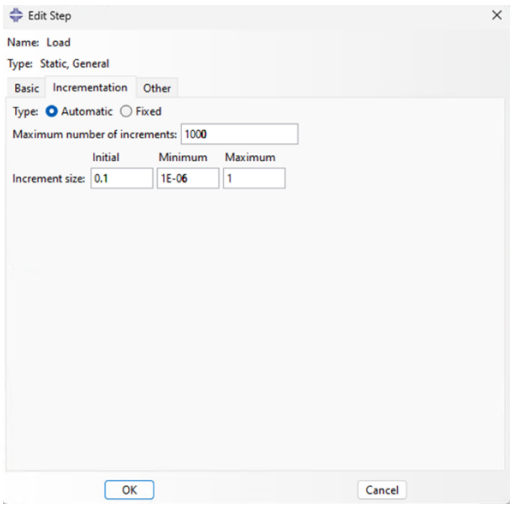
25. Under the Humerus **Model** tree, extend the **Hum** tree and double click **Surfaces**.
    - Name surface into something appropriate (i.e. Humerus Patch).
    - Holding shift, select the contact patch between the Humerus and Scapula. (COMMAND+CONTROL removes contact patch).



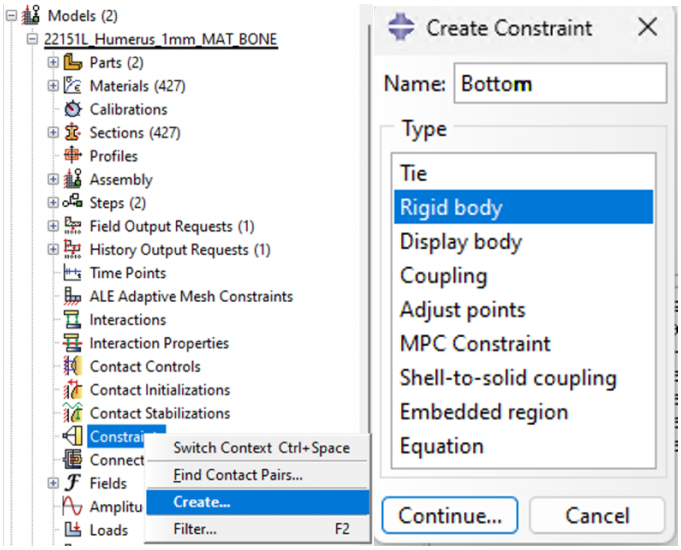
26. To create a load, **Create** a new **Step** and rename it to an appropriate name (i.e. Load).
    - Select Initial.
    - Keep **Procedure Type** to **General** and select **Static, General**.



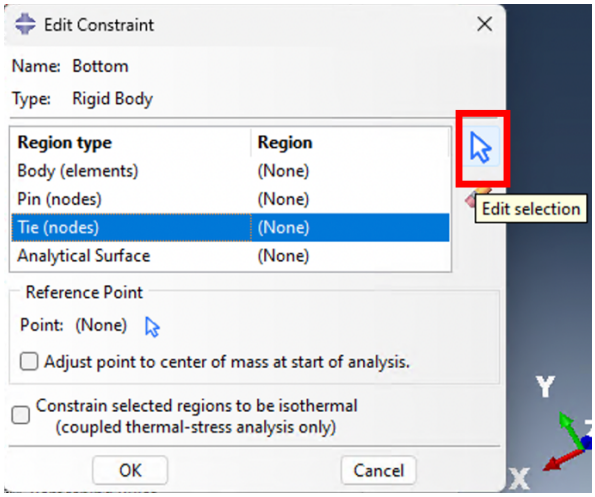
27. A new window will pop up.
    - Under **Incrementation** tab, change to the following:
        - **Maximum number of increments** – 1000
        - **Increment Size** – 0.1
        - **Minimum** – 1E-06
        - **Maximum** – 1
    - Press **OK** after you are done.



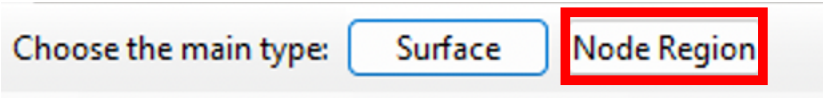
28. **Create** a new **Constraints.**
    - Change to an appropriate name (i.e. Bottom)
    - Change **Type** to **Rigid body**.
    - Select **Continue**.



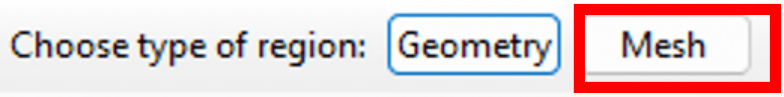
29. Highlight **Tie (nodes)** and select the arrow mouse button to edit selection.



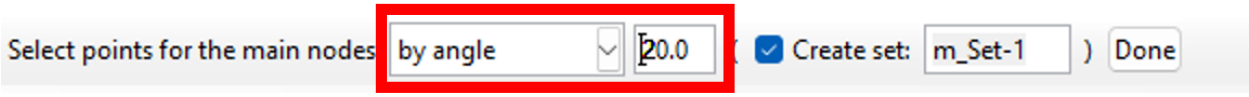
30. Select **Node Region** from the bottom toolbar.



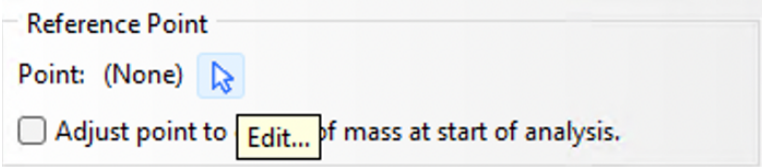
31. Select **Mesh**.



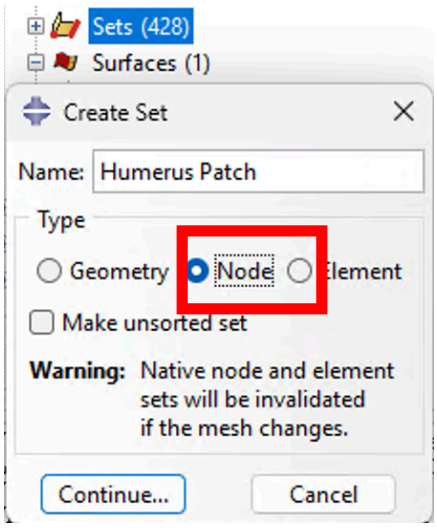
32. Change to **by angle** and leave angle at **20.0** degrees.



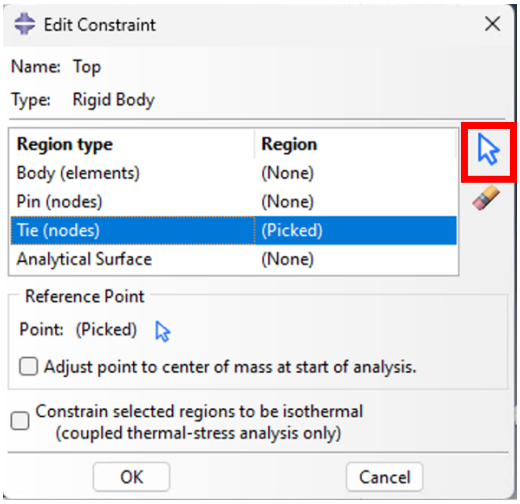
33. Rotate the Humerus to view from the bottom and select the whole bottom region.
34. Can also click on **Sets** on bottom toolbar and select bottom/top section of the humerus.
35. Select arrow mouse button and select **Bottom** reference point.



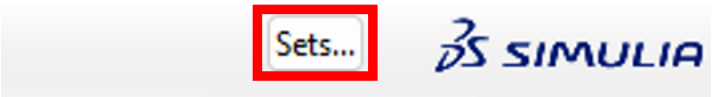
36. Same will be done with the top Humerus Patch but first **Create** another Humerus Patch under **Sets**.
    - Change Name to an appropriate name (i.e. Humerus Patch).
    - Change **Type** to **Node**.
    - Select **Individually** from bottom toolbar and highlight the Humerus Patch
    - Press **Continue**.



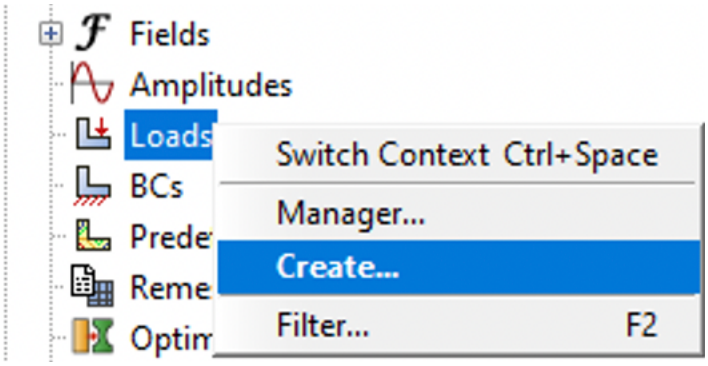
37. For the **Top** constraint, highlight **Tie (nodes)** and press on the mouse button **Edit Selection**.



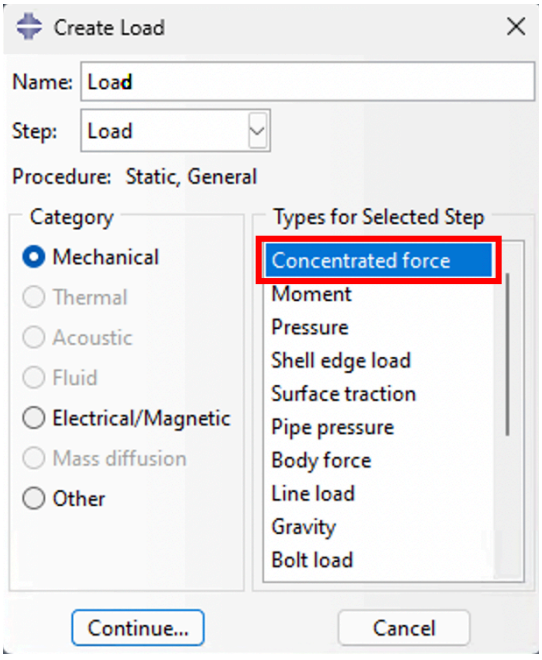
38. Select **Sets** from the bottom toolbar and select the humerus patch previously made.



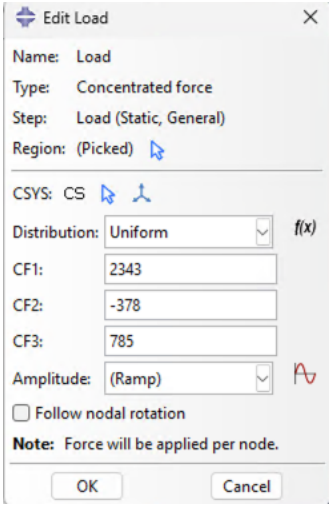
39. Change the reference point in the main window to the **Top** reference point.
40. In the **Loads** tree, right click and **Create** a new one and name appropriately (i.e. Load)



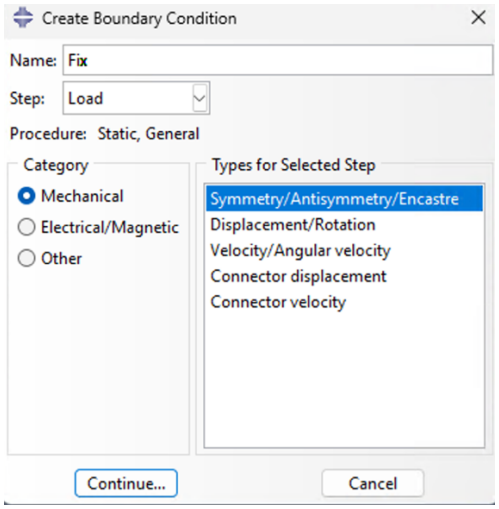
41. In the new window, select the **Load** from the **Steps** that was previously made.
    - The **Types for Selected Step** will be kept at **Concentrated Force**.
    - Click **Continue**.



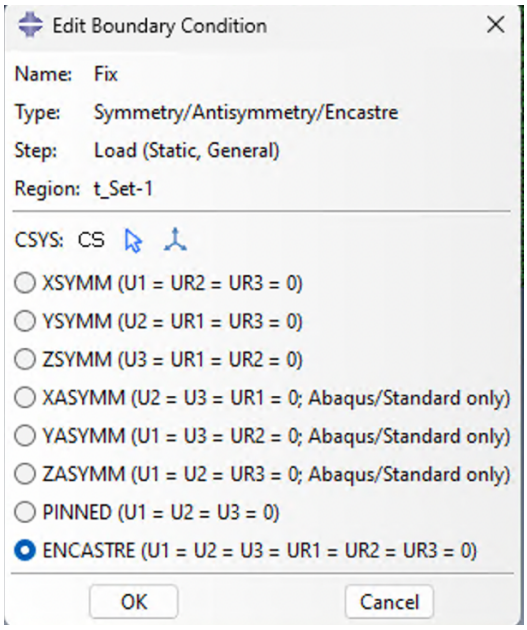
42. Select **Mesh** from bottom toolbar and then select the Humerus Patch from the **Sets** menu.
43. Change the coordinate system (CSYS) into the coordinate system made by clicking on the mouse button.
44. Change the **Region** so that you select the **Top** reference point.
45. Set forces as follows:
    - CF1 – 2343N (z-axis) – lateral
    - CF2 – (-)378N (x-axis) – anterior (left and right) = 2500 x sin(8.7)
    - CF3 – (-)785N (y-axis) – superior (right) = 2500 x sin(18.3)



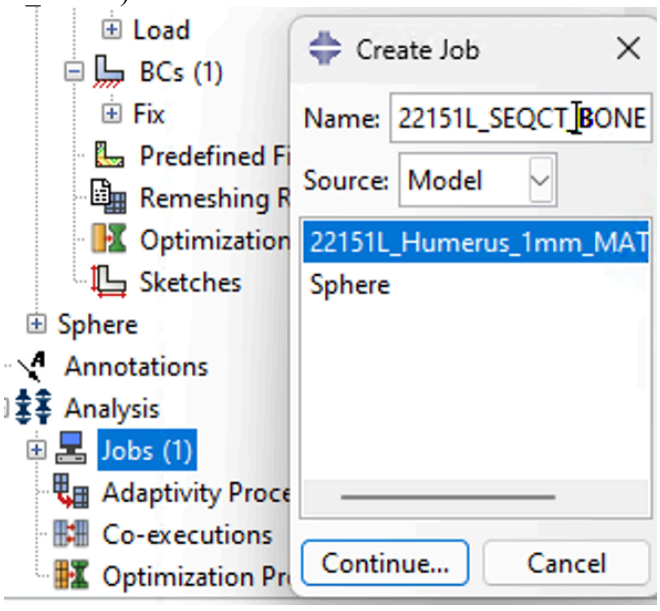
46. In the **BC** tree, right click and **Create** a new boundary condition and name appropriately (i.e. Fix)
    - Category – **Mechanical**
    - Types for Selected Step – **Symmetry/Antisymmetry/Encastre**
    - Click **Continue**.



47. In the Edit Boundary Conditions, select **Encastre** and change the coordinate system to the coordinate system made.
48. Select **Geometry** from the bottom toolbar and select the **Bottom** reference point.



49. In the **Jobs** tree, right click and **Create** a new Job and name appropriately (i.e. 22150L_SEQCT_BONE).



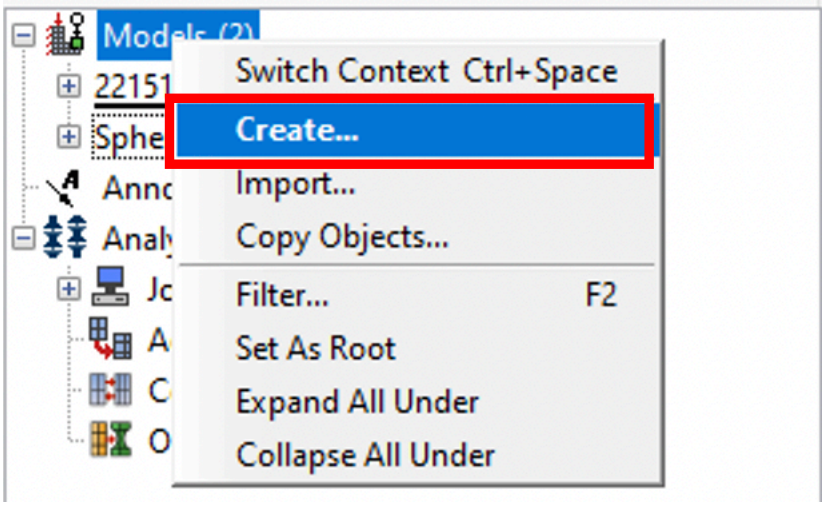
50. Run the Job into a **Data Check** and make sure it is completely processed.
51. Once completely processed, right click and **Write Input** and save in appropriate folder.
52. Make another folder and name it **To Run** and add the .inp file into that folder.
    - This is where everything you are going to run will run.
53. Open **Notepad** from your windows and type the following:
    - (
      abaqus job=22150L_SEQCT_BONE interactive

)
    - The 22150L_SEQCT_BONE is the name of your input file without .inp
54. Save As the Notepad file in the same file as the input file and save it as **Batch.bat** and save it.
    - This will create a batch file so that when you click it, it will run in the background.
55. Double click the batch file.
56. An ODB file will be processed in which strain data can be extracted from.

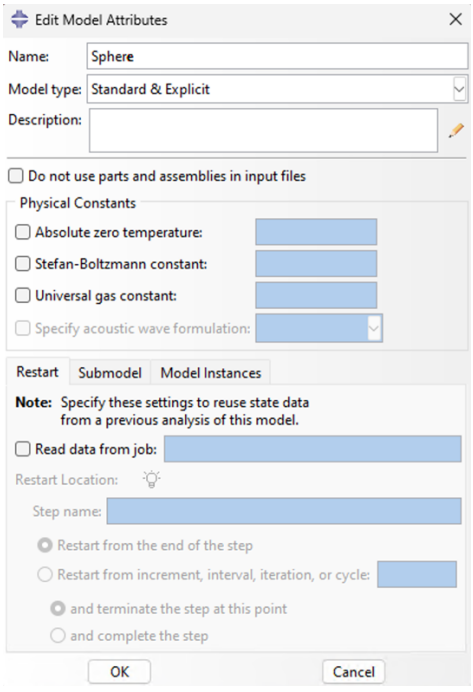
Appendix G

Creating a Sphere to double check point of origin

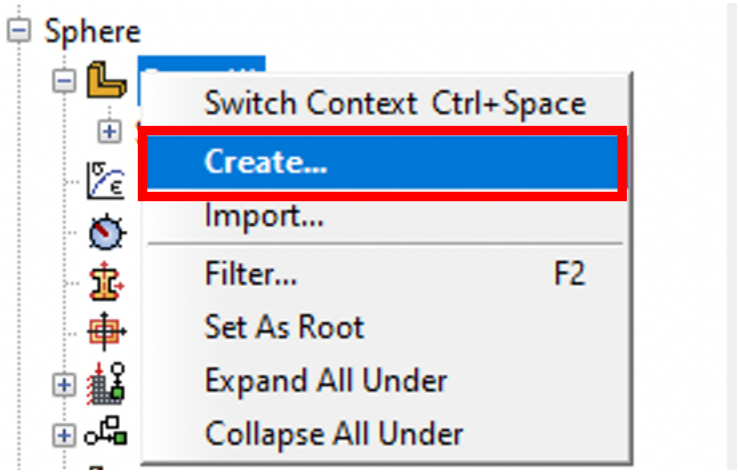
1. Create a new model.



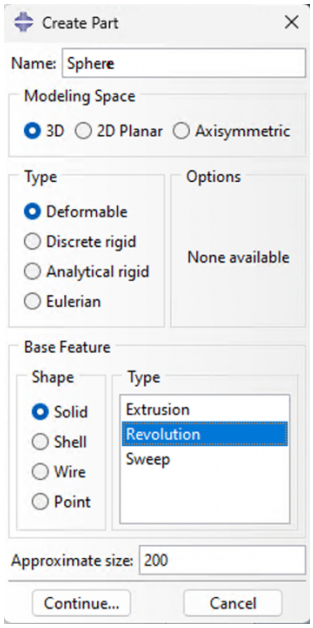
2. Rename model into an appropriate name (i.e. Sphere) and click **OK**.



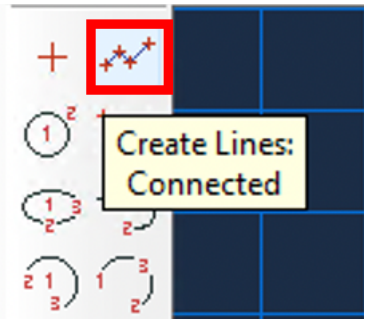
3. Under the **Sphere** tree, expand and **Create** a new **Part**.



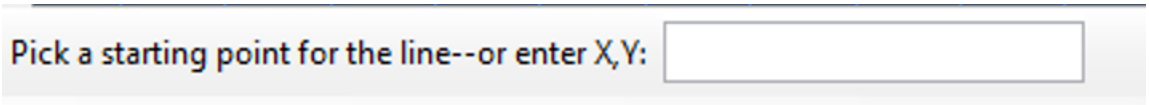
4. Give the **Part** an appropriate name (i.e. Sphere)
    - Set **Modeling Space** to **3D**.
    - Set **Type** to **Deformable**.
    - Set **Base Feature Shape** to **Solid**.
    - Set **Base Feature Type** to **Revolution**.
    - Press Continue.



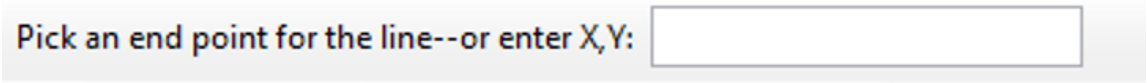
5. We will now sketch the sphere using this button – **Create Lines**



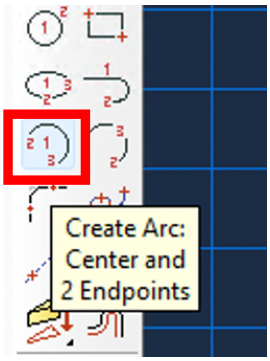
6. Set Starting point for the line by inputting it in the toolbar below or by selecting a point on the graph.



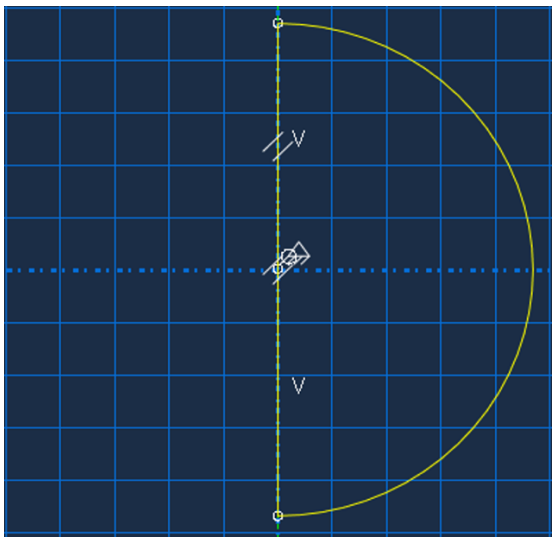
7. Set an end point for the line by inputting it in the toolbar below or by selecting a point on the graph.
    - End point for the line should be the radius of the sphere.



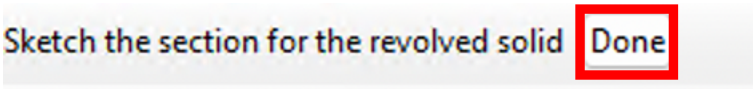
8. Do the same but in the opposite direction, make sure the end point Y-coordinate is in the negative direction.
9. A line should be formed containing 3 different points.
    - The top point of the sphere.
    - The origin.
    - The bottom point of the sphere.
10. The sphere will now be connected using the **Create Arc** button.



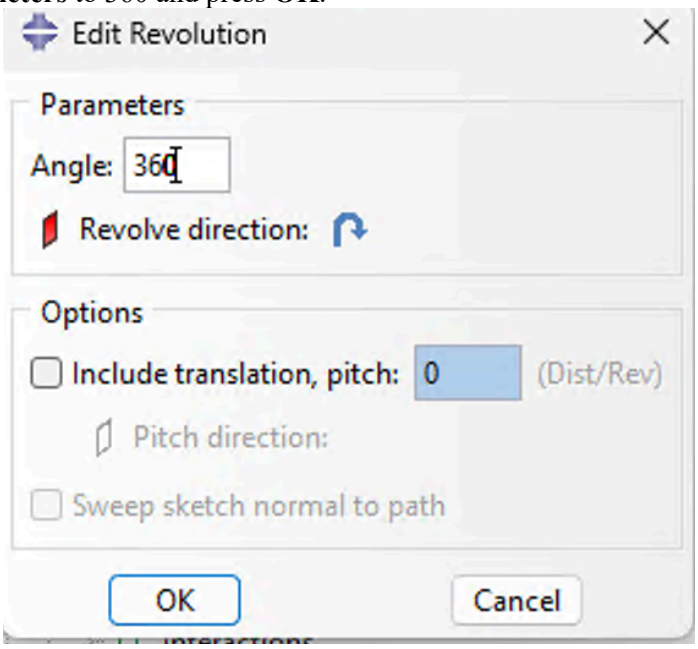
11. Select the end points and origin to form a semi-circle.



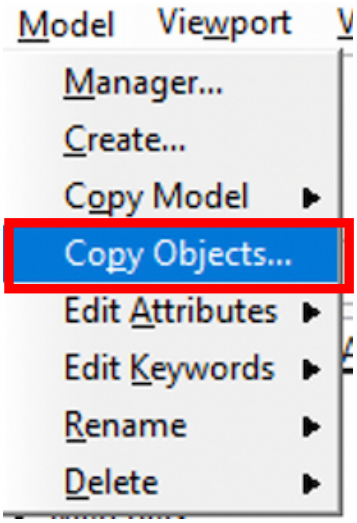
12. Once semi-circle is formed, press **ESC** on keyboard and select **Done** from the toolbar below.



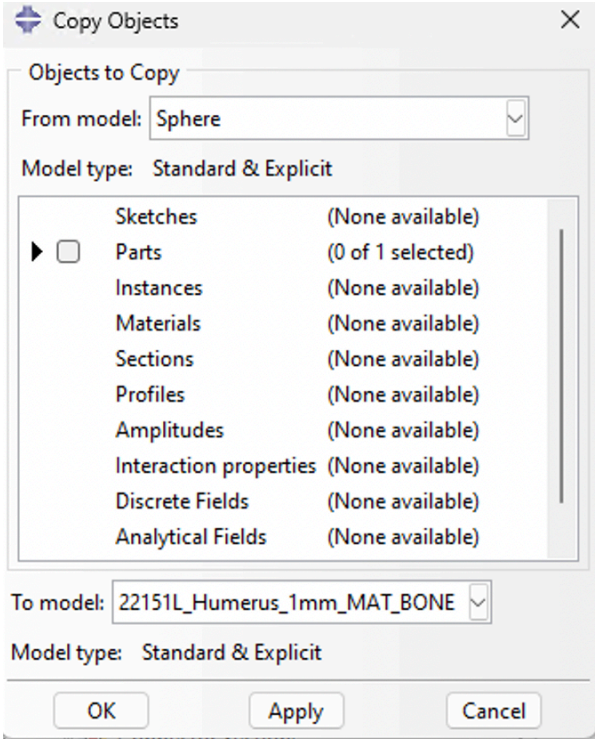
13. Set **Angle Parameters** to 360 and press **OK**.



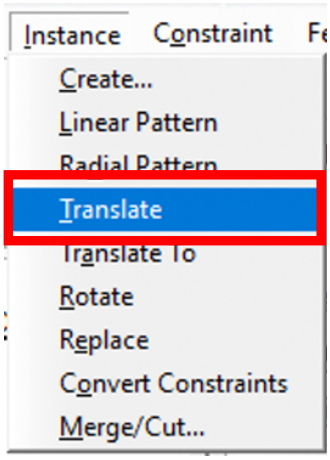
14. In the toolbar menu, select **Model** then **Copy Objects**.



15. Copy the Sphere model to the Humerus model already made and select **Apply**.



16. In the Humerus tree under **Assembly** then **Instances**, the Sphere model will show up.
17. To translate the Sphere to sit in the Humerus, select **Instance** then **Translate** from the toolbar.



18. Select the Sphere then input the point of origin for the Humerus Head below and press **Enter**.

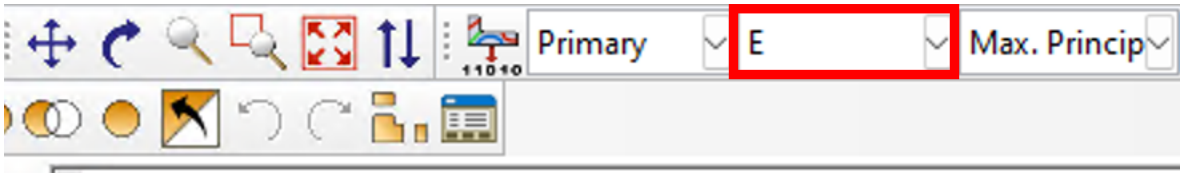
Appendix H

Extracting strain output from Abaqus

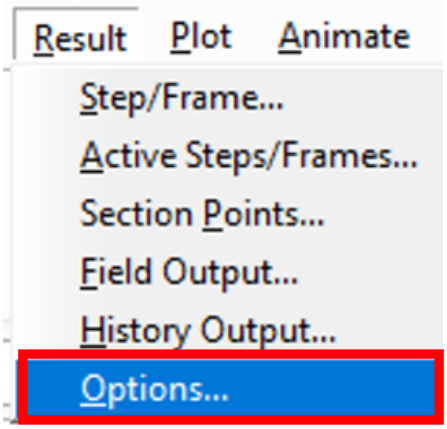
1. Load .inp file containing all boundary conditions and loads into a text editor (e.g. Sublime Text)
2. Add the following code at the end, making sure to add **COORDS** under the "Element Output" line

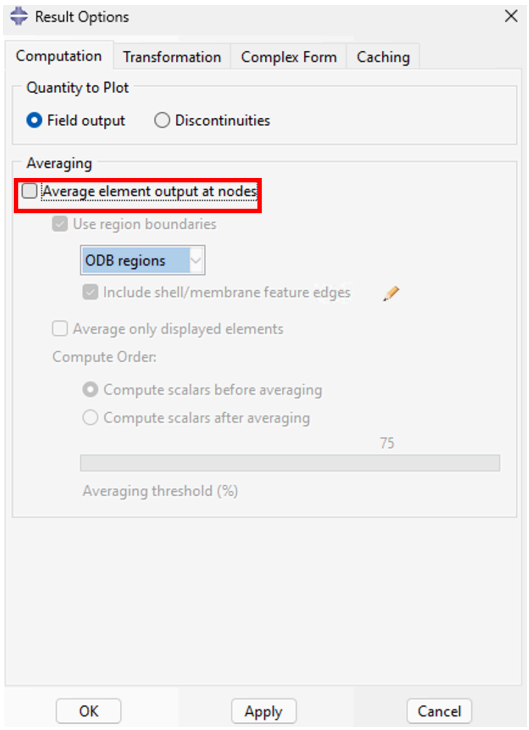
```
52434   **
52435   ** OUTPUT REQUESTS
52436   **
52437   *Restart, write, frequency=0
52438   **
52439   ** FIELD OUTPUT: F-Output-1
52440   **
52441   *Output, field
52442   *Node Output
52443   CF, RF, U
52444   *Element Output, directions=YES
52445   LE, PE, PEEQ, PEMAG, S, COORD
52446   *Contact Output
52447   CDISP, CSTRESS
52448   **
52449   ** HISTORY OUTPUT: H-Output-1
52450   **
52451   *Output, history, variable=PRESELECT
52452   *End Step
52453
```

3. Save and load this .inp file into Abaqus and create a new job under this new file.
4. Run a **Data Check** of this file in an appropriate directory to get a new **ODB** file.
5. Open the ODB file and change to view strain output



6. Extract the strain output without averaging by clicking **Results** then **Options** and deselecting any averaging tabs that are selected.
7. Click **Apply**.

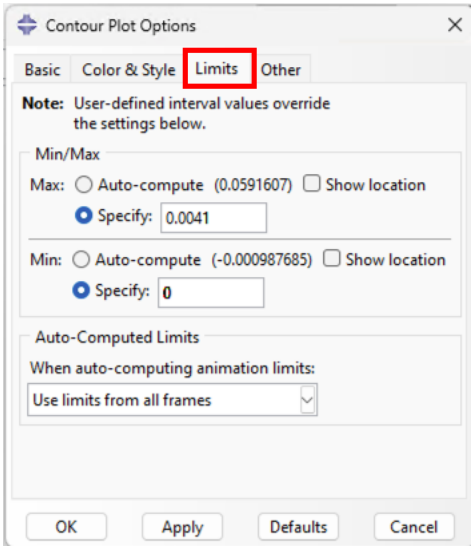




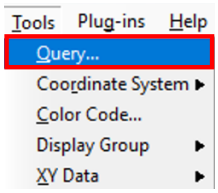
8. Select **Contour Options** to set limits for you maximum/minimum principal strain



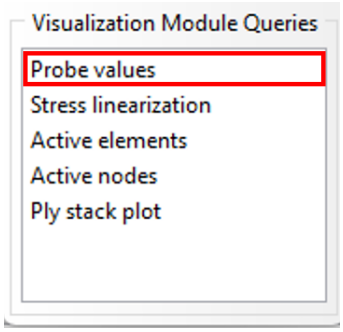
9. Select **Limit** from the top bar and specify your Max/Min principal strain as needed.
10. Click **Apply**



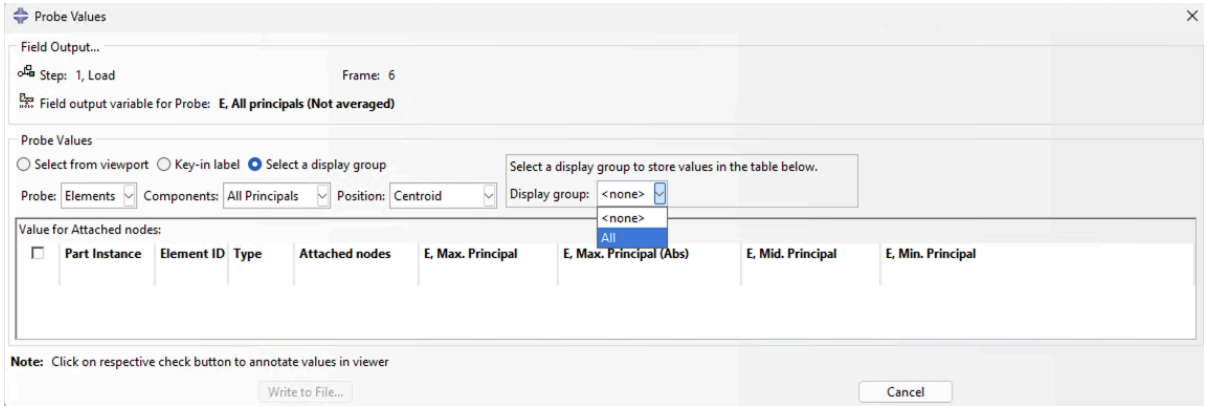
11. To extract Max. Principal and Min. Principal, make sure you are on the final frame and then select **Tools** from the toolbar on the top then **Query**.



12. Select **Probe Values**.



13. Select probe values as needed to obtain Max/Min principal strains for intended elements/nodes from desired position.
14. To obtain data of all elements, select **All** for **Display group**. This will load all strain data for each element in the model



15. Once completed, click **Write to File…** at the bottom and save at an appropriate place.

Glossary

aBMD – Areal bone mineral density

BMD – Bone Mineral Density

BONE – Boneplus reconstruction kernel

CRPP – Closed reduction and percutaneous pinning

DEQCT – Dual Energy Quantitative Computed Tomography

DEXA – Dual-energy X-Ray absorptiometry

FEA – Finite Element Analysis

FEM – Finite Element Modeling

FOOSH – Fall on outstretched hand

GHJ – Glenohumeral Joint

GT – Greater tuberosity

HA – Hemi arthroplasty

HU – Hounsfield Unit

IGHL – Inferior Glenohumeral Ligament

MGHL – Middle Glenohumeral Ligament

ORIF – Open reduction and internal fixation

PHF – Proximal humerus fracture

ROI – Region of interest

RSA – Reverse shoulder arthroplasty

SEQCT – Single Energy Quantitative Computed Tomography

SGHL – Superior Glenohumeral Ligament

STD – Standard reconstruction kernel

vBMD – Volumetric Bone Mineral Density